

Introduction

This portfolio contains a collection of selected works from my undergraduate engineering courses, project-based learning experiences, and capstone design efforts. Each document reflects the progression of technical skills, engineering reasoning, and systems thinking I have developed during my academic career.

Contents

1	Autonomous Aerospace Systems	2
2	Dynamics and Vibrations	51
3	Numerical Methods	77
4	SEC Ignite Competition	115
5	Mechanical Modeling	132
6	Mechanical Measurements	145
7	Solid Mechanics	155
8	Interdisciplinary Engineering ABET Requirements	183
9	Grand Challenges Scholars Program	189
10	Science Influencers Program	210
11	L'SPACE Mission Concept Academy	246

1. Autonomous Aerospace Systems

Ian Wilhite

Aero 489 – Autonomous Systems

2/5/2025

Preliminary (10 points)

- 1) As a search problem, the state must contain the rovers location, the action must include rover traversal in all directions (and account for edge collision), and the search problem must also track the path cost in addition to the state. The world must contain cells with danger and a goal (science).
- 2) Because the environment is known, static, and fully observable, our rover begins the problem knowing all necessary information to search, the information it knows cannot change, and the information it knows is complete. Because it has all information it needs, and that information cannot change, it is not necessary to sense.

Basic Search (20 points)

- 1) Not all algorithms find the optimal solution: Depth-First Search (DFS) does not *always* find the optimal solution, because DFS will pick one potential path from its options and follow it to completion, and will return the first feasible solution it finds, which may or may not be the optimal solution, while other algorithms prioritize less costly solutions. BFS is less efficient than UCS because it must search all parallel paths but significantly outperforms DFS because it is more likely to find a *more* efficient solution in sweeping its options laterally. A* is the most efficient solution because it is the only informed search of the group and can rely on the Manhattan heuristic to approximate the goodness of a cell towards the optimal solution. For random problems, not all methods find the “correct”/optimal solution.
 - a. Optimal Solution:

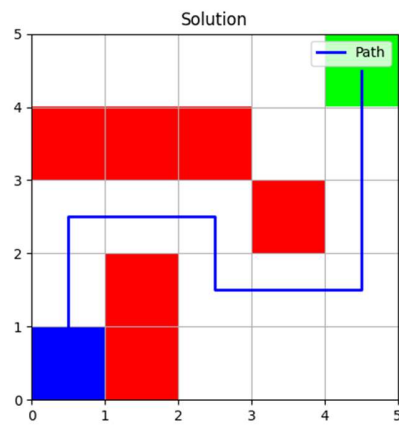


Fig. 1, sample problem with provided solution

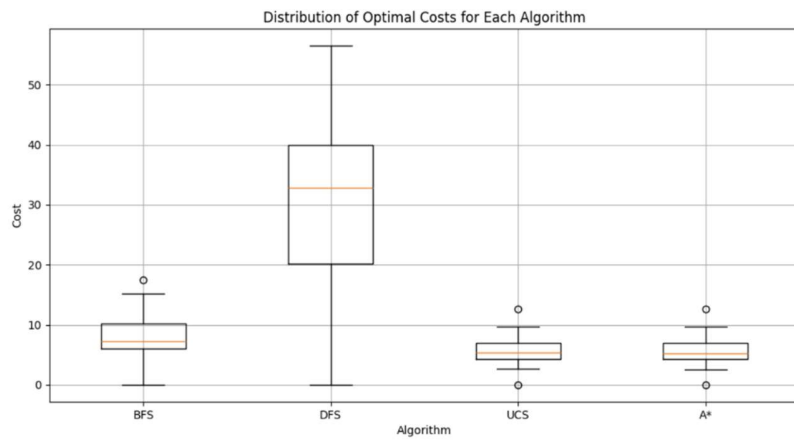


Fig. 2, Costs found by each algorithm

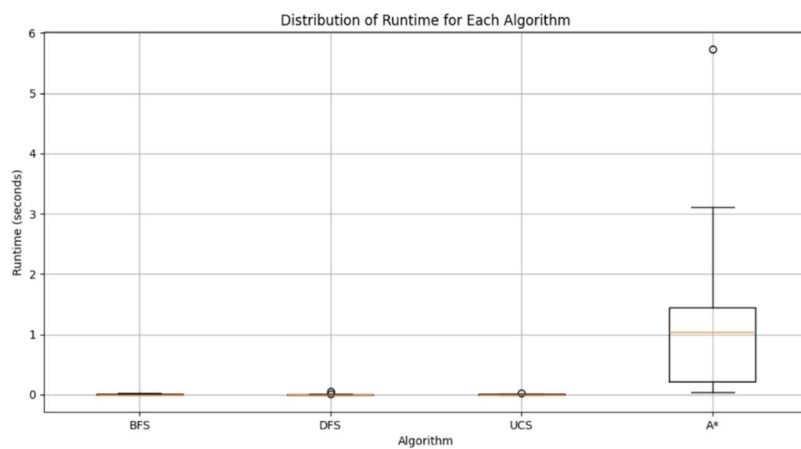


Fig. 3, Runtimes taken by each algorithm

- 2) In cost performance, the DFS did not find the optimal solution due to its tendency to burrow into an incorrect solution and return a local, suboptimal, solution. A* had a much larger runtime to find the solution. This means that the optimal search to use for this situation would be UCS.

Average Cost and Runtime for Each Algorithm:

BFS: Average Cost = 22.25, Average Runtime = 0.0032 seconds

DFS: Average Cost = 319.75, Average Runtime = 0.0032 seconds

UCS: Average Cost = 22.25, Average Runtime = 0.0035 seconds

A*: Average Cost = 22.25, Average Runtime = 0.7053 seconds

Fig. 4, Code output of search algorithms without Danger

- 3) By allowing the search to enter dangerous cells with a penalty, many of the less efficient algorithms average goes up by the increase of possible-but-less-optimal solutions, while A* can take the most advantage of the new opportunity and is the only algorithm to decrease its average cost. All algorithms required more runtime (about double) to search the larger pool of possible solutions.

Average Cost and Runtime for Each Algorithm:

BFS: Average Cost = 34.14, Average Runtime = 0.0073 seconds

DFS: Average Cost = 667.95, Average Runtime = 0.0039 seconds

UCS: Average Cost = 22.52, Average Runtime = 0.0104 seconds

A*: Average Cost = 21.29, Average Runtime = 1.3169 seconds

Fig. 5, Code output of search algorithms with Danger

Part 2:

Non-Deterministic World (30 points)

- 1) Changes:
 - a. Creating transition_with_failure function that only moves the rover 75% of the time, and leaves the rover in its current state 25% of the time.
 - b. Creating a transition_with_danger_and_failure function that is identical to the transition_with_danger except it calls the transition_with_failure for the base transition function then adds danger to the cost.
- 2) I believe that the solution will look similar to the optimal solution found by A*, only with nested conditions such that each step will fall into a conditional while loop where it will perform each action sequentially until the path is complete.
- 3) Yes, the algorithm completes the search, but no, it does not come close to other deterministic methods in terms of performance. It is not reasonable to compare

these, however, because the and-or search cannot assume that each function will work, it is extending additional effort to branch out along each potential option, and is also searching the cases in which the rover does not move, however this causes additional computation as it is simply in the same situation it previously was. It is worth noting that the And-Or search implemented returned solutions similar to those generated with a traditional Depth-First-Search.

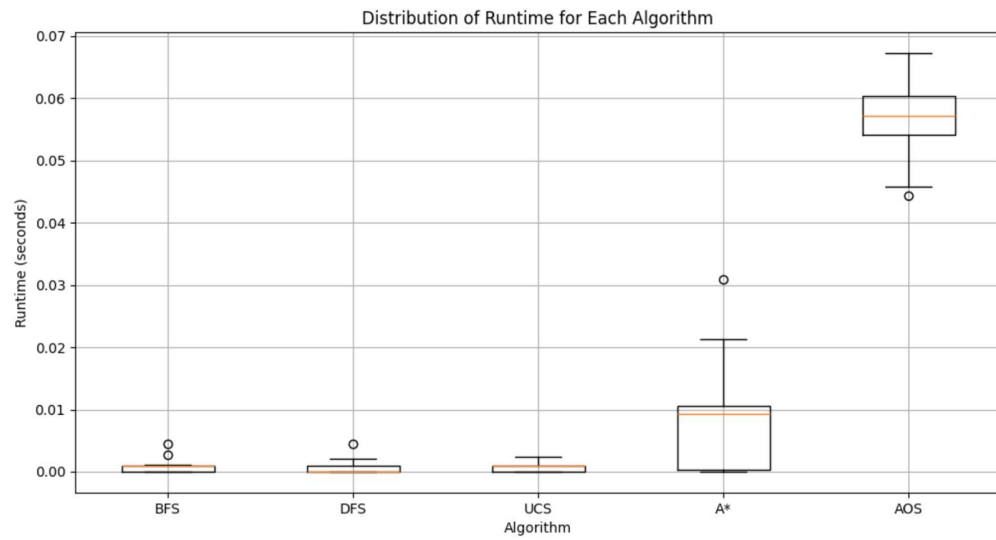


Fig. 6, Runtimes with Danger including AOS

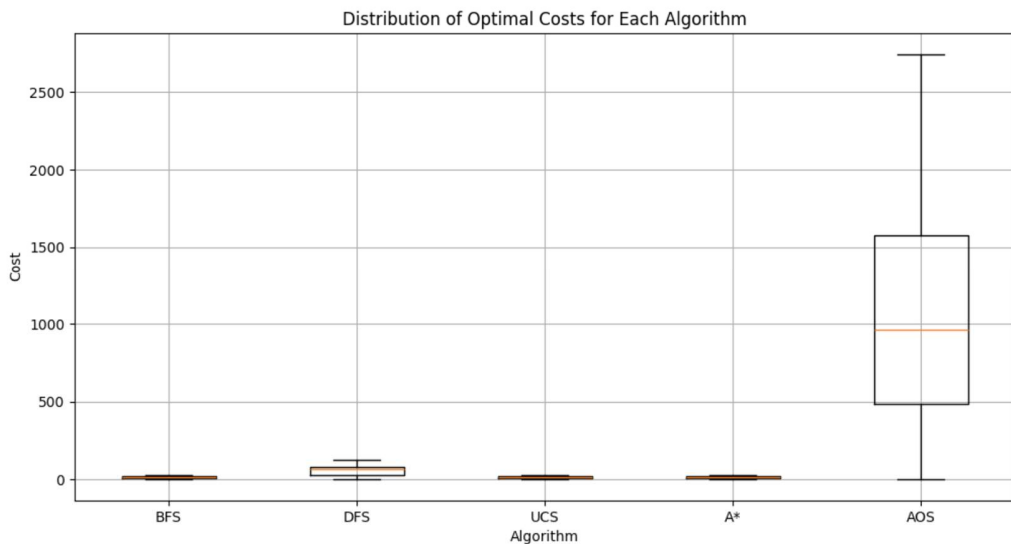


Fig. 7, Costs with Danger including AOS

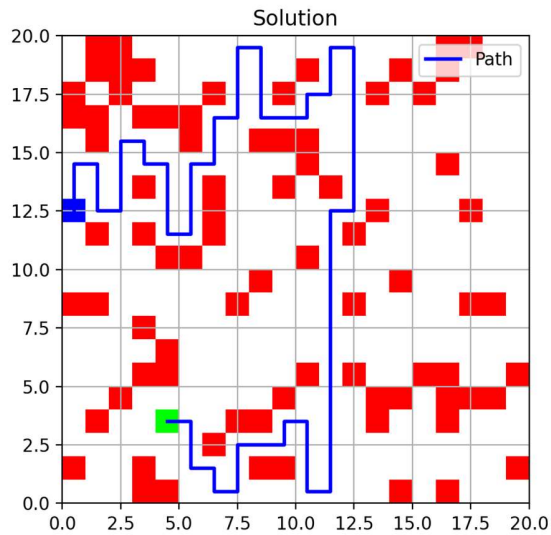


Fig. 8, 1st Sample AOS search solution

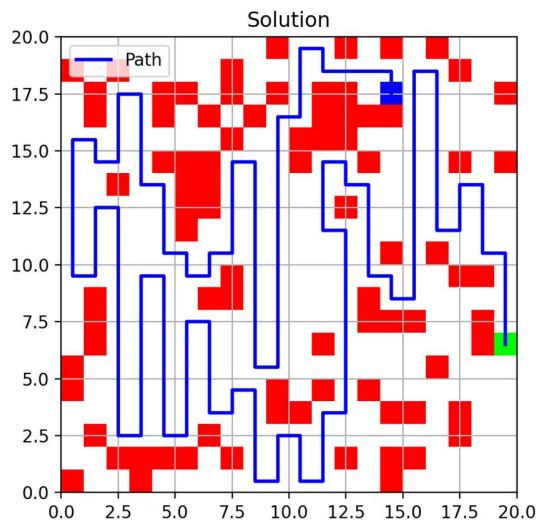


Fig. 9, 2nd Sample AOS search solution

4) Plots provided along with a sample of the path generated from the function.

```
Average Cost and Runtime for Each Algorithm:  

BFS: Average Cost = 14.06, Average Runtime = 0.0009 seconds  

DFS: Average Cost = 76.88, Average Runtime = 0.0005 seconds  

UCS: Average Cost = 9.58, Average Runtime = 0.0012 seconds  

A*: Average Cost = 9.29, Average Runtime = 0.0083 seconds  

AOS: Average Cost = 164.13, Average Runtime = 0.0010 seconds
```

Fig. 10, Code output with Danger including AOS

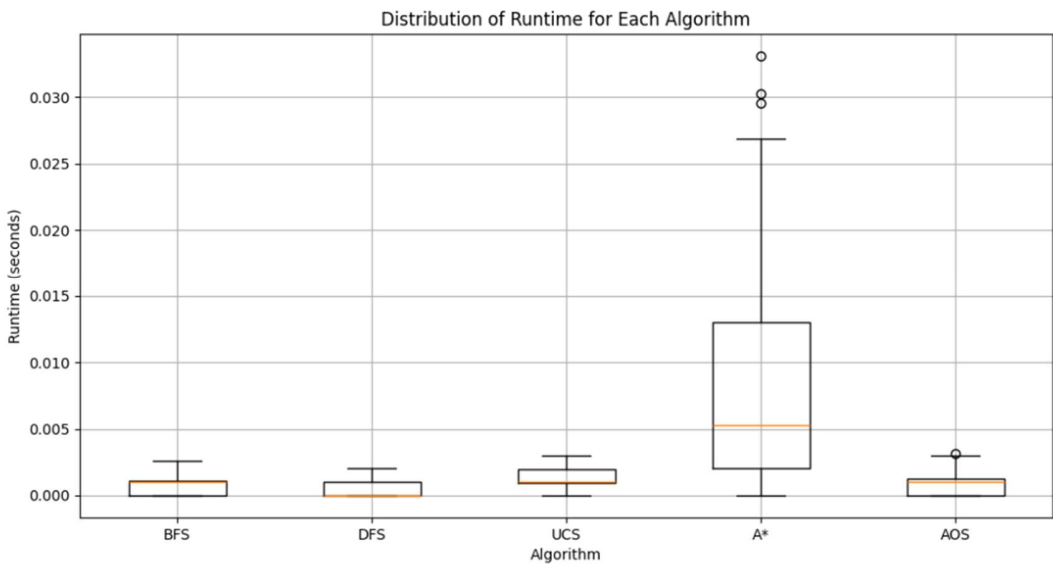


Fig. 11, Runtimes with Danger including AOS

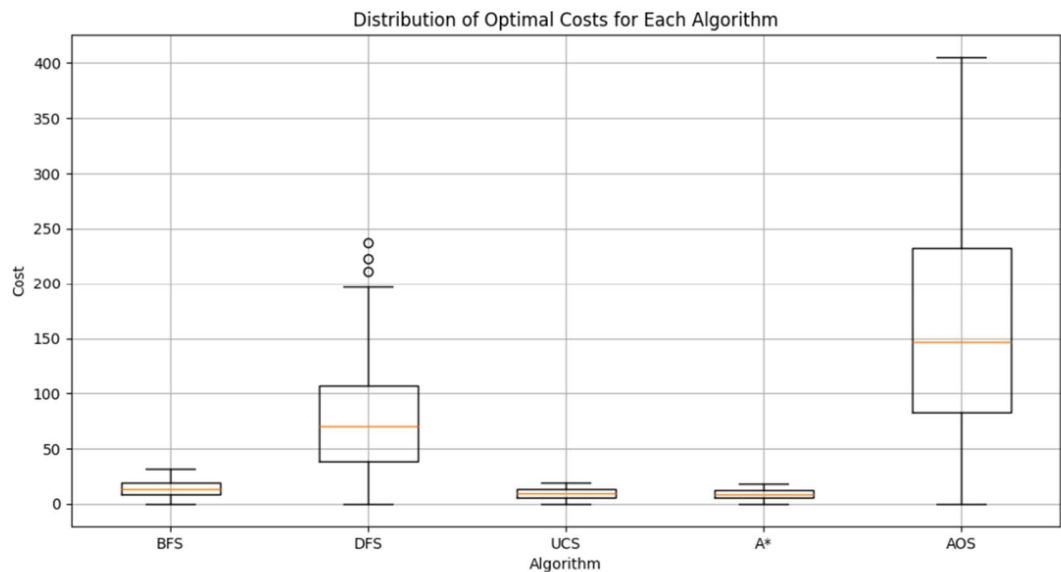


Fig. 12, Costs with Danger including AOS

Unknown World (10 points + 10 bonus)

- 1) To search the world without knowing the location of the alpha cell, a new heuristic would need to be developed for A*, involving the closeness using the spectrometer, given that the conditions for the search heuristic can be met. The noise must not break the admissibility of the heuristic, which a sensor would likely not do so long as the majority of the noise comes from offset and proportional error, and that very little comes from randomness error.

Short questions (10pts)

- 1) Syntax vs semantic
 - a. Syntax is the structure of the notation for the problem. Semantics are the intended meaning of the problem.
 - b. The difference between the two can arise when the syntax of the problem can “misunderstand” the intended result, like in the “everybody loves somebody” example in class that results in one “somebody” that everybody loves.
- 2) Predicate vs Function
 - a. A predicate is a Boolean logical statement that evaluates to true or false. A function maps an input to an output and can return different data types. A predicate can be viewed as a type of function that only returns a Boolean.
 - b. The IsEven(int num) returns [True, False] and would be considered a **predicate**, because the argument is a boolean.
 - c. The SquareNum(int num) returns [int squaredNum], and would be considered a **function** because the return argument is not a boolean.
- 3) Action schema
 - a. The action schema is the notation that describes the outcome of when a given action is applied to an object in a state.
- 4) Ground atomic sentence
 - a. A ground atomic sentence is one that explains a particular relationship or fundamental existence of the world. Ie: Married(John, Jane)
- 5) Database vs standard FOL semantics
 - a. Database semantics assume that information not explicitly given is false.
 - b. FOL semantics will not assume anything about fact, and will claim that it could be either true or false.

Problem 1: FOL

a) Tell rules

```
KB_Family = FolKB([  
    expr('Married(h, w) ==> Married(w, h)'),  
    expr('Child(c, p) ==> Parent(p, c)'),  
    expr('Parent(p, s1) & Parent(p, s2) & Different(s1, s2) ==> Sibling(s1, s2)'),  
    expr('Married(b, w) & Sibling(w, s) ==> BrotherInLaw(b, s)'),  
    expr('Married(s, h) & Sibling(h, b) ==> SisterInLaw(s, b)'),  
    expr('Parent(p, c) ==> Ancestor(p, c)'),  
    expr('Parent(p, c) & Ancestor(c, a) ==> Ancestor(p, a)'),  
    expr('Parent(a, b) & Parent(b, c) ==> Grandparent(a, c)'),  
    expr('Parent(a, b) & Parent(b, c) & Parent(c, d) ==> GreatGrandparent(a, d)'),  
    expr('Child(c, h) & Married(h, w) ==> Child(c, w)')  
])
```

b) Tell facts

```
59     print(f'adding facts to KB...')  
60  
61     KB_Family.tell(expr('Married(George, Mum)'))  
62     KB_Family.tell(expr('Married(Elizabeth, Phillip)'))  
63     KB_Family.tell(expr('Married(Edward, Sophie)'))  
64     KB_Family.tell(expr('Married(Andrew, Sarah)'))  
65     KB_Family.tell(expr('Married>Anne, Mark)'))  
66     KB_Family.tell(expr('Married(Diana, Charles)'))  
67     KB_Family.tell(expr('Married(Spencer, Kydd)'))  
68  
69     KB_Family.tell(expr('Parent(George, Elizabeth)'))  
70     KB_Family.tell(expr('Parent(Elizabeth, William)'))  
71     KB_Family.tell(expr('Parent(Elizabeth, Harry)'))  
72  
73     KB_Family.tell(expr('Child(Elizabeth, George)'))  
74     KB_Family.tell(expr('Child(Margaret, George)'))  
75     KB_Family.tell(expr('Child(Diana, Spencer)'))  
76  
77     KB_Family.tell(expr('Child(Charles, Elizabeth)'))  
78     KB_Family.tell(expr('Child>Anne, Elizabeth)'))  
79     KB_Family.tell(expr('Different(Charles, Anne)'))  
80     KB_Family.tell(expr('Child(Andrew, Elizabeth)'))  
81     KB_Family.tell(expr('Child(Edward, Elizabeth)'))  
82     KB_Family.tell(expr('Different(Andrew, Edward)'))  
83  
84     KB_Family.tell(expr('Child(William, Charles)'))  
85     KB_Family.tell(expr('Child(Harry, Charles)'))  
86     KB_Family.tell(expr('Different(William, Harry)'))  
87     KB_Family.tell(expr('Child(Peter, Anne)'))  
88     KB_Family.tell(expr('Child(Zara, Anne)'))  
89     KB_Family.tell(expr('Different(Peter, Zara)'))  
90     KB_Family.tell(expr('Child(Beatrice, Andrew)'))  
91     KB_Family.tell(expr('Child(Eugenie, Andrew)'))  
92     KB_Family.tell(expr('Different(Eugenie, Beatrice)'))  
93     KB_Family.tell(expr('Child(Louise, Edward)'))  
94     KB_Family.tell(expr('Child(James, Edward)'))  
95     KB_Family.tell(expr('Different(Louise, James)'))  
96  
97     KB_Family.tell(expr('Parent(George, Elizabeth)'))  
98     KB_Family.tell(expr('Parent(Elizabeth, William)'))  
99     KB_Family.tell(expr('Parent(Elizabeth, Harry)'))  
100    KB_Family.tell(expr('Parent(Charles, William)'))  
101    KB_Family.tell(expr('Parent(Charles, Harry)'))  
102    KB_Family.tell(expr('Different(Harry, William)'))  
103    KB_Family.tell(expr('Different(Beatrice, Eugenie)'))  
104  
105    print(f'facts added to KB.')
```

c) Ask

- a. Elizabeth's grandchildren
- b. Eugenie's siblings
- c. Zara's great-grandparents
- d. Eugenie's ancestors

```
[Running] python -u "c:\Users\ianwi\OneDrive\Documents\S4\AER0489\aima-python-61d695b37c6895902081da1f37baf645
creating KB...
KB created.
adding facts to KB...
facts added to KB.
asking Q1
Q1: [{x: Harry}, {x: William}, {x: James}, {x: Louise}, {x: Zara}, {x: Peter}, {x: Beatrice}, {x: Eugenie}]
asking Q2
Q2: [{x: Beatrice}]
asking Q3
Q3: [{x: George}, {x: Mum}]
asking Q4
Q4: []
exiting

[Done] exited with code=0 in 234.011 seconds
```

```
[Running] python -u "c:\Users\ianwi\OneDrive\Documents\S4\AER0489\aima-python-61d695b37c6895902081da1f37baf645
creating KB...
KB created.
adding facts to KB...
facts added to KB.
asking Q1
Q1: []
asking Q2
Q2: [{x: Beatrice}]
asking Q3
Q3: [{x: George}, {x: Mum}]
asking Q4
Q4: [{x: George}, {x: Mum}]
exiting

[Done] exited with code=0 in 297.549 seconds
```

Problem 2: Europa Rover

1) Domain:

- a. Requirements
 - i. STRIPS is the most common basic notation that the PDDL system will use FOL to model the system.
- b. Predicates (variables to track)
 - i. Rover location – the location of the rover on Europa (note: we do not need to track location alpha because it is static and does not move)
 - ii. HasBiosample – whether or not the rover has obtained the sample
 - iii. HasComponent – whether or not the rover has the component
 - iv. BatteryCharged – whether or not the battery is charged

- v. Drilled (based on location) – whether or not the current location has been drilled
- vi. SoftwareUpdated – whether or not the rover software has been updated
- vii. PreheatedDrill – whether or not the drilled has been preheated
- viii. AnalysisCompleted – whether or not the analysis is complete
- ix. ContactAvailable – whether or not transmission contact is available
- x. DataTransmitted – whether or not the data has been transmitted (and the mission has been completed)

c. Actions

- i. Charge
- ii. Move
- iii. Update software
- iv. Retrieve components
- v. Preheat drill
- vi. Drill
- vii. Analyze sample
- viii. Transmit data

2) See attached files.

Ian Wilhite

AERO 489: Selva, Valasek

3/4/2025

Question 1: Formulate this problem as a Markov Decision Process. Specifically, provide the states, actions, rewards, and transition model.

State:

- The location of the rover within the world (x,y)
- The danger of the cells, as stored within the grid.

Actions:

- Move Up, (x,y) -> (x, y + 1)
- Move Right, (x,y) -> (x + 1, y)
- Move Down, (x,y) -> (x, y - 1)
- Move Left, (x,y) -> (x - 1, y)

Rewards:

- Move cost: -0.05 (included on unsuccessful moves)
- Goal reward: +1.00
- Crater cost: -1.00

Transition Model (for all actions):

- Move successfully -> 80%
- Stay in current cell -> 10%
- Slide towards center of grid -> 10%

Question 2: Write code in Python that implements the environment. This should include:

- A function to create a fixed test world (e.g., start cell in (1,1), goal in (5,5), danger cells in (1,4), (2,4), (2,2), (3,4), crater in (4,3)).

```
196 def create_test_problem_5x5(transition): # generates test
197     problem instance
198     grid = np.empty((5, 5), dtype=object)
199     for i in range(5):
200         for j in range(5):
201             science = 0
202             danger = 0
203             grid[i, j] = GridCell(science=science,
204                                   danger=danger)
205             grid[0][3].danger = 0.5
206             grid[1][3].danger = 0.8
207             grid[1][1].danger = 0.9
208             grid[2][3].danger = 0.7
209             grid[3][2].danger = 0.5
210             grid[4][4].science = 1.0
211             initial_state = RoverState(0, 0)
212             return Problem(initial_state, goal_test, grid,
213                            transition_function=transition)
```

- A function to create a random world of this type

```
154 def generate_random_problem(transition): # generates random problem instance of size N
155     n = N
156     grid = np.empty((n, n), dtype=GridCell)
157     n_unsafe = 0
158
159     # Step 1: Initialize the grid with danger values
160     for i in range(n):
161         for j in range(n):
162             if random.random() < percent_cells_with_danger: # 20% chance of an unsafe cell
163                 danger = random.uniform(0.50001, 1)
164                 n_unsafe += 1
165             else: # Safe cell
166                 danger = random.uniform(0, 0.49999)
167
168             grid[i, j] = GridCell(science=0, danger=danger)
169
170     # Step 2: Set the goal cell within the safe cells (with danger < 0.5)
171     (goal_x, goal_y) = np.floor(random.uniform(0, n-1)), np.floor(random.uniform(0, n-1))
172     while (True): # bogo find, but it's fine
173         (start_x, start_y) = np.floor(random.uniform(0, n-1)), np.floor(random.uniform(0, n-1))
174         if goal_x != start_x and goal_y != start_y:
175             grid[goal_x, goal_y].science = 1.0
176             grid[goal_x, goal_y].danger = 0.0
177             break
178
179     # Step 3: Find a random initial position that corresponds with a safe cell
180     while True: # bogo find, but it's fine
181         initial_x, initial_y = random.randint(0, n-1), random.randint(0, n-1)
182         if grid[initial_x, initial_y].danger <= 0.5: # Only pick a safe cell
183             initial_state = RoverState(initial_x, initial_y)
184             break
185
186     return Problem(initial_state, goal_test, grid, transition)
187
```

- Functions implementing the transition model and the reward function. Given a current state and action, they should return the next state and the reward respectively (or you can do this in the same function).

```

def transition_model(state, action, grid):
    """ Implements the stochastic movement model with 80% success, 10% stay, and 10% slide. """

    x, y = state.x, state.y
    # Define sliding move (towards the center of the grid)
    center_x, center_y = (N - 1) / 2, (N - 1) / 2 # 2, 2 for 5x5 grid

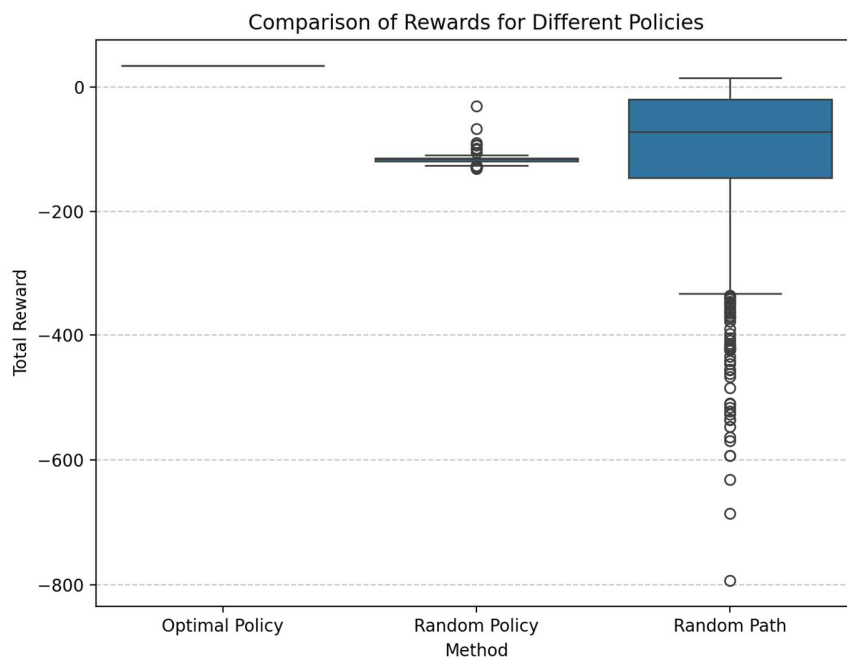
    # Apply probability
    rand_value = random.random()
    if rand_value < 0.8: # 80% chance to move as intended
        new_x = x + action[0]
        new_y = y + action[1]
    elif rand_value < 0.9: # 10% chance to stay in place
        new_x, new_y = x, y
    else: # 10% chance to slide towards the center
        if x < center_x: new_x = x + 1
        elif x > center_x: new_x = x - 1
        if y < center_y: new_y = y + 1
        elif y > center_y: new_y = y - 1

    # Check if move is valid (not out of bounds)
    if 0 <= new_x < 5 and 0 <= new_y < 5:
        return RoverState(new_x, new_y)
    return state # Stay in place if movement is invalid

def reward_function(state, grid):
    """ Returns the reward associated with the given state. """
    if grid[state.x][state.y].is_goal:
        return 1.00 # Goal reward
    if grid[state.x][state.y].danger >= 0.5:
        return -1.00 # Crater penalty
    return -0.05 # Move cost

```

Question 3: Write code for an agent that follows a given policy, specified as a look up table (state, action). Run an agent using a random policy (i.e., that moves randomly in this environment until reaching a terminal state) in the test problem 1000 times. Make a boxplot of the total undiscounted rewards collected by the agent.

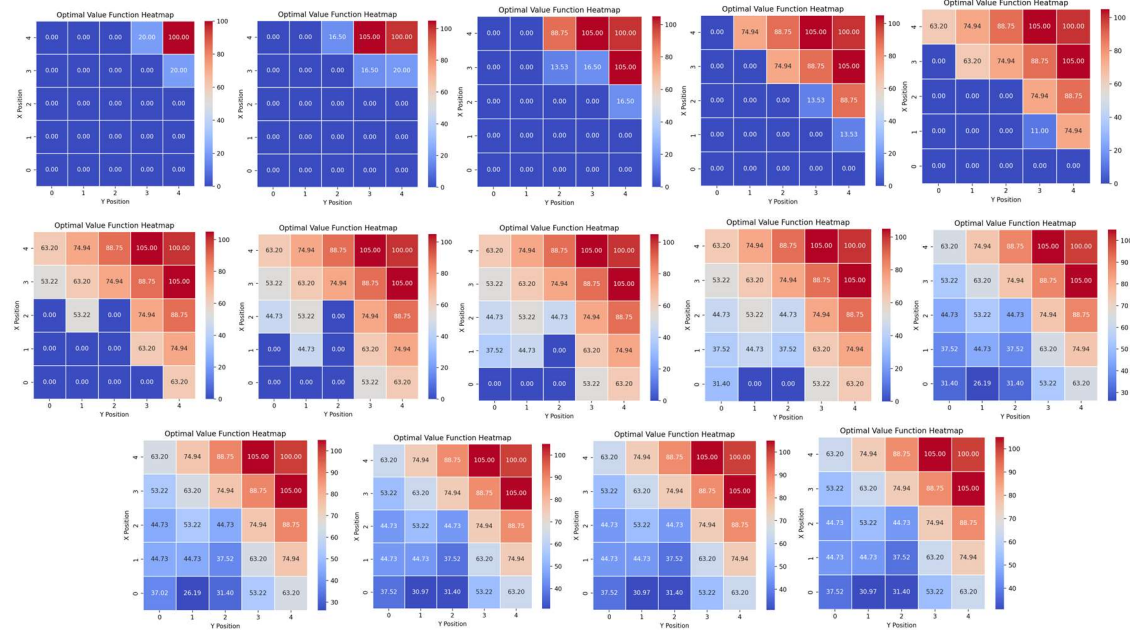


Random policy method represents that a policy was randomly generated then applied, if an infinite loop occurred then a penalty of -100 was applied and the episode terminated. The high cost in the random policy was often a result of the repeated high failure penalty. The random policy method has a cluster just below -100, because its failure is often due to the -100 failure penalty due to looping.

Random path indicates that a random move was applied at each possible situation, where the agent was allowed to cross back over the same location multiple times. The high cost in the random path was often due to the accumulation of the movement cost for 100+ moves to solve the problem. The random path is dispersed much more broadly as it has the chance to converge sooner, and a much lower spread as it allows for repeat cell visits.

The optimal policy agent only has a single value because there is no random element to the design process.

Question 4: Write an algorithm that implements value iteration. Compute the optimal value function and the optimal policy for the test problem using your algorithm (show the outputs visually). Evaluate an agent following the optimal policy and compare the total rewards obtained with those of the agent following a random policy



The optimal policy unsurprisingly performs much better than the other two random-based models at solving the problem and avoiding error. It is worth noting that there is an error in the policy generated in the top middle where the policy directs the agent to move left, when it should move right. This error might be caused by a discrepancy between the values being displayed and the combination of (reward + discount_factor * value[next_state]) which could be caused by the presence of a crater. This type of local maximum would result in an infinite loop in the policy as it would converge on a non-goal value.

```
[Running] python -u "c:\Users\ianwi\OneDrive\Documents\S4\AER0489\hw3.py"
Starting Random Policy Simulation...
Optimal Policy:
> > < > G
^ ^ > > ^
> > v > ^
v > > > ^
> > > > ^
Average Reward (Optimal Policy): 34.95
Average Reward (Random Policy): -116.26707
Average Reward (Random Path): -104.8485

[Done] exited with code=0 in 5.632 seconds
```

AERO 489

Valasek, Selva

4/3/2025

Ian Wilhite

HW4: Q Learning:

- a) The reward matrix to represent the problem contains 100 utility for any move that results in being in the goal state (including staying in the goal state). In the first episode (1), we establish the impossible moves as -1, the successful moves into the goal state with a reward state of 100, and other possible moves as having 0 utility.

$$Q_{ep1} = \begin{bmatrix} 0 & -1 & -1 & -1 & 0 & -1 \\ -1 & 0 & -1 & 0 & -1 & 100 \\ -1 & -1 & 0 & 0 & -1 & -1 \\ -1 & 0 & 0 & 0 & 0 & -1 \\ 0 & -1 & -1 & 0 & 0 & 100 \\ -1 & 0 & -1 & -1 & 0 & 100 \end{bmatrix} \quad (1)$$

- b) In the second episode (2), we iterate based on the potential utility of the options provided to the agent at any given time. We include staying in the current position as a valid option to allow the agent to save the utility of its current position, and to ease the extraction of the convergent utility of the entire system.

$$Q_{ep2} = \begin{bmatrix} 0 & -1 & -1 & -1 & 0 & -1 \\ -1 & 0 & -1 & 0 & -1 & 100 \\ -1 & -1 & 0 & 0 & -1 & -1 \\ -1 & 80 & 0 & 0 & 0 & -1 \\ 0 & -1 & -1 & 0 & 0 & 100 \\ -1 & 0 & -1 & -1 & 80 & 100 \end{bmatrix} \quad (2)$$

$$Q_{ep3} = \begin{bmatrix} 0 & -1 & -1 & -1 & 80 & -1 \\ -1 & 0 & -1 & 64 & -1 & 100 \\ -1 & -1 & 0 & 64 & -1 & -1 \\ -1 & 80 & 0 & 0 & 80 & -1 \\ 0 & -1 & -1 & 0 & 80 & 100 \\ -1 & 0 & -1 & -1 & 80 & 100 \end{bmatrix} \quad (3)$$

$$Q_{ep4} = \begin{bmatrix} 64 & -1 & -1 & -1 & 80 & -1 \\ -1 & 0 & -1 & 64 & -1 & 100 \\ -1 & -1 & 0 & 64 & -1 & -1 \\ -1 & 80 & 0 & 0 & 80 & -1 \\ 64 & -1 & -1 & 64 & 80 & 100 \\ -1 & 0 & -1 & -1 & 80 & 100 \end{bmatrix} \quad (4)$$

$$Q_{ep5} = \begin{bmatrix} 64 & -1 & -1 & -1 & 80 & -1 \\ -1 & 0 & -1 & 64 & -1 & 100 \\ -1 & -1 & 0 & 64 & -1 & -1 \\ -1 & 80 & 51.2 & 0 & 80 & -1 \\ 64 & -1 & -1 & 64 & 80 & 100 \\ -1 & 0 & -1 & -1 & 80 & 100 \end{bmatrix} \quad (5)$$

- c) The final convergent matrix can be found by applying the process many times. After 1000 trials, the convergent matrix was found in (6). Some observations to note include that all columns contain either -1 or a constant. This represents that after converging, moving to that state from any other state will result in the same utility, or conversely, that the value of a given state is independent of the direction of approach. Recalling that the diagonal represents that utility of staying in a given state, combined that all columns contain the same value, the diagonal of the convergent matrix can be utilized to develop a common utility for each state.

$$Q_{conv.} = \begin{bmatrix} 64 & -1 & -1 & -1 & 80 & -1 \\ -1 & 80 & -1 & 64 & -1 & 100 \\ -1 & -1 & 51.2 & 64 & -1 & -1 \\ -1 & 80 & 51.2 & 64 & 80 & -1 \\ 64 & -1 & -1 & 64 & 80 & 100 \\ -1 & 80 & -1 & -1 & 80 & 100 \end{bmatrix} \quad (6)$$

By evaluating the diagonal, we can observe that the convergent Q matrix represents the intuition of the initial problem. The goal state is worth the full goal value of 100. States one and four that allow for one move to the goal state have value of the goal state multiplied by the discount factor, or 80. The subsequent states are each valued at their optimal move value multiplied by the discount factor, or valued at the goal state value multiplied by the discount factor to the power of the minimum number of moves to the goal state. This Q matrix would create an optimal policy to provide an appropriate optimal policy to exit the house.

AERO 489

Valasek, Selva

Ian Wilhite

4/13/2025

Acrobot-v1 Machine Learning Hyperparameter Study

Discussion:

- 1) Gymnasium Environment:
 - a. Environment: Acrobot-v1
 - b. It is a double pendulum driven from the joint between the arms [1]. The objective is to upright the assembly above the center pivot. This environment has a box observation space and a discrete action space with 3 options for the agent at a given timestep: apply positive torque, apply no torque, apply negative torque [1].
- 2) Three candidate algorithms:
 - a. From the stable baselines compatibility table in Figure 1, we can identify that acrobot requires a discrete action space, meaning that Proximal Policy Optimization (PPO), Advantage Actor Critic (A2C), and Deep Q-Network (DQN) would work with the environment [2]. These algorithms were selected based on their popular usage for a variety of applications and Dr. Valasek's common mention of A2C.

Name	Box	Discrete	MultiDiscrete	MultiBinary	Multi Processing
ARS ¹	✓	✓	✗	✗	✓
A2C	✓	✓	✓	✓	✓
CrossQ ¹	✓	✗	✗	✗	✓
DDPG	✓	✗	✗	✗	✓
DQN	✗	✓	✗	✗	✓
HER	✓	✓	✗	✗	✓
PPO	✓	✓	✓	✓	✓
QR-DQN ¹	✗	✓	✗	✗	✓
RecurrentPPO ¹	✓	✓	✓	✓	✓
SAC	✓	✗	✗	✗	✓
TD3	✓	✗	✗	✗	✓
TQC ¹	✓	✗	✗	✗	✓
TRPO ¹	✓	✓	✓	✓	✓
Maskable PPO ¹	✗	✓	✓	✓	✓

Figure 1. Stable Baselines algorithm environment compatibility

3) Hyperparameter Study:

- a. The two hyperparameters I will evaluate are Learning Rate and the Discount Factor. I believe that the learning rate will affect the speed of convergence for the model, as well as the stability of the convergence achieved, whereas the discount factor will determine the performance and aggressiveness of the model in attempting to achieve high performance. An initial investigation can find a workable range for subsequent experiments. Using an average of three trials, a mean can be calculated and plotted in a heat map in Figure 2.

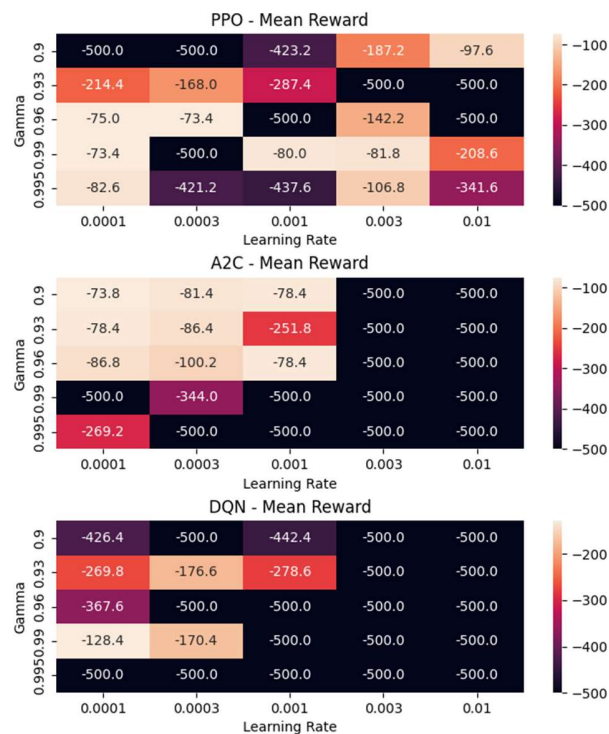


Figure 2. Hyperparameter study for 10,000 episodes

Many of the models simply did not converge, and therefore the training size needed to be increased, however the range seemed promising. It is worth noting that PPO succeeded with little trend, A2C showed a clear successful and unsuccessful region, and DQN showed little progress reinforcing the similar range to A2C.

With an increased timestep, the training curves for each model could be constructed with respect to the discount factor and learning rate. In Figure 4, it can be observed that with lower learning rates (the left columns) that the models converged slower or negligibly, whereas with higher learning rates (the right columns), the models demonstrated oscillation after convergence

or suffered failure altogether. The discount factor showed minimal impact, but broadly that a lower discount factor (top rows) created impatient models, that tended to be more aggressive in improving its rewards per episode, whereas a higher discount factor (bottom rows) created a more patient model that converged slower with fewer instances of decreasing rewards between episodes.

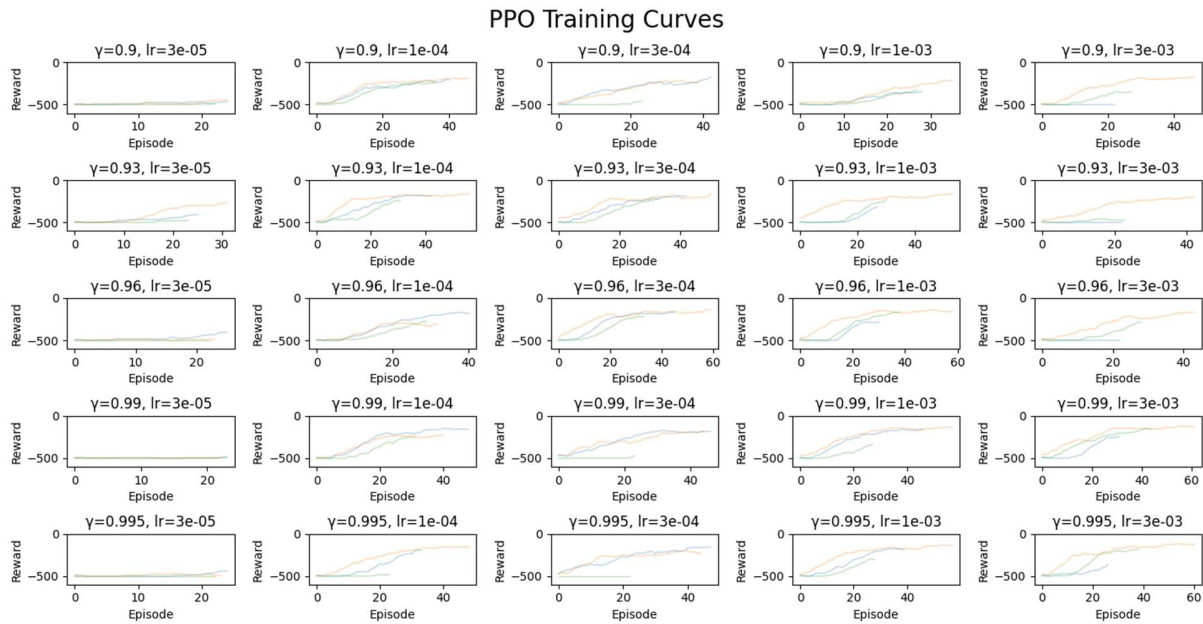


Figure 4. PPO Learning curves for 15,000 episodes w.r.t. discount factor and learning rate

For deep Q learning, all models across the board suffered from increased volatility in convergence. Notably, with very low learning rates they ended training sooner because they converged at negligible rewards.

DQN Training Curves

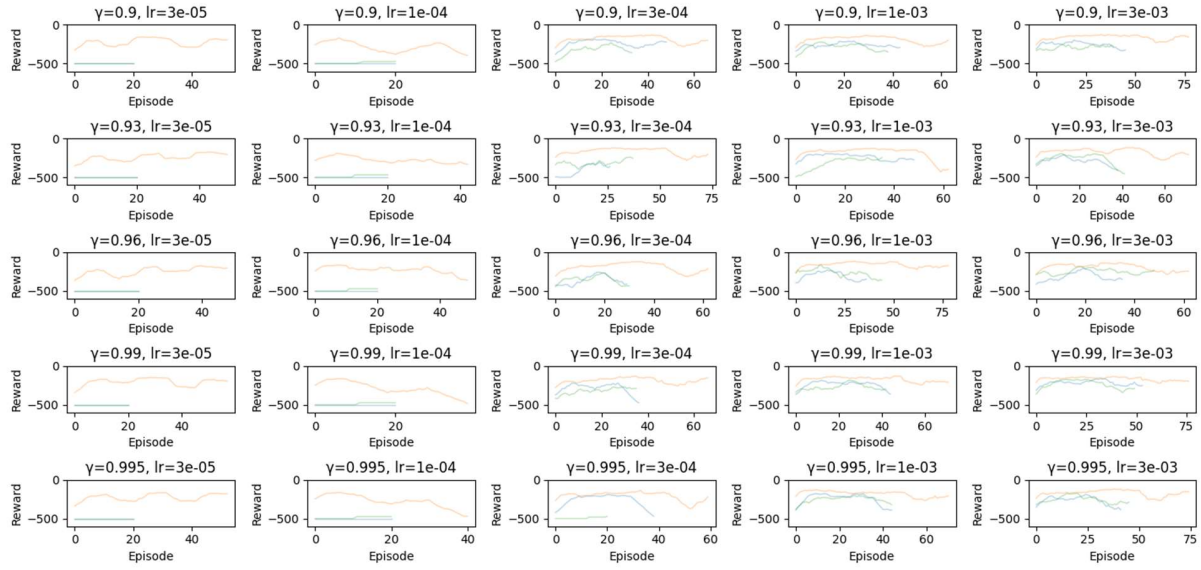


Figure 5. DQN Learning curves for 15,000 episodes w.r.t. discount factor and learning rate

A2C Training Curves

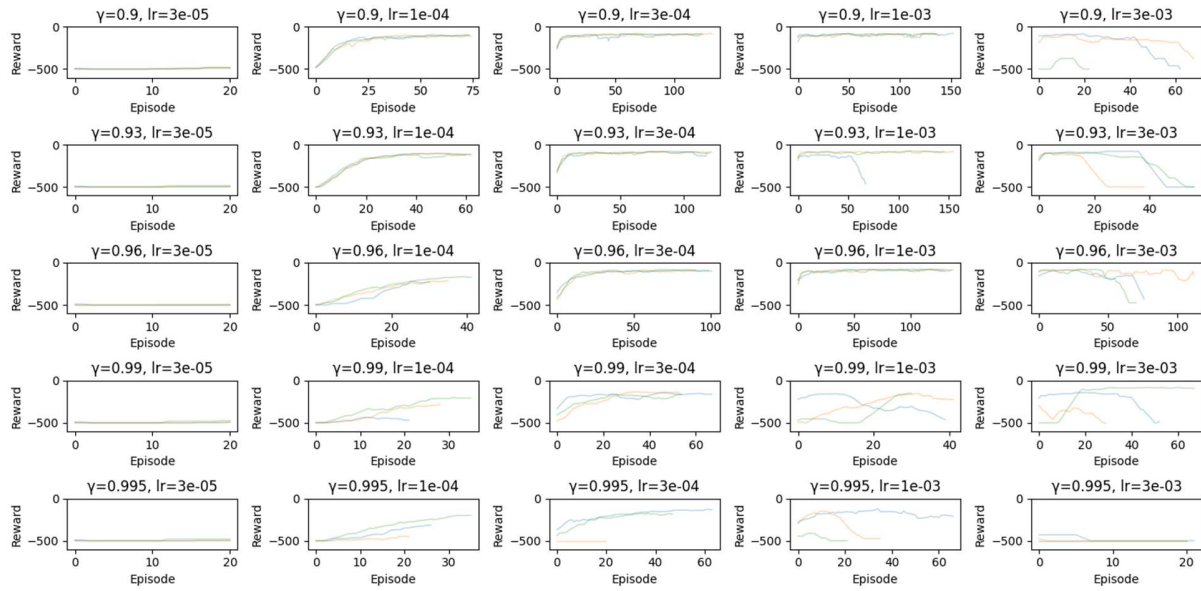


Figure 6. A2C Learning curves for 15,000 episodes w.r.t. discount factor and learning rate

A2C Learning clearly demonstrates the trends stated before, that as the discount factor decreases the model becomes impatient, particularly where the learning rate is effective to converge. When the learning rate is too high, the model does not converge, and when the learning rate is too low, it will not converge or will converge slowly.

4) Direct comparison

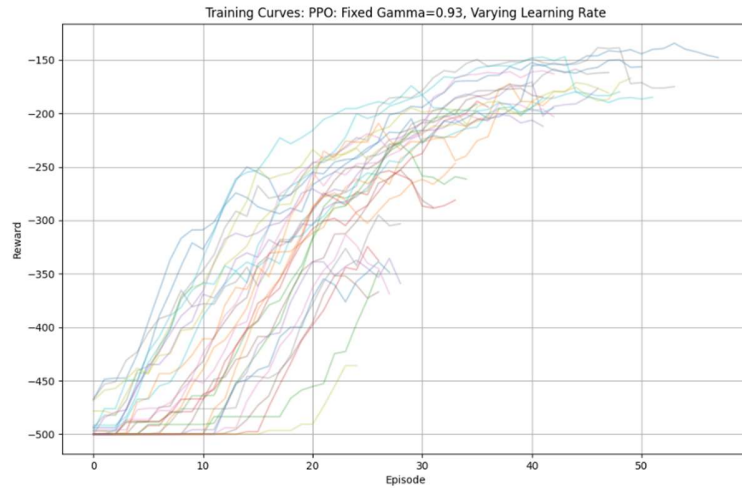


Figure 7. PPO Learning Curves while varying learning rate

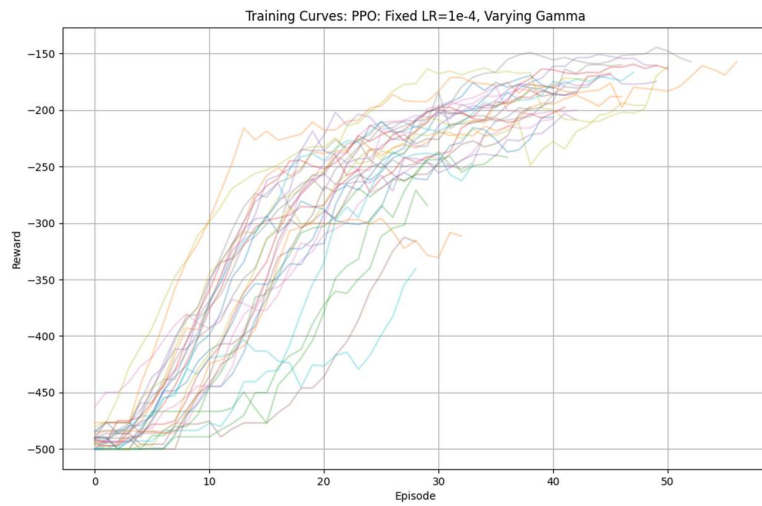


Figure 8. PPO Learning Curves while varying discount factor

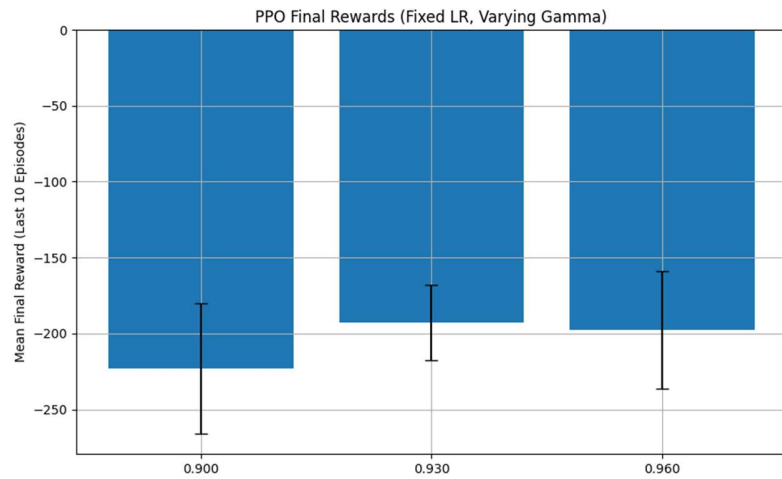


Figure 9. PPO rewards varying discount factor

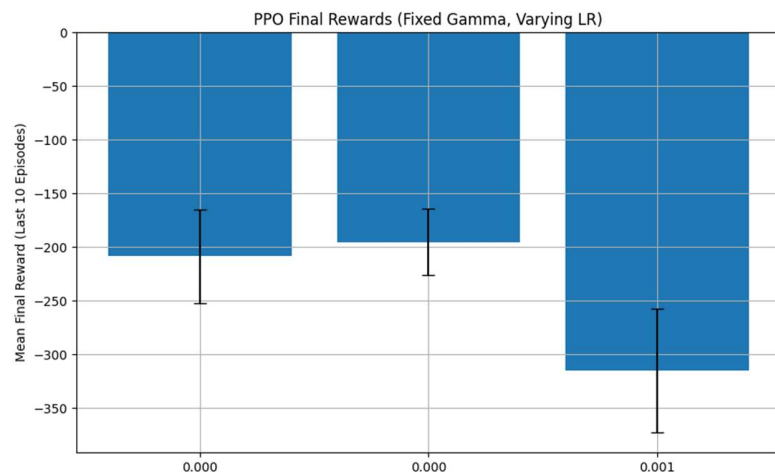


Figure 10. PPO rewards varying learning rate

PPO can be observed as converging consistently, and showing that the lower discount factors decrease the mean resulting reward. It should be noted that the ending rewards are not indicative of the peak rewards or the time to reach peak performance, only that after many iterations

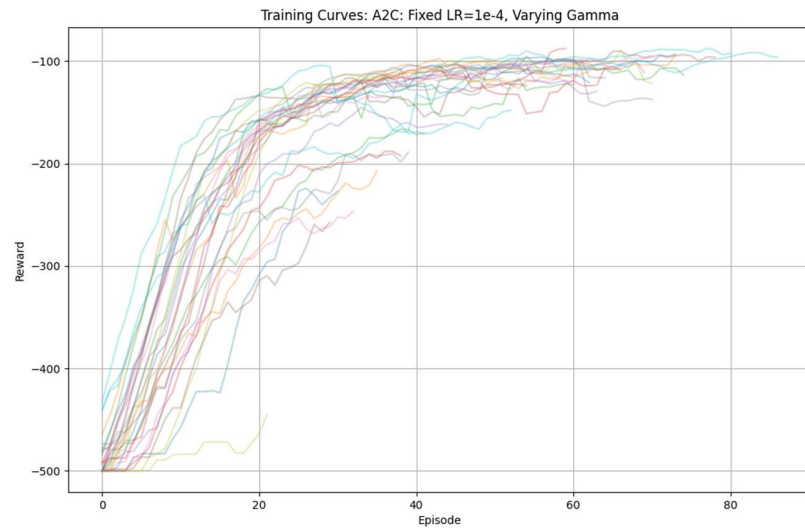


Figure 11. A2C Learning Curves while varying discount factor

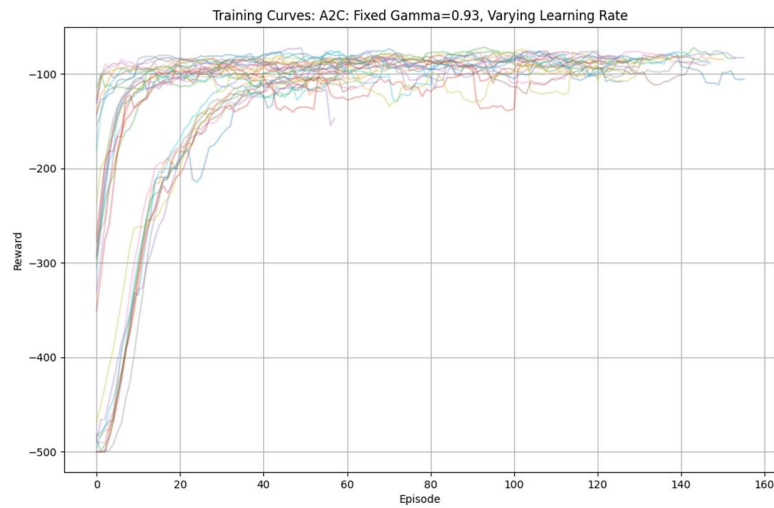


Figure 12. A2C Learning Curves while varying learning rate

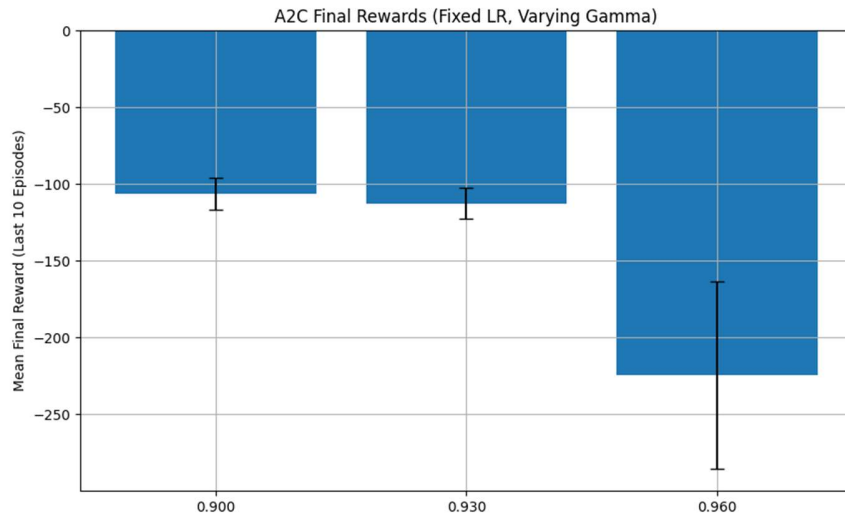


Figure 13. A2C rewards varying discount factor

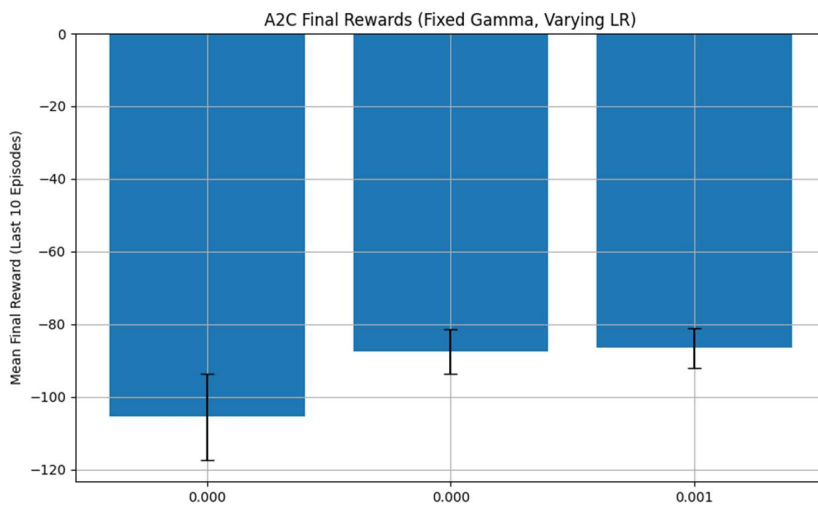


Figure 14. A2C rewards varying learning rate

A2C can be seen as noticeably continuing many of the otherwise observed trends with a lower uncertainty and consistency not only in the final results but also the learning curves path to convergence. The differing learning curves clearly show the paths that each factor takes to convergence. Noting the scale that nearly all of the A2C models outperform the PPO models on similar metrics.

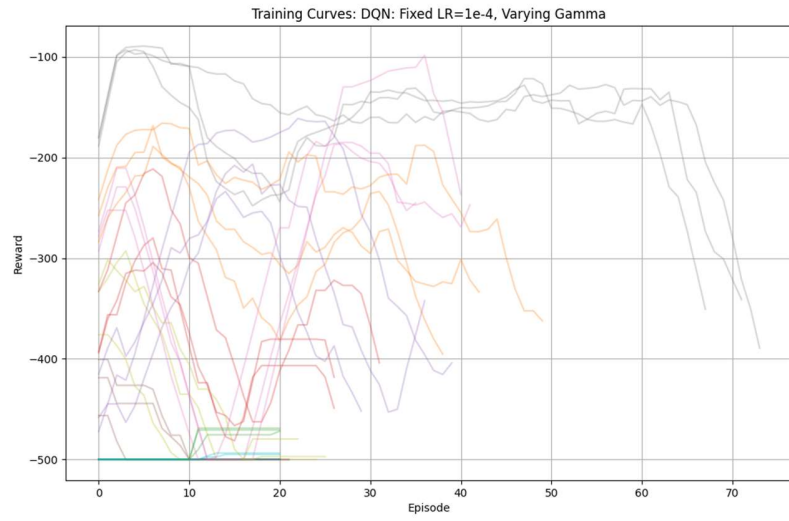


Figure 15. DQN Learning Curves while varying discount

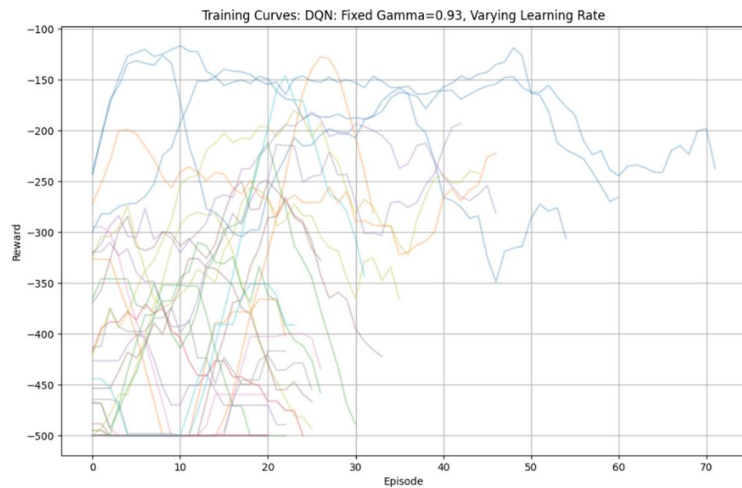


Figure 16. DQN Learning Curves while varying learning rate

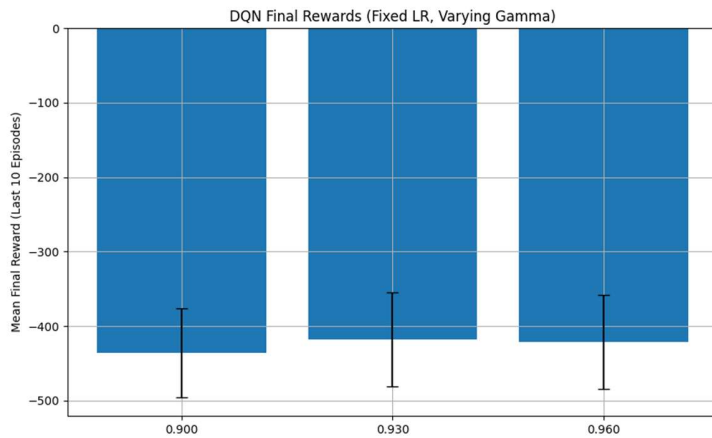


Figure 17. DQN rewards varying discount factor

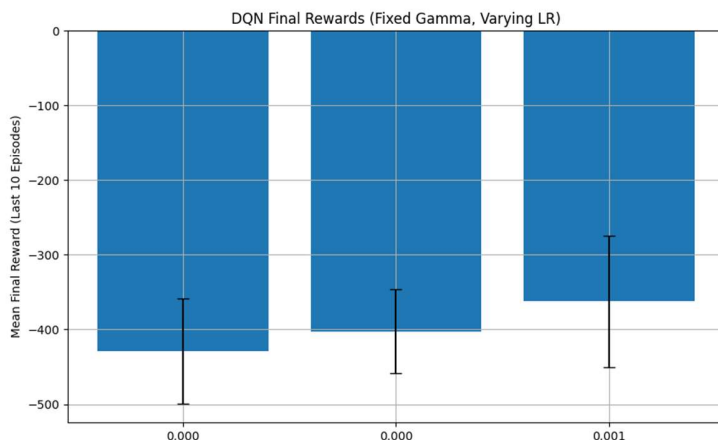


Figure 18. DQN rewards varying learning rate

While PPO demonstrated consistent convergence behavior, A2C outperformed it in both average final rewards and consistency across trials. DQN exhibited unstable learning and failed to converge in most settings, although a few isolated cases approached competitive performance.

5) Conclusion

This study evaluated the impact learning rate and discount factor on PPO, A2C, DQN algorithms using the Acrobot-v1 environment. Results showed that: Low learning rate led to non-convergence, whereas high learning rate led to oscillatory behavior; Low discount factor led to aggressive models that

converged quickly while high discount factors created more patient models that converged slower but rarely took any steps that decreased rewards.

- a. A2C consistently outperformed PPO and DQN in similar ranges, however it is worth exploring a wider range of learning rates and discount factors as trends for optimality indicated that different models preferred different learning rates and discount factors. PPO could benefit from higher discount factors, A2C could benefit from lower discount factors, and DQN had little impact from discount factors. PPO could benefit from a lower learning rate, whereas A2C and DQN could benefit from a higher learning rate.
- b. A2C was the easiest to train, followed by PPO, and I could not get DQN to reliably converge. A2C demonstrated the most consistent convergent given the same hyperparameters.
- c. PPO seemed the easiest to tune in the sense that poor hyperparameters could be accounted for with additional training episodes. A2C had a very clear optimal region of performance with respect to its hyperparameters, meaning that although it was harder to find this optimal region of performance, inside there was consistent and rapidly converging high performance. DQN did not converge consistently across any region of hyperparameters and was consistently exiting training episodes, indicating a need for continued variance in the hyperparameters provided.
- d. This is the most I have worked with machine learning models thus far, and I think it was an interesting way to better understand the role that hyperparameters can play in the training process for various models. I learned about the characteristics of PPO, A2C, and DQN, and the impacts that learning rate and discount factor have on the performance of various algorithms. I think that this has been one of the most beneficial assignments I have seen in the class so far with respect to applications of the concepts that we have been learning up to this point

Future work could include a broader range of learning rates and discount factors applied, increased trials to decrease uncertainty and determine trends more consistently, and optimization techniques applied to identify optimal parameters for different algorithms.

Appendix

[1] Farama Foundation. *Acrobot-v1 Environment Documentation*. Gymnasium Classic Control Environments. Available at:

https://gymnasium.farama.org/environments/classic_control/acrobot/. Accessed April 13, 2025.

[2] Stable-Baselines3 Developers. *Algorithm Guide and Environment Compatibility*. Stable-Baselines3 Documentation. Available at: <https://stable-baselines3.readthedocs.io/en/master/guide/algos.html>. Accessed April 13, 2025.

AERO 489

Project #2: Final

5/5/2025

Ian Wilhite

- 1) I chose to implement the 2-rope ball environment.
 - a. The environment includes a random starting horizontal velocity, bar angle, angular frequency, and vertical velocity.
 - b. The goal as stated was to raise the ball to a height of 10 without falling off the bar, and terminal conditions to ensure the model was meeting real-world constraints.
- 2) The reward structure and agent terminal conditions were structured to aide the agent to complete the assigned task and penalize suboptimalities in its completion of the task.

Reward structure:

- a. Proportional height incentive – rewarding the agent for positive movement towards the goal condition.
- b. Proportional time disincentive – penalizing the agent proportionally for longer solutions.
- c. Nonlinear ball position penalty – minor penalty for small deviations from the middle of the ball, and higher penalties for allowing the ball to be closer to the edges of the bar.
- d. Minor maximum angle penalty – disincentivizing the agent from tilting the bar a large amount because of the time required to untilt the bar.

Terminal condition structure:

- a. Checking the x position of the bar is not off the bar – if the ball has fallen off the edge of the bar the trial has ended.
 - b. Checking the bar is upright – ending the trial if theta between negative and positive one-half pi.
 - c. Checking the height is greater than negative 10 – this was added to prevent agent from falling into the void during training.
 - d. Checking the height is greater than 10 – the success condition.
- 3) I chose to implement PPO because of its broad convergence in a variety of environments, and its notorious ease to train. During the training process, I varied

the ratio between the time and height proportional rewards, as well as the various minor penalties provided until the agent satisfactorily performed.

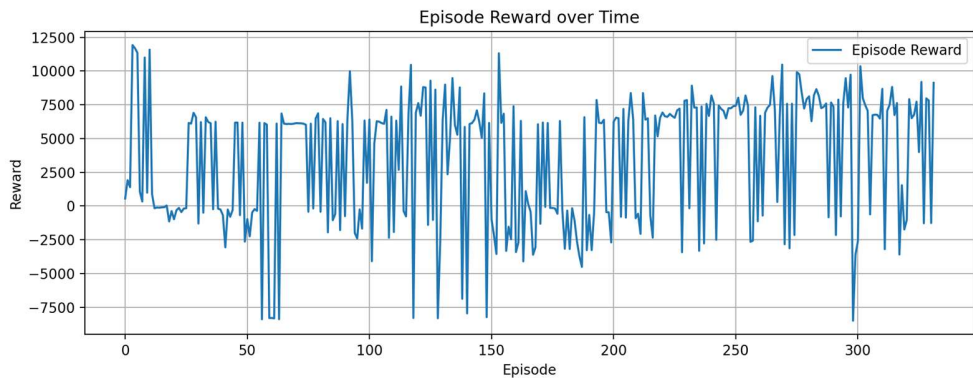
4) Short report:

This project allowed me to learn how to render real world scenarios and to apply the concepts of RL to real situations that I may face in industry. This project truly served to combine many of the skills of this course into a single relevant project relevant to the ways that these tools are currently being applied.

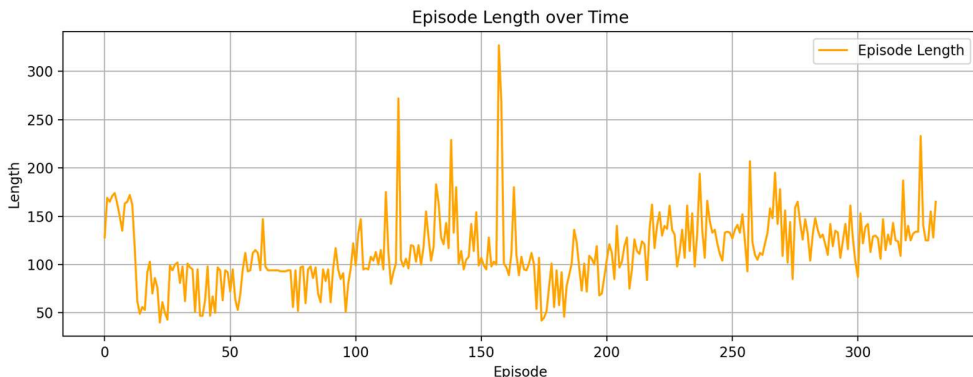
In designing the environment, a major aspect was determining which variables made a major impact on the state and would be required to fully describe any possible given state. Many variables excluded to decrease training time, and therefore the minimum number of variables possible were provided. The horizontal position of the bar and angle were added to represent the position of the system. Their derivatives were added to allow the agent to predict the motion of the system into the future. Their second derivatives were not added because the action the agent took would directly affect it, and therefore the agent did not need to know its own previous action, as it only needed to know what to do next. The height of the bar was intentionally not added to prevent the agent from learning to jerk the cables near the beginning or end, but rather to encourage the agent to act consistently throughout the trial.

The reward structure was revised continuously while the agent was being trained. The combination of linear, nonlinear, and weightings of rewards greatly changed the reaction of the agent to various states, and therefore how it responded to it. Reward shaping drastically affected nearly every aspect of the model's behavior and performance and eventually led to the success of the model. After pivoting to SAV, in tuning, I found that I needed to lower the learning rate to secure a more stable convergence, which finally secured a success rate of 79% in the randomly initialized environment.

I chose to implement Proximal Policy Optimization (PPO) initially because of its known simplicity in convergence as I was testing the environment, however, I chose to pivot to Soft Actor Critic (SAC) for its ability to perform well in environments with high entropy, making it more suitable for modeling a system of multiple variables and lower training times.



The reward over episode graph shows the improvement of the model, both initially and in stability as the frequency of success increases but could still allow for another decrease in the learning rate and additional trials to allow the model to succeed with higher frequency.



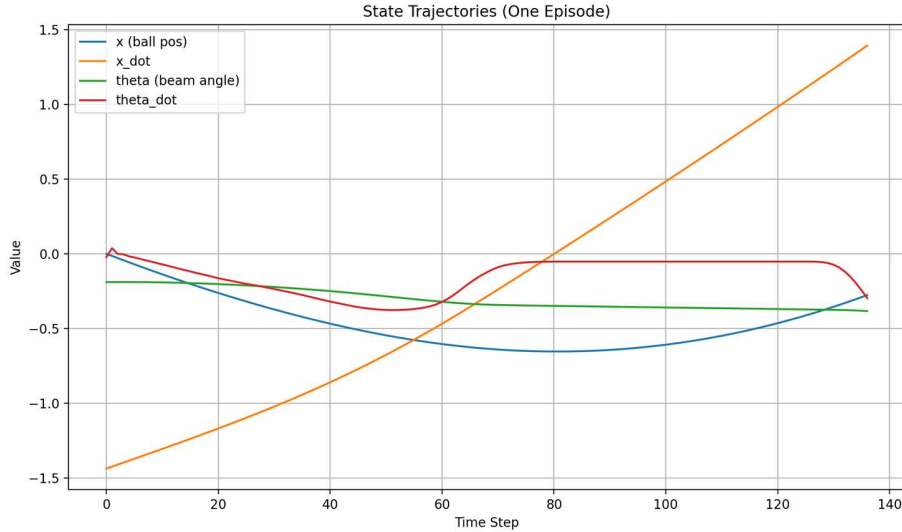
The episode length over time graph shows another perspective of the convergence strength. Initially, there is a sharp decrease in episode time as the model identifies the time penalty, and starts working around it as it learns to stabilize the ball. Around episode 200, the episode length started to rise alongside consistent episodic success, where the model was learning what tradeoffs were worth losing the time penalty points.

```

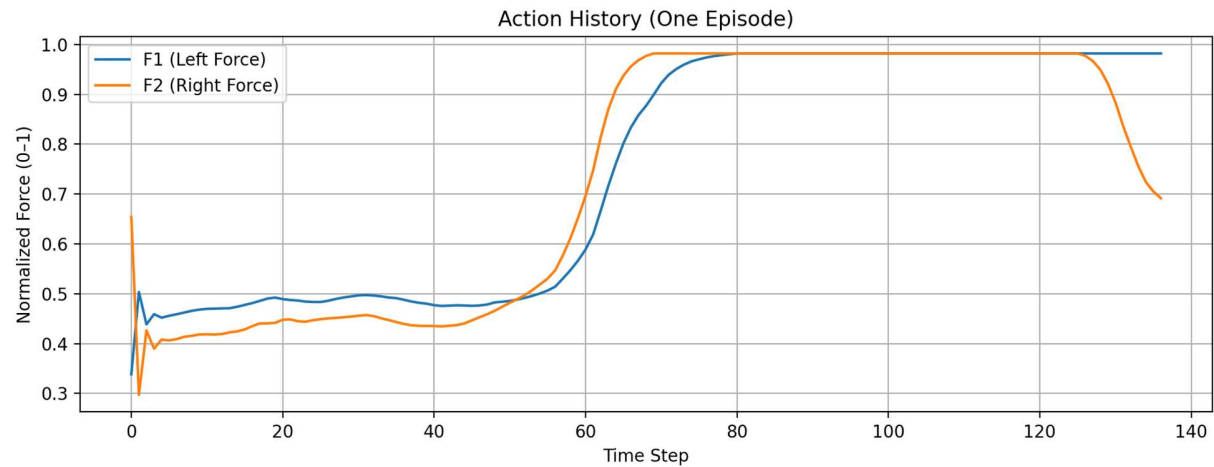
Training complete.
Model saved as 'sac_ropeball_trained'.
Loading the trained model...
Model loaded.
Testing the model over 100 episodes...
Success rate: 79.00%

```

To evaluate the model, 100 episodes with random initial angles, angular velocities, and ball speeds were performed, and the success rate for the trials were identified. The agent succeeded in 79 of the 100 episodes, for a success rate of 79% and securely meeting the established threshold of 70%.



The state trajectories plot indicates the agent is able to observe the negative ball position and velocity, and apply a positive torque to counteract the balls motion. The agent is able to correct for and maintain the bars angle, and minimizes the bar's angular acceleration then maintains it.

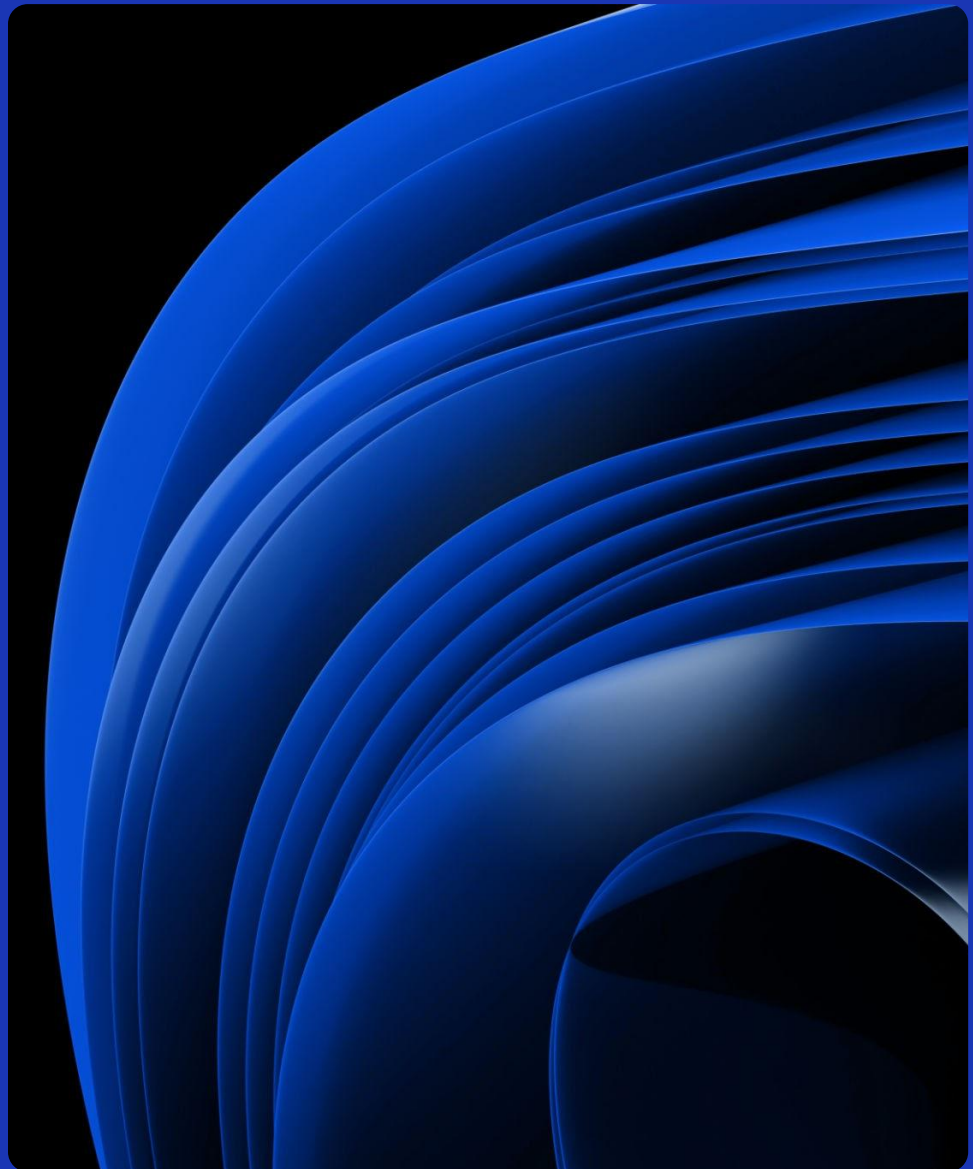


The system can be observed balancing the ball initially until time step 60, then maximizing a consistent force to raise the bar to the desired height as quickly as possible. The agent can be observed near the end of the trial as accounting for the ball's position crossing the center of the bar and beginning to tilt the bar to correct for overshoot.

Overall, the agent has learned to stabilize and raise the bar to the desired position with satisfactory success. The modeling of the environment represents skills used in industry, while the learning and tuning process is a final application of the skills covered in the second half of the course. This has been certainly one of the most unique classes I have taken, and I truly believe that I have learned a lot from it.

Two Rope Ball Balancer

Ian Wilhite
5/1/2025

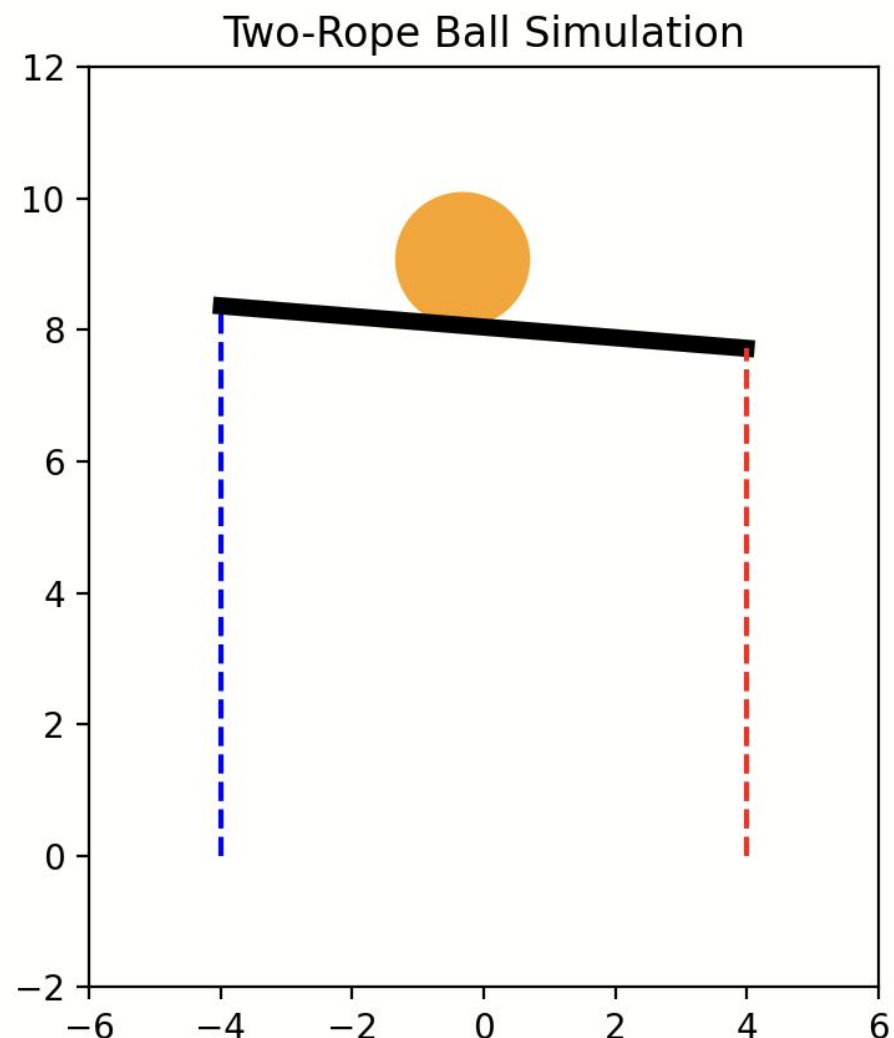


Modeling



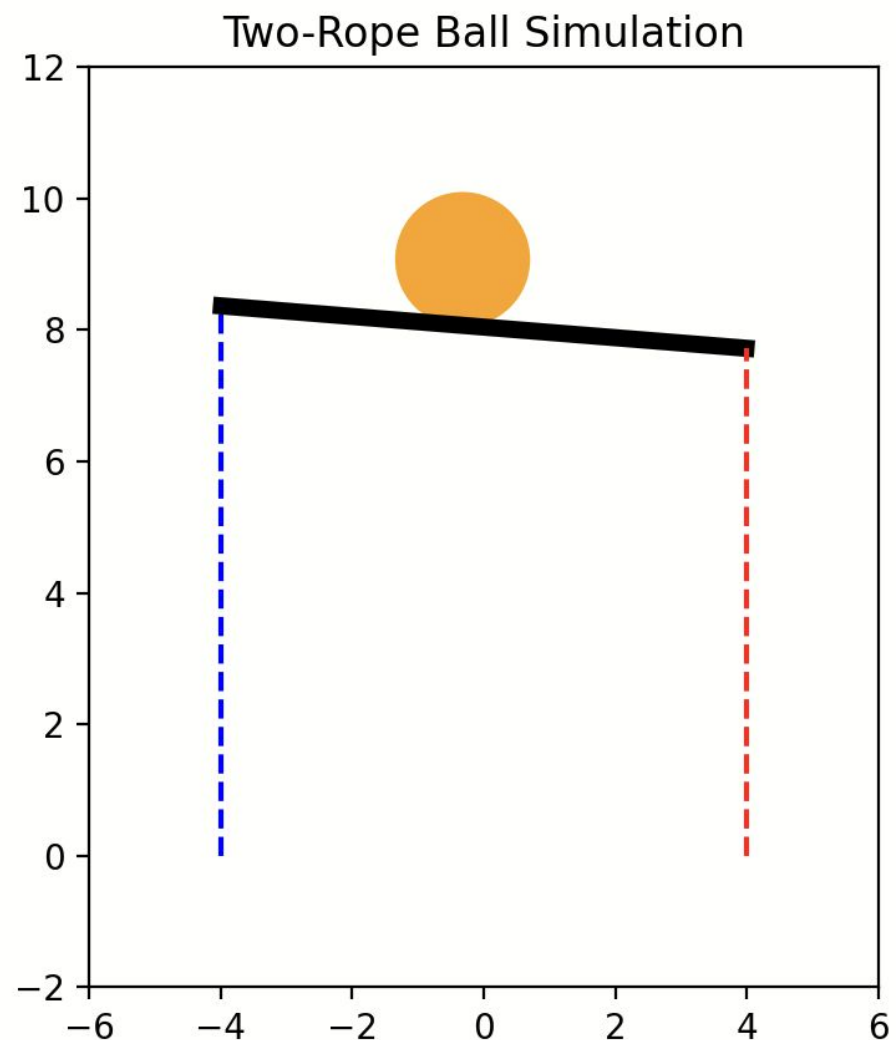
RL setup

- State Space
 - Height
 - Height'
 - Angle
 - Angle'
- Action Space
 - Force on left rope (0, +50)
 - Force on right rope (0, +50)



Two rope model

- matplotlib
- Physics work
- No time penalty (for now)



Training (pt 1)

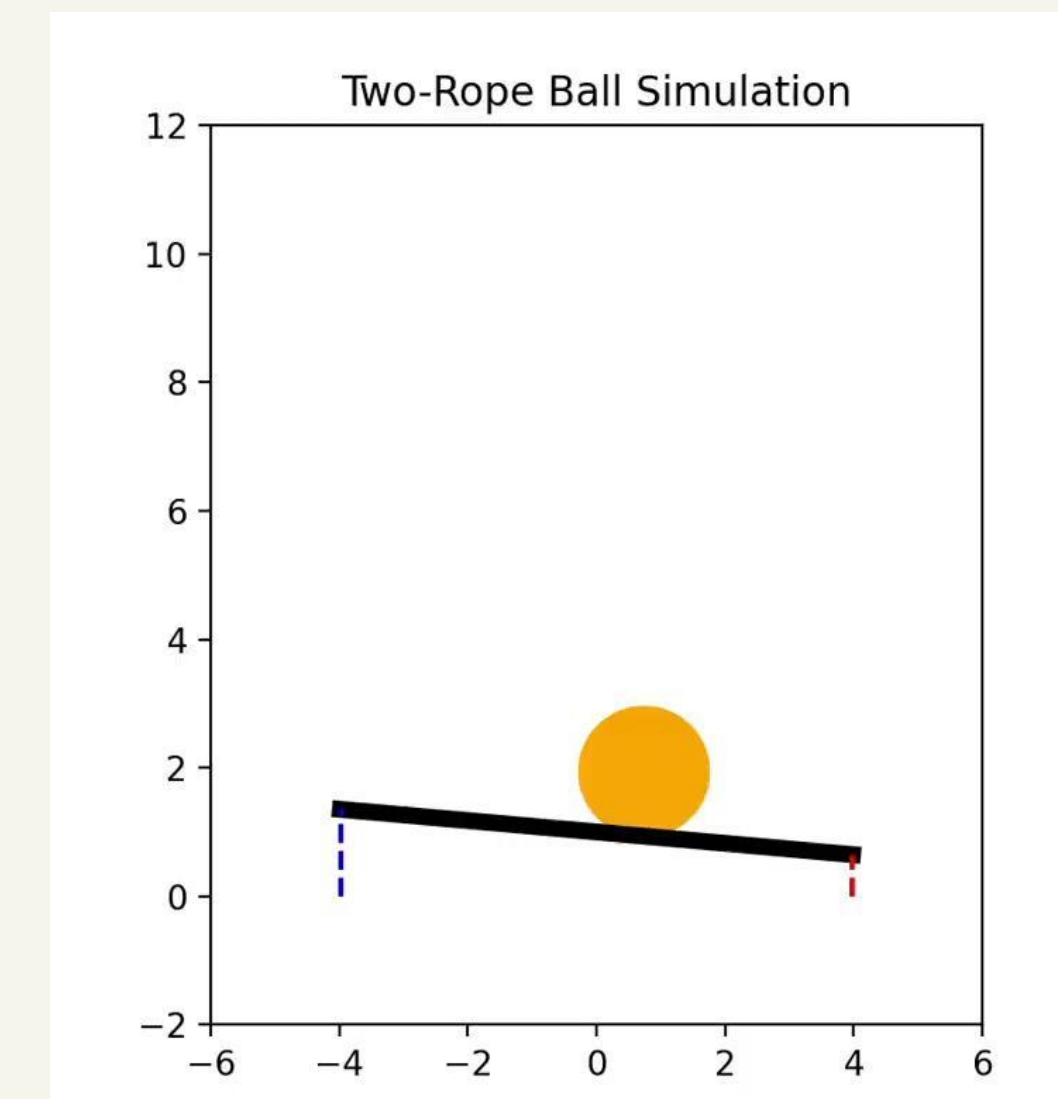
Confidential

Copyright ©

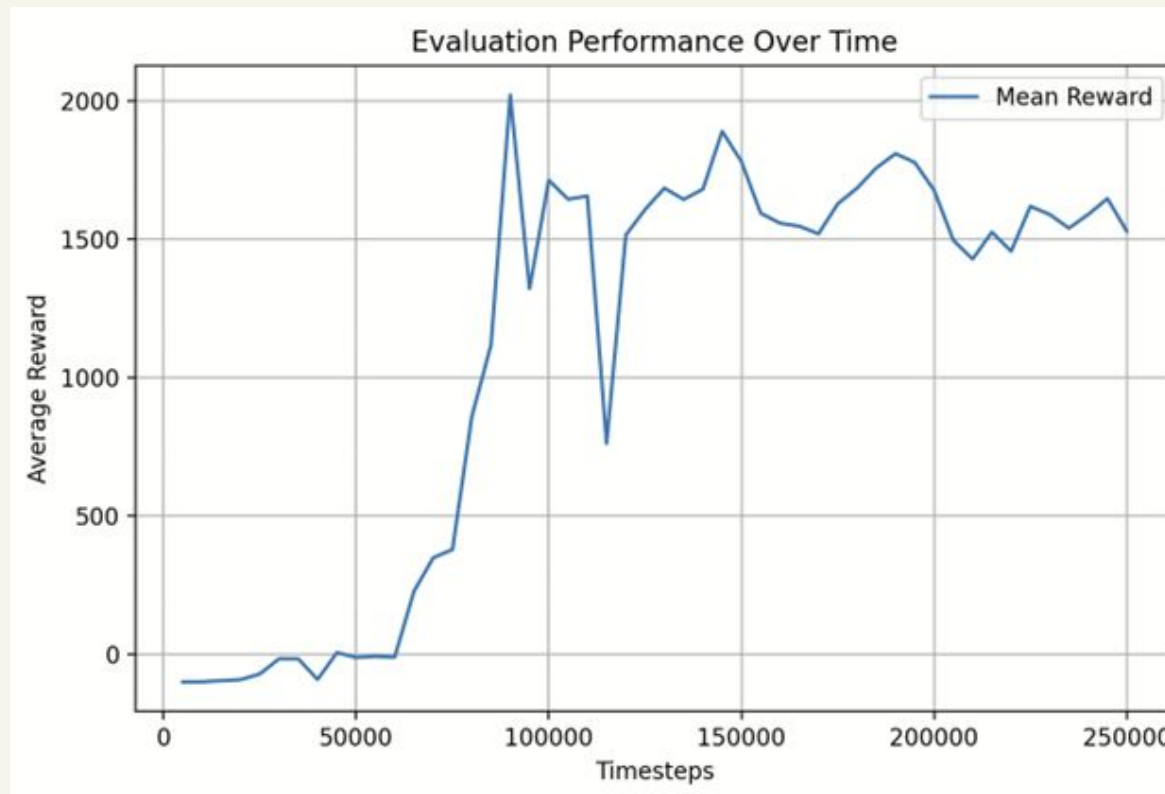


PPO

- Chosen for robustness
- slow
- Worked!
 - High success rate



PPO-V1 learning curve



Training (pt 2)

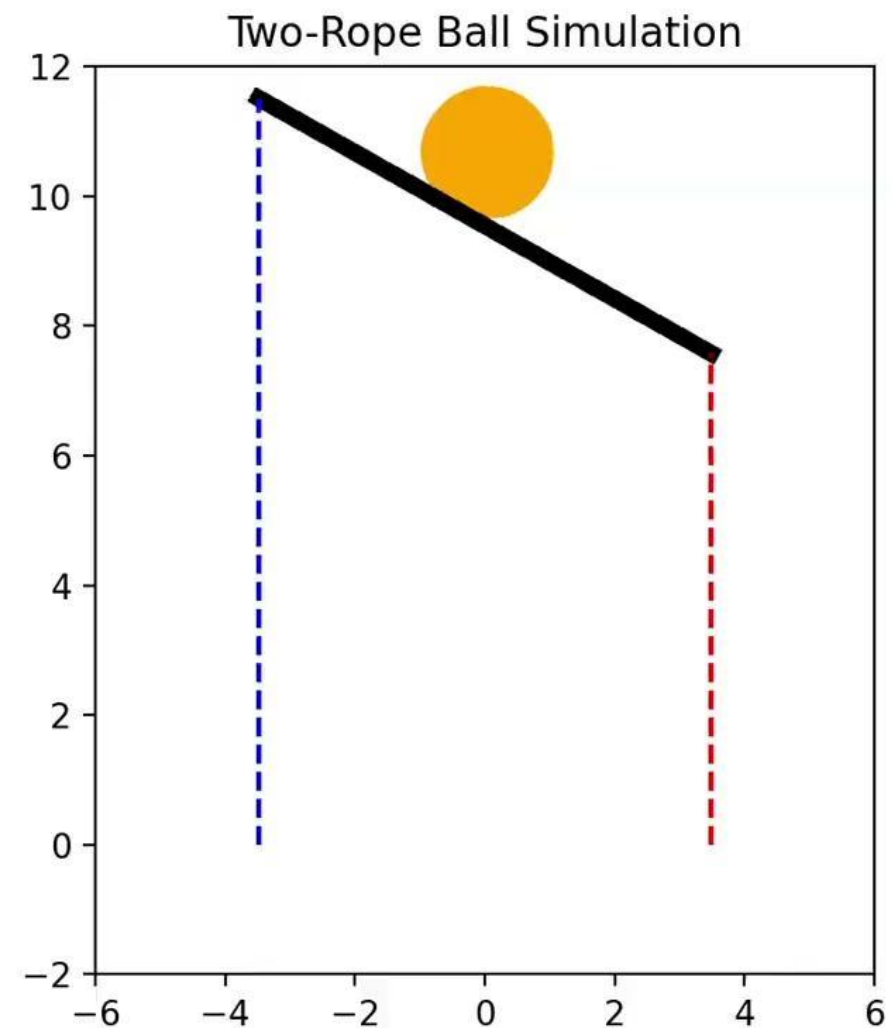
Confidential

Copyright ©

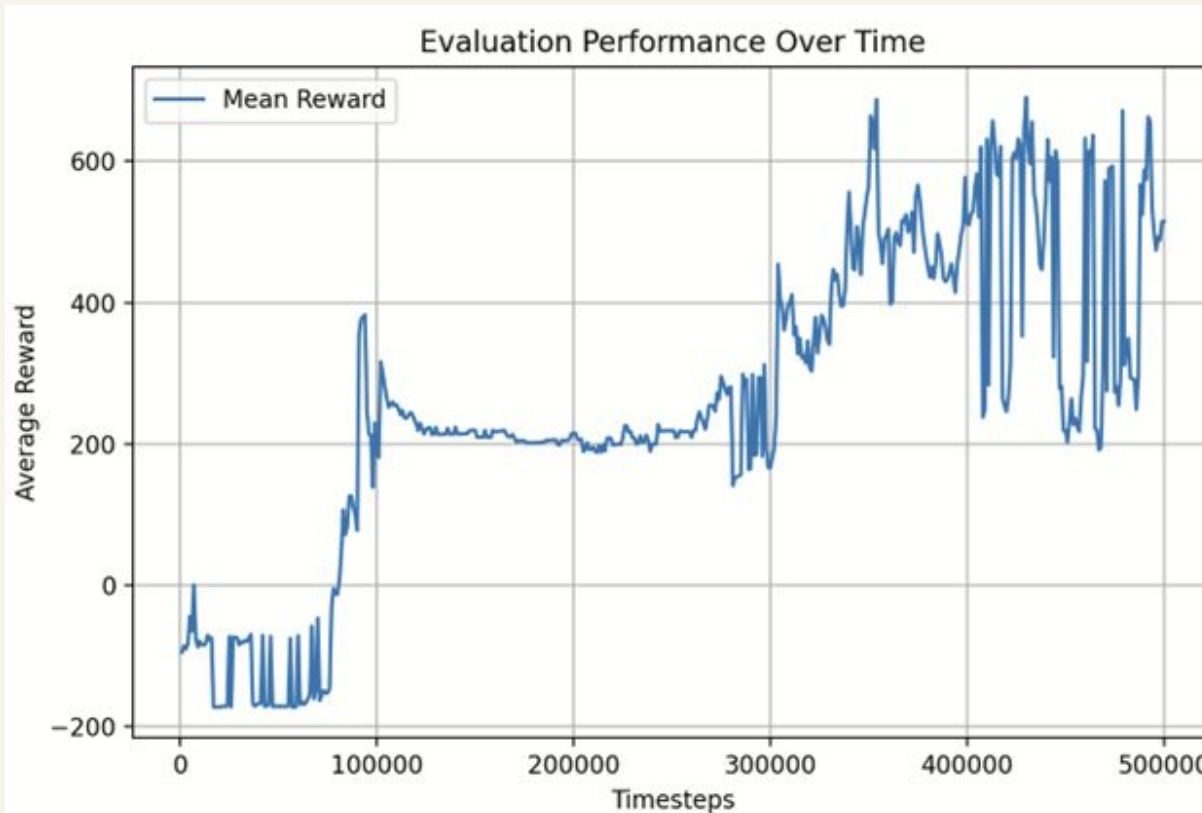


PPO - w linear time penalty

- Lower success rate
- fast!
- worked!



PPO-V2 learning curve



- Initially rewarded jerky movements
-

Success evaluation



Results!

```
[Running] python -u "c:\Users\ianwi\OneDrive\Docum  
Gym RopeBall environment imported successfully!  
Model reloaded successfully!  
Success rate: 86.90%, sample size: 10000  
Evaluation completed successfully!
```

- 86.9% Success Rate!
- There is definitely room for improvement
- worked!

Next Steps



Tuning:

- Hyperparameter study
- Implement A2C
- Replace heavy training with thoughtful training (hyperparameter tuning)

2. Dynamics and Vibrations

Computational Assignment 1 - Bungee Jumping

TO: Adolfo Delgado

FROM: Group 7 of MEEN 363 - 502 (Tori Abell, Alois Campbell, Eddy Silva, Ian Wilhite)

Subject: Assignment 1, Bungee Jumper

Date: 02/21/2025

EXECUTIVE SUMMARY

The objective is to analyze how the bungee cord's material properties affect the jumper's motion. The height of the jump, the weight of the person, the stiffness of the bungee cord material, the damping effect of the material, and the air resistance all affect the motion of the jumper. The equation of motion was derived by using Newton's second law and summing the forces in the vertical direction. Two main equations were formed, one considering the damping from the cord being stretched and the air drag and the other considering when the cord was not in tension, the person only experiencing damping from air resistance. Based on the general equation of motion, the natural frequency of the jumper depends on the cord stiffness (k), and the mass of the person. As expected, a higher stiffness, k , results in a higher natural frequency. A lower cord stiffness requires a higher initial jump height because it allows the cord to stretch more and the person to fall further. A higher cord stiffness would result in a smaller initial jump height required, but the person is more likely to experience injury from a higher acceleration and force acting on them.

METHOD

The first step in creating the equation of motion for the bungee jumper is to create a free-body diagram (FBD). As seen in **Figure 1**, there are three forces acting on the jumper throughout most of the fall; the jumper's weight, total damping, and the spring force in the cord. The result of Newton's Second Law equation from the FBD is **Equation 1**. Using the motion equation and the "solve_ivp" scipy function in Python, a second-order differential equation can be solved for position, velocity, and acceleration. To analyze the effect of the cord's stiffness on the motion of the jumper, 10 evenly spaced k values between 40 N/m and 240 N/m were used in the position, velocity, and acceleration equations and plotted as functions of time. Three plots were then made for the material loss factor (η), seen in **Equation 2**, with values ranging from 0.15 to 0.30. For clarity, the simulations assume an initial jump height of 100m with the cord considered taut at 82m from the ground ($x=0m$).

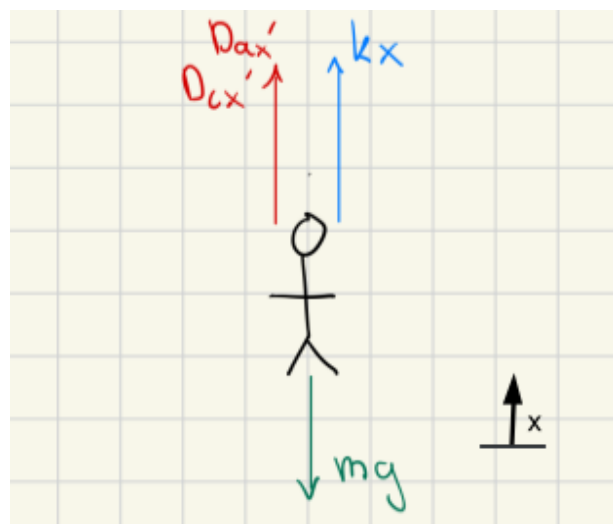


Figure 1: Free Body Diagram of Bungee Jumper

An important factor to consider with this problem is that the damping and spring force caused by the cord are inactive if the jumper is within 18 meters of the platform. 18 meters is the length of the cord so it will only be in tension after that distance. This means in **Equation 2**, D is equal to D_a within 18 meters.

Equations:

Motion Equation:

$$\Sigma F = mx'' = -mg + k(x_0 - l - x) + Dx' \quad \text{Equation 1}$$

- x_0 : Initial Position (m)
- x : Position (m)
- x' : Velocity (m/s)
- x'' : Acceleration (m/s²)
- l : Length of Bungee Cord
- m : Mass (kg)
- k : Cord Stiffness (N/m)
- D : Total Damping Coefficient (Ns/m)

Total Damping Coefficient:

$$D = D_c + D_a = \frac{k\eta}{\omega_n} + D_a \quad \text{Equation 2}$$

- D_c : Viscous Damping Coefficient (Ns/m)
- D_a : Air Resistance Equivalent Damping (8 Ns/m)

To better understand and analyze the jumper's motion, **Equation 3** showcases the natural frequency in terms of the equivalent cord stiffness and mass in the system. Meanwhile, **Equation 4** describes the cord's spring constant in terms of its material and physical properties.

Natural Frequency:

$$\omega_n = \sqrt{\frac{k}{m}} \quad \text{Equation 3}$$

Cord Stiffness:

$$k = \frac{EA}{l} \quad \text{Equation 4}$$

- E : Elastic Modulus (MPa)
- A : Cross-sectional area of Bungee Cord (m²)
- l : Length of Bungee Cord (m)

PROCEDURE

A model was constructed to simulate the motion of the bungee jumper using the initial value problem (IVP) solver built into the Python Scipy library. First, a set of constants and initial values were set such that the simulation could use some values as constants and vary others over a provided range and step. Arrays were constructed to contain the values for each combination of the spring constant and loss factor. Each simulation was run and the arrays were propagated using the solution found with the IVP solver. A free fall curve was plotted to show motion without elastic force or damping resistance. A horizontal line representing the point of zero elastic deflection was plotted. The stored values were then printed to the console and stored as a CSV for

processing.

The equilibrium points approach the point of zero elastic deflection (the rope length from the jump height) as the k value of the spring increases. This phenomenon follows the understanding that stiffer springs will deflect less under equal loading conditions.

In the reported times of maximum acceleration, the third reported value aligning with $k=40$ and $\eta=0.30$ shows the maximum acceleration at $t=0$. This discrepancy can be attributed to the increasing η value which led to the first oscillation having a lower maximum magnitude of acceleration than the free fall region. The reported time value represents the initial acceleration due to gravity, the point of minimum velocity, and before the bungee cord is engaged. This is to be expected because, during the first oscillation, the peak remains below the equilibrium point of the spring. Therefore, the body remains in damped harmonic motion after the initial free fall. As seen in the free fall region of the acceleration chart of **Figure A**, the acceleration begins only due to gravity; however, as the body falls and accelerates, the air resistance increases proportionally to the velocity, leading to an exponential decrease in the magnitude of the acceleration as the downward velocity of the jumper leads to a positive force on the body.

This implies several things: that the acceleration is at a maximum in the free fall region, that once the body enters the damped harmonic motion region it can never re-enter the free fall region, and that within the initial free fall region, the acceleration is at its maximum at the initial state. Therefore, the reported time value for the acceleration must be correct.

For reported values, both parameters were varied simultaneously, but to aid in visualizing trends, each was plotted while the other was fixed, as depicted in **Figures 2 and 3**. The simulations were run for 20 seconds as these would allow for quicker computing times, and the jumper would be considered to be moving slow enough to be recovered safely.

RESULTS and DISCUSSION

With the equations of motion, velocity, and acceleration solved using Python's matplotlib library, **Figures 2 and 3** show the position of the jumper as a function of time with varying K and η values. As per the assumptions, these figures include a "free fall" for the first 18m of descent from an initial position of 100m from the ground ($x=0m$), as well as a sample "free fall" with no bungee cord for reference. The 18m when the cord begins to act on the jumper are also marked by a dotted line in both graphs.

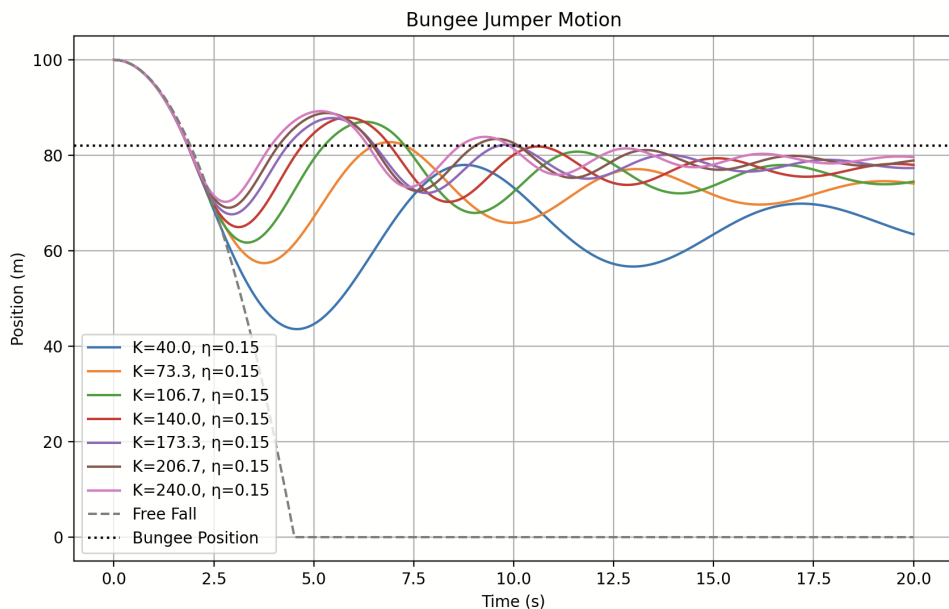


Figure 2: Bungee Jumper position as a function of time with varying K values

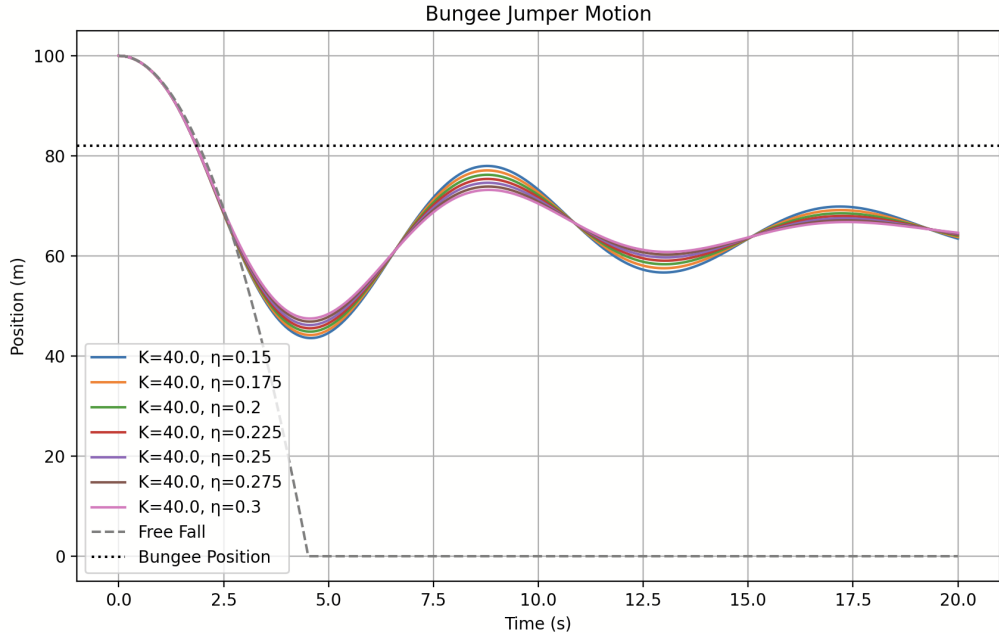


Figure 3: Bungee Jumper position as a function of time with varying η values

From **Figure 2**, it can be seen that there is a lot of variation in both the amplitude and period of the oscillatory motion of the jumper. As these values of k are bounded between 40N/m and 240N/m and η between 0.15 and 0.30, a minimum fall position, maximum velocity, and maximum acceleration can all be identified using **Table A** and interpreting **Figures 2, 3, and A**. At $k=40\text{N/m}$ and $\eta = 0.15$, the absolute lowest point the jumper reaches is 45.8m from the ground after 4.8s, his maximum acceleration of 11.4m/s^2 is obtained after 4.4s and his maximum absolute velocity is 18.7m/s at 2.5s. In terms of his position, this would mean that maximum acceleration is when he is being pulled up before the first bungee recoil and maximum speed is at the end of the freefall. Furthermore, all of these maxima emerge from the first $\frac{1}{2}$ period of motion, further insinuating the importance of the cord's stretching abilities to dictate the subsequent oscillations. Additionally, from varying k and η coefficients, k was noticed to have a larger impact on the behavior of the jump following a trend of lower maximum acceleration and bigger fall height as k decreased. From **Table A**, this is seen by the $k=240\text{N/m}$ value resulting in a maximum acceleration of 27.1m/s^2 and a minimum tower height of 28.2m, which are significantly more dangerous than the previously seen $k=40\text{N/m}$ values. Following this line of reasoning, it would be reasonable to assume that is the reason why jumpers can fall without sustaining serious injury from a high tower. The force experienced at any moment in time by the jumper is slowly being “lost” in the cord the more it stretches and results in a less violent jolt when it comes time to reverse the direction of their trajectory. Meanwhile, maximum velocity remained more or less constant throughout all trials (around -18m/s) at the tail end of the freefall.

As such, the simulation showed that an increasing K coefficient would lead to a higher maximum acceleration, making $k=40\text{N/m}$ the “safest” option while still allowing for the jumper to experience the longest fall. This is consistent, as k depends on the elastic modulus, cross-sectional area, and the original length of the cable. The original cable length is given as 18m. Natural rubber or other elastomers are typically used for the core of the cable. The cable is typically covered by a woven synthetic material such as nylon to protect the rubber from heat/sunlight. Based on these two considerations, the material selection for the core is narrowed down to natural rubber, which has an elastic modulus in the range of 3.45Mpa to 24.1Mpa [1].

Another important consideration is the possibility of stress relaxation and hysteresis of the bungee cable, which would result in permanent deformation and weakening of the cable and safety concerns. “Hysteretic” would refer to the uneven forces being exerted on the person between falling downward and upward. It also is dependent on the uneven compression and tension rope friction properties (i.e. the rope can compress easier than stretch or vice-versa). Since cord manufacturing affects η and K , the mechanical properties of the rope affect the

studied displacement, velocity, and acceleration. Therefore, the manufacturing process of the rubber should involve vulcanization of the rubber to reduce the possibility of stress relaxation. Vulcanization introduces cross-links between the polymer chains, strengthening the material. Research proves that more crosslinks produced during the vulcanization process result in the material being capable of withstanding more stress without permanent deformation[2]. Vulcanization also leads to higher elasticity ($E=1.5\text{ MPa}$ [3]), and consequently, a lower stiffness(k). Furthermore, vulcanization improves the cable's ability to withstand hysteresis, because the cable will also be stronger under compression after vulcanization[2]. In particular, carbon-containing cross-links are proven to increase the lifespan of vulcanizates[2] compared to other materials typically used to vulcanize natural rubber. Assuming the diameter of the cord is around 2.5cm, the resulting stiffness value for a fixed cord length of 18m, using **Equation 4**, is 41 N/m. The k value corresponds to the lowest k value from previous evaluations, indicating that it will meet the vertical distance constraints too. Based on the figures, the k value of 40 N/m results in enjoyable conditions for the jumper, and the jumper will experience minimal amounts of upward acceleration. The maximum acceleration the jumper will reach is just under 15 m/s^2 , or less than $1.5g$, which is less than a person will experience on a typical roller coaster[4], but still more than they experience on a daily basis. They would also experience only around 3 ups/downs within 20 seconds, the assumed time it takes for their velocity to be low enough to be safely recoverable. Thus, the jumper will have fun without putting their safety at risk.

Finally, ride expectations also affect the model in unaccounted-for ways. They have to do with the behavior of the person dropping. As this is a person, they can flail their arms in/out to decrease/expand their surface area in contact with the air. This could make the assumed constant damping coefficient of the air ($\text{Da}=8$) change at a moment's notice - impacting the simulation by slowing or quickening descent.

CONCLUSIONS

In conclusion, the jumper can complete the jump without sustaining injury by observing the parameters that influence maximum acceleration and velocity. Such parameters include the cord stiffness (k), the cord length, the jumper's vertical starting position, the cord's loss factor, and the manufacturing and mechanical properties of the cord. Ultimately, a lower K value and higher η value would mean that the jumper experiences less maximum acceleration while also coming to the equilibrium position as quickly as possible. This would ensure the jumper has a smoother experience that also comes to an end quicker as opposed to violently being pulled back and suspended in oscillation for longer. Overall, taking into account the safety and enjoyment of the person jumping, it is most ideal to choose a vulcanized natural rubber cord with a stiffness of around 40N/m, and for the jumper to start at an absolute minimum height of 55 meters. Then, the jumper will not be injured due to acceleration or due to hitting the ground.

APPENDIX

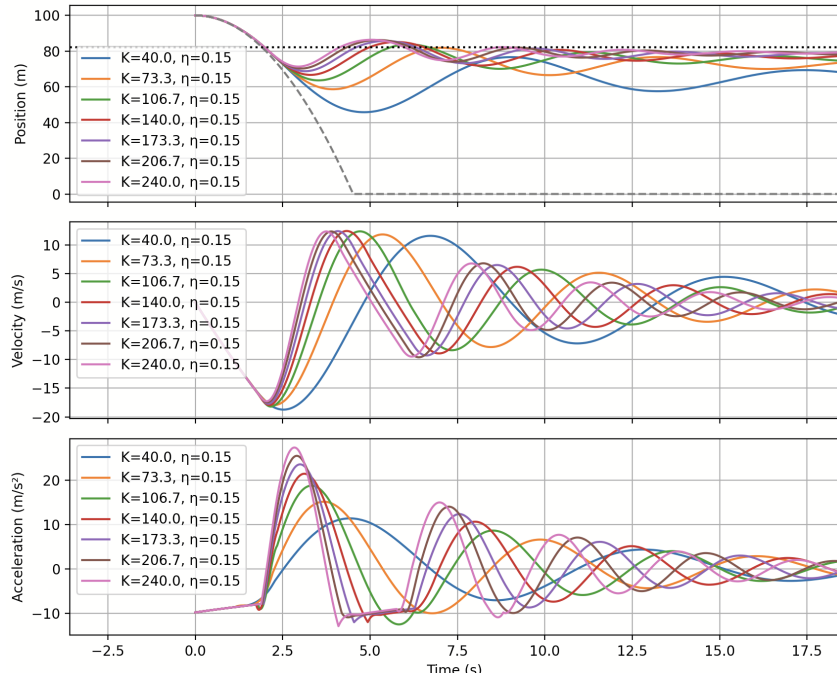


Figure A: Modeled Equations of Motion, Velocity, and Acceleration using varied K and η values.

Table A: Numerical values of select cases in the simulation with accompanying maximum acceleration, velocity, and deflection

Eta	K (N/m)	Max_acc (m/s^2)	Max_acc_time (s)	Max_vel (m/s)	Max_vel_time (s)	Min_pos (m)	Min_pos_time (s)	Minimum Tower Height req. (m)	Cord Stretched Length (m)
0.150	40.0	11.4	4.4	18.7	2.5	45.8	4.8	54.2	36.2
0.225	40.0	10.5	4.3	18.1	2.5	47.8	4.8	52.2	34.2
0.300	40.0	9.8	0.0	17.6	2.4	49.5	4.8	50.5	32.5
0.150	68.6	14.7	3.7	18.0	2.3	57.5	4.0	42.5	24.5
0.300	68.6	12.5	3.6	16.8	2.2	60.3	4.0	39.7	21.7
0.150	97.1	18.0	3.4	18.3	2.2	62.4	3.6	37.6	19.6
0.300	97.1	15.9	3.2	17.8	2.1	64.3	3.6	35.7	17.7
0.150	240.0	27.4	2.8	17.3	2.0	71.3	2.9	28.7	10.7
0.300	240.0	27.1	2.7	18.0	2.1	71.8	2.9	28.2	10.2

REFERENCES

- [1] “NR- Natural Rubber,” Rahco-Rubber, <https://rahco-rubber.com/materials/nr-natural-rubber/>.
- [2]”Natural Rubber, Vulcanized (NR, IR, Polyisoprene),” Matweb, https://www.matweb.com/search/datasheet_print.aspx?matguid=6588439546ac4492965c894ddff3f5da.
- [3] S Baxter, M.A.A Wilson, 1963, “Stress relaxation of vulcanized rubbers III — Experimental study, Polymer,” Volume 4, Pages 163-173, ISSN 0032-3861, [https://doi.org/10.1016/0032-3861\(63\)90023-5](https://doi.org/10.1016/0032-3861(63)90023-5).
- [4] “How a Coaster Moves,” Coaster Force, <https://coasterforce.com/physics/>.

Computational Assignment 2 - Kinematics of Crankshaft and Rod

TO: Adolfo Delgado

FROM: Group 7 of MEEN 363 - 502 (Tori Abell, Alois Campbell, Jake Smith, Eddy Silva, Ian Wilhite)

Subject: Assignment 2, Crankshaft and Rod

Date: 04/02/2025

EXECUTIVE SUMMARY

The objective is to derive and analyze the displacement, velocity, and acceleration of the slider (point B) and the center of mass of the connecting rod (point G) as functions of the crank angle (θ). Using a constant crank angular velocity of 300 rpm, kinematic equations for point B and point G were derived using the geometric method to describe the motion of the system. The analysis was performed for three different crank-to-rod length ratios: $P = 0.1, 0.3, 0.5$. Computational simulations generated time-based plots of position, velocity, and acceleration for both point B and point G over two full revolutions of the crank. The results show significant variation in position, velocity, and acceleration of points B and G depending on the value of P. As P increases, the magnitude and variation of the slider's velocity and acceleration increase, reflecting stronger dynamic effects. This analysis confirms the importance of geometric ratios in crank-slider mechanisms and supports using Newton's Second Law to identify force trends acting on the system components.

METHOD

To obtain kinematic equations for point B, a geometric approach was used. It consisted of adding the horizontal lengths of the members and setting that equal to the i vector position of B (x_B) at any given time.

The vertical distance with respect to B (y_B) was set to 0 as there is no vertical translation at that point.

Nevertheless, a kinematic constraint was determined by setting the bar heights equal to each other. The results are the **Equations (1) and (2)** for position below. Taking the derivative of these equations results in the equations for velocity and acceleration - **Equations 3, 4, 5, and 6**. The position, velocity, and acceleration of point G were then evaluated using vector properties based on the given position of G (center of rod l_2).

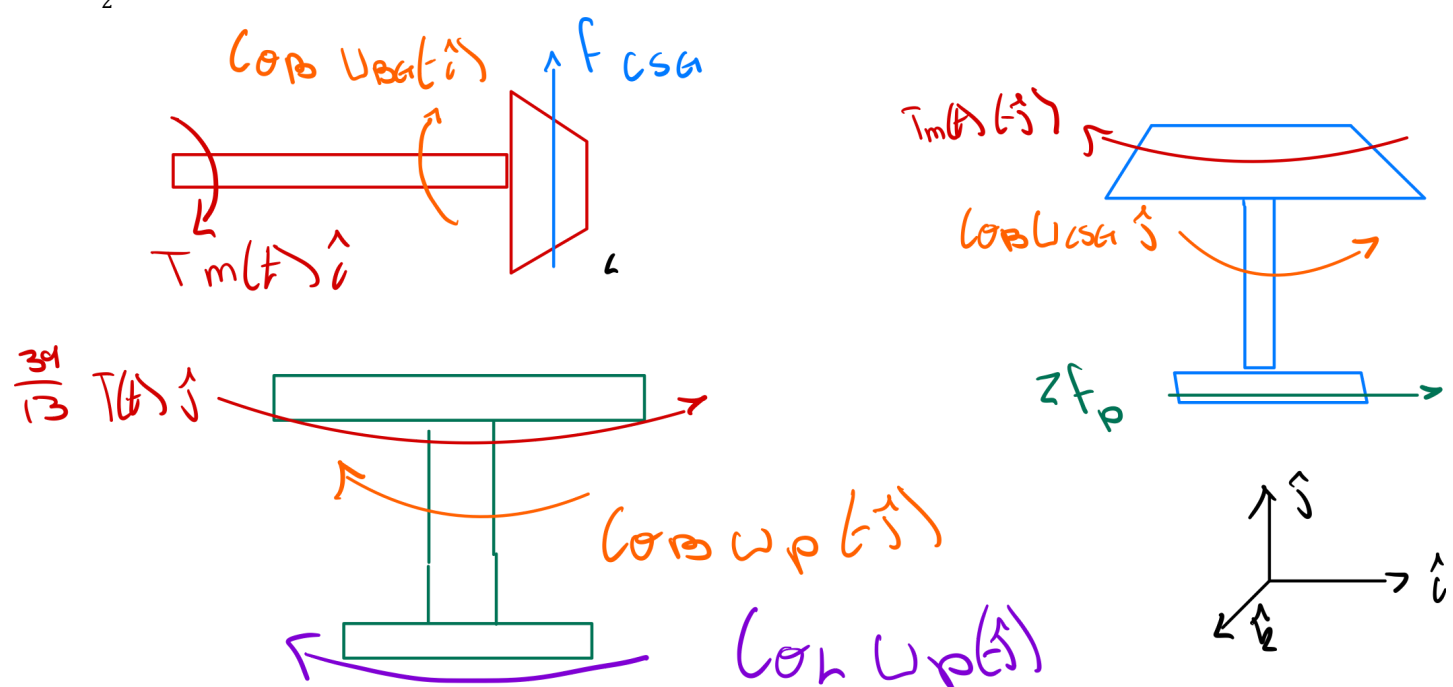


Figure 1: Diagram of Bodies

Geometrical derivation of equations of motion for point B:

Given:

$$P = \frac{l_1}{l_2}, \theta' = \omega = 300 \text{ rpm}, l_T = 7 \text{ ft}, l_T = l_1 + l_2$$

Position (X, Y Components)

$$l_1 \cos(\theta) + l_2 \cos(\phi) = x_B \quad (1)$$

$$l_1 \sin(\theta) = l_2 \sin(\phi) \quad (2)$$

Velocity (X, Y Components)

$$-l_1 \sin(\theta) * \theta' = l_2 \sin(\phi) * \phi' + \dot{x}_B \quad (3)$$

$$l_1 \cos(\theta) * \theta' = l_2 \cos(\phi) * \phi' \quad (4)$$

Acceleration (X, Y Components)

$$-l_1 \sin(\theta) * \theta'' - l_1 \cos(\theta) * \theta'^2 - l_2 \cos(\phi) * \phi'^2 = l_2 \sin(\phi) * \phi'' + \ddot{x}_B \quad (5)$$

$$l_2 \cos(\phi) * \phi'' = l_2 \sin(\phi) * \phi'^2 + l_1 \cos(\theta) * \theta'' - l_1 \sin(\theta) * \theta'^2 \quad (6)$$

* θ'' term goes to 0 due to constant velocity, zero acceleration condition given*

The vector equation properties to find the position, velocity, and acceleration of point G from the EOM derived for point B:

$$r_{OG} = r_{OB} + r_{BG} = x_B(i) + \frac{l_2}{2} * (\cos(\phi)(-i) + \sin(\phi)j) \quad (7)$$

$$v_G = v_B + \omega_{BG} \times r_{BG} = \dot{x}_B(-i) + \phi'(-k) \times \frac{l_2}{2} * (\cos(\phi)(-i) + \sin(\phi)j) \quad (8)$$

$$a_G = a_B + \omega_{BG}' \times r_{BG} + \omega_{BG} \times \omega_{BG} \times r_{BG}$$

$$a_G = \ddot{x}_B(-i) + \phi''(-k) \times \left(\frac{l_2}{2} * (\cos(\phi)(-i) + \sin(\phi)j) \right) + \phi'^2 \left(\frac{l_2}{2} \right) (\cos(\phi)(i) - \sin(\phi)j) \quad (9)$$

Cramer's Rule

To analytically solve for the variables in the equations above, Cramer's Rule was used. Below is an example using the angular velocities.

$$\begin{bmatrix} -l_1 \sin(\theta) & -l_2 \sin(\phi) \\ l_1 \cos(\theta) & l_2 \cos(\phi) \end{bmatrix} \begin{bmatrix} \theta' \\ \phi' \end{bmatrix} = \begin{bmatrix} \dot{x}_B \\ 0 \end{bmatrix}$$

$$\theta' = \begin{vmatrix} \dot{x}_B & -l_2 \sin(\phi) \\ 0 & l_2 \cos(\phi) \end{vmatrix} \div \begin{vmatrix} -l_1 \sin(\theta) & -l_2 \sin(\phi) \\ l_1 \cos(\theta) & l_2 \cos(\phi) \end{vmatrix}$$

$$\phi' = \begin{vmatrix} -l_1 \sin(\theta) & \dot{x}_B \\ l_1 \cos(\theta) & 0 \end{vmatrix} \div \begin{vmatrix} -l_1 \sin(\theta) & -l_2 \sin(\phi) \\ l_1 \cos(\theta) & l_2 \cos(\phi) \end{vmatrix}$$

After finding a general solution for position, velocity, and acceleration about points B and G, Python was used to create a data set spanning 2 periods using time as the x-axis and the solved terms in the y (seen in the figures below).

PROCEDURE

Using the derived kinematic equations (**Equations 1-6**) for point B, the numpy library in Python was used to construct the model and plot the results. The plots were constructed in terms of P, which is the ratio between l_1 and l_2 , to observe the effect of varying the ratio between l_1 and l_2 . These figures were compiled to create three subplots in **Figure 2**.

A similar approach was taken for the kinematic equations of point G (**Equations 7-9**) in **Figures 3, 4, 5, 6, and 7**. To ensure no mistakes were made, the kinematic equations of point A were derived geometrically and averaged with B to determine an alternate expression of G (**Appendix Equations**). Since the AB bar is symmetric, the center of mass must be equally positioned between points A and B, rendering this alternate version acceptable for the simulation. In other words, the X position of G is the average of A and B, and the Y position of point G is found by dividing the Y position of A by two. Since this latter approach was significantly easier to code, it was the approach used in the final simulation.

Once these equations and parameters were set, the given constant velocity of θ' (=300 rpm) and θ'' (=0) were used to solve for the rest of the unknowns using the built-in numpy solver, ultimately rendering all the tables and figures discussed.

RESULTS and DISCUSSION

Figure 2 shows the horizontal position, velocity, and acceleration of point B with varying ratios between l_1 and l_2 (P). When P equals 0.1, for example, l_1 is 10% of l_2 . The length of l_1 plus l_2 is given as 7ft, therefore when P=0.1, $l_1=0.7\text{ft}$ and $l_2=6.3\text{ft}$. When point A moves below y=0 in the positive x-axis, point A and point B begin moving in the -x direction, until link OA and link AB are both horizontal and lying along the x-axis at y=0. At this position, the horizontal location of points B and A will be at their minimum. Point A will be at x = -0.7ft and point B will be at x = 6.3 ft. **Figure 2** displays this expected result when the position of B is at its minimum, at 6.3ft. The same logic applies to all values of P. Furthermore, the graph displays three points at which the horizontal location of B is 7ft. At these points, links OA and AB are both horizontal along the x-axis, and the horizontal location of A is positive. The first time this occurs is when θ and ϕ are zero. Later occurrences occur at the end of each rotation until reaching the max angle simulated (2π radians).

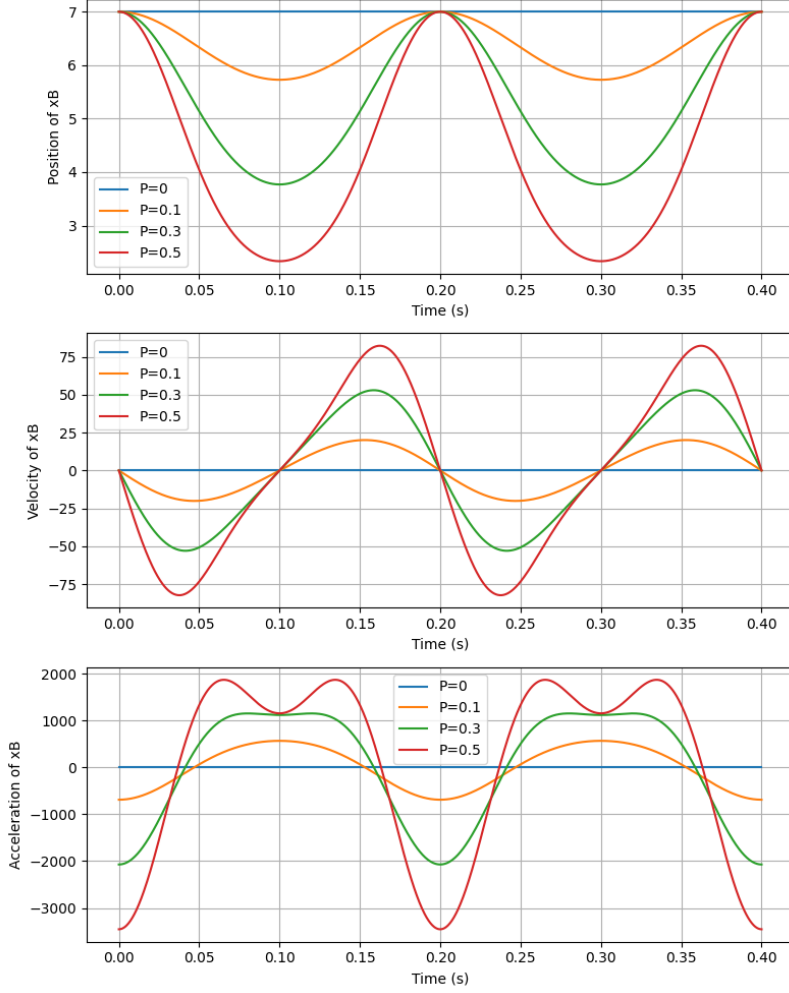


Figure 2: Plot of point B horizontal position, velocity, and acceleration as a function of time with varying P values.

Additionally, the maximum and minimum velocities of point B and the time they occur are displayed in **Figure 2** and recorded in **Table 1** in the appendix. The maximum and minimum acceleration for point B and the time they occur are recorded in **Table 2** in the appendix. The maximum/minimum velocity magnitude is approximately 82.3 ft/s. The magnitude of the minimum acceleration is 3454 ft/s², and the magnitude of the maximum acceleration is approximately 1150 ft/s². Both the maximum and minimum velocities and acceleration occur when P = 0.5, right before and after point A is on the y-axis. The positive maximum acceleration (expanding crankshaft) and by extension the maximum force takes place right before and after the two bars are horizontal to each other, with point A being in the negative x direction. These accelerations also result in accompanying maximum magnitudes of velocity, which come about from these abrupt acceleration local maxima. In the inverse case, where point A is located in the positive x-axis at y=0, the acceleration is at its absolute maximum with the rod fully extended and preparing to contract/expand fully, depending on the cycle direction.

Figure 3 displays the varying vertical position of point G and the corresponding horizontal position. Point G's motion is a combination of a circular motion from the crank rotation, θ , and the back and forth translations of point B. Due to the combined effects, point G's motion is oblong/“egg-shaped”, becoming thicker at the bottom of the stroke than the top. This asymmetrical motion begins to appear differently as L_1/L_2 decreases, looking more like a symmetrical oval. This is because when L_1 is small compared to L_2 , the motion of L_2 acts more like a linear

translation, as the circular motion is less prevalent. This leads to the motion of G being thinner and more symmetrical.

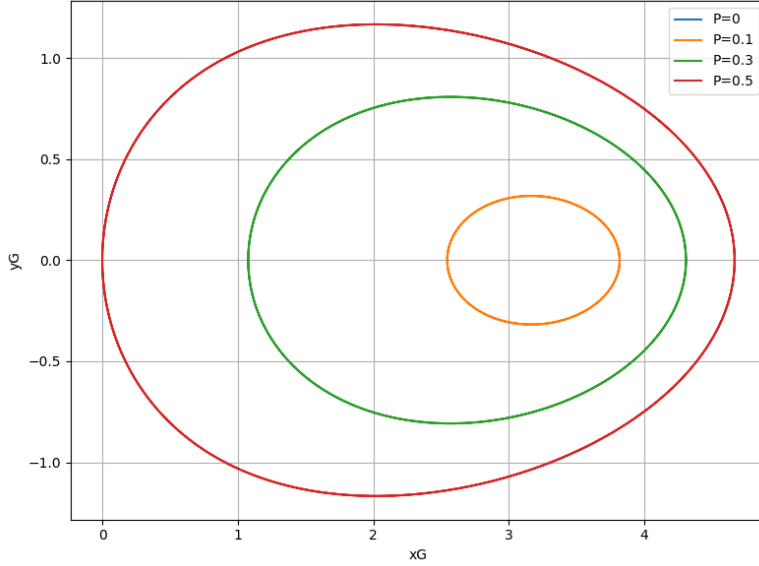


Figure 3: Plot of the motion of point G vertical position vs horizontal position (Y_G vs X_G).

For the $P=0$ case, there is only one fixed geometry solution available. Therefore, it does not show on the graph as there is no variation in position observable. This same logic applies to all other figures for the position, the velocity, and acceleration of points B and G. Since there is no change in geometry due to the constraints, there is no motion and no observable changes, creating a flat slope at 0.

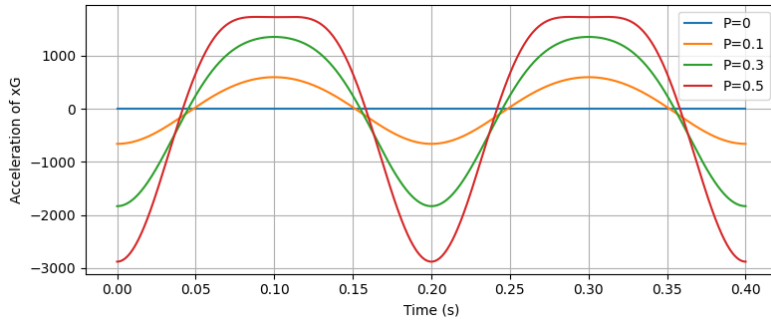


Figure 4: Plot of point G horizontal acceleration as a function of time with varying P values.

Newton's second law can be applied to the problem based on the acceleration. Since force is mass times acceleration, point G and point B experience the greatest force in the x direction, where the magnitude of the acceleration is the greatest, at times indicated by the solution. **Figures 4 and 5** indicate that the acceleration of point G in the horizontal direction has the greatest magnitude where the links reach their maximum or minimum x position (see **Figure 6** in the appendix for the plot of the position and velocity of point G). Therefore, link AB experiences the greatest force at its center of gravity when it changes directions along the x -axis.

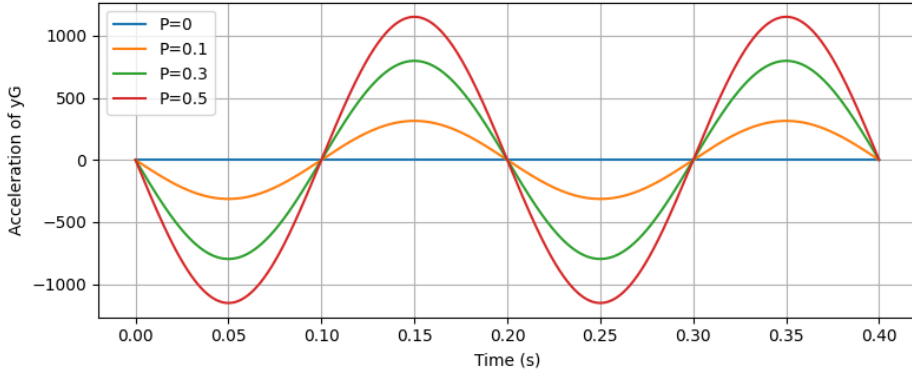


Figure 5: Plot of point G vertical acceleration as a function of time with varying P values.

Figure 5 illustrates the vertical acceleration of point G over time for varying P values. The vertical position in **Figure 7** in the appendix exhibits a sinusoidal pattern that reflects the crank's rotational motion, while the velocity and acceleration curves show how rapidly this vertical motion changes throughout the stroke. As P increases, the vertical velocity and acceleration both grow in magnitude, indicating a stronger vertical influence from the crank's rotation. The peaks in acceleration occur near the midpoints of each stroke, where the vertical direction reverses and inertial forces peak. This vertical dynamic is particularly important in applications like internal combustion engines, where vertical forces translate into vibrations and stresses that impact structural design and operational smoothness.

CONCLUSIONS

In conclusion, the kinematic analysis of the crank-slider mechanism reveals significant dependence on the crank-to-rod length ratio (P). As P increases, the dynamic effects on both point B and point G become more pronounced, with greater velocity and acceleration magnitudes. These findings have direct implications for the design and performance of reciprocating systems, where balancing force transmission and inertial effects is crucial. Newton's Second Law reinforces that maximum force corresponds to maximum acceleration, which occurs at predictable angular positions (fully expanded or contracted). This analysis provides valuable insight into optimizing component dimensions to reduce wear, minimize vibrations, and ensure efficient mechanical performance. Ultimately, this makes the mechanism ideal for the use case given of the crankshaft two-stroke engine.

APPENDIX

Point B Maximum and Minimum Velocities	
Time (s)	Velocity (ft/s)
0.0376	-82.3
0.163	82.3
0.237	-82.3
0.362	82.3

Table 1: Maximum and minimum velocity of point B and the time it occurs.

Point B Maximum and Minimum Acceleration	
Time (s)	Acceleration (ft/s ²)
0	-3454
0.119	1150
0.080	1150
0.200	-3454
.280	1150
0.319	1150
0.400	-3454

Table 2: Maximum and minimum acceleration of point B and the time they occur.

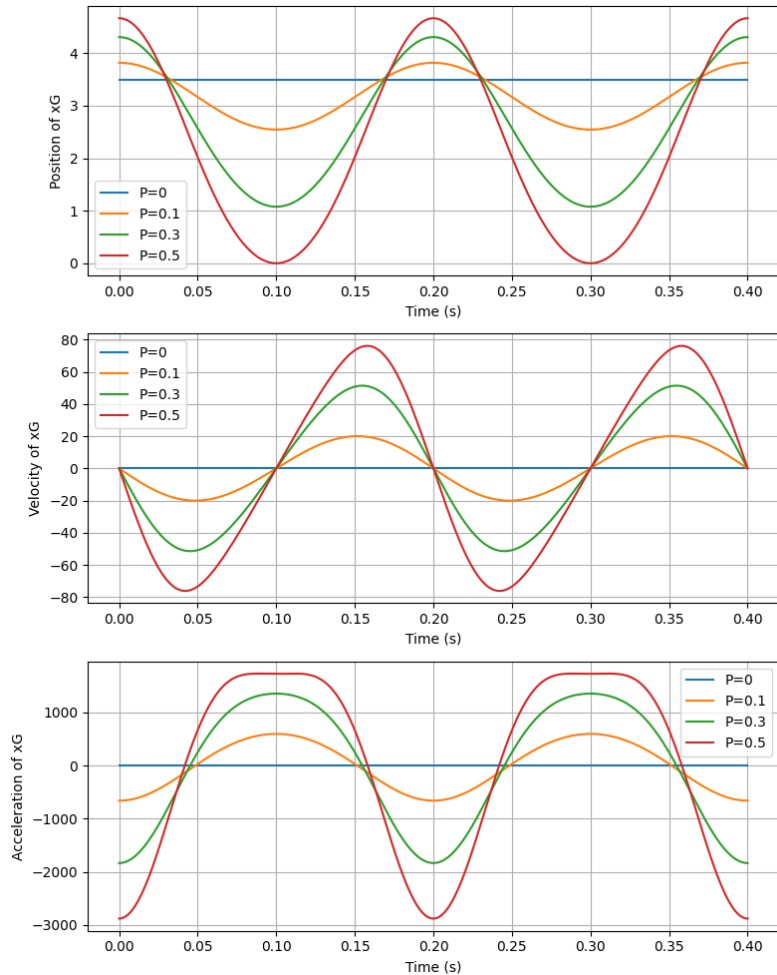


Figure 6: Plot of point G horizontal acceleration as a function of time with varying P values.

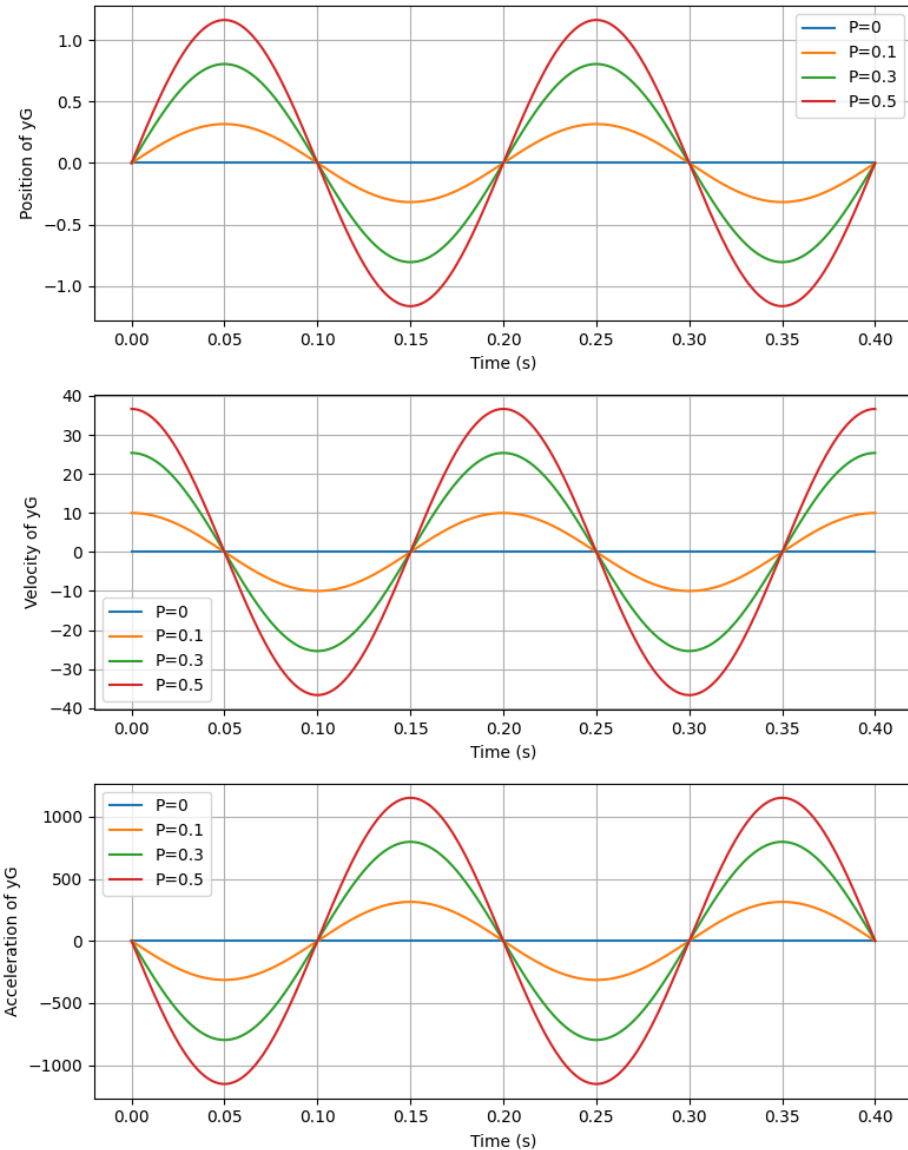


Figure 7: Plot of point G vertical position, velocity, and acceleration as a function of time with varying P values.

Alternative proof for point G, used to verify equations, and the simulation used:

For point G, an average between points A and B was taken:

Point A:

Position (X, Y Components)

$$l_1 \cos(\theta) = x_A \quad (\text{A.1})$$

$$l_1 \sin(\theta) = y_A \quad (\text{A.2})$$

Velocity (X, Y Components)

$$-l_1 \sin(\theta) * \theta' = \dot{x}_A \quad (\text{A.3})$$

$$l_1 \cos(\theta) * \theta' = \dot{y}_A \quad (\text{A.4})$$

Acceleration (X, Y Components)

$$-l_1 \sin(\theta) * \theta'' - l_1 \cos(\theta) * \theta'^2 = \ddot{x}_A \quad (\text{A.5})$$

$$l_1 \cos(\theta) * \theta'' - l_1 \sin(\theta) * \theta'^2 = \ddot{y}_A \quad (\text{A.5})$$

Average of points A and B, for point G:

Position

$$\frac{x_A + x_B}{2} = x_G = (l_1 \cos(\theta) + \frac{1}{2} l_2 \cos(\phi)) \quad (\text{A.6})$$

$$\frac{y_A}{2} = y_G = \frac{1}{2} * l_1 \sin(\theta) \quad (\text{A.7})$$

Velocity

$$\frac{\dot{x}_A + \dot{x}_B}{2} = \dot{x}_G \quad (\text{A.8})$$

$$\frac{\dot{y}_A}{2} = \dot{y}_G = \frac{1}{2} * l_1 \cos(\theta) * \omega \quad (\text{A.9})$$

Acceleration

$$\frac{\ddot{x}_A + \ddot{x}_B}{2} = \ddot{x}_G \quad (\text{A.10})$$

$$\frac{\ddot{y}_A}{2} = \ddot{y}_G = \frac{1}{2} (l_1 \cos(\theta) * \theta'' - l_1 \sin(\theta) * \omega^2) \quad (\text{A.11})$$

* θ'' term goes to 0 due to constant velocity, zero acceleration condition given*

REFERENCES

- [1] Dynamics in Engineering Practice, 11th Ed (only), D.W. Childs & Ap. Conkey, CRC Pubs
<https://www.crcpress.com/Dynamics-in-Engineering-Practice-Eleventh-Edition/Childs-Conkey/9781482250251>

Computational Assignment 3 - Modeling a Mechanical System

TO: Adolfo Delgado

FROM: Group 7 of MEEN 363 - 502 (Tori Abell, Alois Campbell, Jake Smith, Eddy Silva, Ian Wilhite)

Subject: Assignment 3, Modeling a Mechanical System

Date: 04/28/2025

EXECUTIVE SUMMARY

The objective is to derive equations of motion and find the total energy and dissipative power of the system. The equation of motion can be found through two methods. First, an equation of motion for the system is established by summing forces and moments for the five components and implementing the kinematic constraints of the system. The second method for finding the equation of motion is by analyzing the potential, kinetic, and dissipated energy of the system and using the concept of conservation of mechanical energy. Additionally, given specific damping coefficients and the motor speed, the motor torque and paddle speed are calculated. They will require a minimum of 323 newton meters of torque to drive the system, and will take 3.27 seconds from beginning at rest to reach 99% of operating speed. Due to power losses in the system, such as in the bearings, the efficiency of the system is 84%, and it costs \$438 per day, \$75 of which was lost due to friction.

METHOD

The mixer system presented had many moving parts. Under further inspection, they can be broken up into five distinct free bodies:

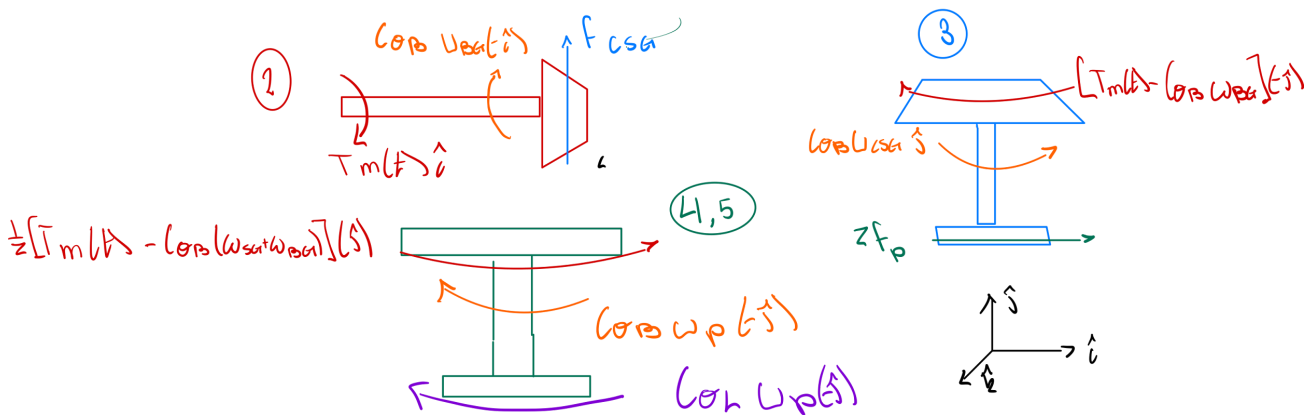
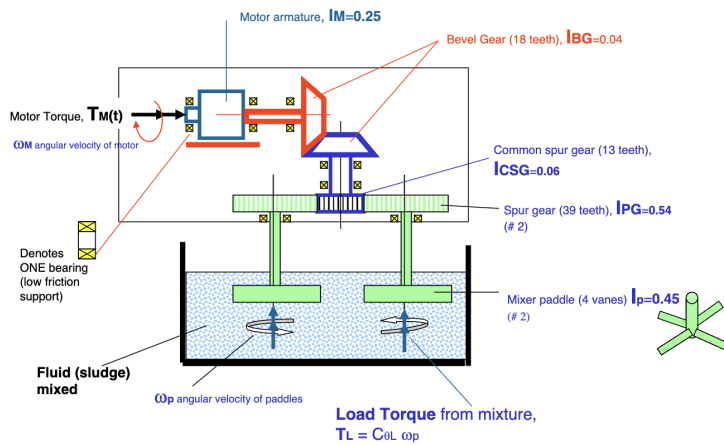


Figure 1: Free Body Diagrams for Components

Using this approach, the system can be described using 5 equations - one for each of the bodies:

$$I_M \theta_1'' = T_M - T_{12} - \theta_1' C_{\theta B} \quad (1)$$

$$I_{BG} \theta_2'' = T_{12} - T_{23} - 2\theta_2' C_{\theta B} \quad (2)$$

$$I_{BG} \theta_3'' = T_{23} - T_{34} - 2\theta_3' C_{\theta B} \quad (3)$$

$$I_{PG} \theta_4'' = T_{34} - T_{45} \quad (4)$$

$$I_P \theta_5'' = T_{45} - T_L = T_{45} - C_{\theta L} \omega_P - \theta_5' C_{\theta B} \quad (5)$$

Furthermore, some kinematic constraints are used to simplify these equations. The defined gear ratios and relationships between the bodies were used to explain how the motor's input torque is converted into output torque at the paddles.

$$\theta_1 = \theta_2 = \theta_3 = \theta_M \quad (6)$$

$$\theta_4 = \theta_5 = \theta_P \quad (7)$$

$$3\theta_M = \theta_P, 3\theta_M' = \theta_P', 3\theta_M'' = \theta_P'' \quad (8)$$

The five motion equations can be simplified to two, where θ_M is the angle of the motor, θ_P is the angle of the paddle, T_{CSG} is the torque of the center spur gear, T_{SG} is the torque of the additional spur gears, and the relationship of the torques are applied:

$$\theta_M''[I_M + 2I_{BG} + I_{CSG}] = T_M - 5\theta_M' C_{\theta B} - T_{CSG} \quad (9)$$

$$T_{CSG} = \frac{13}{39}T_{SG} \quad (10)$$

$$\theta_P''[2(I_{PG} + I_P)] = T_{SG} - 2C_{\theta B}\theta_P' - 2C_{\theta L}\omega_P \quad (11)$$

After this step, the equations are simplified even further, into a single equation.

$$\begin{aligned} & \Rightarrow 9\theta_P''[I_M + 2I_{BG} + I_{CSG}] + \theta_P''[2(I_{PG} + I_P)] = 3T_M - 15\theta_P' C_{\theta B} - 2C_{\theta B}\theta_P' - 2C_{\theta L}\omega_P \\ & \Rightarrow [9(I_M + 2I_{BG} + I_{CSG}) + 2(I_{PG} + I_P)]\theta_P'' = 3T_M + [-47C_{\theta B} - 2C_{\theta L}]\theta_P' \\ & \Rightarrow 3T_M = \theta_P''[9(I_M + 2I_{BG} + I_{CSG}) + 2(I_{PG} + I_P)] + [47C_{\theta B} + 2C_{\theta L}]\theta_P' \end{aligned} \quad (12)$$

Therefore,

$$I_{eq} = 9(I_M + 2I_{BG} + I_{CSG}) + 2(I_{PG} + I_P) \quad (13)$$

$$C_{eq} = 47C_{\theta_B} + 2C_{\theta_L} \quad (14)$$

Using the conservation of mechanical energy equation, P_{diss} (dissipative power) and P_{drive} (external drive power) can be used to describe the non-conservative forces in the system (from the damping and driving torque):

$$\frac{d}{dt}(E_k + E_p) + P_{diss} = P_{drive}, \text{ where } E_k \text{ is the kinetic energy and } E_p \text{ is the potential energy.} \quad (15)$$

$$\frac{d}{dt}E_k = [9(I_M + 2I_{BG} + I_{CSG}) + 2(I_P + I_{PG})]\theta_P'' * \theta_P' \quad (16)$$

$$P_{diss} = C_{\theta_B}(\frac{d}{dt}\theta_1)^2 + 2C_{\theta_B}(\frac{d}{dt}\theta_2)^2 + 2C_{\theta_B}(\frac{d}{dt}\theta_3)^2 + 2C_{\theta_B}(\frac{d}{dt}\theta_5)^2 + 2C_{\theta_L}(\frac{d}{dt}\theta_5)^2 \quad (17)$$

$$P_{diss} = [47C_{\theta_B} + 2C_{\theta_L}](\frac{d}{dt}\theta_P)^2 = [47C_{\theta_B} + 2C_{\theta_L}](\theta_P') * (\theta_P') \quad (18)$$

$$P_{drive} = (T_M) * 3\theta_P' \quad (19)$$

The simplified energy equation is as follows, using (16), (18), and (19):

$$[9(I_M + 2I_{BG} + I_{CSG}) + 2(I_P + I_{PG})]\theta_P'' + [47C_{\theta_B} + 2C_{\theta_L}](\theta_P') = 3(T_M) \quad (20)$$

Therefore, the same I_{eq} and C_{eq} were determined as in the Newtonian approach:

$$I_{eq} = 9(I_M + 2I_{BG} + I_{CSG}) + 2(I_{PG} + I_P) \quad (13)$$

$$C_{eq} = 47C_{\theta_B} + 2C_{\theta_L} \quad (14)$$

PROCEDURE

Using the results obtained from the kinematic constraints, free body diagrams, and equations of motion, the mixer can be analyzed under steady state and transient conditions. Using the values that were provided, this is the current state of the system:

- Motor torque T_M for a constant motor speed of 60 Hz (377 rad/s):
 - $T_M * 3 = \theta_P''[9(I_M + 2I_{BG} + I_{CSG}) + 2(I_{PG} + I_P)] + [47C_{\theta_B} + 2C_{\theta_L}]\theta_P'$
 - $= 0 + [47(0.028) + 2(3.2)](125.66)$
 - $T_M = 323.2 \text{ Nm}$

- Power from the motor:
 - $P = T * \omega$
 - $P = 323.2 * 377$
 - $P = 121.8 \text{ kW}$
- Power lost from bearings:
 - $\omega_{CSG} = \omega_M = 377 \text{ rad/s}$
 - $\omega_P = \omega_M * \frac{N_{CSG}}{N_{PG}} = 377 * \frac{1}{3} = 126 \text{ rad/s}$
 - $P_{diss} = [47C_{\theta B}](\theta_P')^2 = [47(0.028)](126)^2$
 - Total Power Lost, $P = 20.8 \text{ kW}$
- Power from the load:
 - $P_L = T_L * \omega = C_{\theta L} * \omega^2$
 - $P_L = 2 * 3.2 * 126^2$
 - $P_L = 101.1 \text{ kW}$
- Mechanical efficiency:
 - $\eta = \frac{P_L}{P_M} * 100 = \frac{101.1}{121.8} * 100$
 - $\eta = 84\%$
- Cost to operate:
 - $C = 0.15 \frac{\$}{\text{kW} \cdot \text{h}}$
 - $Energy = Power * t = 121.8 * 24 = 2923 \text{ kW} \cdot \text{h}$
 - $Cost Per Day = E * C$
 - $Cost Per Day = \$438$
- Money lost:
 - $Energy Lost = Bearing Power * t = 20.8 * 24 = 499 \text{ kW} \cdot \text{h}$
 - $Cost Per Day = Energy Lost * C$
 - $Money Lost = \$75$
- System time constant:
 - $I_{eq} = 9(I_M + 2I_{BG} + I_{CSG}) + 2(I_{PG} + I_P)$
 - $= 9(0.25 + 2(0.04) + 0.06) + 2(0.54 + 0.45)$
 - $= 5.49 \text{ kg} \cdot \text{m}^2$
 - $C_{eq} = 17C_{\theta B} + 2C_{\theta L} = 47(0.028) + 2(3.2) = 7.72 \frac{\text{Nm}}{\text{rad/s}}$
 - $\tau = \frac{I_{eq}}{C_{eq}} = \frac{5.49}{7.72}$
 - $\tau = 0.711 \text{ s}$
- Time Response:
 - $\omega_p = \omega_{steady}(1 - e^{-t/\tau})$
 - $\omega_p = 126(1 - e^{-t/0.711})$
- Time to reach operating speed:
 - $124.74 = 126(1 - e^{-t/0.711})$
 - 124.74 is 99% of the operating speed. This value is used because $\ln(0)$ does not exist.

- $0.99 = 1 - e^{-t/0.711}$
- $\ln(0.01) = -t/0.711$
- $t = 3.27s$

RESULTS and DISCUSSION

The gear ratios are a significant part of the system and are used to simplify the equations. By applying the gear ratio kinematic constraints and using the Newtonian method, the system is modeled in **Equation 12**. The equations of motion are found by summing forces and torques between the gears, as indicated by the free-body diagrams in **Figure 1**. The system's equivalent inertia and viscous damping coefficient are noted in **Equations 13 and 14**.

Additionally, the energy method is applied to the system to verify the first approach. The two main components in the energy equations are the power lost from the bearings and load, the torque from the motor, and the power due to kinetic energy. The energy method also uses the gear ratio kinematic constraints to simplify the result, and the final equation (**Equation 20**) results in the same equation of motion as the Newtonian method, as expected. The system's equivalent inertia and viscous damping coefficients are equivalent to those calculated using the Newtonian method, which verifies the results of both methods.

Considering the given values, several key quantities from the system are calculated in the procedure, and recorded in **Table 1**. It is important to note that the power in the motor can be calculated from the torque of the system and verified by summing both the dissipated power and the power of the load.

Table 1: Key values from the system.

T_{Motor}	323Nm
P_{Motor}	121.8kW
P_{diss}	20.8kW
P_{Load}	101.1kW
η	84%
<i>Cost Per Day</i>	\$438
<i>Money Lost</i>	\$75
τ	0.711s
<i>Time to reach operating speed</i>	3.27s

The money lost is due to the power losses in the system. To reduce the money lost each day, the frictional losses in the bearings should be reduced by implementing a maintenance routine on the system and applying lubricant to ensure smoother bearings. Furthermore, the paddles could be designed to be more efficient. If the losses are reduced, the efficiency of the system would be improved.

$$126(1 - e^{-t/0.724}) \quad (21)$$

Equation 21 is the equation for the mixer speed as a function of time. **Figure 2** displays a graphical representation of the speed. The time constant, τ , is the value at which the system reaches 63% of its operational speed. **Figure 2** visually confirms the time constant of 0.724 seconds, showing that the speed reaches approximately 63% of its steady-state value. By observation of **Figure 2**, the time at which the system reaches its operating speed is around 3 seconds, validating prior calculations recorded in **Table 1**.

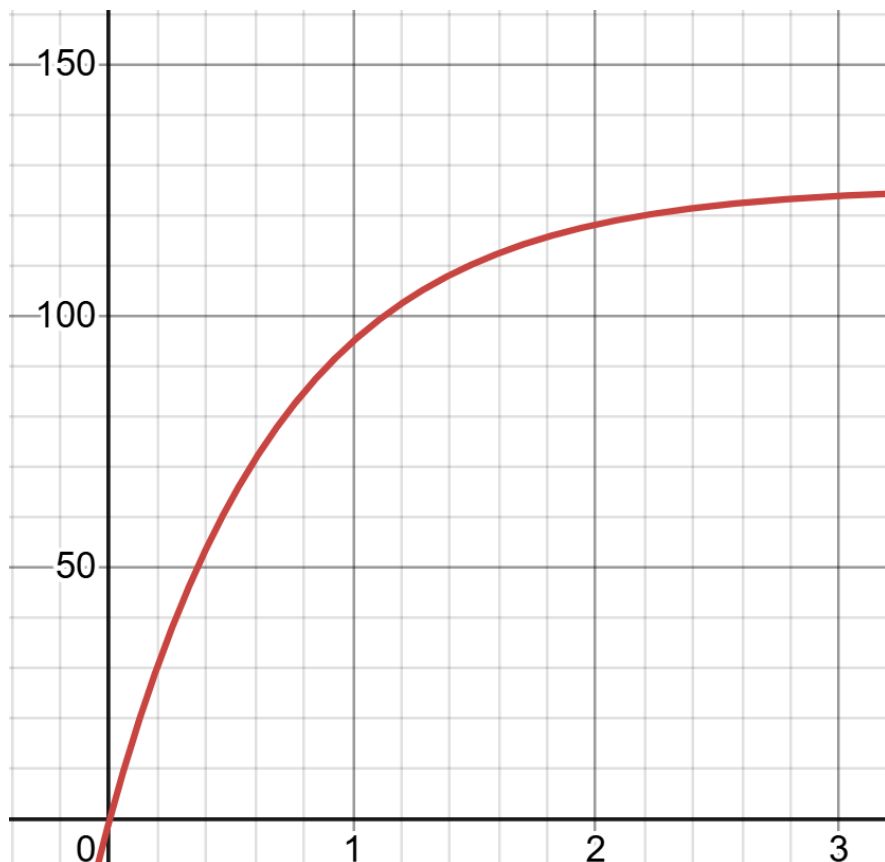


Figure 2. Mixer Speed (rad/s) as a Function of Time (s)

CONCLUSIONS

The mechanical system for the mixer was modeled successfully by applying principles of dynamics and energy conservation. The equivalent inertia and viscous damping parameters were determined consistently through independent approaches. Steady-state performance calculations established the required motor torque, operating speeds, and mechanical power losses within the system. The startup response analysis determined the system time constant and characterized the transient behavior of the paddles. As such, due to its mode of operation, this mixer can probably be classified as a “Paddle industrial mixer” [2]. To further improve its performance, an optimal angle can be set for the viscous fluid being mixed. From certain sources, it can be determined that a 45-degree angle [3] would provide the least amount of resistive torque from the fluid. The modeling effort clearly demonstrates the importance of accounting for mechanical inefficiencies, especially bearing and load damping, to accurately predict system performance. Overall, the work validates the modeling approach and highlights the need for precise dynamic characterization in the design and operation of mechanical systems.

APPENDIX

Detailed steps regarding the derivation of the EOM of the system using the power equation:

From (15) to (16), using the kinematic constraints to simplify:

$$\frac{d}{dt} E_k + 0 = (9I_M \theta_M'' + 2 * 9I_{BG} \theta_M'' + 9I_{CSG} \theta_M'' + 2I_{PG} \theta_P'' + 2I_P \theta_P'') * \theta_P'$$

To determine the left side of (15) in (16):

$$E_k = \frac{1}{2} I_M \theta_1'^2 + \frac{1}{2} I_{BG} \theta_2'^2 + \frac{1}{2} (I_{BG} + I_{CSG}) \theta_3'^2 + 2 \frac{1}{2} I_{PG} \theta_4'^2 + 2 \frac{1}{2} I_P \theta_5'^2$$

$$E_p = 0$$

Using the kinematic constraints to simplify (17) to (18):

$$P_{diss} = C_{\theta_B} \left(\frac{d}{dt} \theta_M \right)^2 + 2C_{\theta_B} \left(\frac{d}{dt} \theta_M \right)^2 + 2C_{\theta_B} \left(\frac{d}{dt} \theta_M \right)^2 + 2C_{\theta_B} \left(\frac{d}{dt} \theta_P \right)^2 + 2C_{\theta_L} \left(\frac{d}{dt} \theta_P \right)^2$$

$$P_{diss} = C_{\theta_B} 9 \left(\frac{d}{dt} \theta_P \right)^2 + 2C_{\theta_B} 9 \left(\frac{d}{dt} \theta_P \right)^2 + 2C_{\theta_B} 9 \left(\frac{d}{dt} \theta_P \right)^2 + 2C_{\theta_B} \left(\frac{d}{dt} \theta_P \right)^2 + 2C_{\theta_L} \left(\frac{d}{dt} \theta_P \right)^2$$

To find the final EOM using energy in (20) from the previous equations:

$$\frac{d}{dt} (E_k + E_p) + P_{diss} = P_{drive}$$

$$[9(I_M + 2I_{BG} + I_{CSG}) + 2(I_P + I_{PG})] \theta_P'' * (\theta_P') + [47C_{\theta_B} + 2C_{\theta_L}] (\theta_P') * (\theta_P') = (T_M) * \theta_M'$$

$$[9(I_M + 2I_{BG} + I_{CSG}) + 2(I_P + I_{PG})] \theta_P'' * (\theta_P') + [47C_{\theta_B} + 2C_{\theta_L}] (\theta_P') * (\theta_P') = \frac{1}{3} (T_M) * \theta_p'$$

(Notice how the θ_P'/ω values cancel out to get a familiar equation of motion.)

REFERENCES

- [1] Dynamics in Engineering Practice, 11th Ed (only), D.W. Childs & Ap. Conkey, CRC Pubs
<https://www.crcpress.com/Dynamics-in-Engineering-Practice-Eleventh-Edition/Childs-Conkey/9781482250251>
- [2] Anderson Process. 2022. "It's in the Mix: Industrial Mixers Defined, Types and Applications." Anderson Process. December 15.
[https://www.andersonprocess.com/its-in-the-mix-industrial-mixers-defined-types-and-applications/.](https://www.andersonprocess.com/its-in-the-mix-industrial-mixers-defined-types-and-applications/)
- [3] Liu, Y., and Zhang, X. 2024. "Design and Analysis of a Novel Hybrid Energy Harvester for Smart Wearable Devices." Advances in Mechanical Engineering. <https://doi.org/10.1177/16878132241269238>.

3. Numerical Methods

MEEN 357 - 501

Authors: Jacob Hargreaves, David Guess, Ian Wilhite

6.1 Coding

Question 1: We had you define the acceleration due to gravity as a field in a structure that you had to pass as an input argument to several functions. Instead, we could have had you type the value for the constant, 3.72 m/s², directly in those functions. Do you believe there is an advantage to how we had you do it? Explain. Would you have done it differently? Explain why or why not.

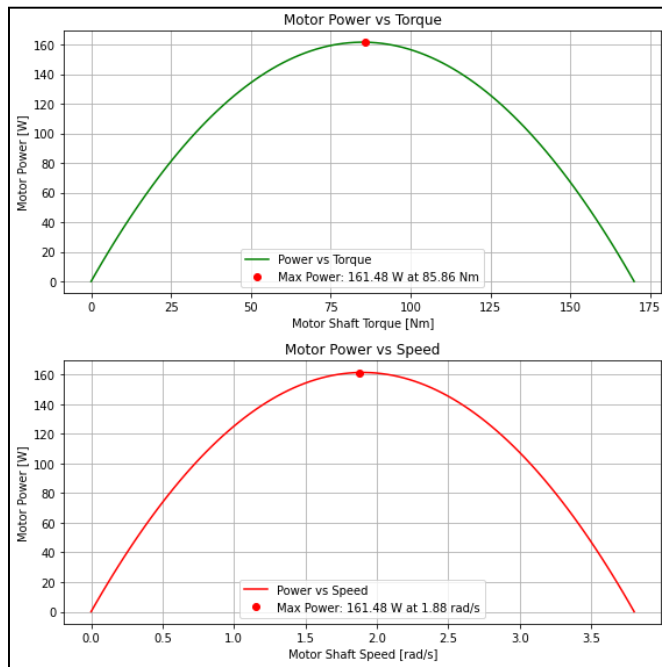
We believe that there are advantages to the way we define acceleration in this project. Because we did not code the gravity constant to simply be the value on Mars, we can update the gravity constant easily if we want to analyze the rover on other planets or moons. If we wanted to change the gravity constant, we could simply alter its structure in one place rather than having to change its value in every single function. It is for these reasons that we would not have done anything differently regarding the acceleration due to gravity.

Question 2: What happens if you try to call F_gravity using a terrain slope of 110 degrees? Is this desirable behavior? Explain why you think this.

When we try to call F_gravity using a terrain slope above 90 degrees, such as a slope of 110 degrees, F_gravity returns a force greater than the force of gravity in free fall. This is because the equation used in this function is $F_{gravity} = -m_{rover} * g * \sin(\alpha)$ and when α (the angle of inclination) is above 90 degrees, the $\sin()$ value is greater than 1. This is not desirable behavior because the rover would never feel a force of gravity greater than the free fall force.

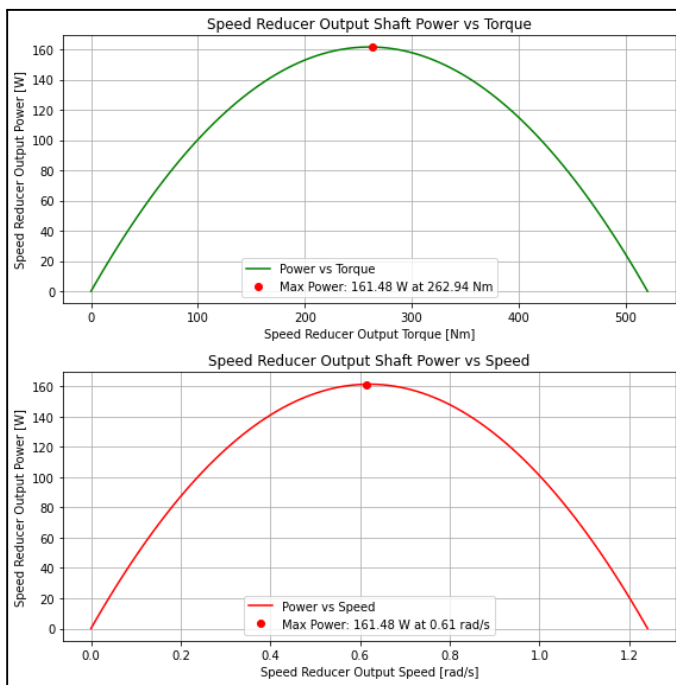
6.2 Motor and Speed Reducer Behavior

Question 3: What is the maximum power output by a single rover motor? At what motor shaft speed does this occur? Provide graphs or other data to support your answer.



As shown in the graph above, the maximum power output by a single rover motor is about 161.48 Watts and occurs at a motor shaft speed of 1.88 rad/s.

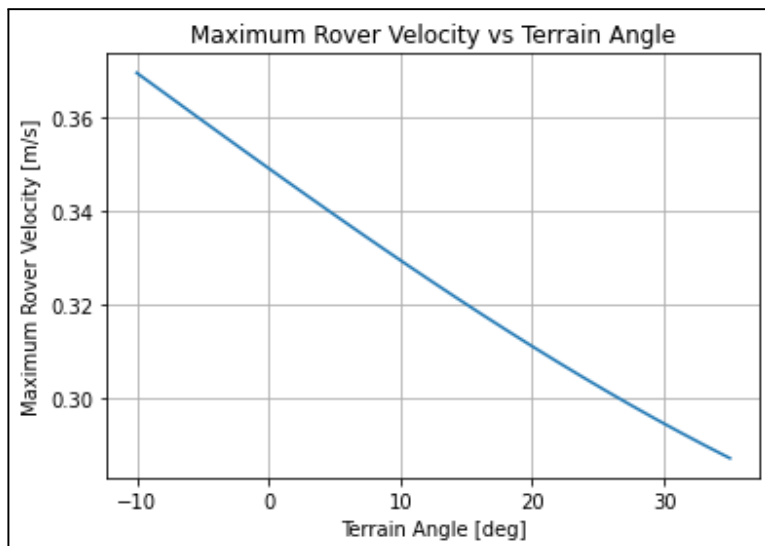
Question 4: What impact does the speed reducer have on the power output of the drive system? Again, provide any graphs or supporting data.



The speed reducer causes the maximum power output of the drive system to occur at a much lower motor shaft speed of 0.61 rad/s, as seen above. The speed reducer does this in order to help the rover overcome resistance such as rough terrain. The rover can better overcome this resistance as it has more torque at a lower speed. The speed reducer allows for more torque overall as compared to the figures in question #3.

6.3 Rover Behavior

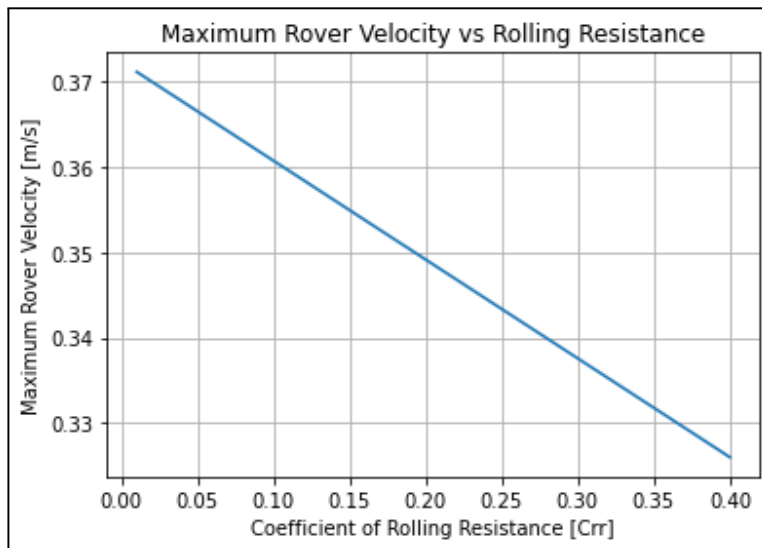
Question 5: Examine the graph you generated using analysis_terrain_slope.py. (Provide the graph in your response for reference.) Explain the trend you observe. Does it make sense physically? Why or why not? Please be precise. For example, if the graph appears linear or non-linear, can you explain why it should be the way you observed? Refer back to the rover model and how slope impacts rover behavior.



This trend from the graph above makes perfect sense. On downhill motion (Negative Terrain Angle) the rover experiences additional acceleration from gravity. Therefore, a higher maximum velocity is obtained. On flat and uphill motion (Positive Terrain Angle), the maximum velocity of the rover steadily decreases. This is because the rover has to overcome both gravity and rolling resistance pulling it backward.

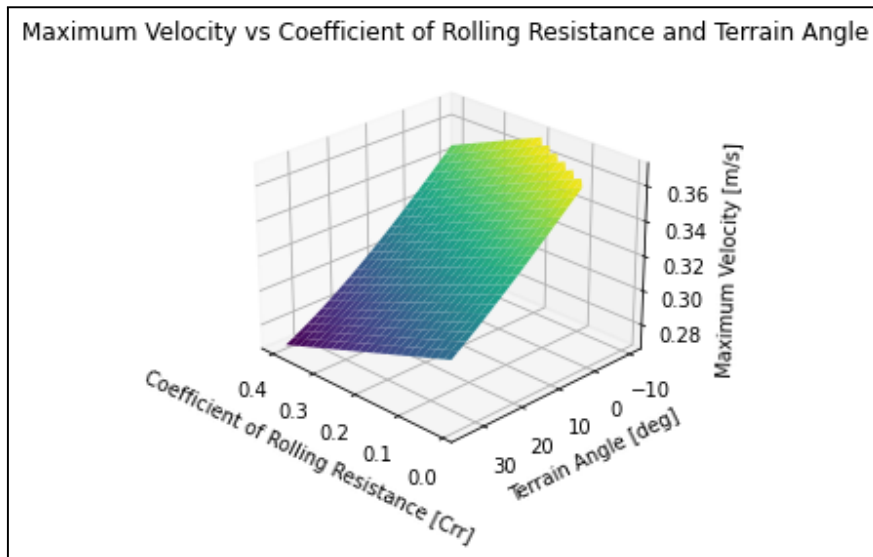
Additionally, the graph appears approximately linear, which suggests that the impact of slope on the rover's speed is proportional, which aligns with the rover model where gravitational forces and resistive forces change linearly with increasing slope.

Question 6: Examine the graph you generated using analysis_rolling_resistance.py. (Provide the graph in your response for reference.) Explain the trend you observe. Does it make sense physically? Why or why not? Please be precise. For example, if the graph appears linear or non-linear, can you explain why it should be the way you observed? Refer back to the rover model and how the coefficient of rolling resistance impacts rover behavior.

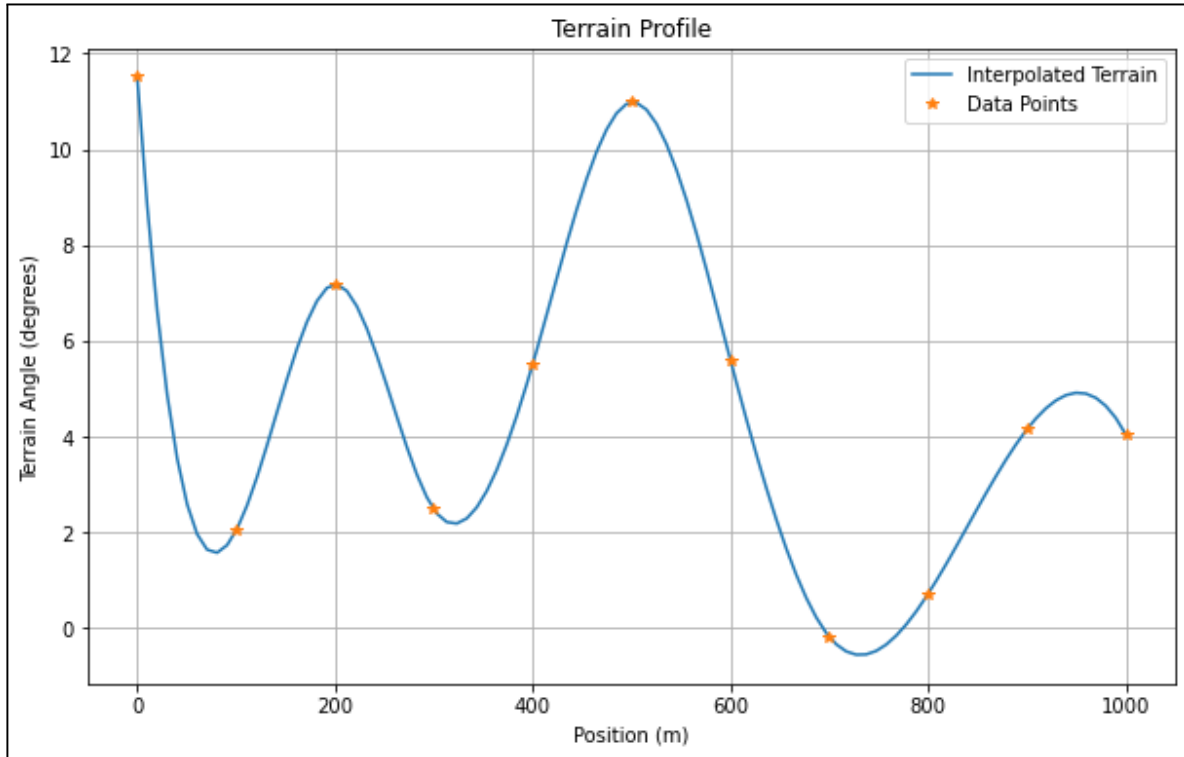


This graph shows a linear decrease in maximum rover velocity as the coefficient of rolling resistance (Crr) increases. This makes sense because rolling resistance is a force that opposes the rover's motion. As Crr increases, the motor has to exert more energy to overcome this resistance. Since the rolling resistance is directly proportional to Crr, the decrease in velocity follows a linear trend. This means that as Crr rises, the rover's maximum achievable speed steadily decreases. This is also consistent with the energy required to counteract the increasing resistance.

Question 7: Examine the surface plot you generated using `analysis_combined_terrain.py`. (Provide the graph in your response for reference.) What does this graph tell you about the physical conditions under which it is appropriate to operate the rover? Based on what you observe, which factor, terrain slope or coefficient of rolling resistance, is the dominant consideration in how fast the rover can travel? Please explain your reasoning.

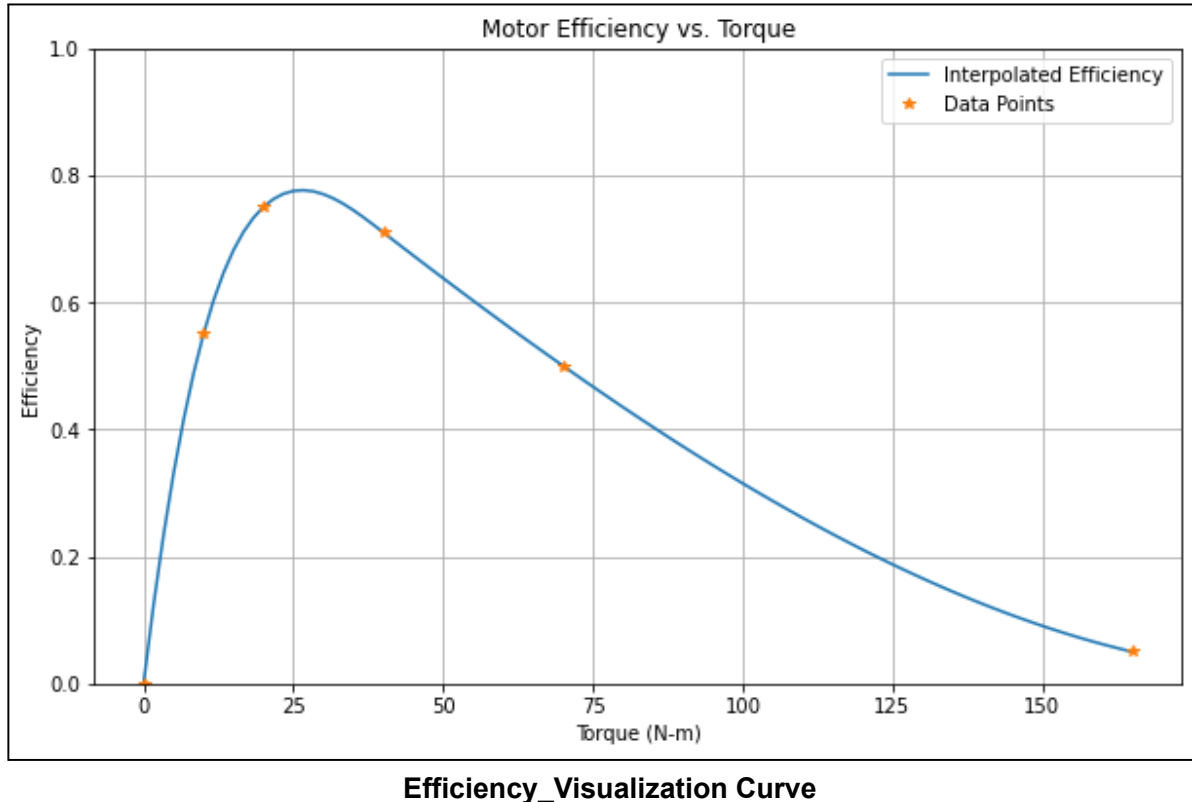


The 3D-surface plot shows that both the terrain slope and the coefficient of rolling resistance (Crr) have a significant impact on the maximum velocity of the rover. As the terrain slope increases, the rover's maximum velocity decreases, and as the Crr increases, the velocity also decreases. However, the graph shows that terrain slope has a more noticeable effect on the rover's speed compared to the rolling resistance. This is evident from the steep gradient along the terrain angle axis, meaning that changes in slope result in larger variations in speed. Therefore, terrain angle is the dominant factor. This is because steeper angles significantly reduce the rover's maximum velocity while rolling resistance primarily adds resistance.

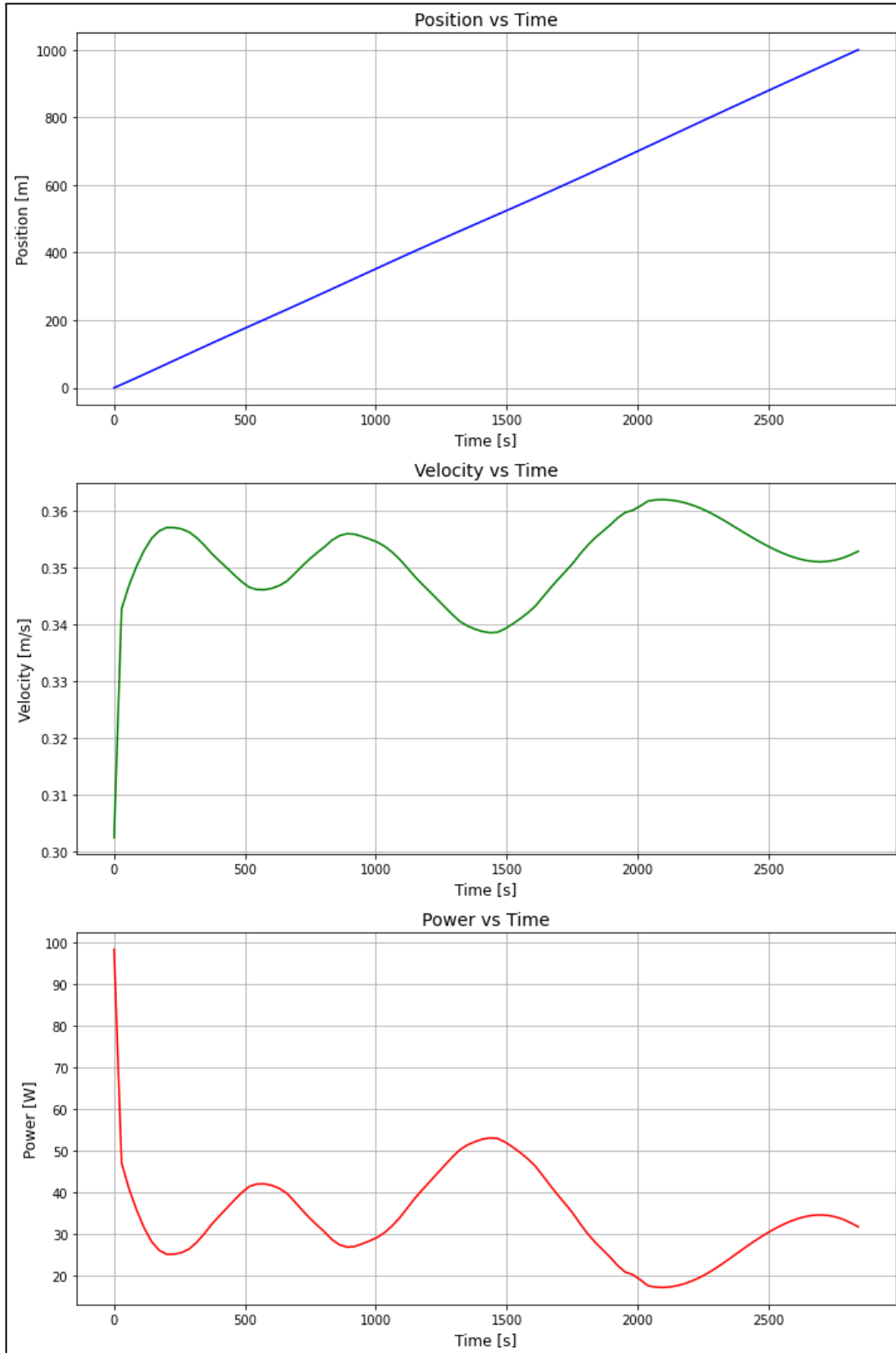
Task 2:

Experiment_Visualization Curve

The terrain profile generated through cubic spline interpolation exhibits smooth characteristics throughout the entire path. The graph shows that the blue interpolated line transitions naturally between the data points (marked by orange stars) without any jarring changes or breaks. This smoothness is from using cubic polynomials between points, which ensures continuous slopes and curvatures at the transitions. Additionally, the curve maintains accuracy to our input data, as evidenced by the interpolated line passing exactly through each orange star marker. This smooth behavior makes sense for modeling real-world terrain since actual landscapes typically don't have abrupt elevation changes.

Task 5:

This motor efficiency curve shares a similar overall shape with Figure 2 from the handout - starting at zero, rising to a peak, then declining - though it operates at a much higher torque range. The curve is smooth throughout due to the cubic spline interpolation used to connect the data points. The interpolated line passes exactly through all six data points (marked with stars), which is a key property of cubic spline interpolation.

Task 8:

(a) Position vs Time: The position-time graph shows a slightly non-linear relationship. While there is an overall upward trend, the slope (which represents velocity) varies over time rather than being constant. This nonlinearity occurs because the rover's velocity changes as it encounters different terrain angles, requiring different amounts of power and resulting in varying speeds across the trajectory.

(b) Velocity-Power Relationship: Looking at the velocity and power plots, there's a clear correlation - when the rover requires more power (shown by spikes in the power graph), there are corresponding changes in velocity. The relationship appears inverse in many cases - when the rover encounters situations requiring more power (likely uphill sections), the velocity tends to decrease slightly. This makes physical sense as the rover needs to expend more energy to maintain motion against gravity on inclines, resulting in slightly reduced velocity.

(c) Velocity Profile and Terrain: The velocity shows periodic variations between approximately 0.34-0.36 m/s, which likely corresponds to changes in terrain elevation. The dips in velocity (around t=1500s) suggest encounters with uphill sections where the rover must work harder against gravity, while slight increases in velocity may correspond to downhill or level sections where less power is required to maintain motion.

(d) Velocity Smoothness: The velocity graph shows smooth transitions rather than abrupt changes. This smoothness is due to two factors:

1. The terrain profile was interpolated using cubic splines, creating smooth transitions between terrain points
2. The rover's inertia and motor characteristics prevent instantaneous velocity changes, leading to gradual transitions as terrain conditions change

Rover Telemetry Data

Variable	Value
completion_time	2842.92 s
distance_traveled	1000 m
max_velocity	0.36 m/s
average_velocity	0.35 m/s
battery_energy	1094725.05 J
batt_energy_per_distance	1094.725 J/m

Task 9:

During Experiment 1, the battery energy used is 1,094.725 kJ. This is greater than the energy provided by the Lithium Iron Phosphate battery pack, as this batter only provides 907.2 kJ. Therefore, no, the rover can not complete the case defined by Experiment 1 with the 0.9072e6 J Lithium Iron Phosphate battery pack. There is not sufficient energy capacity to handle the demands shown in the simulation. We arrived at this conclusion by analyzing the output of Experiment 1.

Phase 3 Report

Jacob Hargreaves
David Guess
Ian Wilhite

Task 1:

define_mission_events.py

mission_events			
<i>Field Name</i>	<i>Value</i>	<i>Units</i>	<i>Description</i>
alt_heatshield_eject	8000	Meters	The altitude where the heat shield ejects
alt_parachute_eject	900	Meters	The altitude where the parachute ejects
alt_rockets_on	1800	Meters	The altitude where the rockets turn on
alt_skycrane_on	7.6	Meters	The altitude where the sky crane turns on

define_planet.py

high_altitude			
<i>Field Name</i>	<i>Value</i>	<i>Units</i>	<i>Description</i>
temperature	-38.94 @ 7000 m	Celsius	The temperature based on altitude above 7000 meters
pressure	0.000646 @ 7000 m	KPa	The pressure based on altitude above 7000 meters

low_altitude			
<i>Field Name</i>	<i>Value</i>	<i>Units</i>	<i>Description</i>
temperature	-31 @ 0 m	Celsius	The temperature based on altitude below 7000 meters

pressure	0.669 @ 0 m	KPa	The temperature based on altitude below 7000 meters
----------	-------------	-----	---

mars			
<i>Field Name</i>	<i>Value</i>	<i>Units</i>	<i>Description</i>
g	-3.72	m/s ²	The value of gravity on Mars
altitude_threshold	7000	KPa	The temperature based on altitude below 7000 meters
low_altitude	-	-	The dictionary low_altitude
high_altitude	-	-	The dictionary high_altitude
density	-	-	The dictionary density

define_rovers.py

wheel, rover 1			
<i>Field Name</i>	<i>Default Value</i>	<i>Units</i>	<i>Description</i>
radius	0.30	Meters	Radius of the wheel
mass	1	kilograms	Mass of wheel

wheel, rover 2			
<i>Field Name</i>	<i>Default Value</i>	<i>Units</i>	<i>Description</i>
radius	0.30	Meters	Radius of the wheel
mass	2	kilograms	Mass of wheel

wheel, rover 3			
<i>Field Name</i>	<i>Default Value</i>	<i>Units</i>	<i>Description</i>
radius	0.30	Meters	Radius of the wheel
mass	2	kilograms	Mass of wheel

wheel, rover 4			
<i>Field Name</i>	<i>Default Value</i>	<i>Units</i>	<i>Description</i>
radius	0.20	Meters	Radius of the wheel
mass	2	kilograms	Mass of wheel

speed_reducer, rover 1			
<i>Field Name</i>	<i>Default Value</i>	<i>Units</i>	<i>Description</i>
type	reverted	-	Radius of the wheel
diam_pinion	.04	Meters	Diameter of the pinion
diam_gear	.07	Meters	Diameter of the gear
mass	1.5	kilograms	Mass of speed reducer

speed_reducer, rover 2, 3, & 4			
<i>Field Name</i>	<i>Default Value</i>	<i>Units</i>	<i>Description</i>
type	reverted	-	Radius of the wheel
diam_pinion	.04	Meters	Diameter of the pinion
diam_gear	.06	Meters	Diameter of the gear
mass	1.5	kilograms	Mass of speed reducer

motor, rover 1			
<i>Field Name</i>	<i>Default Value</i>	<i>Units</i>	<i>Description</i>
torque_stall	170	-	Torque of the motor while stalling
torque_noload	0	N*m	Torque of the motor with no load
speed_noload	3.80	Rad/s	Angular speed of the motor with no load
mass	5.0	kilograms	Mass of the motor

motor, rover 2 & 3			
<i>Field Name</i>	<i>Default Value</i>	<i>Units</i>	<i>Description</i>
torque_stall	180	-	Torque of the motor while stalling
torque_noload	0	N*m	Torque of the motor with no load

speed_noload	3.70	Rad/s	Angular speed of the motor with no load
mass	5.0	kilograms	Mass of the motor

motor, rover 4

Field Name	Default Value	Units	Description
torque_stall	165	-	Torque of the motor while stalling
torque_noload	0	N*m	Torque of the motor with no load
speed_noload	3.85	Rad/s	Angular speed of the motor with no load
mass	5.0	kilograms	Mass of the motor

chassis, rover 1, 2, & 3

Field Name	Default Value	Units	Description
mass	659	kilograms	Mass of chassis

chassis, rover 4

Field Name	Default Value	Units	Description
mass	674	kilograms	Mass of chassis

science_payload, rover 1, 2, & 3

Field Name	Default Value	Units	Description
mass	75	kilograms	Mass of science payload

science_payload, rover 4

Field Name	Default Value	Units	Description
mass	80	kilograms	Mass of science payload

power_subsys, rover 1, 2, & 3			
<i>Field Name</i>	<i>Default Value</i>	<i>Units</i>	<i>Description</i>
mass	90	kilograms	Mass of power subsystem

power_subsys, rover 4			
<i>Field Name</i>	<i>Default Value</i>	<i>Units</i>	<i>Description</i>
mass	100	kilograms	Mass of power subsystem

rover			
<i>Field Name</i>	<i>Default Value</i>	<i>Units</i>	<i>Description</i>
wheel	wheel	-	Dictionary of the wheel
speed_reducer	speed_reducer	-	Dictionary of the speed_reducer
motor	motor	-	Dictionary of the motor

planet			
<i>Field Name</i>	<i>Default Value</i>	<i>Units</i>	<i>Description</i>
g	3.72	m/s^2	Gravity value on the planet (Mars)

define_edl_system.py

parachute			
<i>Field Name</i>	<i>Value</i>	<i>Units</i>	<i>Description</i>
deployed	True	-	True means it has been deployed but not ejected
ejected	False	-	True means the parachute is no longer attached to the system

diameter	16.25	m	Diameter of the parachute
Cd	0.615	-	Coefficient of drag on the parachute
mass	185.0	kg	Mass of the parachute

rocket			
<i>Field Name</i>	<i>Value</i>	<i>Units</i>	<i>Description</i>
on	False	-	Indicates if the rocket is currently on.
structure_mass	8.0	kg	Mass of the rocket structure excluding fuel.
initial_fuel_mass	230.0	kg	Initial mass of fuel.
fuel_mass	230.0	kg	Current fuel mass (less than or equal to initial_fuel_mass).
effective_exhaust_velocity	4500.0	m/s	Effective exhaust velocity of the rocket.
max_thrust	3100.0	N	Maximum thrust generated by the rocket.
min_thrust	40.0	N	Minimum thrust generated by the rocket.

speed_control			
<i>Field Name</i>	<i>Value</i>	<i>Units</i>	<i>Description</i>
on	False	-	Indicates if the speed control mode is activated.
Kp	2000	-	Proportional gain term for speed control.
Kd	20	-	Derivative gain term for speed control.
Ki	50	-	Integral gain term for speed control.
target_velocity	-3.0	m/s	Desired descent speed.

position_control			
<i>Field Name</i>	<i>Value</i>	<i>Units</i>	<i>Description</i>
on	False	-	Indicates if the position control mode is activated.
Kp	2000	-	Proportional gain term for position control.
Kd	1000	-	Derivative gain term for position control.
Ki	50	-	Integral gain term for position control.
target_altitude	7.6	m	Target altitude, reflecting the sky crane cable length.

sky_crane			
Field Name	Value	Units	Description
on	False	-	Indicates if the sky crane is lowering the rover.
danger_altitude	4.5	m	Altitude considered too low for safe rover touchdown.
danger_speed	-1.0	m/s	Speed below which the rover would impact too hard on the surface.
mass	35.0	kg	Mass of the sky crane.
area	16.0	m ²	Frontal area used for drag calculations.
Cd	0.9	-	Coefficient of drag for the sky crane.
max_cable	7.6	m	Maximum length of cable for lowering the rover.
velocity	-0.1	m/s	Speed at which the sky crane lowers the rover.

heat_shield			
Field Name	Value	Units	Description
ejected	False	-	True if the heat shield has been ejected from the system.
mass	225.0	kg	Mass of the heat shield.

diameter	4.5	m	Diameter of the heat shield.
Cd	0.35	-	Drag coefficient of the heat shield.

edl_system			
<i>Field Name</i>	<i>Value</i>	<i>Units</i>	<i>Description</i>
altitude	NaN	m	Current altitude of the system, updated throughout the simulation.
velocity	NaN	m/s	Current velocity of the system, updated throughout the simulation.
num_rockets	8	-	Total number of rockets in the system.
volume	150	m ³	Volume of the system.
parachute	parachute	-	Parachute dictionary with deployment and drag properties.
heat_shield	heat_shield	-	Heat shield dictionary with mass and drag properties.
rocket	rocket	-	Rocket dictionary with thrust and fuel properties.
speed_control	speed_control	-	Speed control dictionary for descent speed management.
position_control	position_control	-	Position control dictionary for altitude management.

sky_crane	sky_crane	-	Sky crane dictionary for rover lowering.
rover	rover	-	Rover dictionary (defined in another file).

Task 2:

get_mass_rover			
<i>Calling Syntax</i>	<i>Description</i>	<i>Input Arguments</i>	<i>Output Arguments</i>
get_mass_rover(edl_system)	Computes the total mass of the rover based on the specifications in the edl_system dictionary, as per Phase 1 requirements.	edl_system: dictionary containing rover components and their respective masses	m: total mass of the rover (float)

get_mass_rockets			
<i>Calling Syntax</i>	<i>Description</i>	<i>Input Arguments</i>	<i>Output Arguments</i>
get_mass_rockets(edl_system)	Returns the current total mass of all rockets on the EDL system.	edl_system: dictionary containing the number of rockets and the masses of the rocket components	m: total mass of all rockets (float)

get_mass_edl			
<i>Calling Syntax</i>	<i>Description</i>	<i>Input Arguments</i>	<i>Output Arguments</i>

get_mass_edl(edl_system)	Returns the total current mass of the entire EDL system, accounting for any ejected components.	edl_system: dictionary containing the masses of the EDL system's components, including parachute, heat shield, rockets, sky crane, and rover	m: total current mass of the EDL system (float)
--------------------------	---	--	---

get_local_atm_properties			
<i>Calling Syntax</i>	<i>Description</i>	<i>Input Arguments</i>	<i>Output Arguments</i>
get_local_atm_properties(planet, altitude)	Returns local atmospheric properties—density, temperature, and pressure—at a given altitude.	planet: dictionary with atmospheric properties and calculation functions for density, temperature, and pressure based on altitude; altitude: altitude above the planet's surface (meters)	density: atmospheric density (kg/m ³); temperature: local temperature (°C); pressure: local pressure (kPa)

F_buoyancy_descent			
<i>Calling Syntax</i>	<i>Description</i>	<i>Input Arguments</i>	<i>Output Arguments</i>
F_buoyancy_descent(edl_system, planet, altitude)	Computes the net buoyancy force acting on the EDL system during descent.	edl_system: dictionary containing volume of the EDL system; planet: dictionary with gravity and atmospheric functions; altitude: altitude above the planet's surface (meters)	F: net buoyancy force (float)

F_drag_descent			
<i>Calling Syntax</i>	<i>Description</i>	<i>Input Arguments</i>	<i>Output Arguments</i>

F_drag_descent(edl_system, planet, altitude, velocity)	Computes the net drag force acting on the EDL system during descent.	edl_system: dictionary containing the components of the EDL system; planet: dictionary with atmospheric properties; altitude: altitude above the planet's surface (meters); velocity: current descent velocity (m/s)	F: net drag force (float)
--	--	--	---------------------------

F_gravity_descent			
Calling Syntax	Description	Input Arguments	Output Arguments
F_gravity_descent(edl_system, planet)	Computes the gravitational force acting on the EDL system.	edl_system: dictionary with the mass of the EDL system; planet: dictionary with gravity parameter	F: gravitational force (float)

v2M_Mars			
Calling Syntax	Description	Input Arguments	Output Arguments
v2M_Mars(v, a)	Converts descent speed to Mach number on Mars as a function of altitude.	v: descent speed (m/s); a: altitude (m)	M: Mach number (float)

thrust_controller			
Calling Syntax	Description	Input Arguments	Output Arguments
thrust_controller(edl_system, planet)	Implements a PID Controller for the EDL system to adjust thrust based on errors in velocity control.	edl_system: dictionary containing the control parameters, telemetry, and rocket specifications; planet: dictionary with gravity information	edl_system: modified dictionary with updated thrust and telemetry data

edl_events			
<i>Calling Syntax</i>	<i>Description</i>	<i>Input Arguments</i>	<i>Output Arguments</i>
edl_events(edl_system, mission_events)	Defines events occurring in EDL System simulation	edl_system: EDL system state, mission_events: mission-specific event altitude/speed values	events: List of event functions for EDL conditions

edl_dynamics			
<i>Calling Syntax</i>	<i>Description</i>	<i>Input Arguments</i>	<i>Output Arguments</i>
edl_dynamics(t, y, edl_system, planet)	Calculates EDL dynamics as it descends to the Mars surface	t: Time, y: State vector, edl_system: EDL system details, planet: Planet details affecting EDL	dydt: Array of rates of change in state vector variables

update_edl_state			
<i>Calling Syntax</i>	<i>Description</i>	<i>Input Arguments</i>	<i>Output Arguments</i>
update_edl_state(edl_system, TE, YE, Y, ITER_INFO)	Updates the status of the EDL system based on simulation events, like ejection, activation, and landing conditions.	edl_system (dict): EDL system state, TE (list): Event times, YE (list): State at event times, Y (array): States, ITER_INFO (bool): Logging flag	edl_system (dict): Updated system, y0 (array): New initial conditions, TERMINATE_SIM (bool): Simulation termination flag

simulate_edl			
<i>Calling Syntax</i>	<i>Description</i>	<i>Input Arguments</i>	<i>Output Arguments</i>

simulate_edl(edl_system, planet, mission_events, tmax, ITER_INFO)	Runs the simulation of the EDL system through iterative time steps until termination based on events or time limit	edl_system (dict): System parameters, planet (dict): Planetary constants, mission_events (dict): Event conditions, tmax (float): Max time, ITER_INFO (bool): Logging flag	T (array): Simulation time steps, Y (array): State vectors, edl_system (dict): Final system state
---	--	---	---

Task 3:

IVP Solver

The while loop in simulate_edl uses solve_ivp with the DOP853 method, an 8th-order Runge-Kutta method that provides higher accuracy compared to other methods like RK45. This higher precision is essential due to the specific event criteria we are monitoring, requiring close alignment with actual values to correctly detect each event.

solve_ivp is called with the following parameters:

- fun: A lambda function representing the system's dynamics, edl_dynamics(t, y, edl_system, planet).
- tspan: A tuple defining the simulation time span, (0, tmax).
- y0: An array of initial state variables, including initial velocity, altitude, fuel mass, and other state indicators.
- method: Set to "DOP853" to ensure high accuracy for Martian descent simulation.
- events: A set of conditions to trigger specific events, as defined by edl_events(edl_system, mission_events).
- max_step: The maximum step size for the solver, set to 0.1 for finer granularity.

Each iteration of solve_ivp simulates until one of the defined events occurs. When an event triggers, the solver captures t (time) and y (state variables like altitude, fuel, etc.), which are then updated within the update_edl_state function.

Updating the EDL System

The update_edl_state function is crucial for this loop, as it processes the event results from solve_ivp and updates edl_system accordingly. This function also sets up the initial conditions y0 for the next loop iteration and checks if the simulation should terminate by updating the TERMINATE_SIM flag.

Key events handled by update_edl_state include:

1. Heat Shield Ejection: Heat shield is detached when a certain altitude is reached.
2. Parachute Ejection: Parachute is released based on altitude criteria.
3. Rockets Activation: Rockets are ignited for descent control at specific altitude.
4. Sky Crane Activation: Sky crane system is engaged to lower the rover.
5. Out of Rocket Fuel: Fuel depletion triggers a termination condition if descent is not complete.
6. Sky Crane Safety Failure: The rover crashes if descent control or sky crane fails.
7. Speed Controller Activation: Engages to maintain a target descent speed.
8. Altitude Controller Activation: Altitude controller engages as the sky crane takes over, disabling speed control.
9. Rover Grounded: Reaches the surface (altitude of zero), ending the simulation.

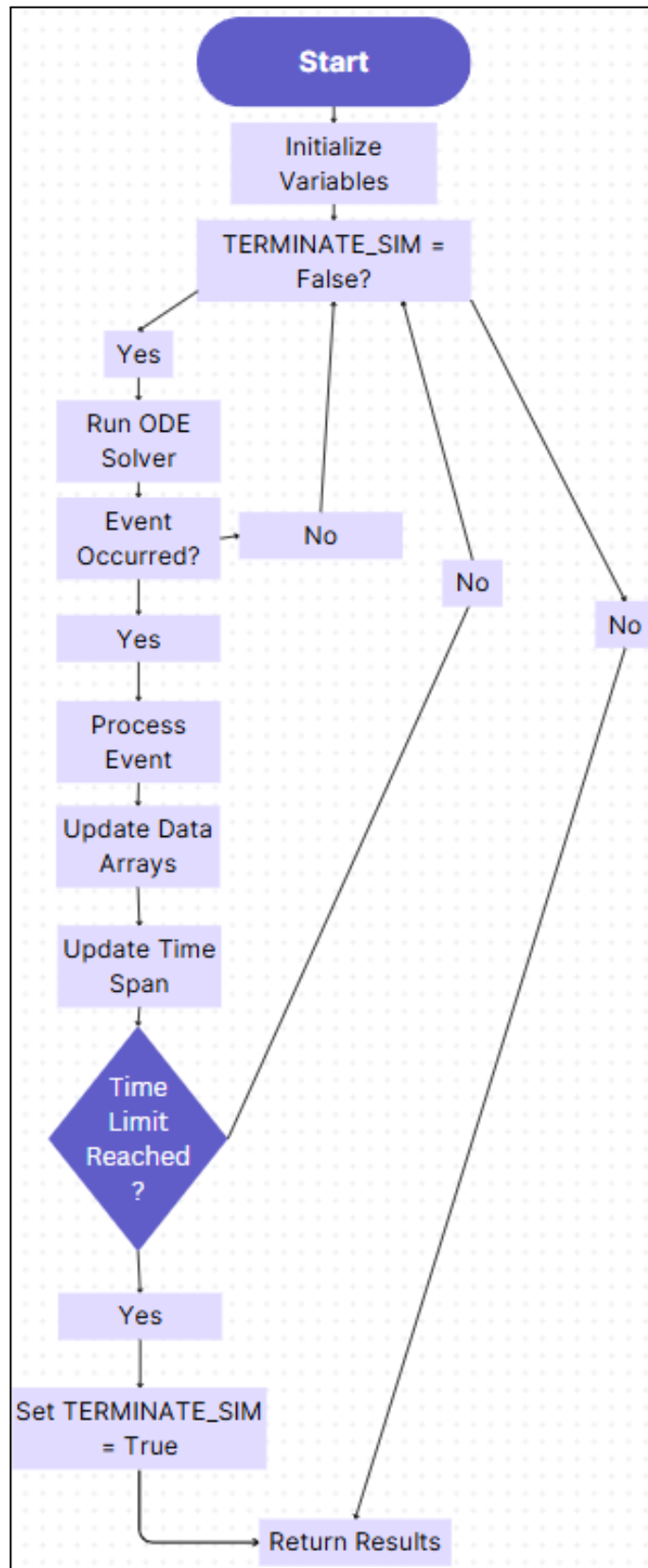
Explanation of the Loop

The while loop in simulate_edl repeats until TERMINATE_SIM is set to True. Termination occurs when time runs out, the rover safely lands, fuel depletes, or a crash is detected.

The process within each loop iteration is as follows:

1. A lambda function for the system dynamics (fun) is passed to solve_ivp.
2. solve_ivp runs the simulation until one of the specified events occurs, producing arrays of t (time) and y (state variables) for the event.
3. update_edl_state then adjusts edl_system, sets y0 for the next pass, and updates TERMINATE_SIM if an exit condition is reached.
4. The loop appends time (T) and state variables (Y) for further analysis, updating tspan with new bounds for the next simulation pass.

This iterative simulation loop accurately models different operational phases of the EDL sequence: parachute deployment, rocket firing, sky crane descent, and finally, rover touchdown.

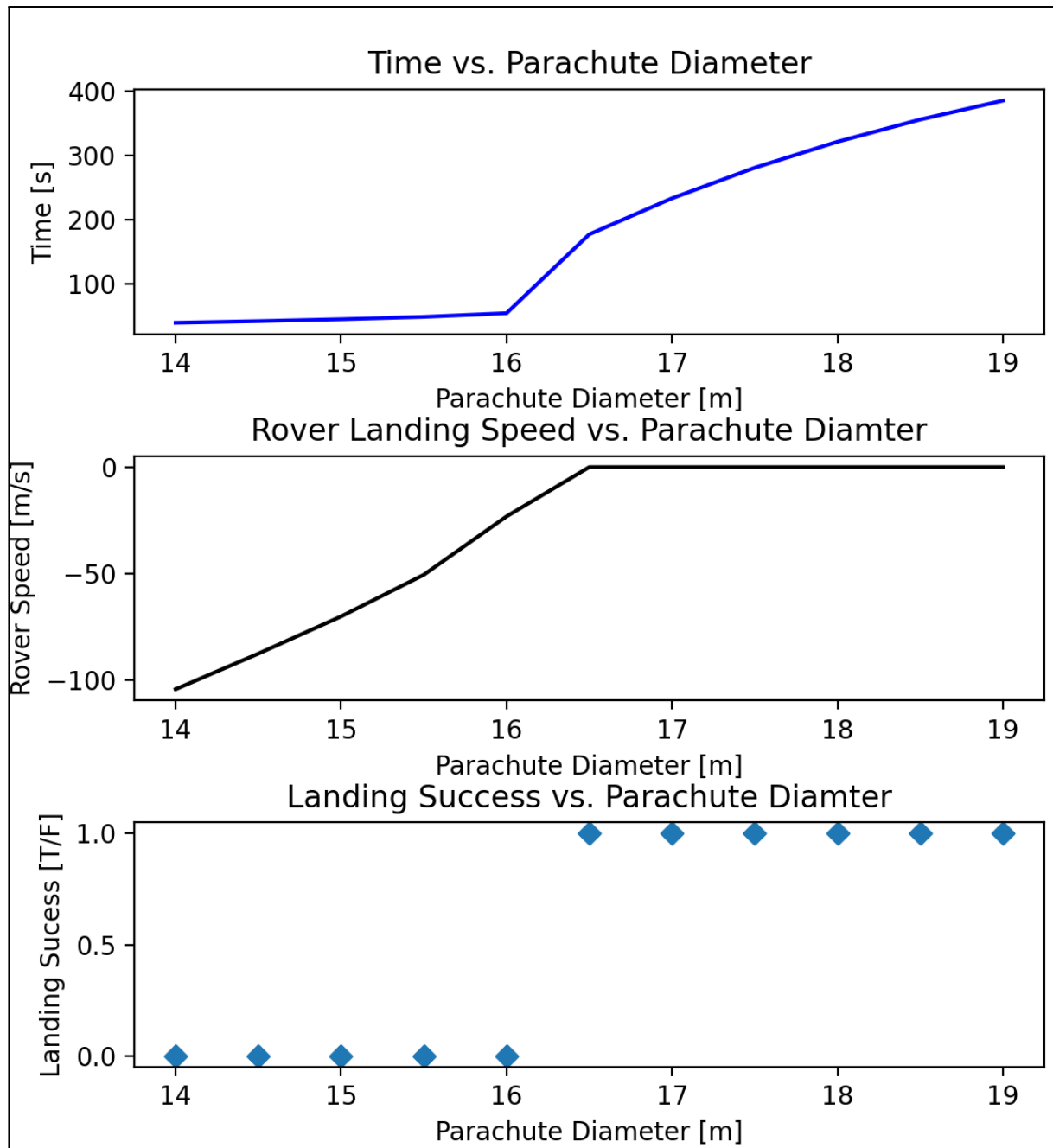


Task 4:



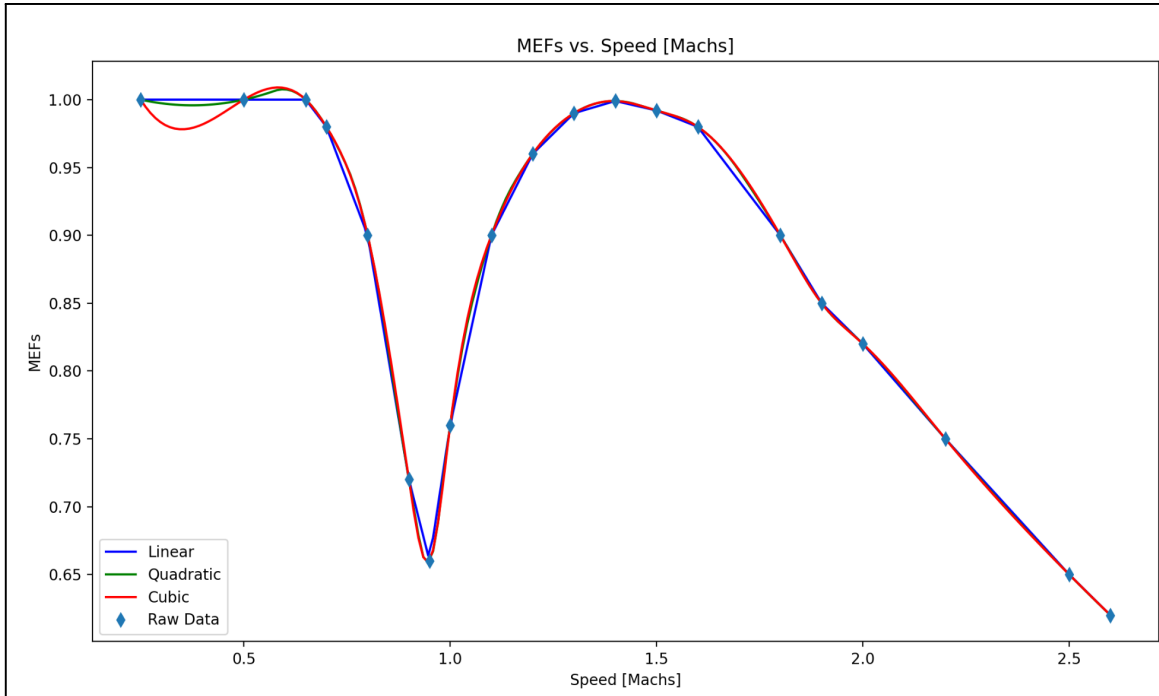
This flowchart begins with the imported files, followed by the loading of key dictionaries. These dictionaries help establish variables that are then passed into `simulate_edl`. Inside `simulate_edl`, we track each function call: the flow splits to cover `edl_events`, `update_edl_state`, and the `solve_ivp` function. From `solve_ivp`, we see the call to `edl_dynamics`, which itself branches out to `get_mass_edl`, `F_gravity_descent`, `F_buoyancy_descent`, and `F_drag_descent`. In turn, `F_gravity_descent` calls `get_mass_edl` again, which then leads to two final functions, concluding this branch. Meanwhile, both `F_buoyancy_descent` and `F_drag_descent` further call `get_local_atm_properties`, completing the flow.

Task 5:



The results in Figure 1 show the effects of parachute diameter on simulation time, rover landing speed, and landing success. To ensure a successful landing, only parachutes with diameters between 16.5 and 19 m are viable, as smaller sizes led to failed landings. Among these, minimizing landing time is preferred, and the first graph confirms that larger diameters increase descent time. Therefore, we recommend a 16.5 m parachute, which provides a safe landing in the shortest time.

Task 6:



6.1)

The continuous model was created by interpolating the data provided. This data came from simulation, meaning that the error is negligible and there is no need for a regression. We chose to use the quadratic interpolation as a representation of the data provided, because it would best extrapolate the data to the range outside the data provided. To generate this plot, we

6.2)

After incorporating the function into the parachute drag model, we re-evaluated our parachute diameter recommendations. By updating the drag coefficient and re-running our analysis, we observed a shift in the recommended parachute diameter range. Our previous recommendation of 16.5 m no longer guaranteed a successful landing, as the range shifted to [17, 19] m. Consequently, we now recommend a 17 m parachute diameter for optimal landing performance within the updated model.

PROJECT PHASE 4:
Optimization Challenge Report

Prepared for

MEEN 357 - Section 501

Team #10

By

Jacob Hargreaves

Ian Wilhite

David Guess

November 29, 2024

Aggie Honor Code: "*On my honor, as an Aggie, I have neither given nor received unauthorized aid on this academic work.*"

"None of the members of the team communicated in any way with other teams with regards to specific coding issues with this project."

Signature: *Jacob Hargreaves* Date: *11/29/2024*

David Guess Date: *11/29/2024*

Ian Wilhite Date: *11/29/2024*

Table of Contents

Table of Contents.....	2
Introduction.....	3
Formulation of the Design Problem.....	3
Considered Design Solutions.....	3
Final Design Selection.....	4
Numerical Methods Used.....	4
Description of Final Design.....	5
Performance Data.....	6

Introduction

The design of an Entry, Descent, and Landing (EDL) system and a rover for a Martian mission is a challenging problem that requires careful consideration of multiple factors.

The goal is to create a system that can safely land on Mars and allow the rover to travel at least 1 kilometer on a single battery charge. This involves optimizing key parameters like landing velocity, rover speed, and energy usage while staying under the \$7.2 million budget. To meet these requirements, we had to choose the best combination of components, such as parachutes, motors, batteries, and chassis materials, while making trade-offs between cost, performance, and weight. This project highlights the complexity of designing systems for real-world space exploration missions.

Formulation of the Design Problem

We aim to design an Entry, Descent, and Landing (EDL) system coupled with a rover capable of traversing at least 1 km on a single battery charge over a predefined Martian terrain. The design must balance key performance metrics: speed, cost, and battery efficiency, while adhering to specific constraints. Among these, speed is prioritized, followed by cost considerations. The design solution should:

- **Maximize rover speed** to reduce the total mission duration.
- **Minimize total cost**, ensuring it stays within the \$7.2 million budget.
- Optimize battery capacity to achieve sufficient energy per meter (J/m) without excessive weight or cost.

Ensure the system satisfies constraints such as:

- Landing velocity below 1 m/s.
- Rover chassis strength exceeding 40,000 units.
- Mass and geometry limits for all components.

Key decision variables include:

- Parachute diameter, fuel mass, wheel radius, and gear diameter (continuous variables).
- Motor type, battery type, number of modules, and chassis material (discrete variables).

Considered Design Solutions

To address the rover's design requirements, we examined multiple options for key components and materials, considering performance and cost.

- 1) **Motor Selection:** The six available motor types were evaluated, focusing on their efficiency, torque, and speed capabilities. High-efficiency motors offered a balance of performance and reasonable cost increases. Both torque_he and speed_he motors stood

out as superior options, with the speed_he motor chosen for its ability to maximize rover speed, a primary objective.

- 2) **Chassis Material:** The three chassis material options—steel, magnesium, and carbon fiber—were compared for cost, strength, and weight. While carbon fiber exceeded budget constraints due to its high cost, magnesium emerged as the optimal choice. Its high specific strength allowed for a lighter chassis, aligning with the weight limits, while maintaining structural integrity and meeting strength requirements.
- 3) **Battery Configuration:** Various battery types and configurations were analyzed for energy efficiency and cost. PbAcid-1 batteries provided a good energy-to-cost ratio, making them a favorable option. Initial testing started with 10 modules to evaluate performance before editing the configuration.

Final Design Selection

We developed a Python program called value_sweep.py designed to comprehensively analyze the EDL process by systematically compiling and evaluating constraint values across multiple iterations. Our approach involved collecting data for each constraint, sorting iterations by time, and strategically eliminating scenarios that did not work.

Unlike traditional methods that focus on optimizing a single parameter, our approach allowed for simultaneous multi-constraint analysis. This methodology provided a more holistic and nuanced optimization strategy, enabling us to maximize overall performance in ways that would have been impossible with a narrow, single-constraint approach. By examining the complex interplay between different constraints, we gained deeper insights into the system's potential.

The effectiveness of this strategy was evident in the progressive evolution of our value_sweep.py outputs. The data range from our initial analysis to the final iterations demonstrated significant improvements in our understanding and optimization of the EDL process, validating the power of our comprehensive analytical approach.

We used this approach to optimize our design and choose the best one, given the constraints and the parameters we wanted to emphasize.

Numerical Methods Used

Our Python script employs several numerical optimization methods for maximizing objectives and solving constraints. These methods are from the `scipy.optimize` library and include:

1. **Trust-Region Constrained Algorithm (trust-constr):**

- This method solves the optimization problem with constraints and bounds defined using a Nonlinear Constraint object. It iteratively updates the solution while respecting constraints like strength, cost, and battery energy limits.
2. **Sequential Least Squares Programming (SLSQP):**
 - This method minimizes the objective function with equality and inequality constraints defined via the `ineq_cons` dictionary. It is also bound-aware.
 3. **Differential Evolution:**
 - A global optimization algorithm that explores the search space more thoroughly compared to local optimizers. It handles constraints through a nonlinear constraint and allows population-based exploration.
 4. **Constrained Optimization BY Linear Approximations (COBYLA):**
 - It deals with constraints by linear approximations and can handle inequality constraints without requiring explicit gradient definitions.

Additionally, grid search is employed in the loops to systematically explore the parameter space before optimization, providing initial guesses (x_0) for the optimization algorithms. This enhances the likelihood of finding a global maximum.

Description of Final Design

We arrived at our final design by optimizing key aspects of our rover in order to minimize the time while staying within the parameters. The following are key parameters found when designing our rover:

- **Parachute:** We found that minimizing the parachute diameter to 14 m allowed our rover to descend the quickest.
- **Wheel Radius:** Our wheel radius is maximized at almost 0.7 m in order to allow the rover to move the furthest that it can in the least amount of rotations.
- **Speed Reducer (d2):** Additionally, the speed reducer is the smallest that it can be at 0.05 m in order to maximize the number of rotations that the wheel has.
- **Fuel and Chassis Mass:** Our fuel mass and chassis mass are both a bit on the heavier side but light enough to allow the rover to land safely and quickly.

We found that the budget constraint was not one of the key factors to create tough decisions in our design. This is shown in our total cost as we are about \$1.25 million under the \$7 million budget.

Table 1: Final Optimized Rover Parameters

Parameter	Value	Units
Optimized Parachute Diameter	14.00	m
Optimized Fuel Mass	200.304121	kg
Time to complete EDL Mission	128.786949	s
Rover Velocity at Landing	-0.100512	m/s
Optimized Wheel Radius	0.699995	m
Optimized d2	0.05	m
Optimized Chassis Mass	375.299577	kg
Time to Complete Rover Mission	395.625	s
Time to Complete Mission	524.412	s
Average Velocity	2.436	m/s
Distance Traveled	1000.00	m
Battery Energy per Meter	541.524	J/m
Total Cost	5751017.33	\$

Performance Data

The final rover design, optimized by using the COBYLA method, meets all mission requirements while achieving high performance in the Entry, Decent, Landing, and traversal phases. Below is a detailed summary of the performance results.

- **Motor:** The high-efficiency speed_he motor was selected to maximize the rover's speed without significantly increasing energy consumption.
- **Chassis Material:** Magnesium was chosen for its lightweight and high strength-to-weight ratio. The cost was also a very big consideration for this choice
- **Battery:** PbAcid-1 batteries were selected for their reliability and cost efficiency. A configuration of 5 battery modules was used to achieve the necessary energy storage.

Table 2: Chosen Rover Specifications

Parameter	Chosen Specification
Motor	<i>speed_he</i>
Chassis Material	Magnesium
Battery	PbAcid-1
Number of battery Modules	5
Optimization Method	COBYLA

```

Normal return from subroutine COBYLA

NFEVLS =   66   F = 5.244124E+02   MAXCV = 0.000000E+00
X = 1.400003E+01   6.999954E-01   3.752996E+02   5.000000E-02   2.003041E+02
Commencing simulation run...

Ejecting heat shield at      t = 5.9742 [s], altitude = 8000.0000 [m], speed = -428.9329 [m/s]
Turning on rockets at        t = 29.7310 [s], altitude = 1800.0000 [m], speed = -169.9525 [m/s]
Ejecting parachute at        t = 36.4478 [s], altitude = 900.0000 [m], speed = -103.0225 [m/s]
Turning on speed control at  t = 52.4011 [s], altitude = 9.1366 [m], speed = -9.0000 [m/s]
Turning on altitude control at t = 52.4029 [s], altitude = 9.1200 [m], speed = -8.9904 [m/s]
Commencing simulation run...

Ejecting heat shield at      t = 5.9742 [s], altitude = 8000.0000 [m], speed = -428.9329 [m/s]
Turning on rockets at        t = 29.7310 [s], altitude = 1800.0000 [m], speed = -169.9525 [m/s]
Ejecting parachute at        t = 36.4478 [s], altitude = 900.0000 [m], speed = -103.0225 [m/s]
Turning on speed control at  t = 52.4011 [s], altitude = 9.1366 [m], speed = -9.0000 [m/s]
Turning on altitude control at t = 52.4029 [s], altitude = 9.1200 [m], speed = -8.9904 [m/s]
Turning on sky crane at     t = 52.5848 [s], altitude = 7.6000 [m], speed = -7.7247 [m/s]
The rover has landed!
t=128.7869 [s], rover pos = 0.0000 [m], rover speed = -0.1005 [m/s] (sky crane at h=7.6202, v=-0.000512)

-----
-----
```

Figure 1: Rover Mission Timesheet

These results demonstrate the efficacy of the chosen design approach and optimization method. The design success highlights its capability to meet the heavy constraints of the Mars Mission.

4. SEC Ignite Competition



Final Report:

Development of a Rocket Landing Simulation

Using a Gimbal and Landing Gear

Eduardo Burciaga-Ichikawa, Kalen Jaroszewski, Julia
Sopala and Ian Wilhite
Ignite Design Challenge
November 23, 2024



Table of Contents

Introduction.....	3
Problem.....	4
Background.....	4
Purpose.....	4
Design Criteria.....	5
Solution.....	6
Overview.....	6
Material Selection.....	6
Gimbal.....	6
Landing Gear.....	8
Nose Cone.....	9
Landing Controls.....	10
Conclusion.....	14
References.....	16



Introduction

This paper explores the development of a rocket landing simulation that aims to enhance the landing efficiency and stability of the rocket landing vertically. Designing efficient and reliable landing systems for rockets remains a crucial challenge to safely and consistently land a rocket. The rocket explored in this paper has been modified to reduce mission costs and play a significant role in advancing reusable space technology. The design implemented gimbals for thrust vector control and robust landing gear systems, along with a redesign of the nose cone to realistically model the rocket that would go through both launching and landing. The design leverages gimbal systems to dynamically adjust thrust direction, ensuring precise control of the rocket's orientation during descent. Additionally, including landing gear improves stability upon touchdown, mitigating the risk of tip-over or damage. This solution addresses two fundamental challenges in rocket landings: maintaining attitude control during descent and ensuring structural integrity upon contact with the ground. By tackling these issues, the design enhances the reliability and efficiency of rocket recovery systems, paving the way for advancements in reusable rocket technology.



Problem

Background

The challenge of landing a rocket upright is both a technical and operational problem central to modern aerospace engineering. Traditional expendable launch systems discard hardware after a single use, driving up costs and limiting the efficiency of space exploration and transportation. In contrast, successful vertical landings of reusable rockets can drastically reduce costs and environmental impact. In industry, notable companies like SpaceX and Blue Origin have pioneered reusable rocket technology by implementing advanced systems such as thrust vector control (TVC) and deployable landing gear [1]. These technologies enable rockets to correct their attitude during descent and safely absorb impact upon touchdown. Thrust vector control, often achieved through gimbaled engines, allows for fine-tuned adjustments to the rocket's trajectory. Additionally, landing gear equipped with damping mechanisms ensures stability during landing, even on uneven surfaces.

Research highlights the complexities of balancing stability, accuracy, and robustness. For example, Reuben Ferrante illustrates how gimbal systems contribute to minimizing drift during descent while investigating computational methods for simulating controlled landings [1]. A second project that influenced the use of gimbals and a redesign of the nose cone is a launch report from the AIAA Regional Student Conferences which tested the launch of a rocket by replacing the fins with a gimbal [2]. These advancements inspire our approach to integrating gimbals and landing gear into a simulation that accurately models the dynamics of a rocket landing while implementing a better thrust-to-weight ratio [3].

Purpose

Landing a rocket upright is a valuable problem to solve due to its implications for cost efficiency, safety, and the feasibility of sustainable space exploration. The difficulty lies in maintaining stability during descent and ensuring a secure touchdown on varying terrains. Without reliable control mechanisms, rockets risk instability, which can lead to mission failure, loss of valuable hardware, and environmental hazards.

This problem affects industries and organizations striving to make space travel more accessible. Reusable rockets can significantly reduce the cost of payload delivery, increasing accessibility to orbital applications for research institutions, private companies, and governments.

Design Criteria

To address the problem quantitatively, our team established the following design criteria:

1. **Stability During Descent:** The rocket must maintain an upright orientation with minimal angular drift, measured as the deviation from vertical (in degrees).



2. **Landing Controls:** The code for the rocket simulation must result in a zero velocity when altitude approaches zero, while maintaining stability to disturbances that can occur during landing.
3. **Impact Absorption:** The landing gear should effectively dampen forces upon touchdown to prevent structural damage, quantified by measuring landing impact forces (in Newtons).
4. **Minimized Mass:** No amount of material should be carried needlessly. All parts should be designed to perform their purpose with the minimum amount of additional material, and of the lightest possible material.



Solution

Overview

Our solution to the problem of landing a rocket upright integrates three key mechanical components: gimbal implementation, landing gear addition, and a nose cone redesign. The material these parts are manufactured from also plays an important role and has been considered carefully. Finally, vertical landing requires robust controllers in both the vertical axis and in the gimbal that can accommodate disturbances introduced from a variety of sources.

Together, these elements address the critical challenges of stability, precision, and impact absorption, as defined in our design criteria. Each component has been developed with an emphasis on efficiency, reliability, and adaptability to ensure successful landings under various conditions.

Topic 1: Material Selection

AISI 321 Annealed Stainless Steel SS

Property	Value	Units
Elastic Modulus	1968040.273	kgf/cm ²
Poisson's Ratio	0.27	N/A
Tensile Strength	6322.201972	kgf/cm ²
Yield Strength	2390.422007	kgf/cm ²
Tangent Modulus		kgf/cm ²
Thermal Expansion Coefficient	1.7e-05	/°C
Mass Density	0.0080000001	kg/cm ³
Hardening Factor	0.85	N/A

Figure 1: Material Properties of AISI 321

Stainless steel was selected for numerous reasons. The most significant factor is the ability to maintain a high yield strength at increasing temperatures. Compared to 6061 Aluminum, AISI 321 stainless steel is significantly heavier and more expensive. The thrust from the engines was adequate to compensate for the additional mass, while the ability to withstand higher temperatures accounted for the additional price. The need to withstand high temperatures is very important as the rocket will travel above the speed of sound. The choice of stainless steel for large rockets has been proven with the most notable example being SpaceX Starship.



Topic 2: Gimbal Implementation

Gimbal systems are crucial for thrust vector control, enabling the rocket to adjust its trajectory during descent. By tilting the engine's thrust direction relative to the rocket's center of mass, gimbals allow for fine-tuned corrections to stabilize orientation and counteract disturbances such as wind or uneven terrain below.

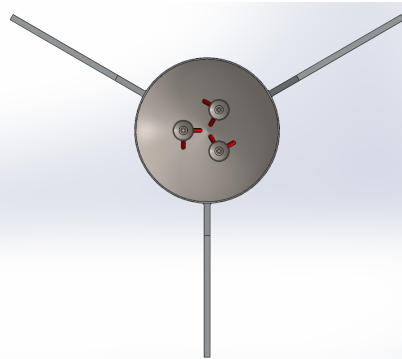


Figure 2: Bottom and side view of the gimbal engines at the base of the rocket

Design Approach

The design incorporates three thrusters mounted on gimbals, which adjust the orientation of each thruster to dynamically control the thrust vector based on real-time feedback from onboard sensors. A proportional-integral-derivative (PID) controller processes data from gyroscopes and accelerometers to maintain vertical alignment, minimizing angular drift even under external disturbances. Stability is further enhanced by strategically positioning the fins, as seen in **Figure 3**, and ensuring the center of pressure is located behind the center of gravity, promoting aerodynamic balance throughout descent. The three engines are designed around the specifications of Raptor V3 with a slightly heavier gimbal. The red linkages are hydraulic actuators for thrust vector control. The first of the orthogonal actuators is for the x position, while the other is for the y position. Three engines are used as this would allow for finer control in series with the gimbal to increase the precision of control.

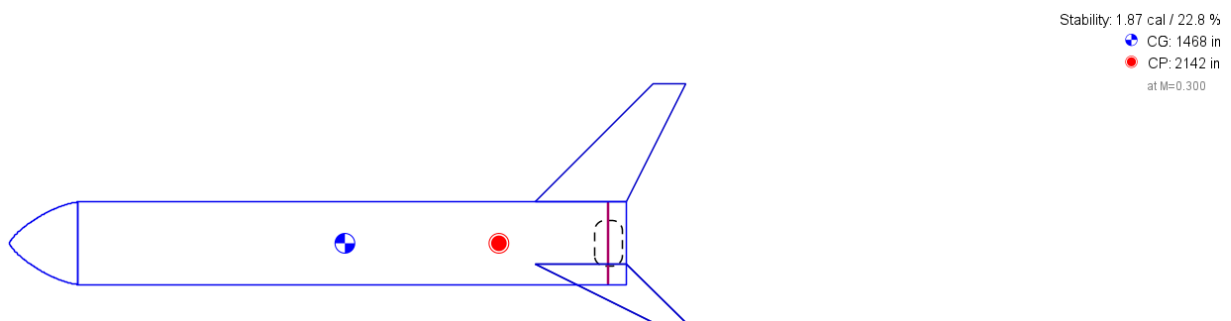


Figure 3: OpenRocket Simulator modeled rocket.



Topic 3: Landing Gear Addition and Topology Optimization

Landing gear provides critical support to absorb impact forces and stabilize the rocket upon touchdown. The design incorporates collapsible legs with shock-absorbing mechanisms to prevent tipping or structural damage.

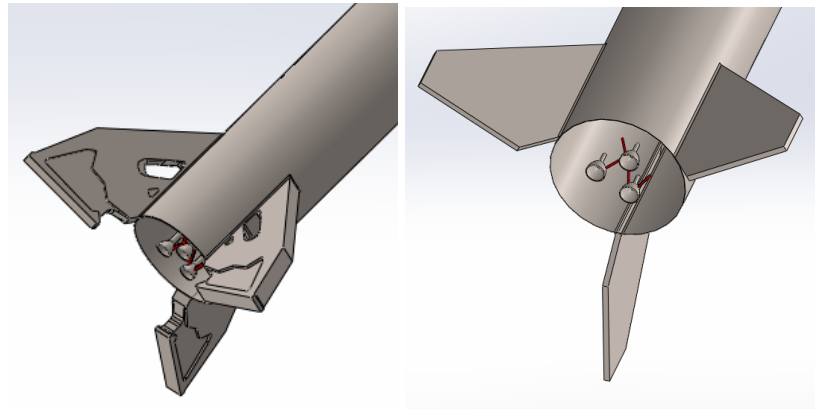


Figure 4: Isometric view of the original landing gear/fins vs final design

Design Approach

The landing gear consists of stainless steel fins equipped with pneumatic dampers that compress upon impact to dissipate energy. The legs are arranged around the rocket's base to maximize stability and are foldable to minimize drag during ascent. In the future, the system should also include footpads designed to distribute forces evenly, even on uneven terrain.

Implementation and Results

Using SolidWorks Topology Optimization, the design space was iteratively refined to remove unnecessary material while retaining the structural integrity required to support the calculated loading weight. The final design achieves a 28% weight reduction with respect to the base mold while meeting all performance criteria for impact absorption validated through FEA with a Factor of Safety of 8.3, as seen in **Figure 5**.

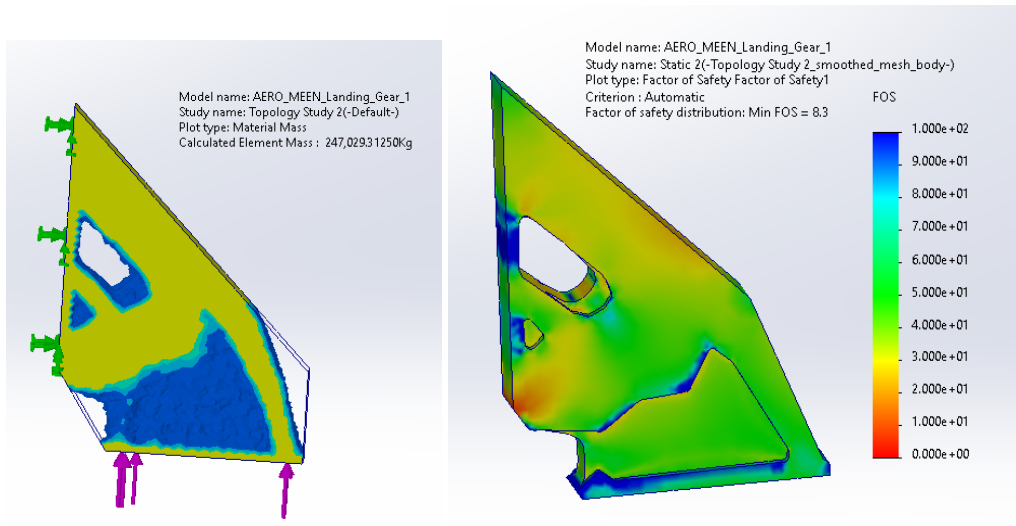


Figure 5: Landing gear topology and FEA analysis

Topic 4: Nose Cone Re-design and Computational Fluid Dynamics (CFD)

The nose cone plays an essential role in aerodynamics during ascent and stability during descent. By optimizing its shape and material properties, we improved its performance in both phases of flight.

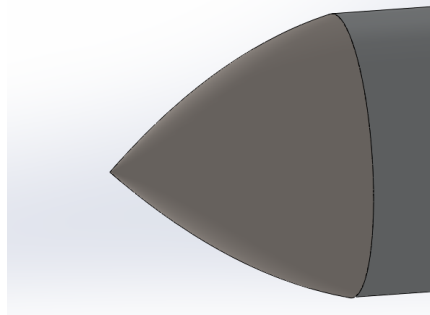


Figure 6: 3/4 Parabolic nose cone design, side view

Design Approach

The redesigned nose cone (**Figure 6**) features a 3/4 parabolic shape that minimizes drag during ascent and promotes aerodynamic stability during descent. The 3/4 parabolic shape is one of the most efficient shapes at supersonic speeds [7]. The nose cone also houses sensors that work in conjunction with the gimbal system to monitor wind patterns and atmospheric conditions.

Implementation and Results

Using SolidWorks' Flow Simulation, the nose cone design was tested at standard flight conditions during the ascent stage (500 m/s). Compared to the cone design, the new nose cone



resulted in a 12.5% reduction in drag forces and a lower distribution of pressures at the nose cone caused by the supersonic flows, as seen in **Figure 7**.

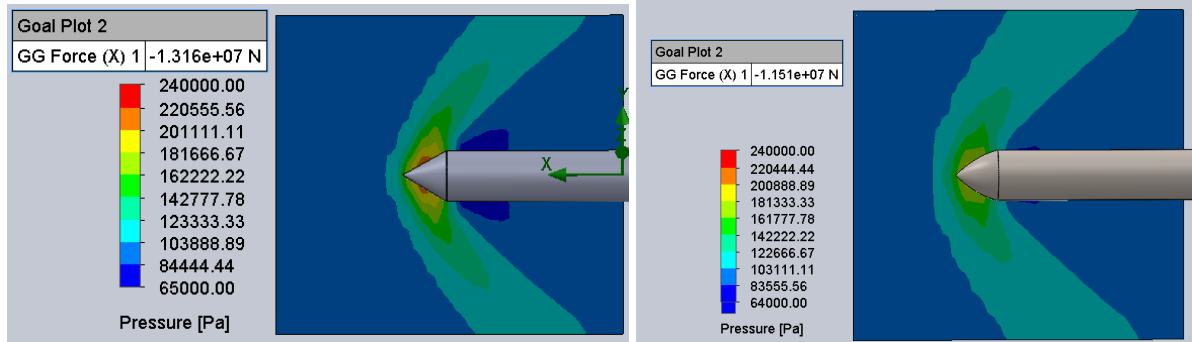


Figure 7: Nose cone CFD analysis of old vs final design at supersonic speeds

Additionally using CFD, the coefficient of drag was calculated from the model by using the coefficient of drag equation and the drag forces. The flow was directed upward from the bottom of the rocket to simulate the downward movement upon descent at 50 m/s. This resulted in a coefficient of drag of 1.427 (**Figure 8**), which was used for the trajectory simulations.

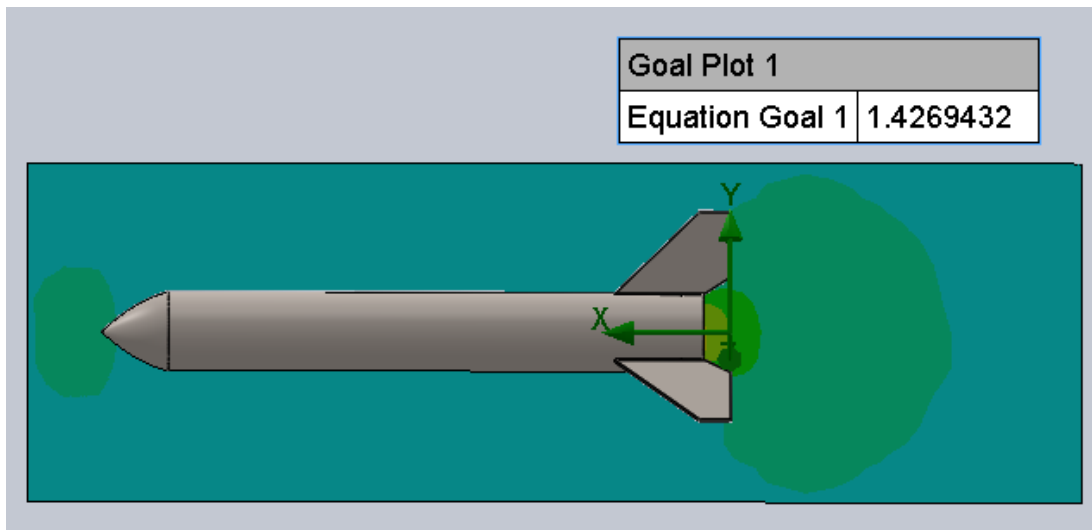


Figure 8: CFD of the rocket in descent & drag coefficient

Topic 5: Landing Controls

The control algorithm for the descent and landing process is a crucial element of the success of a rocket's performance. The descent must be controlled, feasible, and minimize the normal force of landing applied to the rocket as it touches down. There are many factors that could be considered, including but not limited to fuel efficiency, landing time, peak force minimization, thruster performance accommodations or acceleration constraints. Regardless, a solution



focusing on optimization would require an in-depth cost function analysis of these parameters. Solving for an optimal solution to this very complex problem [6]; however, for the scope of this report, only feasibility and force minimization will be considered.

```
# --- Constants Section ---
g = 9.81 # Acceleration due to gravity in m/s^2
mass = 685000 # mass in kg
Cd = 1.427 # Drag coefficient from CFD simulation
rho = 1.225 # Air density at sea Level in kg/m^3
A = 0.5 # Cross-sectional area of the rocket in square meters
engine_thrust = 3.2*1000000 # thrust per engine
num_engines = 3 # number of engines
```

Figure 9: Rocket landing forces script inputs

```
Rocket Landing Forces:
Time to touchdown: 36.60 [s]
Touchdown Velocity: 0.190 [m/s]
Deceleration during landing: 0.018 [m/s^2]
Impact Force: 6.732 [MN]
Normal Force at landing: 13.452 [MN]
Net Power Applied 75.744 [GW]
```

Figure 10: Rocket landing forces script output

Design Approach

The landing controls system ensures the rocket maintains stability and lands upright by processing real-time sensor data to dynamically adjust thrust and orientation. This system combines a model representing a stable hover with an error-driven controller that integrates feedback from onboard sensors with control algorithms, enabling precise adjustments to gimbals and thrusters during descent. This system demonstrates effective landing in reasonable conditions with a minimal touchdown velocity **[Figure 10]**.

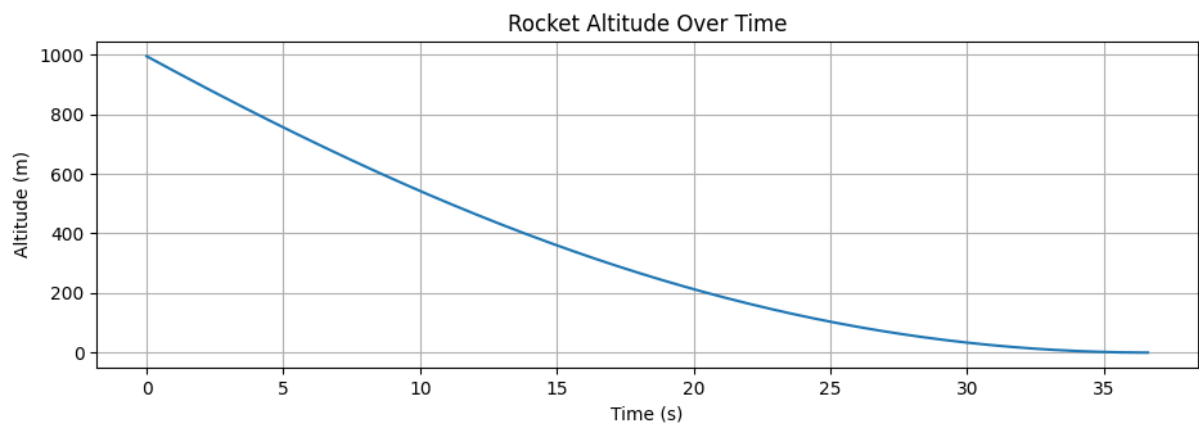


Figure 11: Simulated rocket altitude while landing

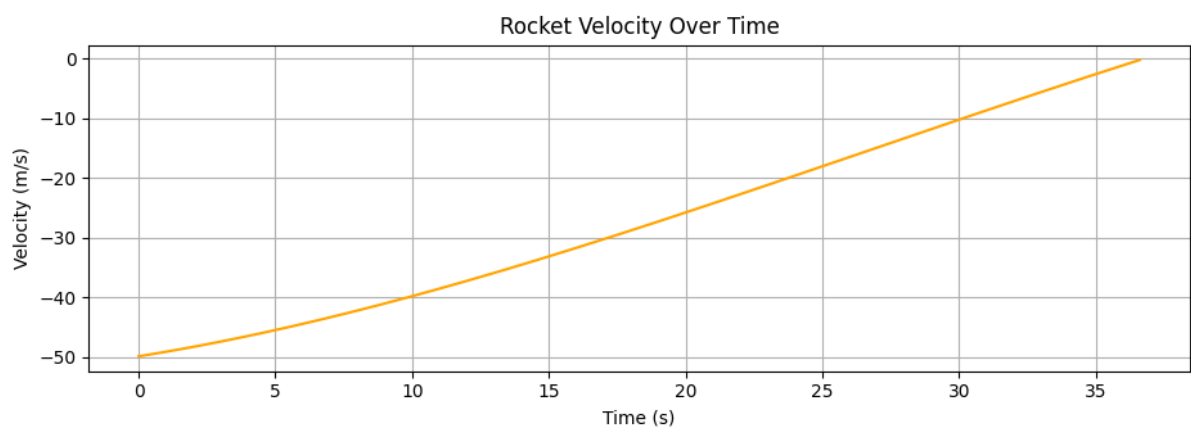


Figure 12: Simulated rocket velocity while landing

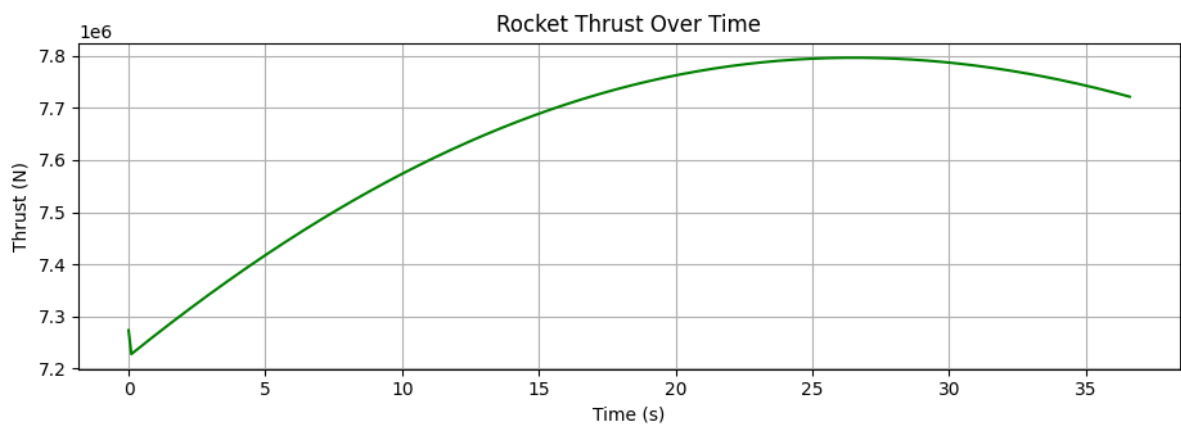


Figure 13: Simulated rocket thrust while landing



Altitude Control Algorithm Design

The control system is based on a Hybrid Controller or Model Predictive Controller (MPC) containing both a model term and an error-driven term. The model term is based on precalculated values known about the object being controlled and its current position, whereas the error-driven Proportional-Integral-Derivative (PID) controller element processes data from accelerometers, tachometers, and altimeters to correct the actual differences between setpoints and real-time measured outputs [**Figure 9**], [**Figure 10**]. The model calculates the thrust required to maintain the current velocity by accounting for the weight and drag forces known, and the PID algorithm calculates the necessary adjustments to the thrust output to account for all variance from equilibrium. This system has advantages over purely Model Driven approaches as it can account for disturbances during flight to ensure that disturbances cannot accumulate into large errors. This system has advantages over purely error-driven approaches as the model accounts for a majority of the thrust required, and the PID controller can be more narrowly refined to account exclusively for the adjustments to the model [**Figure 11**], [**Figure 12**], [**Figure 13**]. This system will likely have a marginally slower refresh rate as compared to either of the previously discussed approaches, however, the increased reliability and performance would consistently outperform the alternatives [**4**].

The starter code provided the foundations for solving the dynamics problem while leaving the controller open-ended, with a bias towards an open-loop controller with no feedback [**9**]. The solution implemented has the advantage of resilience towards disturbances.

Gimbal Control Algorithm Design

The gimbal control system would be based purely on an error-driven PID controller, which processes data from gyroscopes, accelerometers, magnetometers and an Internal Measurement Unit (IMU) to minimize the error between the current state of the rocket and the neutral vertical position. The PID algorithm calculates the necessary adjustments to the gimbals to maintain vertical alignment and counteract external forces such as wind or drift. This system does not require a model driven element in the current application as it is meant to purely maintain the stability of the flight. If a model were to be implemented in this system, it would be based on a two-dimensional inverted pendulum, for which each axis could be solved independently [**5**]. This kind of extended functionality would allow for horizontal displacement correction, allowing for precise control over the location of landing.



Conclusion

The challenge of safely and efficiently landing a rocket upright is pivotal in advancing reusable spaceflight technology. Our solution integrates three key innovations: gimbal implementation for thrust vector control, landing gear to absorb impact forces and maintain stability, and a redesigned nose cone for improved aerodynamics and sensor integration. Together, these components address the critical design criteria of stability during descent, precision of landing, and effective impact absorption, demonstrating a holistic approach to solving this complex engineering problem.

Challenges and Lessons Learned

Throughout the project, the team faced several challenges, including balancing lightweight designs to durability, ease of simulation and accuracy, and accurately simulating real-world conditions. The team also had to work on parallel development and understanding how one layer of analysis affected the others. For example, as we were performing the Computation Fluid Dynamics, we realized that an error meant that there was a slightly different drag coefficient, and we needed to retune the PID controller for this new value. Many times in industry, this kind of thing will happen, and this experience demonstrates the need for organized planning and coordination for dependent processes.

Overall, these challenges highlighted the fundamentally interdisciplinary nature of many classically-disciplined engineering challenges that occur in industry and research, while underscoring the importance of iterative testing, collaborative development and project planning.

From this experience, we learned to approach engineering problems systematically, breaking them into manageable components and validating each step through simulations. Additionally, we gained insights into how theoretical knowledge translates into practical design considerations.

Contributions

- **Ian Wilhite:** Designed the control algorithms for the landing, ensuring stable descent.
- **Eduardo Burciaga-Ichikawa:** Led the development of the landing gear, including material selection and impact testing, along with running topology and CFD analysis.
- **Kalen Jaroszewski:** Designed and tested the aerodynamic properties of the nose cone, integrating sensors for enhanced feedback.
- **Julia Sopala:** Consolidated data, and ensured alignment of all components with the design criteria and reporting it.

Room for Growth

Looking forward, next steps for the project could include a more in depth comparison of materials and consideration of design for manufacturing of parts, testing the design under more



variable environmental conditions, and prototyping scaled physical models for validation. The controllers could be expanded to utilize the varied power between the three thrusters, or to include drag manipulators like flaps. Testing could include further validity testing with the current altitude controller, and implementation of the gimbal controller and full system simulations. In implementing the ideas discussed, this system could become a reliable method for assisting rocket landing accuracy and improving affordability of space missions.



References

- [1] R. Ferrante, "A robust control approach for rocket landing," *Theses Univ. Edinburgh*, 2017.
- [2] C. Fang *et al.*, "Gru & Vector Gimbal Rocket Design and Launch Report," in *2024 Regional Student Conferences*, 2024, p. 85702.
- [3] C. Trom, "Development of a vertically landed rocket design challenge for expanding the pipeline and enhancing education of students pursuing careers in space," University of Illinois at Urbana-Champaign, 2022.
- [4] Z. Hou and Z. Wang, "From model-based control to data-driven control: Survey, classification and perspective," *Information Sciences*, vol. 235, pp. 3–35, 2013, doi: 10.1016/j.ins.2012.07.014.
- [5] İ. Yiğit, "Model free sliding mode stabilizing control of a real rotary inverted pendulum," *International Journal of Control, Automation and Systems*, vol. 23, no. 10, 2015, doi: 10.1177/1077546315598031.
- [6] C. Wang and Z. Song, "Trajectory optimization for reusable rocket landing," in *2018 IEEE CSAA Guidance, Navigation and Control Conference (CGNCC)*, Xiamen, China, 2018, pp. 1-6, doi: 10.1109/GNCC42960.2018.9019105.
- [7] V. K. Shah, "Determination of the optimum nose cone geometrical shape for supersonic missile," *Aerospace Science and Technology*, vol. 133, 2023, doi: 10.1016/j.ast.2022.106774.
- [8] A. Aboelhassan, M. Abdelgeliel, E. E. Zakzouk, and M. Galea, "Design and implementation of model predictive control based PID controller for industrial applications," *Energies*, vol. 13, no. 24, p. 6594, 2020, doi: 10.3390/en13246594.
- [9] B. Borovic, A. Q. Liu, D. Popa, H. Cai, and F. L. Lewis, "Open-loop versus closed-loop control of MEMS devices: choices and issues," *Journal of Micromechanics and Microengineering*, vol. 15, no. 10, p. 1917, 2005, doi: 10.1088/0960-1317/15/10/018.

5. Mechanical Modeling

FIDGET FUN

GROUP 13: MEEN 210-S05
FALL '24 PROJECT

By Ryan Welty, Mckenzie
McCain, Ian Wilhite
and Astrid Garcia



THE TEAM

MEEN 210-505 FALL SEMESTER
MEEN 210-505 FALL SEMESTER

IAN WILHITE



RYAN WELTY



ASTRID GARCIA



MCKENZIE MCCAIN



VIDEO ADVERTISEMENT





WHAT IS FIDGET FUN

A customizable, modular fidget toy that transforms into endless puzzle track configurations! Simply snap the pieces together, and let the magic unfold as a smooth ball glides along the creative paths you design.



CONCEPTS

Elderly Toy Concept Design

Tuesday, September 17, 2024 6:51 PM

TOPICS: Memory & Dexterity

- 1. marble game
- 2. bingo-related?
- 3. puzzle / puzzle box
- 4. magnet fishing
- 5. jigsaw
- 6. matching game
- 7. farming game

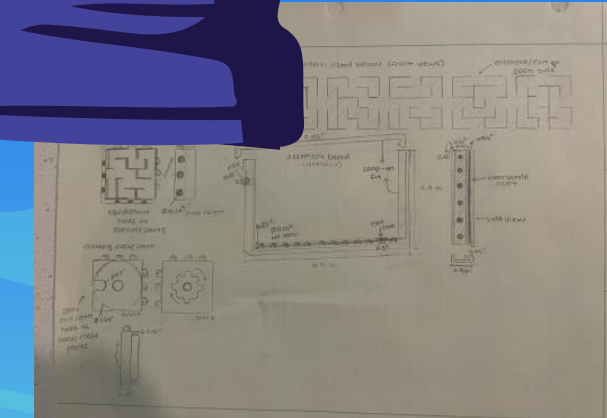
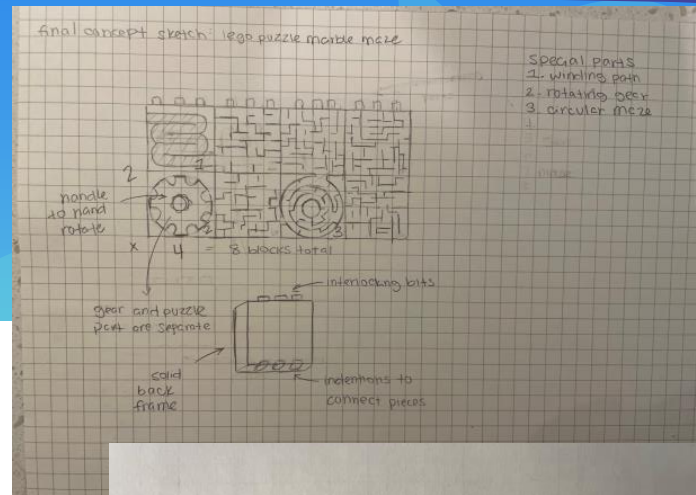
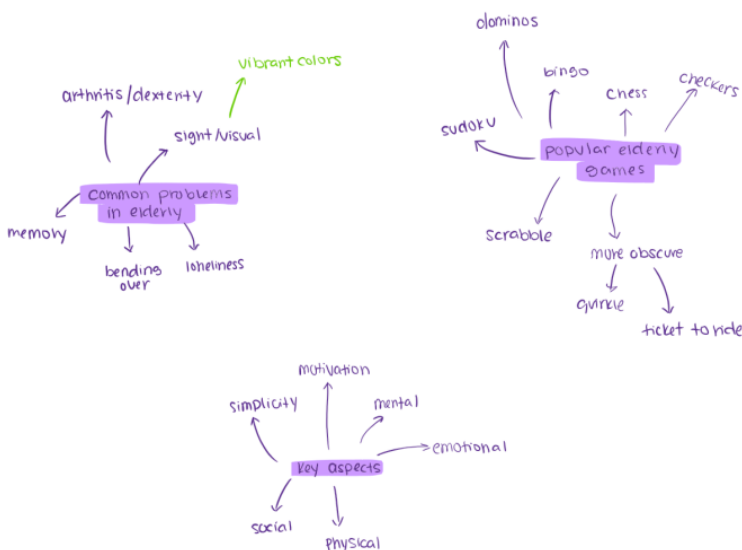
Requirements

- ≥ 4 non-trivial parts
- ≥ 1 3d printed part
- ≥ 1 moving parts

* can be powered by hand or motor

Moving Part Ideas

- spring-loaded mechanism
- rotating dial



Elderly Toy Concept Design

Tuesday, September 17, 2024 6:51 PM

TOPICS: Memory & Dexterity

- 1. marble game
- 2. bingo-related?
- 3. puzzle / puzzle box
- 4. magnet fishing
- 5. jigsaw
- 6. matching game
- 7. farming game

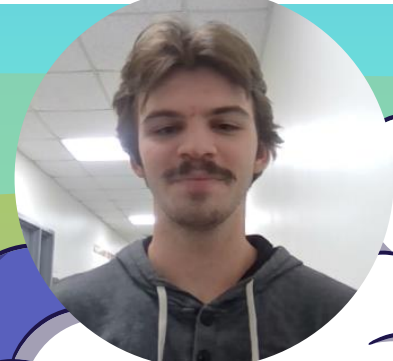
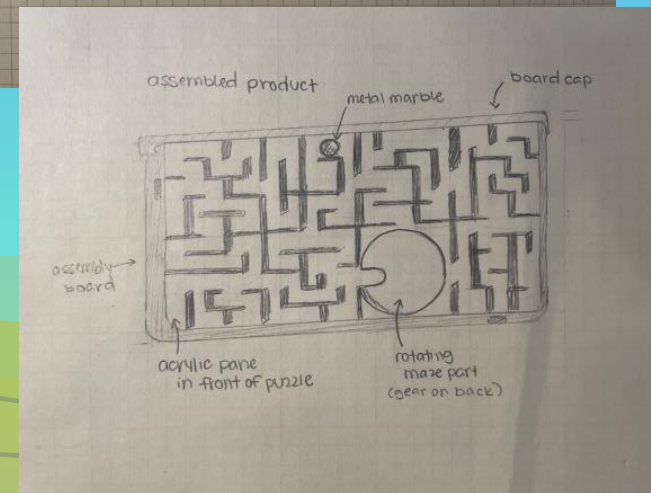
Requirements

- ≥ 4 non-trivial parts
- ≥ 1 3d printed part
- ≥ 1 moving parts

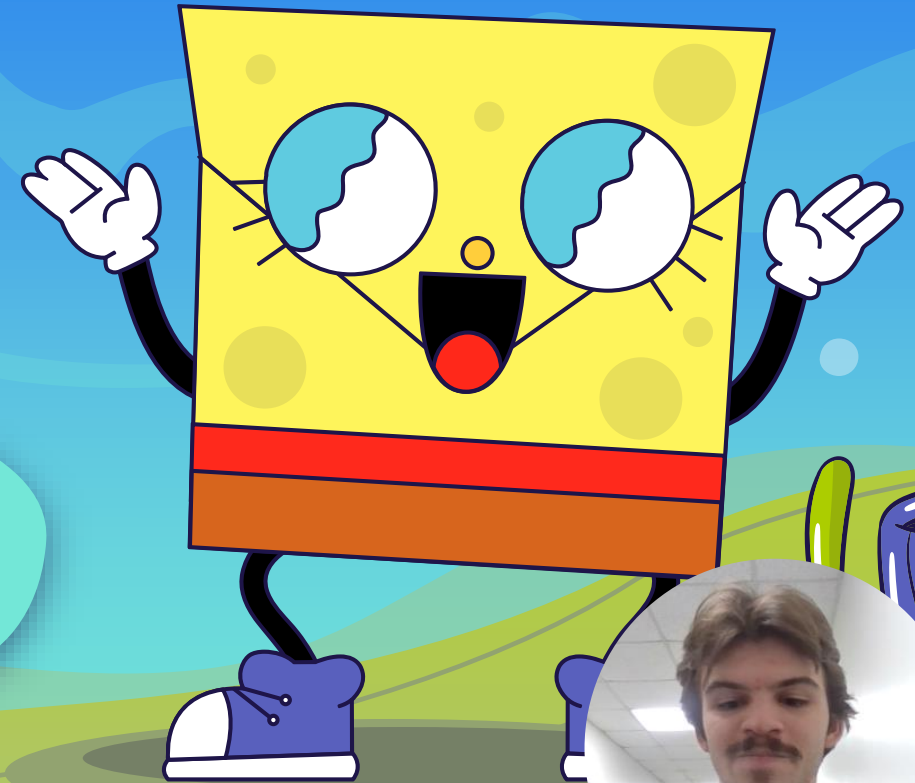
* can be powered by hand or motor

Moving Part Ideas

- spring-loaded mechanism
- rotating dial



THE PRODUCT :



PROBLEM & NEEDS

"My grandma loves gardening, reading, and solving puzzles. Recently, she has started noticing changes. Her hands feel stiff when she tries to grab plates from the cabinets or even when she goes to grab her favorite book. She has also noticed that she often forgets where she places her keys and has found it hard to concentrate for long periods of time. This has begun to make her sad and frustrated because her body doesn't work the way it used to. She needs something that will engage her mind and helps her feel calm and in control"



PROBLEM & NEEDS

Target Audience

- Intended for anyone in the elderly age range group, someone 65 years or older. Although it is not restricted to just this age group. This product is also intended for people suffering from medical conditions such as Alzheimer's or dexterity /mobility issues.

Why & How would they use your product?

- Why: Fun, colorful, and easy to use!
- How: Just snap the pieces together and watch the ball glide through the path

Needs Statement

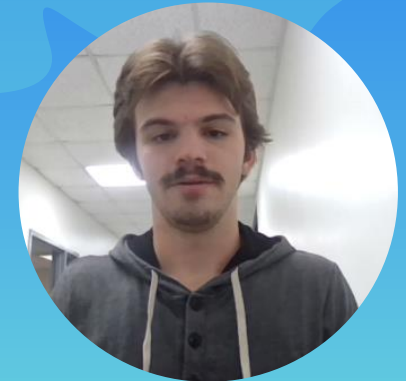
- Engaging mental stimulation
 - Price-conscious
 - The key aspects should include topics: social, physical, mental, or emotional
 - Accommodating to elderly individuals
 - Intuitive gameplay mechanics
- Based off the project outlines from milestone 0, we were able to produce our needs statement



ENGINEERING REQUIREMENTS

Design Components:

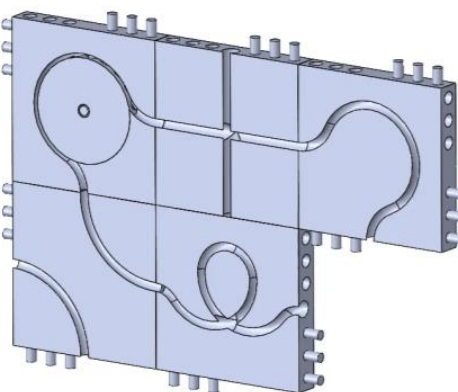
- Block Width
- Block Thickness
- Ball Diameter (from stock ball bearing)
- Tolerance around ball
- Length of pegs
- Depth of path



Name	Value / Equation
Global Variables	
"block_width"	= 100mm
"block_thickness"	= 15mm
"ball_dia"	= 0.25in
"ball_tol"	= 2mm
"peg_dia"	= 6mm
"peg_tol"	= 1mm
"patt_offset"	= 3mm
"peg_len"	= 10mm

MODELING

Animated Exploded View of Fidget Fun Assembly



FABRICATION PROCESS

MACHINE USED: Creality K1 3D printer

MATERIAL: Smooth PLA
Washer & Screw

23 hr print time, 310.96 grams

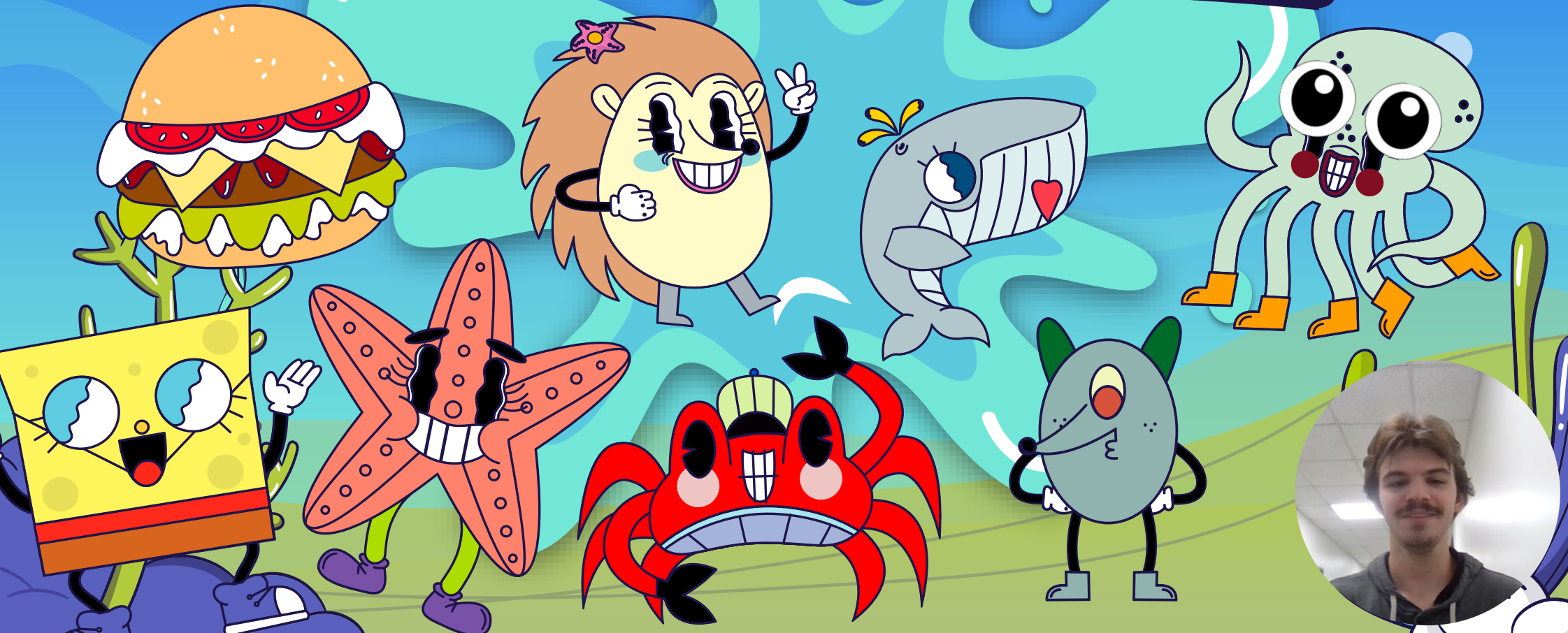
Same scale print

Conformity :

- The washer and screw
- The tolerance
- Size of ball bearing
- Scratched board design
- Orientation of the plates



THANKS AND GIG EM'



6. Mechanical Measurements

3/23/2025

To: Dr. Heather Lewis

From: Ian Wilhite, *ICW*

Subject: Experimental natural frequency analysis

Abstract

In many mechanical systems that undergo typical harmonic excitation, vibrations are inevitable. Engines, buildings, and generators all undergo some type of vibration and oscillation and must determine the extent that harmonic excitation may impact a system, and therefore engineers need a robust methodology to numerically determine and experimentally verify the natural frequency of their system. In this experiment we seek to predict and experimentally verify the natural frequency of vibration for the mechanical systems provided. The beam's dimensions were measured, and the Virtual Instrument (VI) in LabVIEW captured displacement traces under different loads [1]. Calculated damping ratios, logarithmic decrements, and natural frequencies were compared against theoretical values derived from beam theory. Experimental natural frequencies for both deflection magnitudes averaged 93.79 rad/s, while the theoretical value was 167.95 rad/s. A 95% confidence interval and two-sample t-test confirmed consistency across both trials. Furthermore, linear regression was used to calibrate strain measurements and predict an unknown weight, validating the effectiveness of the calibration process. Sources of error in the collected values of the traces include calibration uncertainty, temperature fluctuations, and sensor noise. Results deviated from theoretical predictions, likely due to accumulation of sources of error in measured values and sensor calibration for experimental values. This reiterates the importance of analysis on the vibrations of harmonically excited mechanical systems and the impacts that those vibrations can have on the performance and life cycle of those systems. Future work could include additional trials to mitigate the impact of inconsistencies in trials and analysis on additional peaks pending on the noise in the sensors used to measure amplitude.

Introduction

The experiment performed is designed to analyze the effects of the vibrations in a cantilevered beam. These vibrations, if not properly accounted for, can lead to fatigue, noise, inefficiency, or catastrophic failure in components ranging from engine mounts and turbine blades to bridges and aerospace structures. Understanding the methodologies to predict the natural frequency is essential to many oscillating systems which receive harmonic excitation including engines, heavy machinery, and large structures [3]. In this experiment, the cantilever beam's dimensions were measured to calculate the equivalent

system mass and area moment of inertia across the axis of deflection. These processes rely on the generated trend between collected datapoints, which

The Virtual Instrument (VI) in LabVIEW was utilized to capture the displacement of the beam under loading conditions [1]. The experimentally found traces were used to calculate the logarithmic decrement, damping ratio, and natural frequency for the vibrations under small and large deflection. The theoretical natural frequency was determined using beam theory and compared to the experimental values obtained from the displacement traces. A 95% confidence interval was constructed to find the bounds of the natural frequency. Similarly, various masses were applied, and the deflection of the beam was determined. Then a trendline was created and used to predict an unknown mass. This process highlights the validity of the sensors and data collection processes, and their ability to verify the calibration and determine the predictive value in the data collected.

Procedure

First the properties of the beam should be found including length, width, and thickness of the cantilever beam. The material should be noted so that the material properties can be referenced later.

$$M_e[kg] = 0.23 * M_{beam}[kg] + m_{applied}[kg] \quad (1)$$

The equivalent mass can be found using Equation (1), which requires the mass of the beam and the mass applied to the end of the beam. The area moment of inertia for the beam can be found applying Equation (2) using the base width of the beam and the height of the beam.

$$I_{area}[m^4] = \frac{1}{12} b[m] * (h[m])^3 \quad (2)$$

Using the known properties of the beam, we can apply beam theory to determine the natural frequency of oscillation using Equation (3).

$$\omega_n \left[\frac{rad}{sec} \right] = \sqrt{\frac{3EI}{M_e l^3}} \left[\frac{rad}{sec} \right] \quad (3)$$

Where omega is the undamped natural frequency of the beam in unit radians per second, E is Young's modulus of the beam material in unit pascal, I is the area moment of inertia of the beam cross-section in unit meter to the fourth, Me is the equivalent system mass in kilograms, which accounts for the effective mass of the cantilever beam in vibration, and l is the length of the bar in meters.

Using the known masses, the gauge can be calibrated to accurately measure the displacement of the beam. For the first trial, we displaced the beam a small amount and recorded the displacement over time for the vibration until the displacement amplitude decayed to equilibrium. For the second trial, we displaced the beam a large amount and similarly recorded the displacement over time for the vibration of the beam. From the data, we extracted the peak amplitudes and the time at which they occurred, then applied Equation (4) to determine the logarithmic decrement of the system.

$$\delta = \frac{1}{n} \ln \left(\frac{x_n}{x_{n-1}} \right) \quad (4)$$

The damping ratio could then be calculated using the logarithmic decrement between each pair of peaks using Equation (5).

$$\xi = \frac{\delta}{\sqrt{4\pi^2 + \delta^2}} \quad (5)$$

In order to construct a confidence interval for each parameter, the t-score must be identified for the scenario. To construct a 95% confidence interval, we identify that for six measured peaks, there are five found logarithmic decrement values, five damping ratios, and five natural frequencies calculated, therefore, to construct a confidence interval, we identify that there are four degrees of freedom and an alpha value of 0.05. We can then use Equation (6) to determine the confidence intervals for the natural frequency of the small and large excitations.

$$CI = \bar{x} \pm t \frac{s}{\sqrt{n}} \quad (6)$$

Using the damped natural frequency and the known eta value, the natural frequency can be experimentally determined for each of the trials known. The relationship between damped and undamped natural frequency is given traditionally by Equation (7).

$$\omega_d = \omega_n \sqrt{1 - \xi^2} \quad (7)$$

Which can be rearranged into a form more useful for analysis as seen in Equation (8).

$$\omega_n = \frac{\omega_d}{\sqrt{1 - \xi^2}} \quad (8)$$

Using the relationship provided for the natural frequency in Equation (8), the propagation of uncertainty can be applied to determine the uncertainty of the experimental natural frequency using Equation (9) [2][4].

$$\delta \omega_n = \sqrt{\left(\delta \omega_d * \frac{\partial \omega_n}{\partial \omega_d} \right)^2 + \left(\delta \xi * \frac{\partial \omega_n}{\partial \xi} \right)^2} = \sqrt{\left(\delta \omega_d * \frac{1}{\sqrt{1 - \xi^2}} \right)^2 + \left(\delta \xi * \omega_d * \frac{-\xi}{(1 - \xi^2)^{3/2}} \right)^2} \quad (9)$$

In the second part of the experiment, strain measurements were taken as known weights were incrementally applied to the cantilever beam. Using the “Lab04-PartB.vi” file in LabVIEW, the strain (in Ohms) was recorded for masses of 0g, 50g, 100g, 120g, 150g, and 200g. After all known weights were measured, an unknown mass was applied and its strain recorded. These data points were used to perform a linear regression in Excel, enabling the prediction of the unknown weight.

Results and Discussion

The primary goal of the first part of this experiment was to determine the natural frequency of a cantilever beam and compare theoretical predictions with experimental

measurements. The data obtained from small and large displacement traces were utilized to calculate logarithmic decrement, damping ratio, and natural frequency.

Table 1: Material properties for the cantilever beam.

Characteristic	Value	Unit
Material	Steel	n/a
Width	51.17	mm
Thickness	1.56	mm
Length	22.3	cm
Moment of Inertia	1.619×10^{-11}	m^4
Density	7.85	g/cm^3
Youngs Modulus	207×10^9	Pa
Mass	139.7	g

As shown in Table 1, the beam was made of steel with a width of 51.2 mm, a thickness of 1.56 mm, and a length of 22.3 cm. Using beam theory and Equation (3), the theoretical natural frequency was calculated as 167.95 rad/s.

Table 2 and Table 3 summarize the extracted peak amplitudes, time intervals, and calculated parameters from the vibration traces.

Using the experimentally determined damped frequency and damping ratio, the natural frequency can be experimentally determined for each trial, which is displayed in Table 2.

Table 2: Trace natural frequencies and confidence intervals

Trace	Natural Frequency (rad/s)	Uncertainty (rad/s)	Confidence Interval
Small displacement	93.79	1.229	(92.56, 95.02)
Large displacement	93.79	1.229	(92.56, 95.02)

From Table 1, the mean natural frequency for the small displacement trace was 93.79 rad/s with a standard deviation of 0.99 rad/s. The mean damping ratio was calculated as 0.0035, and the logarithmic decrement was found to be 0.0193.

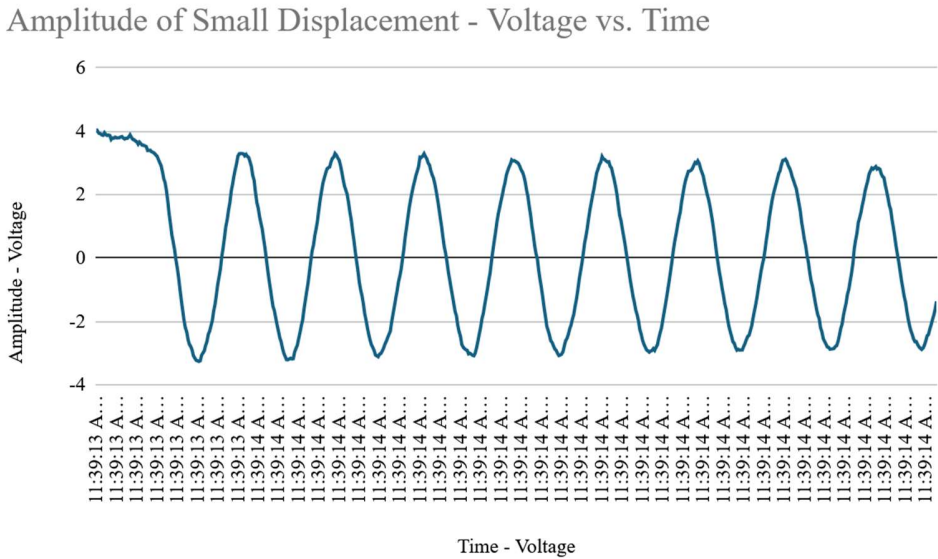


Figure 1: Amplitude of small excitation

For the large displacement trace, the mean natural frequency remained 93.79 rad/sec with a standard deviation of 0.99 rad/sec. The damping ratio and logarithmic decrement were calculated to be 0.0031 and 0.0193, respectively.

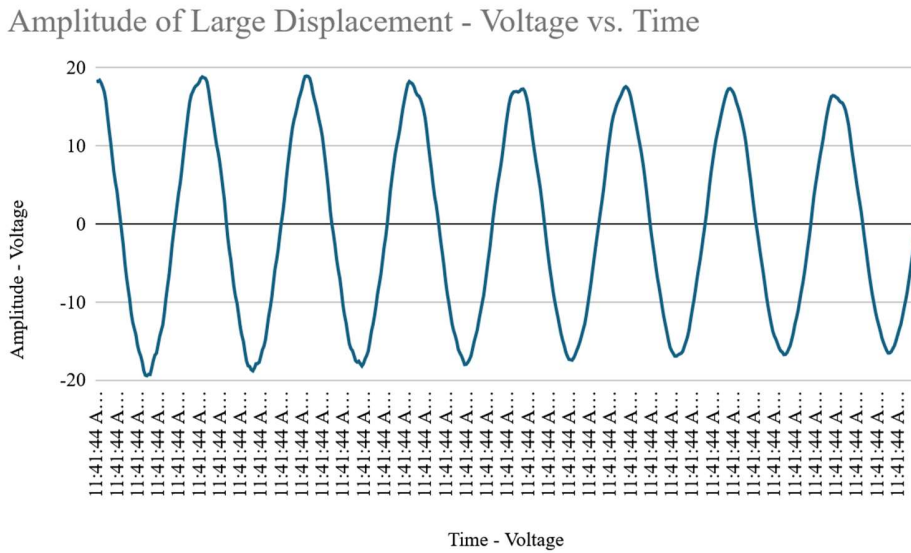


Figure 2: Amplitude of large excitation

A two-sample t-test was performed to determine whether the natural frequencies obtained from the small and large displacement traces were statistically different. The test yielded a t-value of 0.0595, which was less than the critical value of 2.306 for a 95% confidence level and 8 degrees of freedom. Therefore, we fail to reject the null hypothesis, indicating that the two frequencies are statistically equivalent.

The theoretical natural frequency of 167.95 rad/sec deviated significantly from the experimentally determined value of 93.79 rad/sec for both small and large displacements. This difference indicates many sources of error.

After applying the masses to the beam, the resistance values were determined for various masses applied and presented in Table.

Table 3: Summary of found values.

Mass (grams)	Resistivity (Ohms)
0	-0.00370511
50	-0.00367987
100	-0.00365754
120	-0.00365266
150	-0.00363531
200	-0.00361276

The collected data from Table 3 was then plotted in Figure 3 and a trendline plotted.

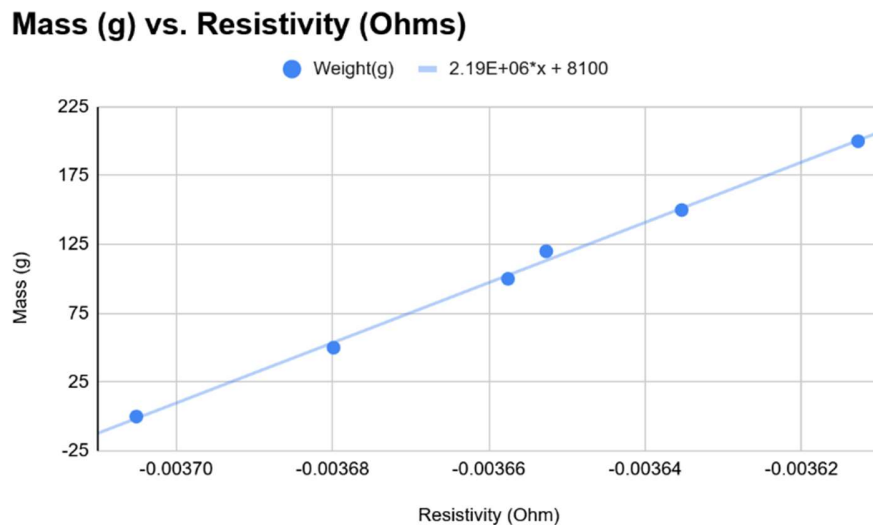


Figure 3: Plotted experimental mass over resistivity

The strain measurements under known weights produced a highly linear relationship ($R^2 = 0.996$) shown in Equation (10), validating the strain gauge's consistency in the static loading scenario. Using the linear regression model, the unknown mass was predicted with high accuracy, demonstrating the practical utility of the gauge system in low-frequency or static load measurements.

$$W[g] = 2.19 * 10^6 * R + 8100$$

10

The unknown strain measurement of -0.00357253 ohms was input into the regression equation, yielding a predicted mass of 276.2 grams.

There were likely errors in the calibration of the strain gauge, which could have introduced a small offset to the measurements or a linear scaling factor into the amplitude

but likely not a major effect on the time of the peaks. Minor error could be attributed to temperature fluctuations, material defects, or beam bending asymmetry. Sensor noise during the measurement of the amplitudes likely played a significant role in the noise of the logarithmic decrement which propagated into the damping ratio and the calculated undamped natural frequency. The sensor noise could be identified in the “capping” of the peaks of the displacement graph as well as the general increase in noise at the maximum displacement due to hysteretic effects potentially acting to smooth the amplitude data while the beam was in motion. These effects can be observed in Figures 1 and 2.

Other sources of error could include material defects or other vibrations in the testing assembly supporting the beam being analyzed.

A 95% confidence interval was constructed for both displacement traces to assess the variability in natural frequency. Using Equation (5), the confidence interval was determined and presented in Equations (6), and (7).

Conclusion/Summary

After performing a two-sample t-test, it can be concluded that there is a statistically significant difference between the damped natural frequency and the undamped natural frequency.

The objective of this experiment was to analyze the vibrational behavior of a cantilever beam and compare the theoretical and experimental natural frequencies. Using beam theory, the theoretical natural frequency was calculated to be 167.95 rad/sec, while the experimentally determined values for small and large displacement traces were approximately 93.79 rad/sec. The results demonstrated a significant deviation between theoretical and experimental frequencies. These results indicate major sources of error in the experimental procedure applied or the methodologies presented.

A 95% confidence interval was constructed for both traces, indicating that the experimental results were consistent across different displacement magnitudes. Additionally, a two-sample t-test confirmed that there was no statistically significant difference between the small and large displacement traces, reinforcing the reliability of the measured values.

The second half of the experiment demonstrated the practical use of strain gauge calibration through linear regression. The unknown mass was predicted with high accuracy, validating the reliability of the calibration procedure and the strain gauge system. Together, these two experimental methods showcase the importance of both frequency analysis and accurate calibration in mechanical measurement systems.

Despite the discrepancies observed, the experiment provided valuable insights into the importance of accounting for measurement errors and environmental factors when analyzing vibrational systems [3]. Future works could include minimizing sensor noise, or refining calibration methods. Overall, this experiment emphasized the need for additional work in understanding and predicting the natural frequencies of mechanical systems.

References

- [1] Gilman, J., and Glasofer, J., 2003, "Introduction into LabVIEW Programming, MEEN 260 Laboratory Manual," Texas A&M University.
- [2] Beckwith, T. G., Marangoni, R. D., and Lienhard, J. H., 2007, *Mechanical Measurements*, 6th ed., Pearson Prentice Hall, Upper Saddle River, NJ.
- [3] Rao, S. S., 2011, *Mechanical Vibrations*, 5th ed., Pearson, Upper Saddle River, NJ.
- [4] Clough, R. W., and Penzien, J., 2003, *Dynamics of Structures*, 3rd ed., McGraw-Hill, New York.

Appendix

$$\omega_n \left[\frac{\text{rad}}{\text{sec}} \right] = \sqrt{\frac{3EI}{M_e l^3}} \left[\frac{\text{rad}}{\text{sec}} \right] = \sqrt{\frac{3(207 * 10^9 [\text{Pa}]) (1.619 * 10^{-11} [\text{m}^4])}{(0.23 * 0.140 [\text{kg}]) (0.223 [\text{m}])^3}} = 167.95 \left[\frac{\text{rad}}{\text{sec}} \right] \quad (11)$$

Table 4: Cantilever beam free vibration trace with *small* displacement.

Time (sec)	x _i (Peak amplitude) (Volts)	T _d (sec)	δ (log decrement)	ζ (damping ratio)	ω _n (natural frequency) (rad/s)
t ₁ =0.998	x ₁ =3.2318	T _{d1} =0.068	0.0420	0.0067	92.40
t ₂ =1.066	x ₂ =3.0988	T _{d2} =0.066	0.0010	0.0002	95.20
t ₃ =1.132	x ₃ =3.0957	T _{d3} =0.067	0.0363	0.0058	93.78
t ₄ =1.199	x ₄ =2.9854	T _{d4} =0.067	-0.0173	-0.0028	93.78
t ₅ =1.266	x ₅ =3.0376	T _{d5} =0.067	0.0478	0.0076	93.78
t ₆ =1.333	x ₆ =2.8957	-	-	-	-
Mean:	0.0670		0.0193	0.0035	93.79
Std deviation:	0.00071		0.0102	0.0045	0.99

Table 5: Cantilever beam free vibration trace with *large* displacement.

Time (sec)	x _i (Peak amplitude) (Volts)	T _d (sec)	δ (log decrement)	ζ (damping ratio)	ω _n (natural frequency) (rad/s)
t ₁ =0.556	x ₁ =18.2464	T _{d1} =0.066	0.0097	0.0015	95.20
t ₂ =0.622	x ₂ =18.0709	T _{d2} =0.067	0.0354	0.0056	93.78
t ₃ =0.689	x ₃ =17.4425	T _{d3} =0.067	0.0231	0.0037	93.78
t ₄ =0.756	x ₄ =17.0434	T _{d4} =0.068	0.0142	0.0023	92.40
t ₅ =0.824	x ₅ =16.8022	T _{d5} =0.067	0.0142	0.0023	93.78
t ₆ =0.891	x ₆ =16.5645	-	-	-	-
Mean:	0.0670		0.0193	0.0031	93.79
Std deviation:	0.00071		0.0102	0.0016	0.99

Table 6: Summary of found values.

Value	Units	<i>Small</i>	<i>Large</i>
ω_n	rad/sec	93.8	93.8
$\delta\omega_n$	rad/sec	1.2	1.2
ξ	n/a	0.0035	0.0031
$\delta\xi$	n/a	0.0056	0.0020
ω_d	rad/sec	93.8	93.8
$\delta\omega_d$	rad/sec	1.2	1.2

7. Solid Mechanics

Design and Analysis of a 2D Truss

MEEN 305-500 – Project 1

By Ian Wilhite, David Wood, Nick Licon, and Andres Pinzon

Introduction

In this project, we designed and analyzed a two-dimensional truss structure to determine an optimal layout with optimal cross-sectional geometry for each truss member to carry multiple point loads. To simplify our design process and analysis, we (1) generated truss designs with point loads applied exactly at joint locations, (2) assumed the weight of truss members to be negligible, and (3) assumed “smooth pins” at all truss member joints so that bending moments are neglected. These assumptions allowed us to treat each truss member as two-force members, either in tension or compression. Therefore, the only factors to consider when testing the structural integrity are the yield strength and critical buckling load.

The two-dimensional truss was required to fulfill the following specifications:

- Span a distance of 20 ft.
- Be made of A-36 steel.
- Support a 15-kip load at its center, a 10-kip load located 4 ft from one side, and a 5-kip load 4 ft from the other.
- Contain a minimum safety factor of 1.5 for all truss members under any potential failure mechanism (either yielding or buckling)
- For all truss members to have circular cross-sections

The first part of our design process was to brainstorm potential truss models. Each team member generated at least one unique truss design based on their analysis as seen in **Figures 1-5**. We then determined the minimal amount of mass required to satisfy the design constraints listed above for each truss design, accounting for failure due to either yielding or buckling. The design with the least amount of mass required to satisfy the design requirements was selected as the best model. Finally, we verified our results by calculating the individual factor of safety for each member of our final design, ensuring that they were all at least 1.5.

Truss Model

Individual Models:

As a part of the collaborative brainstorming process, multiple proposals were generated. They intended to take vastly different approaches to the problem to ensure a wide variety of possible solutions were considered. A common analysis process was then generated as a method to effectively determine the best model.

Method 1: Square Frame - Ian Wilhite

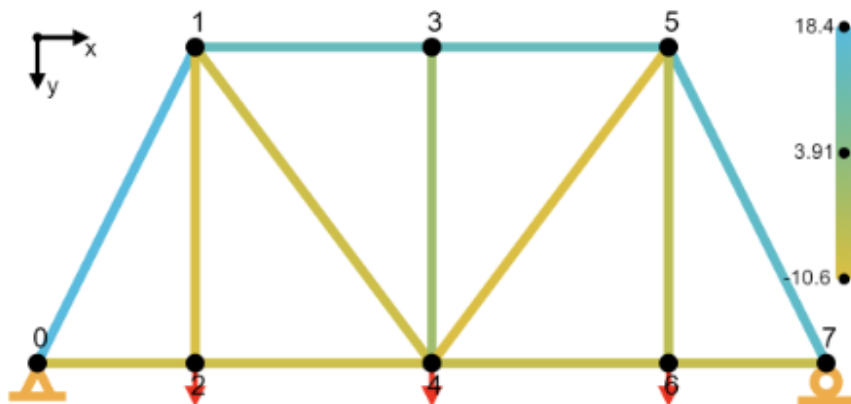


Figure 1. Visual analysis for square frame truss.

This method was intended to take inspiration from many train bridges across the country, and their very square or rectangular appearance by creating parallel beams and adding cross branches to support each segment. The segment widths were modified to allow for loading at the correct increments for analysis.

Method 2: Webbed Frame - David Wood

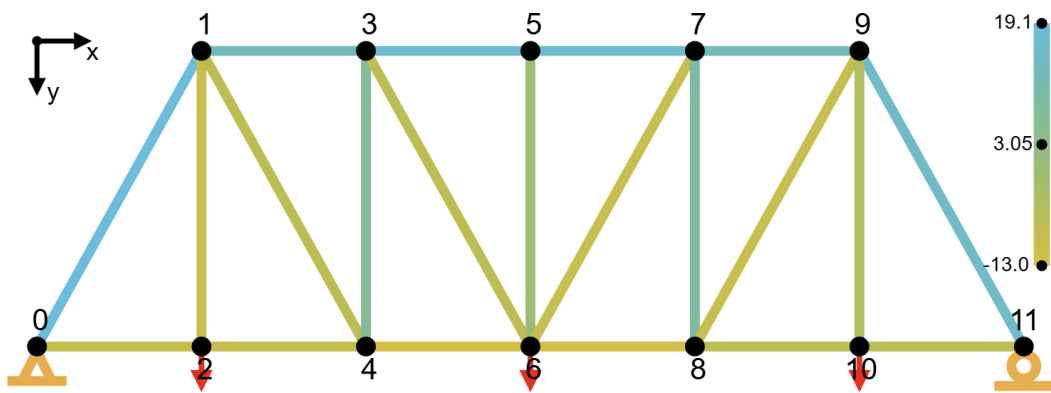


Figure 2. Visual analysis for webbed frame truss.

This model explored whether it would be worth increasing the number of webs in the truss to reduce the overall load for each truss member. While more webs correspond to more

needed material, making the bridge heavier, it also contains members significantly shorter in length. This makes them much more resilient to buckling or bending. However, the actual tensile/compressive stress exerted per member remained approximately the same, compared to this same bridge above with 1 web.

Method 3: Parabolic-inspired Frame - Nicholas Licon

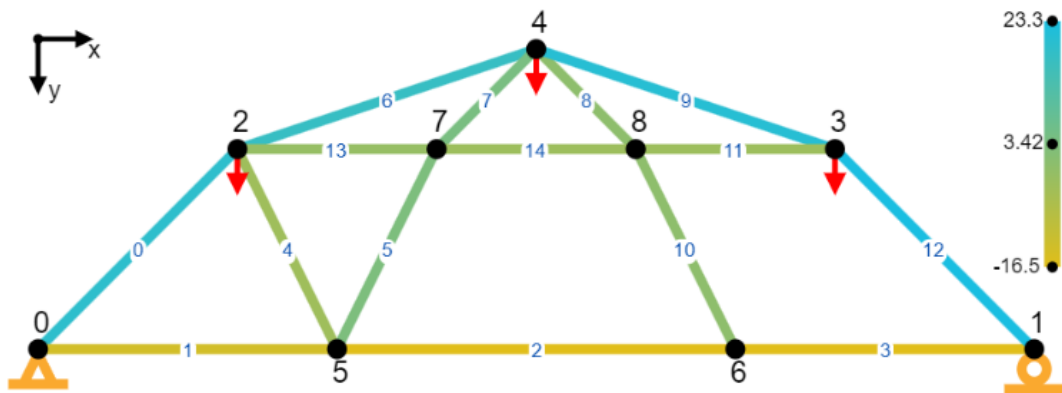


Figure 3. Visual analysis for the Parabolic-inspired Frame.

This shaped truss came from the idea that forces applied to a curved structure are often stronger than others. The shape of a “parabolic” structure distributes the load along the curve of the structure creating members of compression spaced out along the curve as shown with the blue two force members.

Method 4: Pentagonal Frame - Andres Pinzon

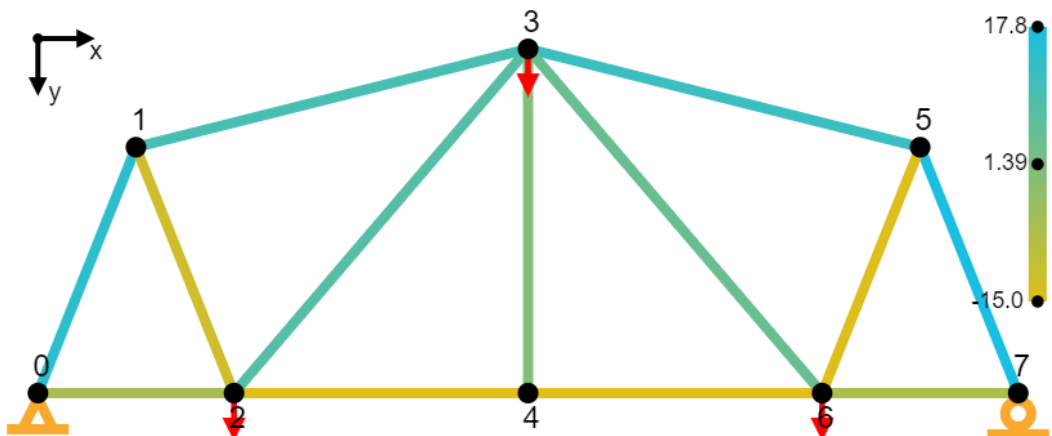


Figure 4. Visual analysis for pentagonal frame truss.

This model was created based on modifications to an already existing warren bridge. The main change is increasing the main member's height. This created a more pentagonal look

to the frame and it was noticeably stronger than a simple warren bridge model. The axial force each member sustained was minimized to keep each member's area from growing too much.

Method 5: Triangular Frame - Ian Wilhite

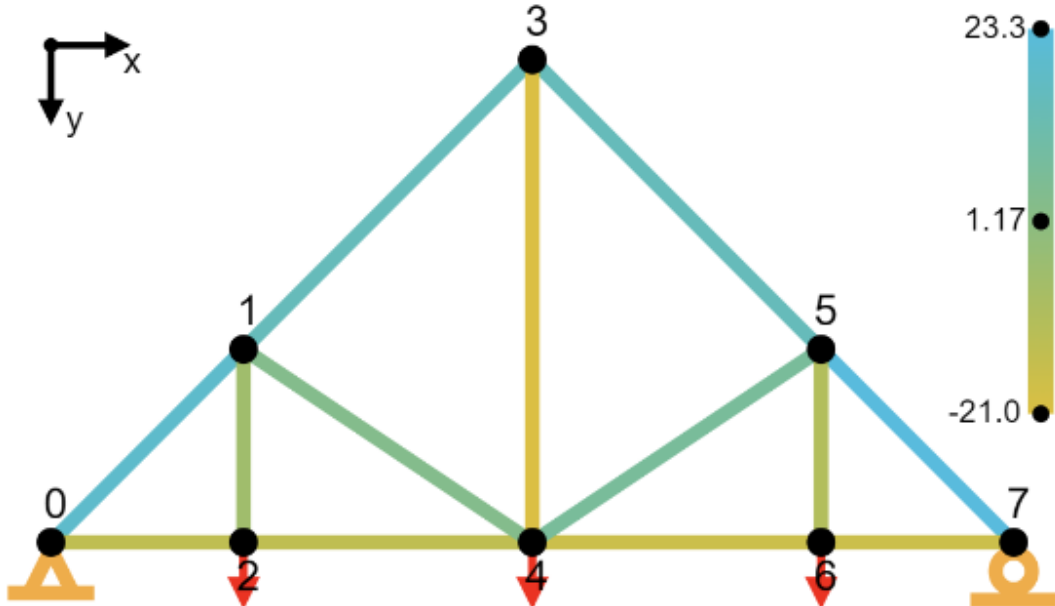


Figure 5. Visual analysis for triangular truss.

This model was meant to remain as simple as possible to theoretically take advantage of the roundup error in frames with many small beams all being rounded up to the nearest quarter inch. This resulted in a substantially weaker truss because the fewer members resulted in less optimal placement of each.

Chosen Model: Parabolic Inspired - Nicholas Licon

This model reduced the total volume of material needed to support the weight. This model leverages a proper balance between linkage placement and roundup radii to generate a truss that can effectively support the loading provided.

Justification of Choice

Each truss was analyzed to determine the total volume of material it would require. The total volume of each truss was then compared to determine the optimal design for the loading conditions.

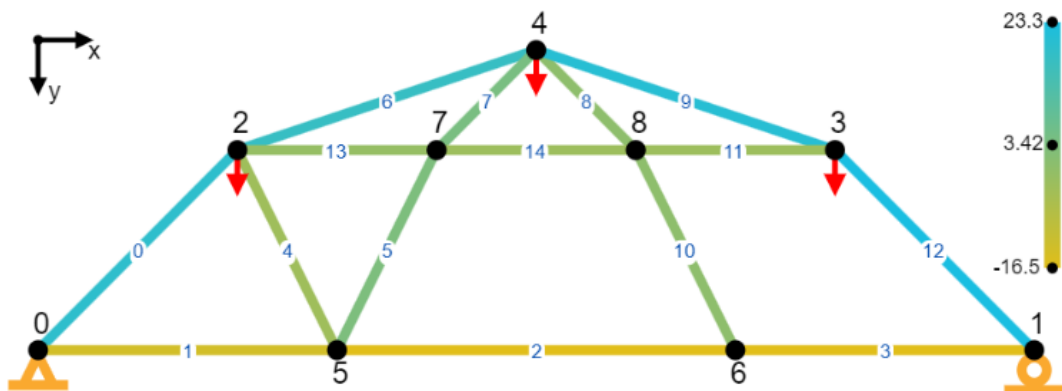
#	Name	Designer	Volume Required (in^3)	Weight Required (lb)
1	Square Frame	Ian Wilhite	2444.240	694.164
2	Webbed Frame	David Wood	1596.073	453.284
3	Parabolic Inspired	Nicholas Licon	1227.537	348.621
4	Pentagonal Frame	Andres Pinzon	2204.261	626.010
5	Triangular Frame	Ian Wilhite	3690.243	1048.029

Table 1. Comparison of bridge designs.

Analysis Process

Each truss presented was analyzed initially using an online calculator which performed the node forces for each truss and presented the forces per member given the loading conditions. These results were imported into a spreadsheet in which each truss could be compared to intake the force, safety factor, and failure stress, to output the total volume and weight of the truss.

Geometric Properties



Density of A-36 steel = 0.284 lb/in³

RED = Compression			BLUE = Tension		
Member	Length (in)	Area (in ²)	Volume (in ³)	Weight (lbs)	FOS
0	67.884	1.767	119.961	34.069	2.555
1	72	0.785	56.545	16.060	2.0943
2	96	0.785	75.398	21.413	1.714
3	72	0.785	56.549	16.060	1.714
4	53.664	0.196	10.537	2.992	2.108
5	53.664	1.227	65.856	18.703	3.551
6	75.9	3.142	238.447	67.719	2.244
7	33.936	0.785	26.653	7.570	2.875
8	33.936	0.0491	1.666	0.473	N/A
9	75.9	3.142	238.447	67.719	1.899
10	53.664	0.0491	2.634	0.748	N/A
11	48	0.196	9.425	2.677	2.356
12	67.884	2.405	163.280	46.372	2.091
13	48	0.196	9.425	2.677	4.712
14	48	0.196	9.425	2.677	2.356

Table 2. Analysis of parabolic inspired truss.

TOTAL VOLUME, TOTAL WEIGHT: 1227.537 in³, 348.621 lbs

Tasks and Responsibilities

Each member was expected to participate in group brainstorming, generate one truss design, and a brief description of their approach and inspiration for their truss. There was also a strong collaborative effort in gaining a fundamental understanding of the equations, simulation tools, and theory behind what constitutes a good truss.

Ian Wilhite - Ian was responsible for creating the spreadsheet to analyze the trusses, the framework of the report, the chosen model, and Tasks and Responsibilities.

Nicholas Licon - Nicholas was responsible for the Introduction.

Andres Pinzon Diaz - Andres was responsible for the geometric properties, excel appendix.

David Wood - David was responsible for the Introduction, and the generation of Geometric Properties for the selected truss.

Appendix

Matlab code for solving forces:

```
% Number of nodes and members
n_nodes = 9;
n_members = 15;

% Node coordinates (x, y)
nodes = [0, 0; 20, 0; 4, 4; 16, 4; 10, 6; 6, 0; 14, 0; 8, 4; 12, 4];
% External forces (Fx, Fy) at each node
forces = [0, 0; 0, 0; 0, -5; 0, -10; 0, -15; 0, 0; 0, 0; 0, 0; 0, 0];
% Connectivity matrix (start node, end node)
members = [0, 2; 0, 5; 5, 6; 6, 1; 2, 5; 7, 5; 2, 4; 4, 7; 4, 8; 4, 3; 6, 8; 3,
8; 3, 1; 2, 7; 7, 8] + 1;

% Initialize system of equations
n_eqs = 2 * n_nodes; % 2 equations (Fx and Fy) per node
A = zeros(n_eqs, n_members + 3); % Matrix of coefficients
b = zeros(n_eqs, 1); % Vector of constants
% Reaction forces (supports at nodes 0 and 1)
% Loop through each member and define equations based on equilibrium
for member_id = 1:n_members
    n1 = members(member_id, 1);
    n2 = members(member_id, 2);

    % Calculate direction cosines (l, m)
    dx = nodes(n2, 1) - nodes(n1, 1);
    dy = nodes(n2, 2) - nodes(n1, 2);
    L = sqrt(dx^2 + dy^2);
    l = dx / L;
    m = dy / L;

    % For node n1 (Fx and Fy)
    A(2*n1-1, member_id) = l; % Fx equation for node n1
    A(2*n1, member_id) = m; % Fy equation for node n1
```

```

% For node n2 (Fx and Fy)
A(2*n2-1, member_id) = -1; % Fx equation for node n2
A(2*n2, member_id) = -m; % Fy equation for node n2
end
A(1, n_members+1) = 1; A(2, n_members+2) = 1;
A(4, n_members+3) = 1;
for i = 1:n_nodes
    b(2*i-1) = forces(i, 1); % Fx
    b(2*i) = forces(i, 2); % Fy
end
% Solve for forces in each member and support reactions
disp(A);
disp(b);
x = A \ b;
% Display the results
forces_in_members = x(1:n_members);
reaction_forces = x(n_members+1:end);
disp('Forces in members (kips):');
disp(forces_in_members);
disp('Reaction forces (kips):');
disp(reaction_forces);

```

Output of MatLab code:

Forces in members (kips):

```

19.0919
-13.5000
-16.5000
-16.5000
-3.3541
3.3541
17.3925
4.2426
0.0000
20.5548
0.0000
-3.0000
23.3345
-1.5000
-3.0000

```

Reaction forces (kips):

```

0.0000
-13.5000
-16.5000

```

Truss visualization:

trussanalysis.com

Excel sheets used to calculate geometric properties:

2	Young's Modult A-36 Yield Strength			Factor of Safety					
3	29000		36000	1.5					
4				36					
6	A	B	C	D	E	F	H	I	J
7	Member ID	Start -> End Nod	Length (ft)	Axial Force (kips)	force * FoS	Area (in^2)	Radius - yield (in)	Moment of Inertia, I (lb Radius - gyration (in)	
8	0	0 → 2	5.657	19.09	28.635	0.7954166667	0.50	0.79	0.88
9	1	0 → 5	6	-13.5	-20.25	0.5625	0.42	0.05	0.00
10	2	5 → 6	8	-16.5	-24.75	0.6875	0.47	0.05	0.00
11	3	6 → 1	6	-16.5	-24.75	0.6875	0.47	0.05	0.00
12	4	2 → 5	4.472	-3.354	-5.031	0.13975	0.21	0.00	0.00
13	5	7 → 5	4.472	3.354	5.031	0.13975	0.21	0.12	0.50
14	6	2 → 4	6.325	17.39	26.085	0.7245833333	0.48	0.79	0.90
15	7	4 → 7	2.828	4.243	6.3645	0.1767916667	0.24	0.05	0.42
16	8	4 → 8	2.828	0	0	0	0.00	0.00	0.00
17	9	4 → 3	6.325	20.55	30.825	0.85625	0.52	0.79	0.94
18	10	6 → 8	4.472	0	0	0	0.00	0.00	0.00
19	11	3 → 8	4	-3	-4.5	0.125	0.20	0.00	0.00
20	12	3 → 1	5.657	23.33	34.995	0.9720833333	0.56	0.79	0.92
21	13	2 → 7	4	-1.5	-2.25	0.0625	0.14	0.00	0.00
22	14	7 → 8	4	-3	-4.5	0.125	0.20	0.00	0.00
2				Total Vol (in ^3) Total Mass (lb)					
3				1227.537		348.621			
6	K	L	M	N	O	P	Q	R	X
7	Radius - Failure (Radius to 1/8th (in)	Area(in^2)		Volume (in^3)	Weight (lb)	FOS t	Pcr	FOS c	FOS Consolidated
8	0.88	1.00	3.14	213.26	60.57	5.92	48.78	2.56	2.56
9	0.42	0.50	0.79	56.55	16.06	-2.09	2.71	0.00	2.09
10	0.47	0.50	0.79	75.40	21.41	-1.71	1.52	0.00	1.71
11	0.47	0.50	0.79	56.55	16.06	-1.71	2.71	0.00	1.71
12	0.21	0.25	0.20	10.54	2.99	-2.11	0.30	0.00	2.11
13	0.50	0.63	1.23	65.86	18.70	13.17	11.91	3.55	3.55
14	0.90	1.00	3.14	238.45	67.72	6.50	39.02	2.24	2.24
15	0.42	0.50	0.79	26.65	7.57	6.66	12.20	2.88	2.88
16	0.00	0.13	0.05	1.67	0.47 N/A		0.05	0.00	0.00
17	0.94	1.00	3.14	238.45	67.72	5.50	39.02	1.90	1.90
18	0.00	0.13	0.05	2.63	0.75 N/A		0.02	0.00	0.00
19	0.20	0.25	0.20	9.42	2.68	-2.36	0.38	0.00	2.36
20	0.92	1.00	3.14	213.26	60.57	4.85	48.78	2.09	2.09
21	0.14	0.25	0.20	9.42	2.68	-4.71	0.38	0.00	4.71
22	0.20	0.25	0.20	9.42	2.68	-2.36	0.38	0.00	2.36

Equations for Excel Columns:

Column	A	B	C
Equation	Member ID	Member Start->End	Length

Column	D	E	F
Equation	Axial Force (kips)	=D8*\$E\$3	=abs(E8*1000/\$C\$3)

Column	H	I	J
Equation	=sqrt(F8 / PI())	=PI()/4*L8^4	=if(D8>0, (E8*1000*C8*C8*12^2/(PI())^3*\$B\$3*1000*0.25))^(1/ 4),0)

Column	K	L	M
Equation	=max(J8,H8)	=floor(K8, 1/8) + 0.125	=pi()*L8^2

Column	N	O	P
Equation	=C8*pi()*L8^2*12	=N8*0.284	=\$C\$4/(D8/M8)

Column	Q	R	X
Equation	=(PI()^2 * 29000*I8) / (C8*12)^2	=if(D8>0,Q8/D8,0)	=if(P8<0,-P8,R8)

Meen 305 Project 2: Flower Petal Loadings

By David Wood, Nick Licon, Andres Pinzon, and Ian Wilhite

Section 1: Problem Summary

The client has a flower solar panel of 8 blades. The task provided was to design a truss and column structure that could support the mass of the blades and their loading during usage. The objective of this design is to minimize the mass of the column and truss with a given deflection while keeping reasonable factors of safety.

Section 2: Design Process

The column must not fail due to yielding/fracturing due to stresses, buckling due to applied load, or laterally deflect more than 0.3 in.

To get a radius that would create a maximum deflection of 0.3 in, Equations () were used. Then, the maximum stresses at critical points were calculated on either side of the column to make sure the column would not yield under the load. Additionally, the critical buckling load was calculated so that we could ensure the column would not buckle, since oftentimes a column will buckle before it yields under a compressive load.

There were a number of design constraints applied to ensure valid :

- Lateral deflection not to exceed 0.3 inches.
- Factor of safety on all calculated values of at least 2.
- Constant thickness of the column vertically (as opposed to varied thickness as a function of height) for ease of manufacturing and ability to use existing commercial products.
- Column may be hollow to allow for more efficient use of material.
- All column measurements must be in increments of $\frac{1}{4}$ inch for ease of manufacturing.

Failure due to Yielding:

The first thing we noticed for the column was the column would experience maximal stress when the solar panels were in the vertical (90°) position. This is because the sum of the panel components acts as a concentrated load 1 ft away from the column's central axis, generating a bending stress. Furthermore, the wind force, which is also modeled as concentrated load, is also highest when the panels are in the vertical position. If the wind force acts in the direction so that it hits the back of the panels, it will generate an additional bending moment and stress in the same direction. To illustrate this, three free body diagrams with different configurations are provided below to display our thought process and logically lead to the highest failure scenario for the column.

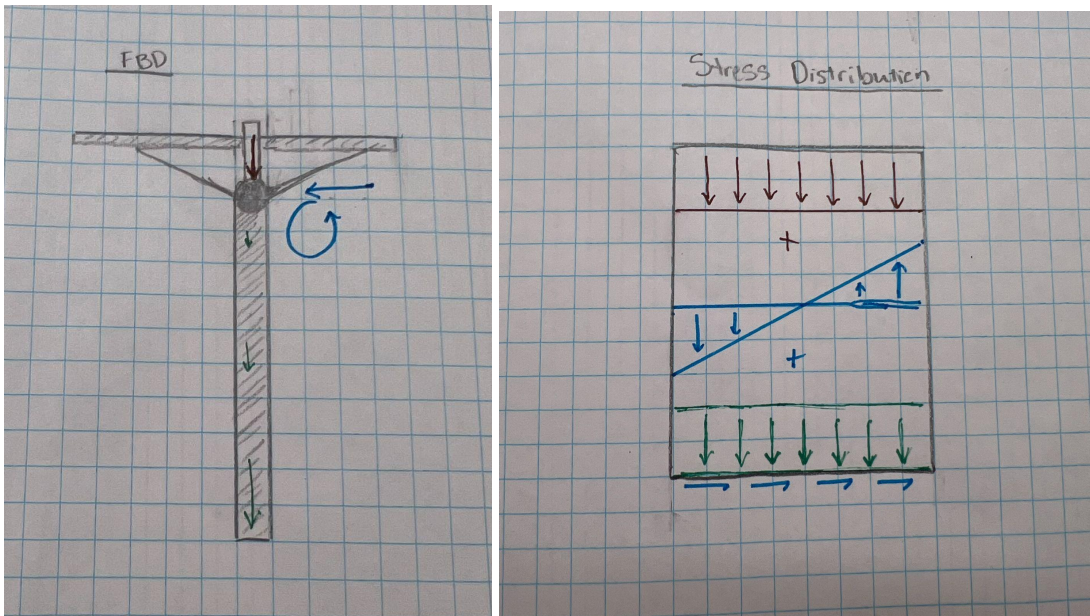


Figure 1. Force/Moment Diagram and Stress Distribution for Flat Position

In this configuration, there is no bending stress generated by the solar panels. Furthermore, the bending stress generated by the wind is smaller because the wind force data is provided and approximated at a lower value of 40 lbs. The column should not be designed to avoid failure under this scenario because there are other configurations that can generate much higher stresses. The same logic applied for the angled (45°) position. There is some bending stress generated by the weight of the solar panels, and the bending stress generated by the wind is also higher too (wind force modeled at 85 lbs), but they are both not as great as the vertical position.

A moment is calculated by multiplying the magnitude of a force and its perpendicular distance from an axis by which it revolves. In the case of the bending stress generated by the solar panels, the *radius* is maximal in the vertical position. For the bending stress generated by the wind, the *force* is maximal in the vertical position. Therefore, we decided to not design the column based on an angled configuration because, logically, there are other configurations that generate higher stresses.

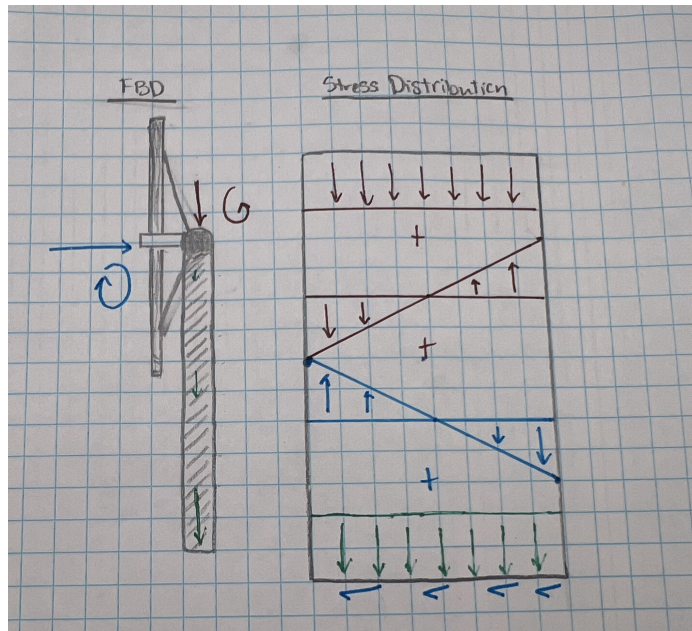


Figure 2. Force/Moment Diagram and Stress Distribution for Oncoming Wind

In this configuration, the bending moments generated by the weight of the solar panels and the wind partially offset each other because they are acting opposite in direction. As seen in **Figure 2**, on the left side of the column, the solar panels generate a maximum compressive stress, while the wind force generates a maximum tensile stress. On the right side of the column, the solar panels generate a tensile stress and the wind force generates a compressive stress. Regardless of where, the bending stresses are always cancelling each other out to some degree.

The last consideration is where the force is applied on the back side of the panels. This would generate much higher stresses because the bending moments would be acting in the same direction, with maximum compression on the left side and maximum tension on the right, as you can see below:

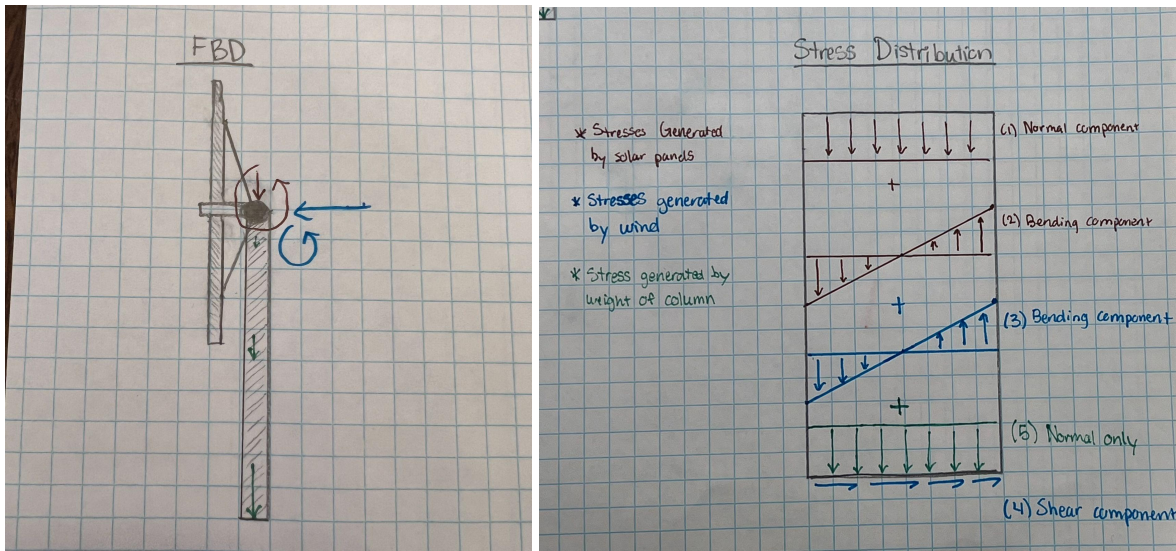


Figure 3. Force/Moment Diagram and Stress Distribution of Highest Failure Scenario

This is the configuration for the column by which the most stress is generated, and the one we need to design around. As you can see, the weight of the solar panels generates a stress that has both normal and bending components, while the wind force generates a stress that has shear and bending components. The weight of the column itself generates stress too, but unlike the other stresses, it varies with the length of the column. The normal stress due to the weight of the column is maximal at the bottom and zero at the top of the column.

The normal stress components have a uniform distribution, meaning that the magnitude and direction of the stress is constant at any individual location within the column's cross-section. Bending stresses, on the other hand, have a linear distribution based on the distance it is from the central axis of the column. The magnitude of this stress is the same in either direction from the center but opposite in direction, depending on whether you are closer or further away from where the moment-inducing force is being applied. On the left side, it generates a maximum compressive stress, while on the right it generates a maximum tensile stress.

The formulas used to calculate all stresses exerted on the column are summarized below:

<u>Normal Stress</u>	<u>Shear Stress</u>	<u>Bending Stress</u>	<u>Torsional Stress</u>
$\sigma = \frac{P}{A}$	$\tau = \frac{VQ}{It}$	$\sigma = -\frac{My}{I}$	$\tau = \frac{T\rho}{J}$

Brittle Materials

Brittle materials have different strengths in the tensile and compressive directions, being much stronger in compression than tension. This rules out our ability to use the **maximum normal stress theory**, which is derived based on the assumption that the material is equally

strong in compressive/tensile directions. Instead, we will find the locations in the column where stress is maximum in either compressive or tensile directions, and compare them to the compressive/tensile stresses provided for each material.

We determined that there are two locations on the beam where failure is most likely to occur. Referencing the two-dimensional stress distribution layout in **Figure 3**, these points would be the lower left-hand corner and the upper-right hand corner. As the lower left location, the column is under **maximal compressive stress**. The compressive stresses add upon each other, and, due to the nature of each distribution, they accumulate to a maximum at this location. In the upper right location, the column is potentially under **maximal tensile stress**.

NOTE: The word “potentially” is used because the downward normal components acting on the right side of the column may be greater in magnitude than the upward components due to bending, but this is highly unlikely.

Ductile Materials

There is no data given on compressive/tensile strengths for the ductile materials. This is likely because yielding in ductile materials is dominated by shear mechanisms, and they are not super direction-dependent. Therefore, we will assume that the ductile materials are equally strong in compressive/tensile directions and use the **maximum shear stress theory** (or Tresca criterion) to determine if it will yield under compressive loads. Note that the magnitude of maximum compression at a location will be greater than the maximum tension at another. The yield strength is estimated based on the formula:

$$\tau_{\text{abs max}} = \frac{\sigma_1 - \sigma_2}{2} = \frac{\sigma_y}{2}$$

The shear stress generated by the wind is neglected because it is relatively small (see **Appendix B.3**), so there is no need to determine the principal stresses. The maximum stress will simply be the lower-left corner (see **Figure 3**) where it is under maximum compression.

Failure Due to Buckling

Buckling also had to be taken into consideration as the weight of the column could cause it to fail on itself. This occurs when the forces acting on the column overcome its ability to resist bending, and this depends on its stiffness (bending rigidity, EI), how it's supported, and its length. In this case, with a fixed-free setup, the column's weight itself can create enough stress to make it buckle when it reaches a critical value. It's like a battle between the column's rigidity and the load trying to push it into instability.

$$W_c = 7.84 \frac{EI}{L^2}$$

This critical weight required to maintain the integrity of the column did not make much of an impact in the end. Since we were minimizing the weight of the column, our results yielded values that were much lower. Nonetheless, these calculations are important to make as they ensure this specific part of the design is secure and it adds an extra layer of credibility to our final design.

Minimizing Lateral Deflection to less than 0.3 inches

To make sure the column did not deflect more than 0.3 inches there were two scenarios that had to be considered. First we were tasked with finding the most suitable design without any wind forces, so the only thing causing the column to deflect was the bending moment caused by the blades.

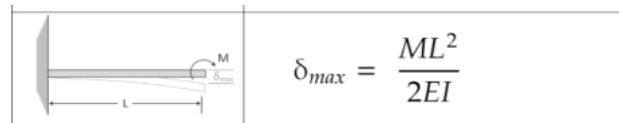


Figure 4. Deflection due to bending stress

Due to this bending effect, the lateral deflection of the column was found using the equation seen in **Figure 4**. A design was then optimized to have a FOS that was less than 2.

Once wind was taken into consideration, another deflection was required to be calculated. This time the column was going to be deflected due to a force that pushes sideways and would make the column bow out over its length.

Beam and load cases	Maximum Beam Deflection
<p>A diagram of a horizontal beam of length L. A downward force P is applied at the center of the beam, causing it to bow upwards. A coordinate system is shown at the left end with the origin at the point of zero deflection.</p>	$\delta_{max} = \frac{PL^3}{3EI}$

Figure 5. Deflection due to Force

With a new input causing a deflection on the column by the amount seen in the equation in **Figure 5**, our FOS changed from our minimum of 2 down to less than 1 for our chosen model. This would mean that the column would deflect more than the expected 3 inches. A new inner and outer radius were constructed to make sure that the sum of the deflections caused by both the wind and the bending would not exceed 3 inches.

Column Conclusions

For the column, it was clear that limiting the deflection to 0.3 inches was the primary limiting factor for design optimization. Calculations of failure due to buckling or yielding/fracturing did not even come close to their determined limits.

Section 2.2 Design Considerations for Truss:

The Truss must not fail due to buckling or normal stress under the load of the panel and must pass with a factor of safety greater than 2. The analysis of the truss problem is a statically indeterminate problem. Connected to a rigid wall there are 3 unknowns due to the cantilever beam-like properties it will have. Additionally, the force of the truss acts upward three feet from the wall. This means that we must use analysis of beam deflection to determine the fourth equation to solve for all four unknowns. To solve the beam deflection problem we will assume the compatibility to be no deflection at the end of the panel meaning that at what the truss is supporting the weight the displacement is 0 ($L=3$, $v = 0$).

Once the force acting on the truss is found a test for both brittle materials and ductile materials will be performed as well as for what the radius of the cylindrical solid truss should be.

Position one of the flowers allows us to ignore the truss in that position due to the compatibility of the orientation and the bar. With the weight going straight down the only compatibility for the panel that we know is that the displacement of the bar in the x direction is zero, meaning that the truss can exert any force upon the panel in that position leading no force to be placed on the truss in this position.

$$\text{Volume} = \text{Area} * \text{length}$$

$$\text{Density(lbs/in}^3\text{)} = \text{Density(lbs/ft}^3\text{)} / (12^3)$$

Material	Minimum radius	Volume	Weight
Gray cast iron 30	0.220in	5.7699in ³	1.402lbs
Gray cast iron 60	0.205in	5.01in ³	1.450lbs
Stainless steel 304	0.189in	4.258in ³	0.4189lbs
Aluminum Alloy	0.243in	7.0395in ³	0.387lbs

Table 1. Evaluation of Truss

Aluminum Alloy gives the same amount of support as the others for the minimized weight of the truss making it the best material to use for our given case.

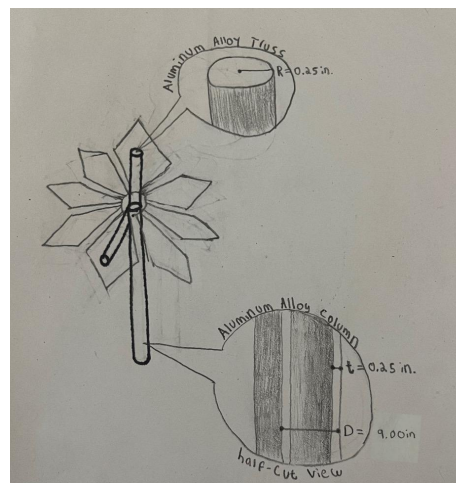


Figure 6. Sketch of Truss6

Section 3: Results

Section 3.1 Calculated Values

Parameter	Value
Maximum Lateral Deflection	0.3 [in]
Flower Weight	40 [lbs]
Column Height	10 [ft]
Number of Flowers	8
Minimum Factor of Safety	2
End condition factor	0.25

Table 2. Assumed parameters

Material	Material Type	Inner Radius (in)	Outer Radius (in)	Density (lb/ft^3)	Mass (lb)	FOS
Cast Iron 30	Brittle	3.75	4	420	177.5	2.127
Cast Iron 60	Brittle	3.5	3.75	500	197.7	2.322
Stainless steel 304	Ductile	3.00	3.25	170	58.0	2.047
Aluminum Alloy	Ductile	4.25	4.50	95	45.3	2.071

Table 3. Evaluation of Column

Section 3.1 Final Recommendations

Section	Material	Mass (lb)
Truss	Aluminum	0.387
Column	Aluminum	45.3
Total		45.7

Table 4. Chosen Masses

To minimize weight, both parts should be made of the aluminum alloy option, and the total structure will have a total weight of 45.7 lbs.

Conclusion

For the column, it was clear that limiting the deflection was the primary limiting factor for design optimization. Calculations of failure due to buckling or yielding/fracturing did not even come close to their determined limits. It could be inferred that in future analysis, this limit could be revisited as a design constraint. For the truss, the main limiting design factor was critical buckling load. The designs proposed meet the specified design constraints, and would perform as expected if constructed. Next steps for the project could include verification of calculated values via simulation, or scale tests to ensure the assumptions provided hold true. The design implemented effectively minimizes the weight of the material of the structure, minimizing the error from excluding their weight while calculating stresses.

Section 4: Member Contributions

The following is a summary of the contributions each member provided to the generation of the design and report presented:

- David Wood: David worked on developing the calculator for the column, specifically for the brittle materials. He also evaluated the columns compressive and tensile strength, and took the lead on debugging the calculator.
- Nick Licon: Nick developed the calculator for the truss for both ductile and brittle materials. He also introduced many of the analysis techniques that were crucial to evaluating the column.
- Andres Pinzon Diaz: Andres primarily worked on understanding the column buckling equations and their applications, then their implementation in the column.
- Ian Wilhite: Ian worked on developing the calculator for the column, specifically for the ductile materials. He also worked on preliminary reporting and approach structure.

Appendix

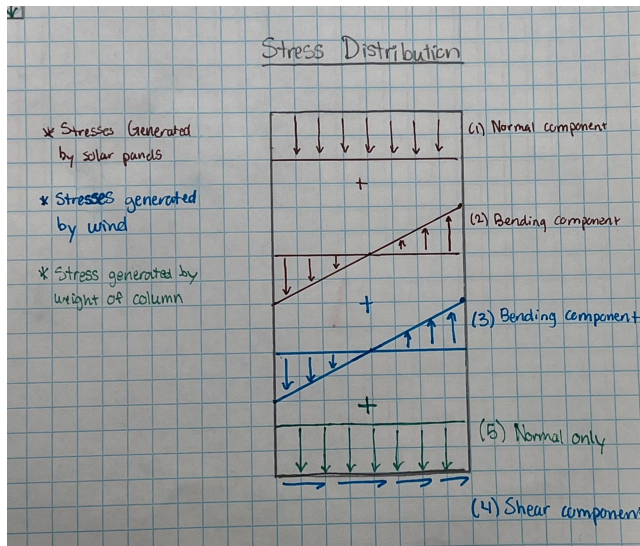
A. Tables

Table 1 Material Properties

Material	Density (lb/ft ³)	Elastic Modulus (ksi)	Tensile Yield Stress (ksi)	Tensile Ultimate Stress (ksi)	Compressive Ultimate Stress (ksi)	Shear Yield or Ultimate Stress (ksi)
Gray cast iron 30	420	15000		30	100	15
Gray cast iron 60	500	20000		60	180	30
Stainless steel 304	170	27500	40			20
Aluminum Alloy	95	10150	43			20

B. Calculations

B.1 Column Stress Analysis and Dimensional Optimization of Brittle Material Options



- Max compressive stress (lower left corner) = $\sigma_{\text{panels, normal}} + \sigma_{\text{panels, bending}} + \sigma_{\text{wind, bending}} + \sigma_{\text{column weight}}$
- Max Tensile Stress (upper right corner) = $\sigma_{\text{panels, normal}} + \sigma_{\text{panels, bending}} + \sigma_{\text{wind, bending}}$

SIGN CONVENTION: Negative sign is used for compression; positive sign is used for tension. So stresses must be greater than the maximum (negative) compressive stress, and less than the maximum (positive) tensile stress

$$\sigma_{\max, \text{compression}} = -\frac{(320 \text{ lbs})}{\pi(r_o^2 - r_i^2)} - \frac{(320 \text{ ft-lbs}) \cdot r_o}{\frac{\pi}{4}(r_o^4 - r_i^4)} - \frac{(120 \text{ lbs} \cdot 120 \text{ in}) \cdot r_o}{\frac{\pi}{4}(r_o^4 - r_i^4)} - \frac{\rho \cdot \pi(r_o^2 - r_i^2)(120 \text{ in}) \cdot g}{\pi(r_o^2 - r_i^2)}$$

$$\sigma_{\max, \text{tension}} = -\frac{(320 \text{ lbs})}{\pi(r_o^2 - r_i^2)} + \frac{(320 \text{ ft-lbs}) \cdot r_o}{\frac{\pi}{4}(r_o^4 - r_i^4)} + \frac{(120 \text{ lbs} \cdot 120 \text{ in}) \cdot r_o}{\frac{\pi}{4}(r_o^4 - r_i^4)}$$

Gray Cast Iron 30: $r_o = 4.0 \text{ in}$, $r_i = 3.75 \text{ in}$

$$\begin{aligned} \sigma_{\max, \text{compression}} &= -\frac{(320 \text{ lbs})}{\pi(4^2 - 3.75^2)} - \frac{(320 \text{ ft-lbs}) \cdot 4}{\frac{\pi}{4}(4^4 - 3.75^4)} - \frac{(120 \text{ lbs} \cdot 120 \text{ in}) \cdot 4}{\frac{\pi}{4}(4^4 - 3.75^4)} - \frac{0.243 \cdot \pi(4^2 - 3.75^2)(120 \text{ in}) \cdot 32.2}{\pi(4^2 - 3.75^2)} \\ &= -2.586619605 \text{ ksi} > -100 \text{ ksi}; \text{ well within failure limit} \end{aligned}$$

*The density was converted to lbs/in³

$$\begin{aligned}\sigma_{max, tension} &= -\frac{(320 \text{ lbs})}{\pi(4^2 - 3.75^2)} + \frac{(320 \text{ ft-lbs}) \cdot 4}{\frac{\pi}{4}(4^4 - 3.75^4)} + \frac{(120 \text{ lbs} \cdot 120 \text{ in}) \cdot 4}{\frac{\pi}{4}(4^4 - 3.75^4)} \\ &= \mathbf{1.542307995 \text{ ksi} < 30 \text{ ksi}; \text{ well within failure limit}}$$

Gray Cast Iron 60: $r_o = 3.75 \text{ in}$, $r_i = 3.50 \text{ in}$

$$\begin{aligned}\sigma_{max, compression} &= -\frac{(320 \text{ lbs})}{\pi(3.75^2 - 3.5^2)} - \frac{(320 \text{ ft-lbs}) \cdot 3.75}{\frac{\pi}{4}(3.75^4 - 3.5^4)} - \frac{(120 \text{ lbs} \cdot 120 \text{ in}) \cdot 3.75}{\frac{\pi}{4}(3.75^4 - 3.5^4)} - \frac{0.289 \cdot \pi(3.75^2 - 3.5^2)(120 \text{ in}) \cdot 32.2}{\pi(3.75^2 - 3.5^2)} \\ &= \mathbf{-3.000360171 \text{ ksi} > -180 \text{ ksi}; \text{ well within failure limit}} \\ \sigma_{max, tension} &= -\frac{(320 \text{ lbs})}{\pi(4^2 - 3.75^2)} + \frac{(320 \text{ ft-lbs}) \cdot 4}{\frac{\pi}{4}(4^4 - 3.75^4)} + \frac{(120 \text{ lbs} \cdot 120 \text{ in}) \cdot 4}{\frac{\pi}{4}(4^4 - 3.75^4)} \\ &= \mathbf{1.769908297 \text{ ksi} < 60 \text{ ksi}; \text{ well within failure limit}}$$

B.2 Column Stress Analysis and Dimensional Optimization of Ductile Material Options

- Stress, is any direction, must be less than $\sigma_{yield} = 2 * T_{ultimate}$, per Tresca criterion. $\sigma_{yield} = 2 * 20 \text{ ksi}$ (for both ductile materials) = **40 ksi**.
- The maximum stress in compression will always be greater than the maximum stress in tension, so there is no need to calculate maximum tension.

Stainless Steel 304: $r_o = 3.25 \text{ in}$, $r_i = 3.0 \text{ in}$

$$\begin{aligned}\sigma_{max, compression} &= -\frac{(320 \text{ lbs})}{\pi(3.25^2 - 3^2)} - \frac{(320 \text{ ft-lbs}) \cdot 3.25}{\frac{\pi}{4}(3.25^4 - 3^4)} - \frac{(120 \text{ lbs} \cdot 120 \text{ in}) \cdot 3.25}{\frac{\pi}{4}(3.25^4 - 3^4)} - \frac{0.0984 \cdot \pi(3.25^2 - 3^2)(120 \text{ in}) \cdot 32.2}{\pi(3.25^2 - 3^2)} \\ &= \mathbf{-2.914629187 \text{ ksi} > -40 \text{ ksi}; \text{ well within failure limit}}$$

*The density was converted to lbs/in³

Aluminum Alloy: $r_o = 4.5 \text{ in}$, $r_i = 4.25 \text{ in}$

$$\begin{aligned}\sigma_{max, compression} &= -\frac{(320 \text{ lbs})}{\pi(4.5^2 - 4.25^2)} - \frac{(320 \text{ ft-lbs}) \cdot 4.5}{\frac{\pi}{4}(4.5^4 - 4.25^4)} - \frac{(120 \text{ lbs} \cdot 120 \text{ in}) \cdot 4.5}{\frac{\pi}{4}(4.5^4 - 4.25^4)} - \frac{0.0549 \cdot \pi(4.5^2 - 4.25^2)(120 \text{ in}) \cdot 32.2}{\pi(4.5^2 - 4.25^2)} \\ &= \mathbf{-1.505973093 > -40 \text{ ksi}; \text{ well within failure limit}}$$

*The density was converted to lbs/in³

B.3 Calculations for Shear Stress in Column (why it's neglected)

The shear stress for the cast iron 30 was determined using the formula:

$$\tau_{wind} = \frac{V_{wind} \cdot Q}{It} = \frac{120 \text{ lbs} \cdot \frac{2}{3}(r_o^3 - r_i^3)}{\frac{\pi}{4}(r_o^4 - r_i^4) \cdot 2r_o} = \mathbf{0.001939119528 \text{ ksi.}}$$

Since it was so small, we decided to exempt it in our stress analysis for simplicity.

B.4 Calculations for deflection

$$M = n * w * 1ft * \sin\theta$$

Where n is the number of petals, w is the weight of each, and theta is the angle it makes with the x axis

$$M_{90^\circ} = 3840 \text{ lbm*in}$$

$$\delta_{max} = \frac{ML^2}{2EI}$$

$$\delta_{max} = \frac{PL^3}{3EI}$$

Gray Cast Iron 30: $r_0 = 4.0 \text{ in}$, $r_i = 3.75 \text{ in}$

$$\delta_{max} = \frac{3840*120^2}{2*15000*45.74} = 0.0403 \text{ in}$$

+ wind

$$\delta_{max} = \frac{120*120^3}{3*15000*45.74} = 0.101 \text{ in}$$

$$= 0.141 \text{ in}$$

Gray Cast Iron 60: $r_0 = 3.75 \text{ in}$, $r_i = 3.5 \text{ in}$

$$\delta_{max} = \frac{3840*120^2}{2*20000*37.46} = 0.0369 \text{ in}$$

+ wind

$$\delta_{max} = \frac{120*120^3}{3*20000*37.46} = 0.0922 \text{ in}$$

$$= 0.129 \text{ in}$$

Stainless Steel 304: $r_0 = 3.25 \text{ in}$, $r_i = 3.0 \text{ in}$

$$\delta_{max} = \frac{3840*120^2}{2*27500*24.01} = 0.0419 \text{ in}$$

+ wind

$$\delta_{max} = \frac{120*120^3}{3*27500*24.01} = 0.105 \text{ in}$$

$$= 0.147 \text{ in}$$

Aluminum Alloy: $r_0 = 4.5 \text{ in}$, $r_i = 4.25 \text{ in}$

$$\delta_{max} = \frac{3840*120^2}{2*10150*65.82} = 0.0413 \text{ in}$$

+ wind

$$\delta_{max} = \frac{120*120^3}{3*10150*85.82} = 0.103 \text{ in}$$

$$= 0.145 \text{ in}$$

*All below the max deflection that would give us a FOS of 2 (0.15in)

B.5 Calculations for buckling

$$W_c = 7.84 \frac{EI}{L^2}$$

Gray Cast Iron 30: $r_0 = 4.0 \text{ in}$, $r_i = 3.75 \text{ in}$

$$= 407898 \text{ lb}$$

$$W_c = 7.84 \frac{15000*45.7}{120^2}$$

$$= 373217 \text{ lb}$$

Gray Cast Iron 60: $r_0 = 4.0 \text{ in}$, $r_i = 3.75 \text{ in}$

$$W_c = 7.84 \frac{20000*37.46}{120^2}$$

Stainless Steel 304: $r_0 = 3.25 \text{ in}$, $r_i = 3.0 \text{ in}$

$$W_c = 7.84 \frac{27500*24.01}{120^2}$$

$$= 359483 \text{ lb}$$

Aluminum Alloy: $r_0 = 4.5 \text{ in}$, $r_i = 4.25 \text{ in}$

$$W_c = 7.84 \frac{10150*65.82}{120^2}$$

$$= 363729 \text{ lb}$$

B.6 Truss Calculations

Use superposition to derive an expression for displacement of the cantilever beam.

Total deflection

| |
Weight of the bar

$$v = \frac{-PL^2}{48EI} (6x - L) \quad L/2 \leq x \leq L$$

+

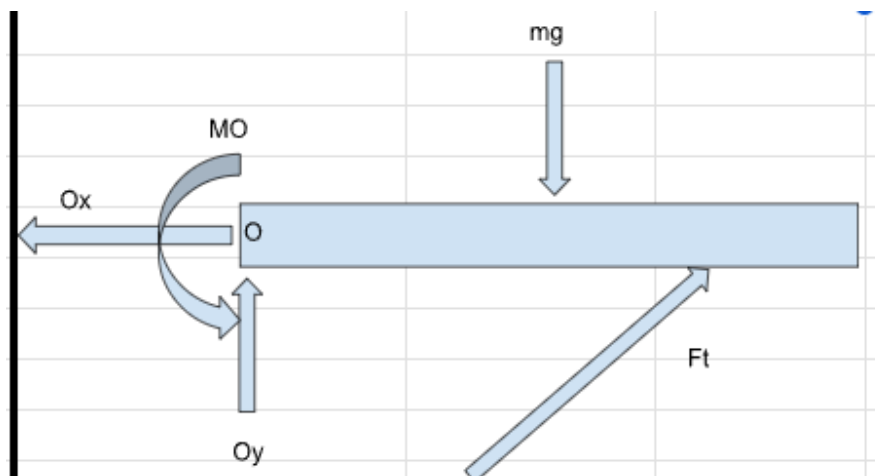
Force of the truss acting upward

$$y = \frac{Px^2}{6EI} (3a - x) \quad \text{for } 0 < x < a$$

$$L = 60 \text{ in}, x = 36 \text{ in}, a = 36 \text{ in}$$

Find highest force on truss in all three positions:

Ideal position:



Knowns: $mg = 40 \text{ lbs}$, $EI = 145000 \text{ kip/in}^2$

Unknowns: Ox , Oy , Mo , Ft

Compatibility: At $x = 36$; $v = 0$ (where the truss connects)

$$\Sigma F_x = 0 = Ox + Ft \cos(18.434)$$

$$\Sigma F_y = 0 = Oy + Ft \sin(18.434) - mg$$

$$\Sigma Mo = 0 = Mo + Ft \sin(18.434) \cdot 36 \text{ in} - mg \cdot 30 \text{ in}$$

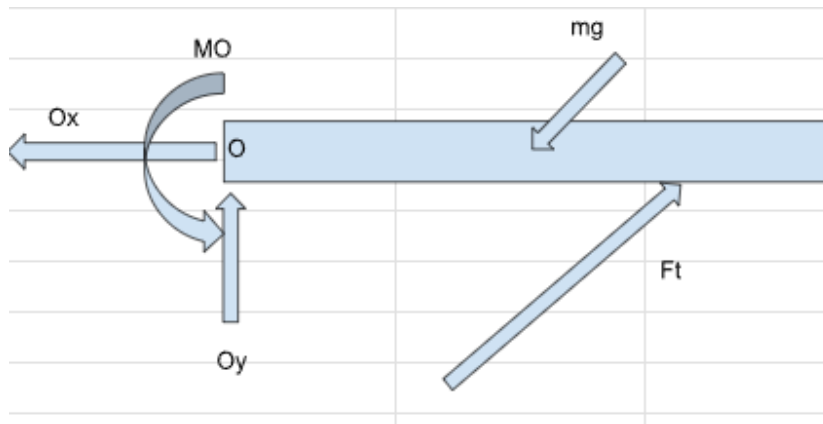
$$v = \frac{1}{EI} \left(\frac{mg \cdot (60in)^2}{48} (6 \cdot 36in - 60in) - \frac{Ftsin(18.434) \cdot (36in)^2}{6} (3 \cdot 36in - 36in) \right)$$

Find Ft with v = 0

$$0 = \left(\frac{(40) \cdot (60in)^2}{48} (6 \cdot 36in - 60in) - \frac{Ftsin(18.434) \cdot (36in)^2}{6} (3 \cdot 36in - 36in) \right)$$

$$Ft = \frac{\frac{(40) \cdot (60in)^2}{48} (6 \cdot 36in - 60in)}{\frac{\sin(18.434) \cdot (36in)^2}{6} (3 \cdot 36in - 36in)} = 95.161 \text{ lbs}$$

Top side of position 2:



Knowns: $mg = 40 \text{ lbs}$, $EI = 145000 \text{ kip/in}^2$

Unknowns : Ox , Oy , Mo , Ft

Compatibility: At $x = 36$; $v = 0$ (where the truss connects)

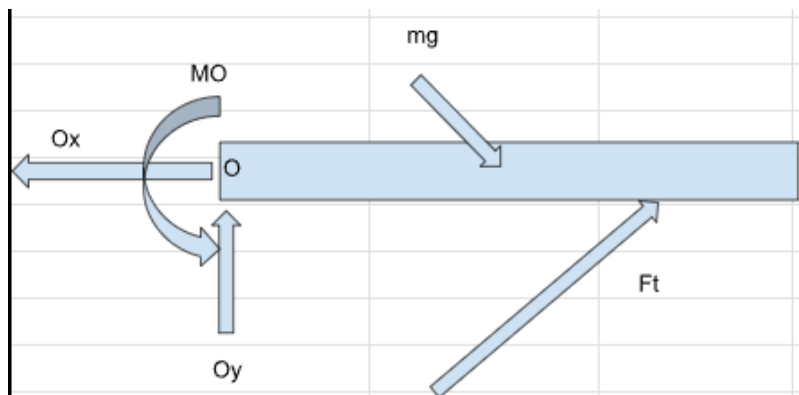
$$\Sigma Fx = 0 = Ox + Ft \cos(18.434) - mg \cos(45)$$

$$\Sigma Fy = 0 = Oy + Ft \sin(18.434) - mg \sin(45)$$

$$\Sigma Mo = 0 = Mo + Ft \sin(18.434) \cdot 36in - mg \sin(45) \cdot 30in$$

$$v = \frac{1}{EI} \left(\frac{mg \sin(45) \cdot (60in)^2}{48} (6 \cdot 36in - 60in) - \frac{Ftsin(18.434) \cdot (3in)^2}{6} (3 \cdot 36in - 36in) \right)$$

Bottom side of position 2



Knowns: $mg = 40\text{lbs}$, $EI = 145000 \text{ kip/in}^2$

Unknowns : Ox , Oy , Mo , Ft

Compatibility: At $x = 36$; $v = 0$ (where the truss connects)

$$\Sigma F_x = 0 = Ox + Ft \cos(18.434) + mg \cos(45)$$

$$\Sigma F_y = 0 = Oy + Ft \sin(18.434) - mg \sin(45)$$

$$\Sigma Mo = 0 = Mo + Ft \sin(18.434) \cdot 36in - mg \sin(45) \cdot 30in$$

$$v = \frac{1}{EI} \left(\frac{mg \sin(45) \cdot (6in)^2}{48} (6 \cdot 36in - 60in) - \frac{Ft \sin(18.434) \cdot (3in)^2}{6} (3 \cdot 36in - 36in) \right)$$

V equation same for both to find Ft

Find Ft with $v = 0$

$$0 = \left(\frac{(40 \sin(45)) \cdot (60in)^2}{48} (6 \cdot 36in - 60in) - \frac{Ft \sin(18.434) \cdot (3in)^2}{6} (3 \cdot 36in - 36in) \right)$$

$$Ft = \frac{\frac{(40 \sin(45)) \cdot (60in)^2}{48} (6 \cdot 36in - 60in)}{\frac{\sin(18.434) \cdot (3in)^2}{6} (3 \cdot 36in - 36in)} = 67.289 \text{ lbs}$$

Vertical position



Knowns: $mg = 40\text{lbs}$, $EI = 145000 \text{ kip/in}^2$

Unknowns: Ox , Oy , Mo , Ft

Compatibility: At $x = 36\text{in}$; $v = 0$ (where the truss connects)

$$\Sigma F_x = 0 = Ox + Ft \cos(18.434) + mg$$

$$\Sigma F_y = 0 = Oy + Ft \sin(18.434)$$

$$\Sigma Mo = 0 = Mo + Ft \sin(18.434) \cdot 36 \text{ in}$$

$$v = \frac{1}{EI} \left(- \frac{Ft \sin(18.434) \cdot (3in)^2}{6} (3 \cdot 36in - 36) \right)$$

When $v = 0$

$$0 = \frac{1}{EI} \left(- \frac{Ft \sin(18.434) \cdot 36^2}{6} (3 \cdot 36 - 36) \right)$$

Ft must be 0

Since position 3 has the most force on it it will fail first so we will test materials and design in that orientation

$$F_t = 95.161 \text{ lbs}$$

Calculate radius of the truss for the force applied with all 4 materials

$$P_{cr} = \frac{\pi^2 EI}{L^2}$$

$$\sigma = \frac{P}{A}$$

$$A = \pi r^2$$

$$L = 3.162 \text{ ft} = 37.947 \text{ in}$$

$$P_{cr} = F * F.O.S$$

$$P_{cr} = \frac{\pi \cdot (EI)}{(L)^2}$$

$$I = \frac{\pi r^4}{4}$$

Brittle:

Gray cast iron 30

$$EI = 15000 \text{ ksi}$$

$$I = \frac{\pi r^4}{4}$$

$$\sigma_{ult} = 100 \text{ ksi}$$

$$\sigma_{allow} = 50 \text{ ksi}$$

$$\sigma_{allow} = F / \pi r^2$$

$$r = \sqrt{\frac{95.161 \text{ lbs}}{50000 \text{ lbs/in}^2 \cdot \pi}} = 0.0246 \text{ in}$$

$$P_{cr} = F * F.O.S = 190.322 \text{ lbs}$$

$$P_{cr} = \frac{\pi \cdot (EI)}{(L)^2}$$

$$P_{cr} = \frac{\pi \cdot (15000000 \text{ lbs/in}^2 \cdot \frac{\pi r^4}{4})}{(37.947 \text{ in})^2}$$

$$r = \sqrt[4]{\frac{4 \cdot (37.947 \text{ in})^2 \cdot 190.322 \text{ lbs}}{\pi^3 \cdot 15000000 \text{ lbs/in}^2}} = 0.220 \text{ in}$$

Gray cast iron 60

$$EI = 20000 \text{ ksi}$$

$$\sigma_{ult} = 180 \text{ ksi}$$

$$\sigma_{allow} = 90 \text{ ksi}$$

$$\sigma_{allow} = F / \pi r^2$$

$$r = \sqrt{\frac{95.161 \text{ lbs}}{90000 \text{ lbs/in}^2 \cdot \pi}} = 0.0183 \text{ in}$$

$$P_{cr} = F * F.O.S = 190.322 \text{ lbs}$$

$$P_{cr} = \frac{\pi \cdot (EI)}{(L)^2}$$

$$P_{cr} = \frac{\pi \cdot (20000000 \text{ lbs/in}^2 \cdot \frac{\pi r^4}{4})}{(37.947 \text{ in})^2}$$

$$r = \sqrt[4]{\frac{4 \cdot (37.947 \text{ in})^2 \cdot 190.322 \text{ lbs}}{\pi^3 \cdot 20000000 \text{ lbs/in}^2}} = 0.205 \text{ in}$$

Ductile:

Stainless steel 304

$$EI = 27500 \text{ ksi}$$

$$\sigma_{yield} = 40 \text{ ksi}$$

$$\sigma_{allow} = 20 \text{ ksi}$$

$$\sigma_{allow} = F/\pi r^2$$

$$r = \sqrt{\frac{95.161 \text{ lbs}}{20000 \text{ lbs/in}^2 \cdot \pi}} = 0.0389 \text{ in}$$

$$Pcr = F * F.O.S = 190.322 \text{ lbs}$$

$$Pcr = \frac{\pi \cdot (EI)}{(L)^2}$$

$$Pcr = \frac{\pi \cdot (27500000 \text{ lbs/in}^2 \cdot \frac{\pi r^4}{4})}{(37.947 \text{ in})^2}$$

$$r = \sqrt[4]{\frac{4 \cdot (37.947 \text{ in})^2 \cdot 190.322 \text{ lbs}}{\pi^3 \cdot 27500000 \text{ lbs/in}^2}} = 0.189 \text{ in}$$

Aluminum Alloy

$$EI = 10150 \text{ ksi}$$

$$\sigma_{yield} = 43 \text{ ksi}$$

$$\sigma_{allow} = 21.5 \text{ ksi}$$

$$\sigma_{allow} = F/\pi r^2$$

$$r = \sqrt{\frac{95.161 \text{ lbs}}{21500 \text{ lbs/in}^2 \cdot \pi}} = 0.375 \text{ in}$$

$$Pcr = F * F.O.S = 190.322 \text{ lbs}$$

$$Pcr = \frac{\pi \cdot (EI)}{(L)^2}$$

$$Pcr = \frac{\pi \cdot (10150000 \text{ lbs/in}^2 \cdot \frac{\pi r^4}{4})}{(37.947 \text{ in})^2}$$

$$r = \sqrt[4]{\frac{4 \cdot (37.947 \text{ in})^2 \cdot 190.322 \text{ lbs}}{\pi^3 \cdot 10150000 \text{ lbs/in}^2}} = 0.243 \text{ in}$$

8. Interdisciplinary Engineering ABET Requirements

Ian Wilhite
ECS developed for ITDE 201

PREAMBLE:

The field of Robotics and Controls is dedicated to designing and implementing systems that enhance efficiency, safety, and precision across a wide range of applications, from industrial automation to critical healthcare devices. As these systems increasingly interact with humans and impact essential societal functions, the need for a robust ethical framework becomes paramount. A clear code of ethics ensures that engineers prioritize public welfare, maintain professional integrity, and navigate the complex challenges of this rapidly evolving discipline responsibly. This code serves as a guiding document to uphold trust, accountability, and excellence in all endeavors within Robotics and Controls engineering.

EXPLANATION OF HOW THIS CODE WAS WRITTEN:

This code was developed by referencing existing professional ethical guidelines, including the National Society of Professional Engineers (NSPE) Code of Ethics, the American Society of Mechanical Engineers (ASME), and the Institute of Electrical and Electronics Engineers (IEEE) Code of Ethics. These codes provide foundational principles that were adapted to reflect the unique nature of Robotics and Controls engineering.

CANONS AND REFLECTIONS:

1. Robotics and Controls Engineers shall hold paramount the safety, health, and welfare of the public.

Reflections - Robotics and Controls engineers often work in industrial applications, and in doing so are creating systems to work alongside humans, and the results of a malfunction could be catastrophic. This canon emphasizes that public safety shall always be prioritized over efficiency or cost reduction. Robotics and Controls engineers must ensure machines are operating in a safe manner around humans.

2. Robotics and Controls Engineers shall issue public statements only in an objective and truthful manner.

Reflections - Robotics is a growing field with questions constantly being raised on safe practices, reliability, and new developments. Robotics and Controls engineers shall issue statements only with proper research, knowledge, and relevance. Transparency is crucial for any communications, along with potential downsides and dangers to new methodologies.

3. Robotics and Controls Engineers shall perform services only in the areas of their competence.

Reflections - Robotics and Controls engineering spans a vast range of specialties, from artificial intelligence to biomechanical systems. Engineers in this field must recognize and respect the boundaries of their expertise, seeking further education or consulting specialists when necessary. This ensures that projects are approached with adequate knowledge and skill, reducing the risk of errors that could jeopardize safety or functionality. Competence also involves staying updated with advances in technology

and ethical standards, as a lack of proficiency can lead to unintended harm or diminished trust in the profession.

4. Robotics and Controls Engineers shall act for each employer or client as faithful agents or trustees.

Reflections - The Robotics and Controls industry is still emerging, making trust between clients, employers, and the public critical to its success. Engineers must prioritize honesty, integrity, and quality in their work to uphold this trust. By acting as dependable agents, they strengthen the field's credibility and lay a reliable foundation for future innovations. This trustworthiness is not only vital for current projects but also reinforces the profession's reputation, encouraging wider acceptance and investment in the field.

5. Robotics and Controls engineers shall ensure reliability in accountability measures.

Reflections - As automation grows in scale and applicability, there is an increasingly prevalent need for redundant safety measures. As automation becomes more commonplace, the public will trust it more, and will act with less caution around potentially dangerous machinery, requiring more robust safety measures and control systems.

6. Robotics and Controls Engineers shall uphold and enhance the honor, integrity, and dignity of the growing profession.

Reflections - As pioneers of a new space, the public perception of the discipline is very malleable, bringing all the more importance to the upholding ethical standard to protect the public. When one bridge collapses, it is a tragedy, but people don't lose faith in every bridge ever built; if one robot kills someone, then the entire industry is brought to a standstill. Without trust, there is no future for this industry, the American nuclear engineering sector can demonstrate that much; while this field is still growing and defining its role, it is incredibly important that the public perception be upheld.

Personal Development Plan:

By Ian Wilhite

Vision Statement:

My vision is to lead and innovate in the field of robotics and control engineering, developing cutting-edge solutions that enhance the intersection between technology and humanity. I aim to create systems that not only drive efficiency and precision in industrial applications but also improve safety and accessibility in critical areas such as healthcare, disaster response, and sustainable infrastructure. By fostering collaboration, engaging in continuous learning, and adhering to the highest ethical standards, I strive to bridge the gap between emerging technologies and the needs of society, ensuring that the advancements in robotics serve as a force for good in the world.

Note: struck through items were placed on the plan as a part of an earlier revision and have been accomplished since being initially added.

Development Themes

- Learning
 - 1) 2025-2026: I will obtain relevant certificates in the immediate future to demonstrate to employers and institutions of higher education proof of my tangible skills.
 - a) ~~Study for the Certified SolidWorks Associate certification (CSWA) and sit for the exam by December 2024 (free in the Zach FEDC)~~
 - b) Utilize online certificates to learn and recognize skills that I wish to learn such as:
 - i) ~~2024: Matlab Onramps Certification~~
 - ii) 2025: Linkedin Learning Github Essentials
 - 2) 2026-2028: I will obtain degree(s) to demonstrate my knowledge to employers.
 - a) 2026-2028: Maintain efforts in coursework and monitor degree plans to ensure meeting appropriate requirements. I will maintain a semesterly GPA above a 3.5.
 - b) 2026: I will graduate in May of 2026 with a Bachelors in Interdisciplinary Engineering.
 - c) 2027-2028: I will either graduate from an A&M Masters program in May of 2027, or a reputable non-A&M Masters program in May of 2028.
 - 3) 2029-2031: I will obtain professional licenses to certify the quality of my work.
 - a) Take the FE exam in 2026/2027 and begin the working hours to qualify for the PE exam.
 - b) Prepare for and take the PE exam in 2030/2031 (>4 years after FE)

- c) Begin hours for Project Management Professional (PMP) Certification in 2027 (Only if relevant, PE/PhD is plenty, and although another certificate would help, it would not be particularly relevant)
 - d) Prepare for and take the PMP exam in 2030/2031 (>3 years of work)
- Networking
 - 1) 2025-2027: I will be actively involved in a student chapter of a professional society in school to find connections to my peers as well as internships and full time employment.
 - a) 2024: I will uphold my office as an executive, and continue to plan and execute events for the remainder of the 2024-2025 academic year.
 - b) 2025: I will run for president and use the opportunity to advocate for structural changes to our events calendar to better engage new members.
 - c) 2025-2026: I will remain involved in the organization by remaining engaged in leadership, and being engaged in the big/little program.
 - d) 2024-2026: I will attend the SEC and ASME career fairs and industry nights to learn about and network with companies that hire Controls, Automation, and Systems Engineers.
 - 2) 2026-2029: I will engage with professional societies for conferences, networking events, and professional growth opportunities.
 - a) ~~NERC - UMASS 9/2024~~
 - b) IEEE conferences: ICRA 5/2025
 - c) TEROS 4/30/24 @UT
 - d) Ubiquitous Robotics (UR) Conference 6/2/2025 @ TAMU
 - 3) 2027-2029: I will find ways to support student chapters of professional organizations through mentorship, networking with recruiters, and technical consulting
 - a) I will be engaged in professional networks through the TAMU Industry Advisory Council; ASME national mentorship programs; any company specific mentorship programs
 - 4) 2024-2030: I will develop a respectable online presence through the use of social media platforms to make myself visible to employers and
 - a) 2024: Upkeep LinkedIn, maintain a positive image on Instagram.
 - b) 2025: establish personal projects Instagram/Youtube account.
 - c) 2026: Github personal academic website.
 - d) 2027-2028: I will maintain a consistent image and watch for new emerging popular technologies.
- Experience
 - 1) 2025-2026: I will participate in interdisciplinary collaborative projects to apply my skills early in my career
 - a) 2024: set project objectives and tasks for DRON project with TURTLE
 - b) 2025: find additional personal projects relevant to robotic employers, potentially with publishable content
 - c) 2026: find an undergraduate role in a research lab where I can collaborate in robotic projects with a novel purpose

- d) 2025-2026: identify persons for a robotics-related senior design project
 - e) 2026: successfully deliver a senior design project.
- 2) 2025-2027: I will find early career opportunities that allow me to learn a variety of skills, ideally in a rotational program
 - a) 2025: I will find and complete an internship or research fellowship that allows me to work professionally in the robotics field.
 - b) 2026: I will find and complete a research oriented program that supports research for graduate programs.
 - c) 2027: I will find summer programs that support masters programs by bringing varied skills, ideally through travel or rotational programs.
- 3) 2027-2030: I would like to find roles where I can learn in a hands-on manner by applying lessons learned to tangible projects - ideally in a research or a private R&D environment
 - a) 2027-2030: find work post-masters either in industry working in R&D or academia in a PhD program
- Leadership
 - 1) 2025-2026: I will look to student organizations for leadership opportunities in *social* and professional development roles
 - a) 2025: continue to serve as ASME Secretary; support the goals and ambitions of my officers; ensure to utilize events as opportunities to meet new people.
 - b) 2026: look for additional roles to network within electrical, mechatronic, and interdisciplinary groups.
 - c) 2025-2026: look for leadership positions within professional organizations in robotics-related groups.
 - 2) 2026: I will look to student organizations for leadership opportunities in *technical* and project management style roles
 - a) 2025: I will continue as a project lead in TURTLE and effectively coordinate my subteams to grow my skills in technical leadership, my understanding of autonomous systems, and help develop the skills of others.

Last Updated: December 2024.

9. Grand Challenges Scholars Program

ENGR 499

Ian Wilhite

UIN: 333008004

GCSP Outside Activities

Outside Activity 1: Research (3/4/2024)

Since January, I have been assisting Dr. Thomas's team in the Human-Empowering Robotics and Controls (HERC) lab. I was placed on the hip exoprosthesis 'human gripper' project under PhD student Jadon Kaercher. In many exoskeleton projects, the largest challenge comes in the time delay, which is commonly solved with some level of path prediction. The goal of the hip exoprosthesis project is to create a system by which the user leg moves as little as possible so that the motors (which are significantly faster and stronger than the leg of the user) can do more of the work, faster. The goal of the 'human gripper' project is to create a frame that can effectively transfer the now increased forces between the metal frames and actuators and the much softer (but force-driving) leg of the user. Many systems that allow for a large amount of 'slop' in their systems add bad data into their path tracking models, which can lead to disastrous results in incorrect movements of the frame. This creates the unique challenge to be addressed by the 'human gripper', to comfortably but tightly hold the leg of the user, and on that sub-project, I am responsible for the ankle and foot mounting system.

Outside Activity 2: Multicultural (3/4/2024)

For the last 5 years (since 5/5/2018), I have been a member of The Order of the Arrow, an honor society that takes a large part of our ceremonial practices from local native American tribes. Nationally, our organization takes inspiration from the Lenne Lenape tribe (also called the Delaware Indians), however our local lodge has chosen to work with local representatives from the Caddo and Commanche tribes to ensure that our regalia is accurate to the period we intend to represent. Normally, I use the Caddo-inspired regalia, however because of some last-minute logistical challenges, this weekend I used Commanche regalia. Through working with this organization, I have had the incredible opportunity to go many incredible places, but this weekend, I was hosting what for many tenured members is their final ceremony. Each year, the lodge (~1000 members) is allowed to select 2% of its membership that to receive what is known as The Vigil Honor. I delivered the Vigil ceremony to 7 of my peers that I have had the privilege of mentoring and working with over the course of the last 5 years.

ENGR 499

Ian Wilhite

UIN: 333008004

GCSP Outside Activities

Outside Activity 3: Viable Business (4/29/2024)

This semester I have taken ENGR 462 with Shayla Rivera, where I have had the privilege to listen to the stories of over a dozen successful entrepreneurs—and former aggies. Through the class, I have had the chance to learn an incredible amount of the internal workings of a fledgling business first getting its feet off the ground. The single greatest takeaway I have had from the class is that nothing occurs in a vacuum; in any situation, your work will be applied in more than just the single situation in which you intend it. By understanding the broader environment surrounding your work and application of your work, you can better fit your solutions to the problems and environments in which they will be applied.

Outside Activity 4: Social Consciousness (4/29/2024)

For the last semester, I have served as the Vice President of Marketing and Communication (VP MarComm) for the Residential Housing Association (RHA). In my role, I have had the privilege to spearhead our outreach to new residents and to help to better involve new students on campus, support the community councils, and represent the student body to the department of reslife as they seek input on housing development, dining improvements, and transportation services. In my experiences in RHA, I have had the privileged to meet with dozens of incredibly dedicated individuals and witness firsthand the impact of their incredible dedication to their work. I am proud to have worked alongside them in making a positive impact to the on-campus community.

Outside Activity 4: Multidisciplinary (4/29/2024)

I plan on getting a minor in Math, and out of the five required classes, I have completed three, have one in progress, and intend to complete the final class in the spring. For the upper-level classes, I have already completed linear algebra, and am currently in differential equations, but for the 400-level class, I intend to take complex analysis because of its numerous applications in controls theory. By taking linear algebra, I have already seen the numerous benefits of understanding matrix properties, and how being able to apply them in sticky situations can make a complex problem much easier. The applications of linear algebra are incredibly broad, from statics and truss analysis to the linearization in differential equations, and being more familiar with those tools has already given me a leg up in approaching various situations.

Carbon Sequestration Methods

By Ian Wilhite and
Anagha Dharmavaram



Table of contents

O1 Carbon
Emitters

O2 Carbon
Capture Tech

O3 Carbon
Sequestration

O4 Looking
Forward

O1

Carbon Emitters

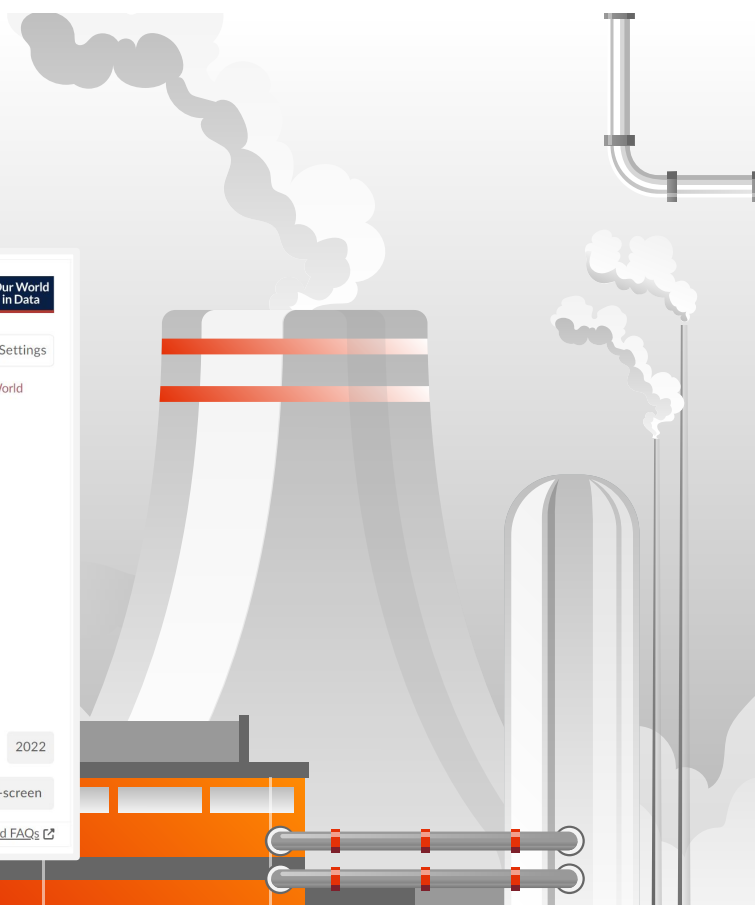
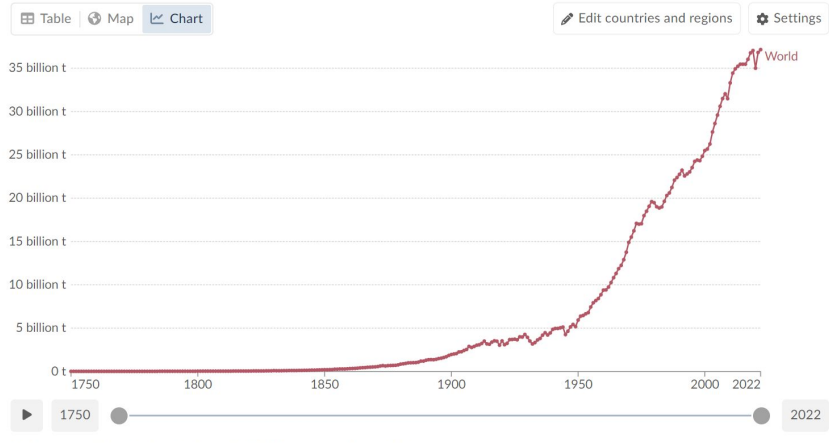
Where are emissions coming from?



CO₂ Emissions since 1750

Annual CO₂ emissions

Carbon dioxide (CO₂) emissions from fossil fuels and industry. Land-use change is not included.



Carbon Sources



Transportation

Mostly smaller engines,
often without filters



Industrial

Factories, warehouses,
and large-scale
operations



Agriculture

Cows, fertilizers, and
pesticide-related effects



Electric Power

The costs in generating
power for the public



Commercial / Residential

The energy along the
main power grid

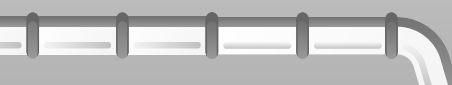


Miscellaneous

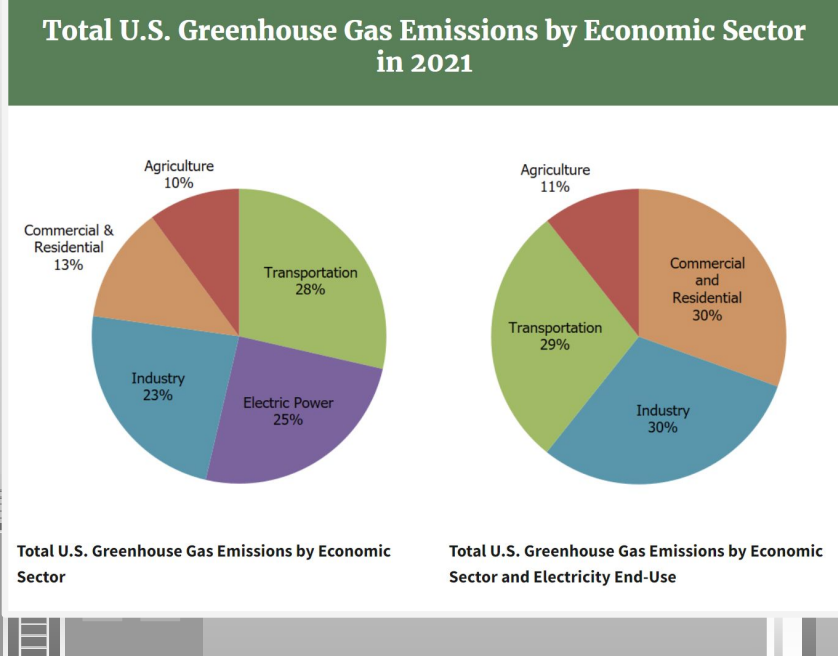
The smaller, sometimes
unintentional polluters



Companies working in Capture



CO₂ Emissions By Economic Sector



02

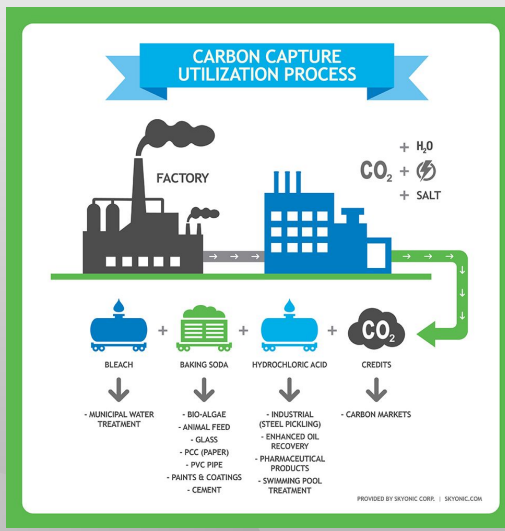
Carbon Capture

What technology is
currently in use?



Carbon Utilisation

Carbon utilisation involves converting carbon dioxide into useful products like fuels, chemicals, and building materials to reduce greenhouse gas emissions.

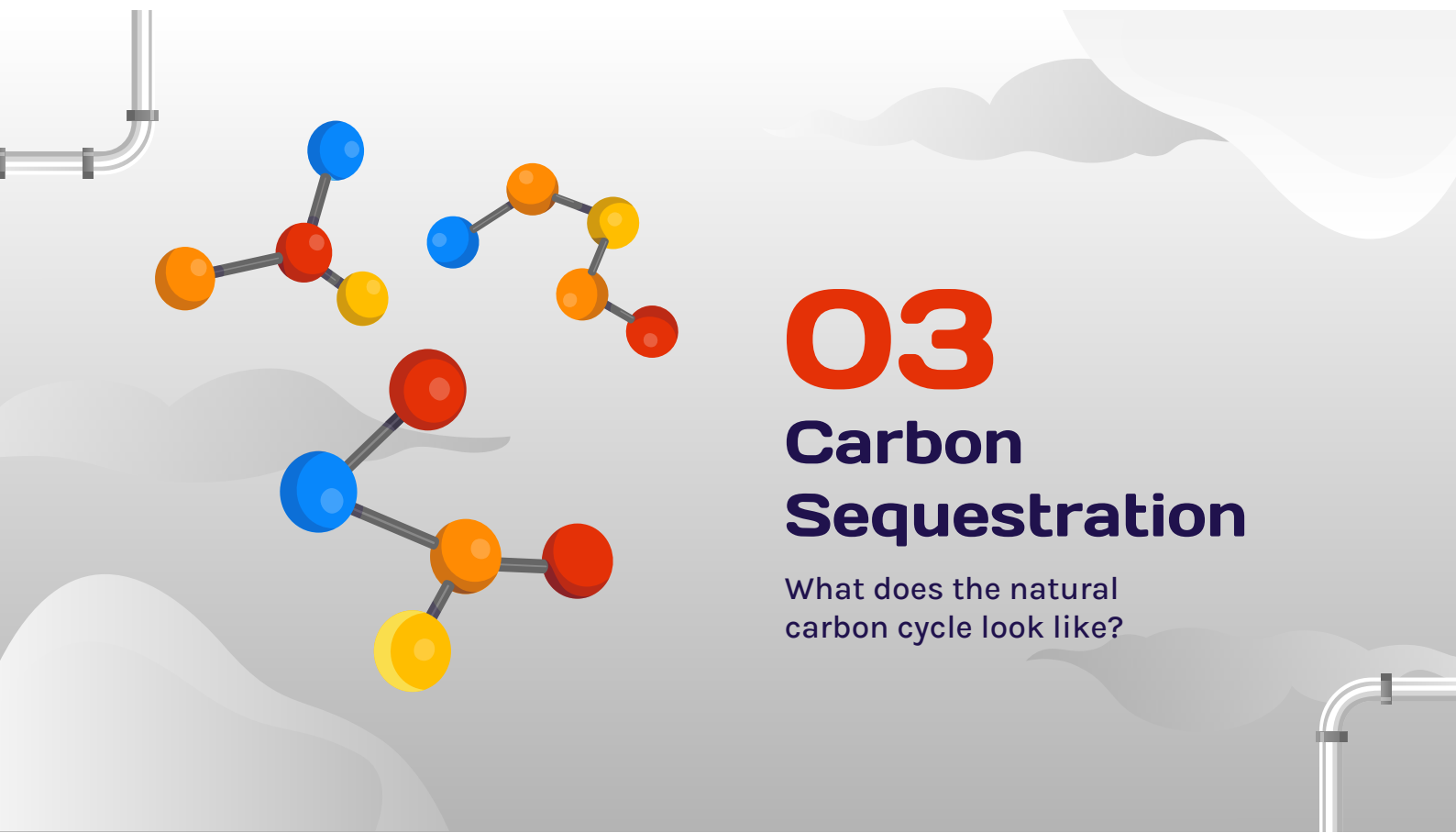




Carbon Capture History

How long do you think carbon capture has been around?

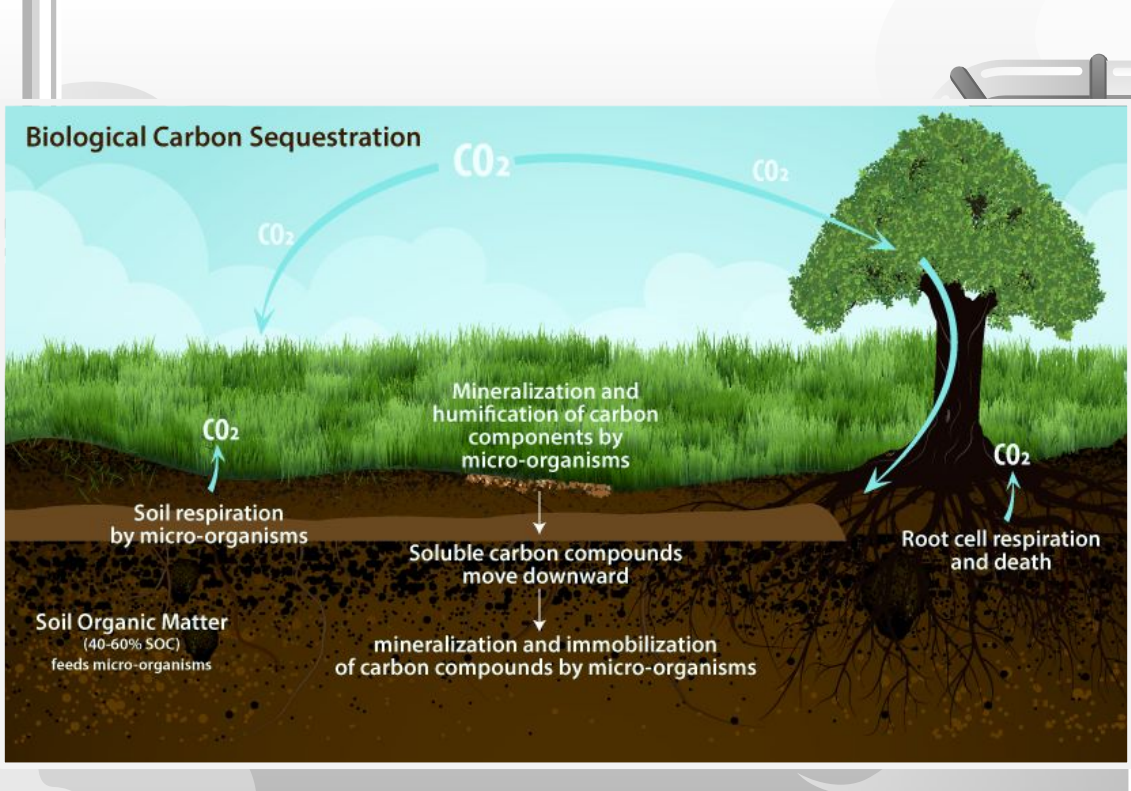
- A) 10 years
 - B) 50 years
 - C) 100 years
 - D) Since the Beginning of time
- 



03

Carbon Sequestration

What does the natural
carbon cycle look like?





TYPES OF ENGINEERING | 21 ICONS



ELECTRICAL
ENGINEERING



CIVIL
ENGINEERING



MECHANICAL
ENGINEERING



ENVIRONMENTAL
ENGINEERING



COMPUTER
ENGINEERING



BIOMEDICAL
ENGINEERING



AEROSPACE
ENGINEERING



AUTOMOTIVE
ENGINEERING



ELECTRONIC
ENGINEERING



CHEMICAL
ENGINEERING



NUCLEAR
ENGINEERING



HEALTH AND SAFETY
ENGINEERING



PETROLEUM
ENGINEERING



SOFTWARE
ENGINEERING



MATERIALS
ENGINEERING



SYSTEMS
ENGINEERING



GEOTECHNICAL
ENGINEERING



MARINE
ENGINEERING



MANUFACTURING
ENGINEERING



MINING
ENGINEERING



AGRICULTURAL
ENGINEERING



04

Looking forward

What lies ahead in the future of
carbon capture technology?

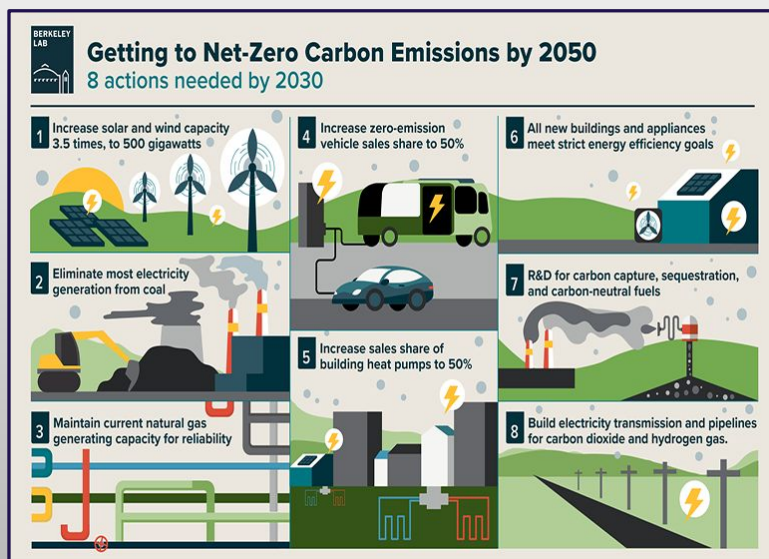
Increased Efficiency

The future of carbon capture technology is bright, with advancements likely to reduce costs and enhance efficiency, encouraging broader adoption and support from governments and industries to help combat climate change.



In the next 50 years...

What are the obstacles in the way?



Quiz Time!



A stylized illustration of an industrial facility. On the left, there's a large building with a red roof and several vertical pipes. In the center, there's a tall, grey cylindrical structure with a spiral staircase and a walkway. To its right is another grey building with a flat roof and windows. Large plumes of grey smoke rise from the buildings, creating a hazy atmosphere.

Thanks!

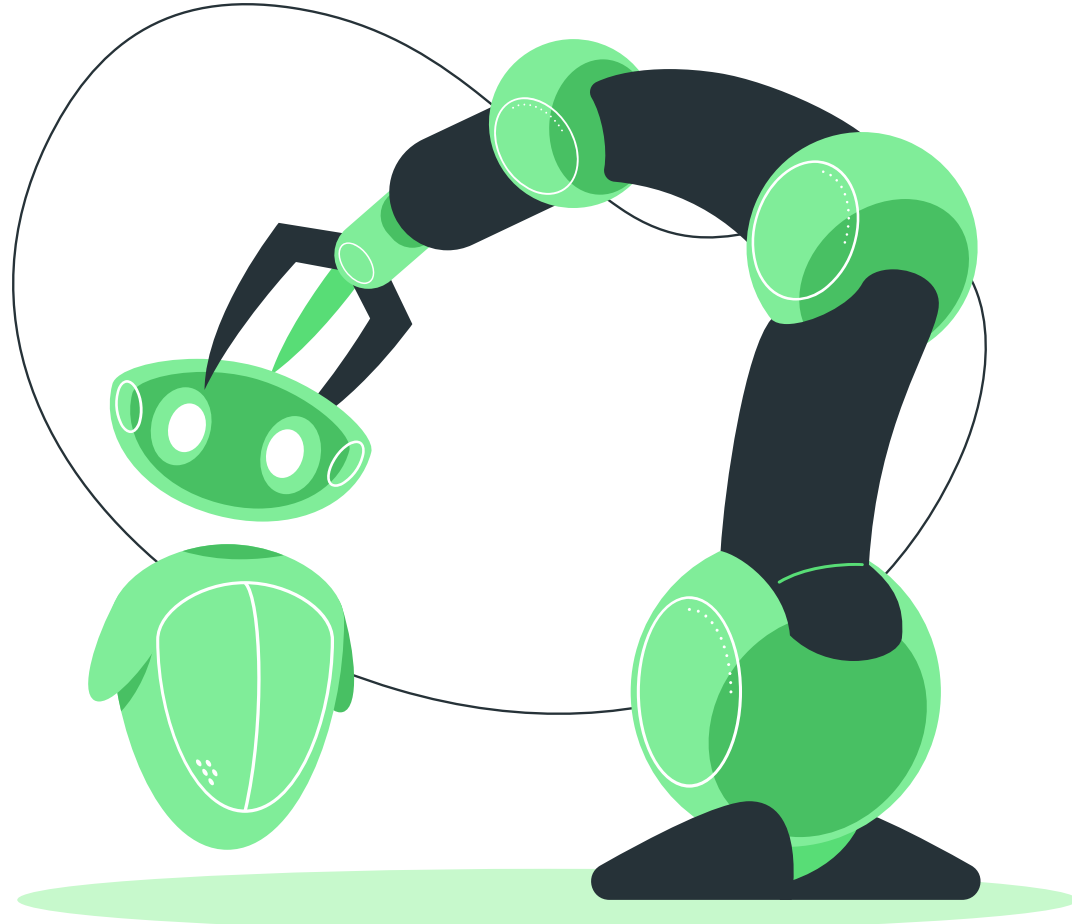
Does anyone have any questions?

CREDITS: This presentation template was created by [Slidesgo](#), including icons by [Flaticon](#), and infographics & images by [Freepik](#)

10. Science Influencers Program

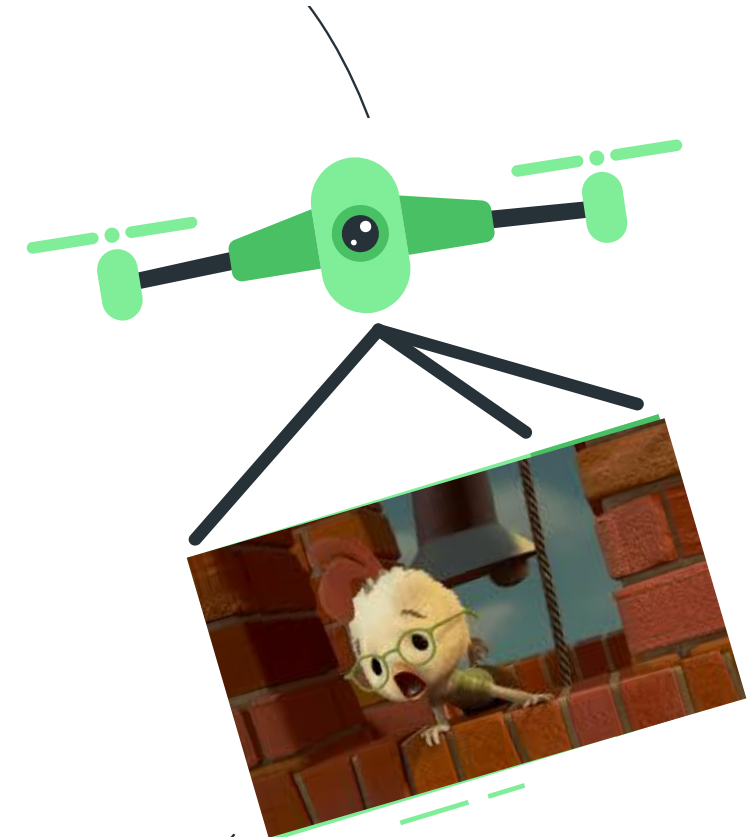
Tesla, AI, & Automation

Ian Wilhite

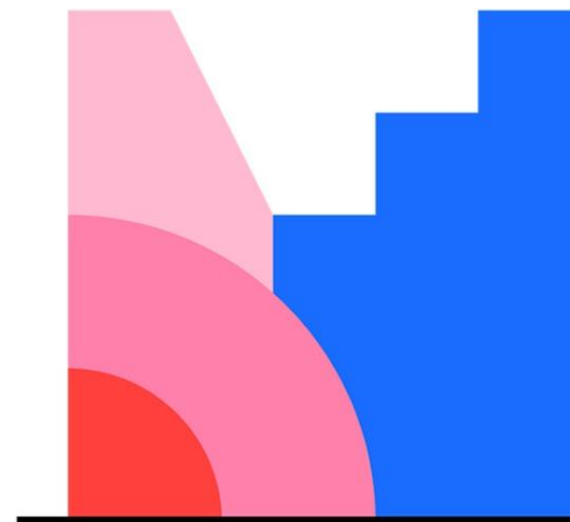


What is AI?

Can someone give a functional definition for Artificial Intelligence?



Menti!



Mentimeter

AI is an Agent that...

Processes input

Either from sensors,
input, or training data



Applies models to
analyze data

Provides Output

Makes decisions,
predictions, or actions



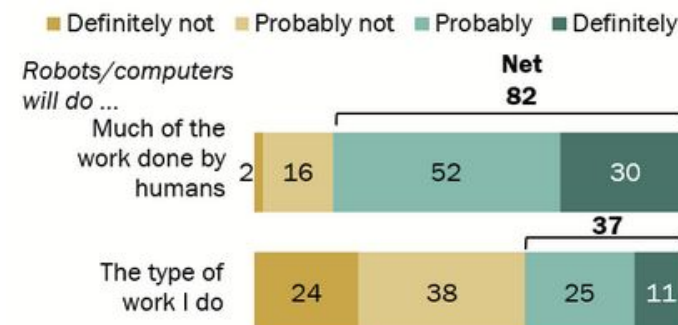


Who cares?

Pew Research Center

Public says robots will take over much of the work done by humans, but most workers don't think it will affect their own type of work

% saying, within the next 30 years, each of the following will ___ happen



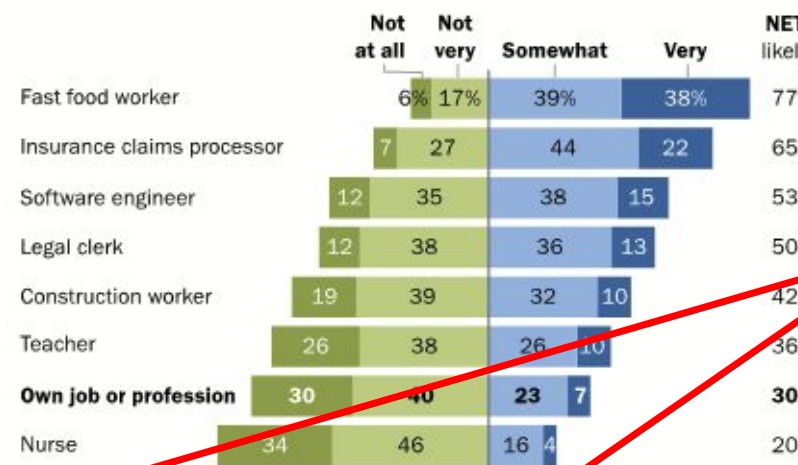
Note: Lower panel based on employed adults. Share of respondents who didn't offer an answer not shown. Figures may not add to subtotals due to rounding.

Source: Survey of U.S. adults conducted Dec. 11-23, 2018.
"Looking to the Future, Public Sees an America in Decline on Many Fronts"

PEW RESEARCH CENTER

Americans view certain professions as being at greater risk of automation than others

% of U.S. adults who say it is ___ likely that the following jobs will be replaced by robots or computers in their lifetimes



Note: Data for "own job or profession" is based on those who are currently employed. Respondents who did not give an answer are not shown.
Source: Survey conducted May 1-15, 2017.
"Automation in Everyday Life"

PEW RESEARCH CENTER

In 2017 & 2018!

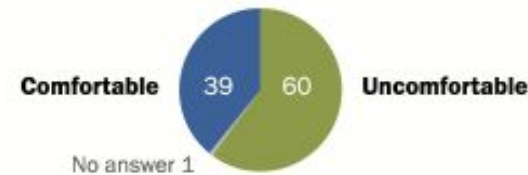
What has happened since 2018?

Pew Research Center – newer!

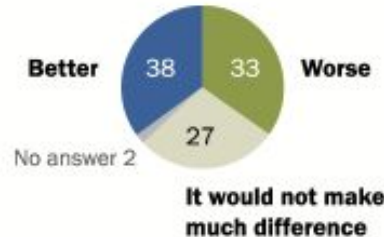
Fewer than half in U.S. expect artificial intelligence in health and medicine to improve patient outcomes

% of U.S. adults who say that thinking about the use of artificial intelligence in health and medicine to do things like diagnose disease and recommend treatments ...

They would feel __ if their health care provider relied on it for their medical care



It would lead to __ health outcomes for patients



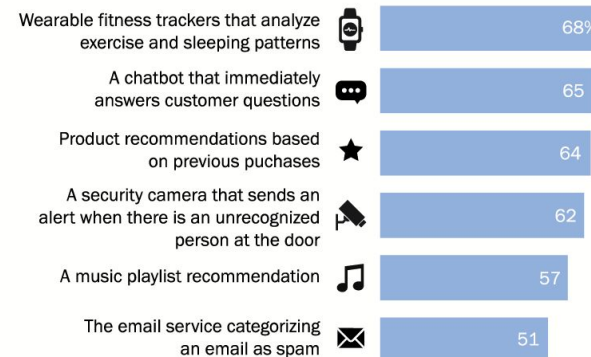
Source: Survey conducted Dec. 12-18, 2022.

"60% of Americans Would Be Uncomfortable With Provider Relying on AI in Their Own Health Care"

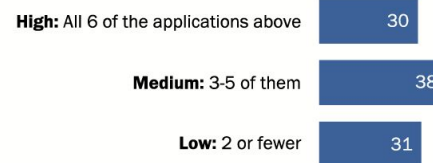
PEW RESEARCH CENTER

Half of Americans or more aware of common uses of AI, but fewer can identify AI's role in all six examples

% of U.S. adults who identify that the following use artificial intelligence in multiple choice questions



% of U.S. adults who correctly identify __ as using AI



Note: All questions are multiple choice; for full question wording, see topline.

Source: Survey conducted Dec. 12-18, 2022.

"Public Awareness of Artificial Intelligence in Everyday Activities"

PEW RESEARCH CENTER

Vocab!

Neural Network

Layered network that processes data

Convolutional Neural Network (CNN)

A Neural Network for image processing

Natural Language Processor (NLP)

The step that encodes words into vectors

Recurrent Neural Network (RNN)

A Neural Network for serial data input

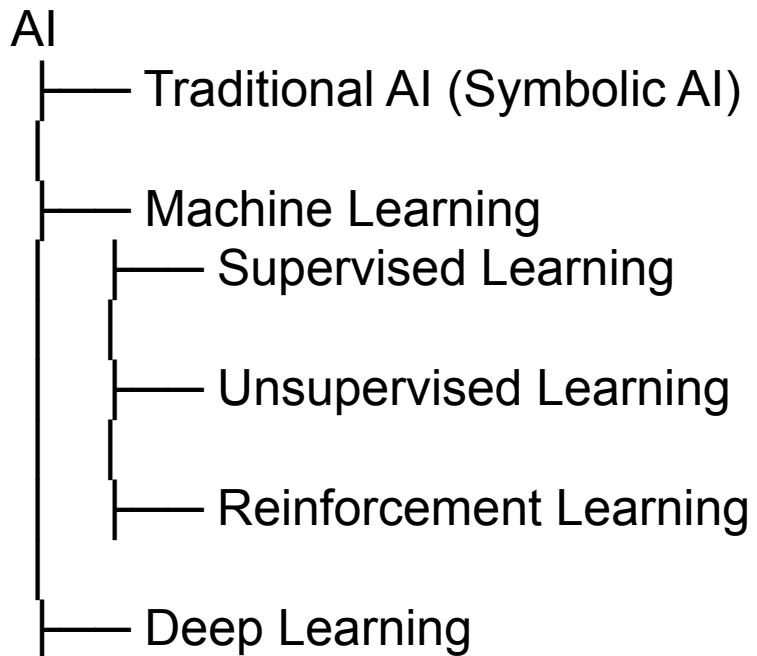
Machine Learning (ML)

trains algorithms to recognize patterns (*stats!*)

Training Data

Content libraries used to develop relationships

AI Overview



AI

— GOFAI (Good Old-Fashioned AI or Symbolic AI)

— Rule-Based Systems

Control Algorithms

— Search Algorithms

— Knowledge Representation

— Planning & Reasoning

— Deep Learning

— Convolutional Neural Networks (CNNs) – Image Processing

— Recurrent Neural Networks (RNNs) – Sequence Modeling

— Transformer Models – Natural Language Processing (e.g., GPT)

— Generative Models – Data Synthesis (e.g., GANs, VAEs)

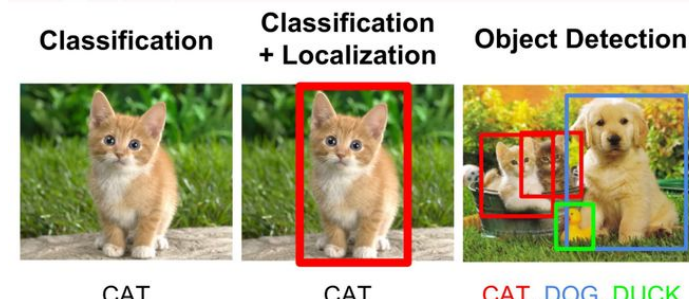
— Deep Reinforcement Learning – AlphaGo, Robotics

AI

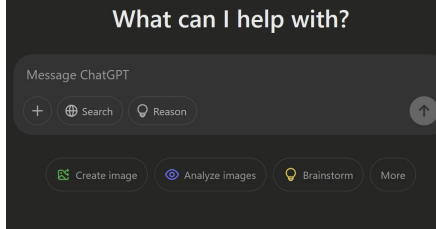
Machine Learning

Supervised Learning

- Regression (e.g., Stock Prediction)
- Classification** (e.g., Spam Detection, Medical Diagnosis)
- Natural Language Processing** (ChatGPT)
- Computer Vision (e.g., Facial Recognition, Object Detection)



What can I help with?

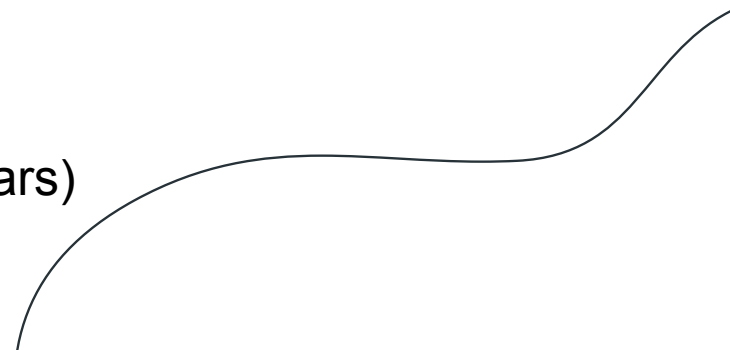


Unsupervised Learning (*just statistics!*)

- Clustering (e.g., Customer Segmentation)
- Dimensionality Reduction (e.g., Data Compression)
- Generative Models (e.g., GANs for Image & Data Generation)

Reinforcement Learning

- Model-Free (e.g., Q-Learning, Policy Gradient)
- Model-Based (e.g., Monte Carlo Tree Search)
- Deep Reinforcement Learning** (e.g., Self-driving cars)
- Robotics (e.g., Path Planning, Control Systems)





History

Statistics was invented in **1662** by John Graunt working for the London census

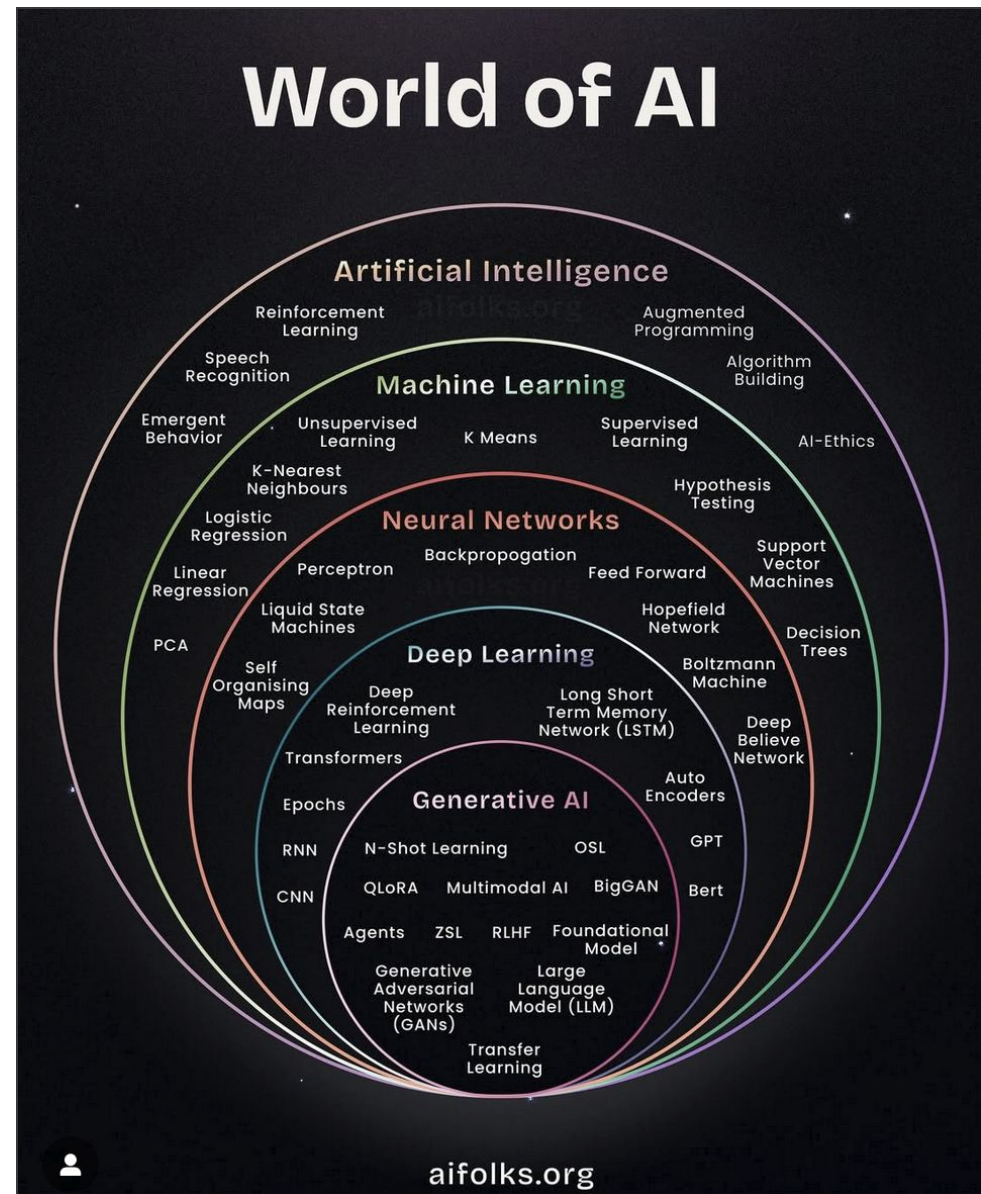
Alan Turing laid the foundation for **search** algorithms through logical agents in **1948**

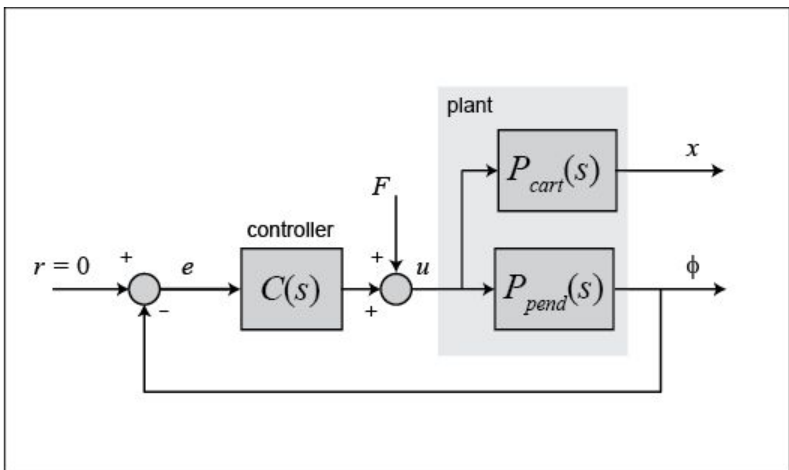
Machine Learning was invented in **1952** at IBM by Arthur Samuel using checkers

John McCarthy holds the Dartmouth Conference to discuss “thinking machines”

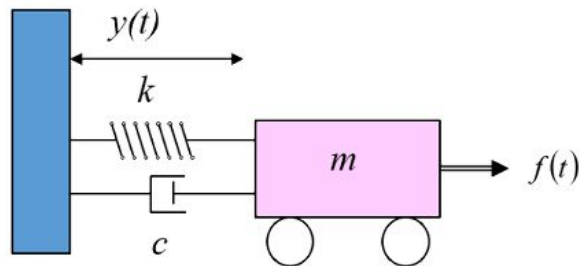
MIT **chatbot** ELIZA in **1966** used for therapy passes Turing test

OpenAI (non-profit) develops the first Large Language Model (**LLM**) GPT-1 in **2018**





Spring-mass-damper response theory



Sum of forces acting on suspension

$$F_m + F_d + F_k = f(t)$$

$$\frac{m}{g_c} \frac{d^2y}{dt^2} + c \frac{dy}{dt} + ky = f(t)$$

Mass acceleration

$$F_m = ma; \quad a = \frac{dv}{dt}; \quad v = \frac{dy}{dt} \Rightarrow a = \frac{d^2y}{dt^2}$$

$$F_m = \frac{m}{g_c} \frac{d^2y}{dt^2}$$

Damping force

$$F_d = c \frac{dy}{dt}; \quad c [=] \text{damping coefficient} \quad \frac{lb_f}{ft/sec}$$

Spring force

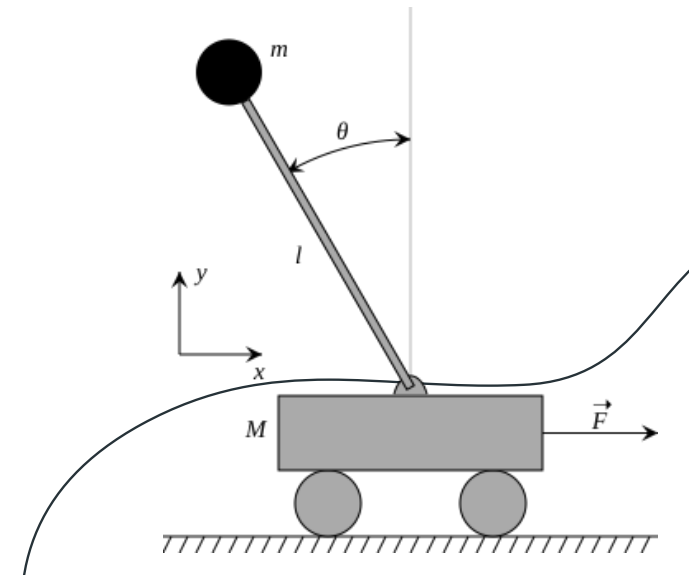
$$F_k = ky; \quad k [=] \text{spring constant} \quad \frac{lb_f}{ft}$$

Driving bump force

$$f(t) [=] \text{bump force} \quad lb_f$$

Controls Engineering allows us to **solve** for closed-form solutions to problems

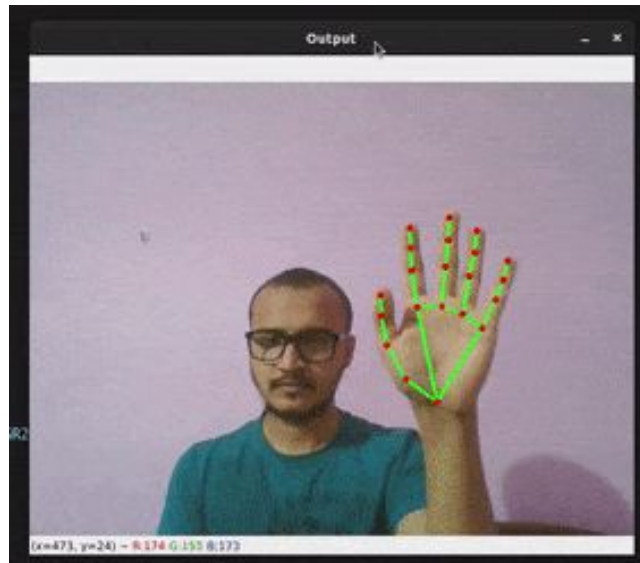
This is what I do!



Machine Learning (ML):

- Trained model
- Easier but slower
- Models make **mistakes**

Eg: a car turns the wrong way



Controls Engineering:

- Closed form solution
- Harder but faster
- Controls has **uncertainty**

Eg: car will turn left with a radius of 20ft +/- 0.5ft

Google Search Trends

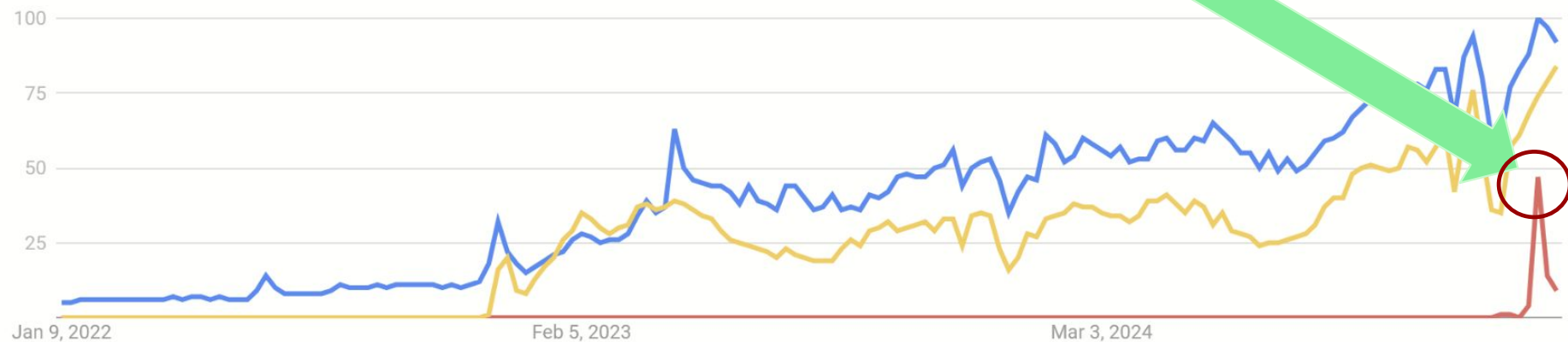
● Artificial intelligence ● deepseek ● Chatgpt

United States, 1/14/22 - 2/14/25

Interest over time ?

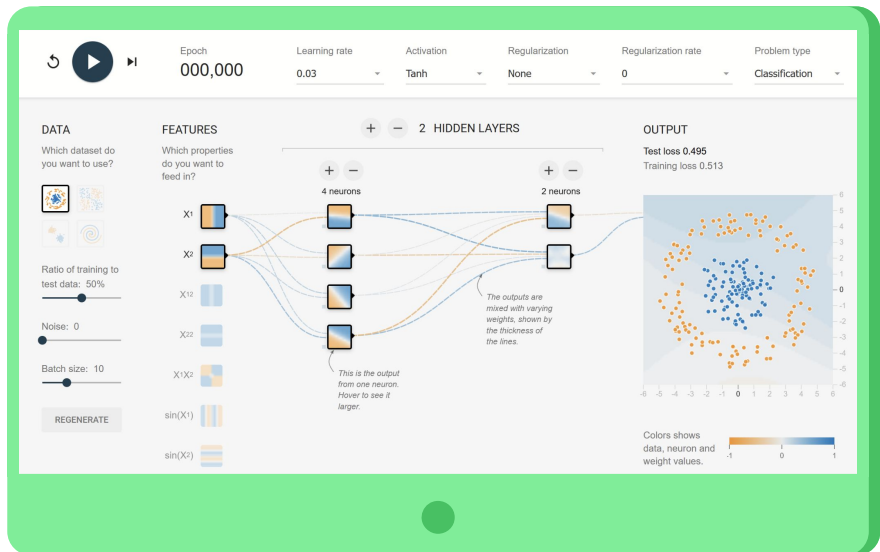


Feb 1st



ML Activity!

playground.tensorflow.org



NN Training Speedrun:

Model - the output of the final node in a neural network

Feature - a simple function applied to the input data

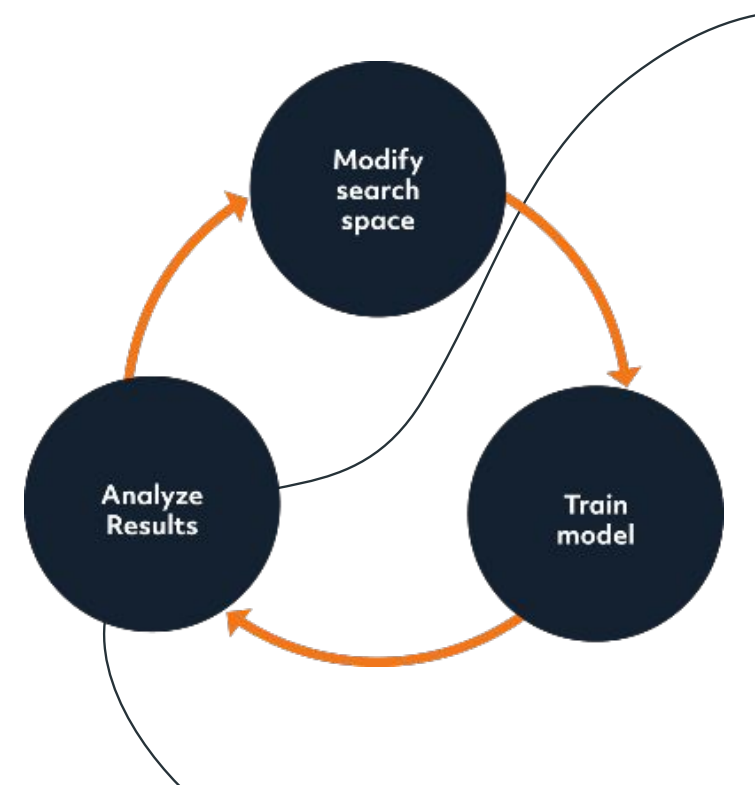
Neuron - a weighted combination of previous nodes

Layer - a step of neurons to tune

Training - automatically tuning the parameters neurons based on model *test loss*

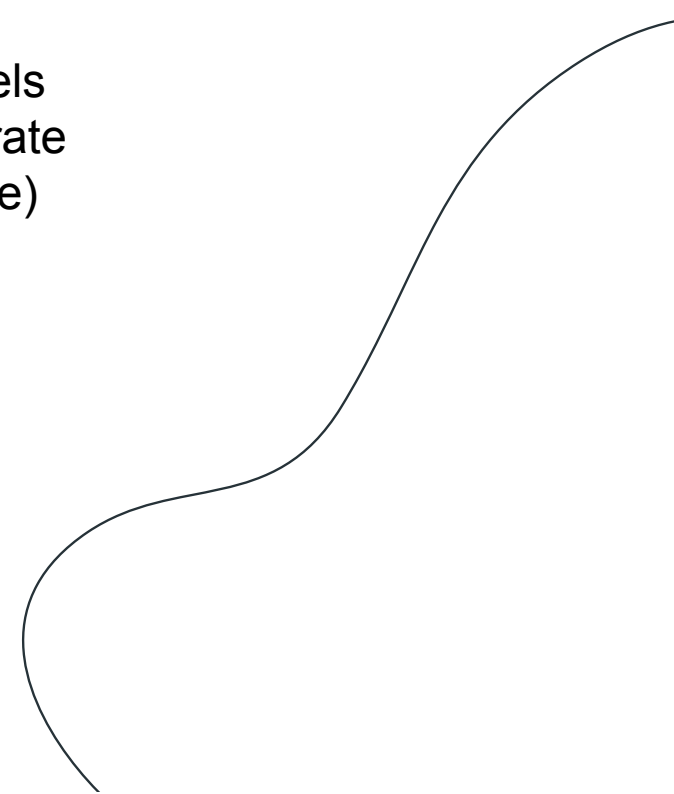
Training loss - % error model makes on training data

Test loss - % error model makes on unseen data



Tips:

- Simpler models will converge faster
- Larger models can approximate more complex systems
- You should enable input features that resemble the systems
- Larger number of layers will allow for more complicated models
- More features will allow more tools for your model to incorporate
- Common testing ratio of 20-30% (testing is an entire discipline)



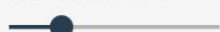
Overview

DATA

Which dataset do you want to use?



Ratio of training to test data: 30%



Noise: 25



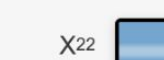
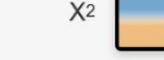
Batch size: 20



REGENERATE

FEATURES

Which properties do you want to feed in?



+

-

2 HIDDEN LAYERS

+

-

3 neurons



2 neurons



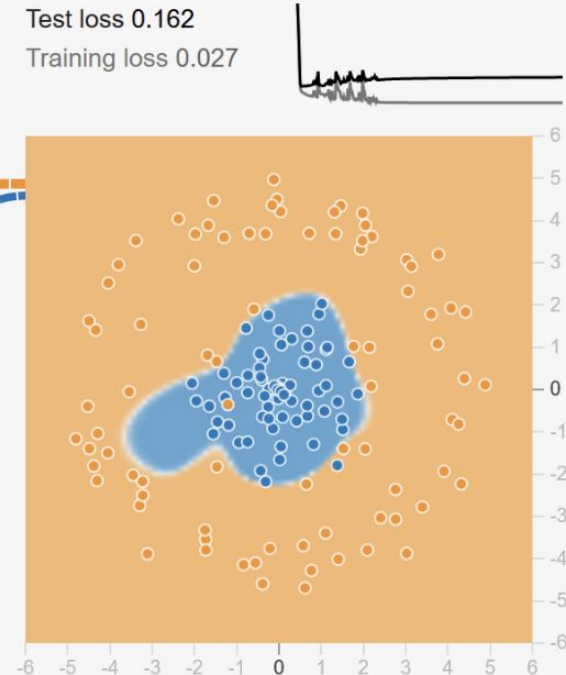
This is the output from one neuron.
Hover to see it larger.

The outputs are mixed with varying weights, shown by the thickness of the lines.

OUTPUT

Test loss 0.162

Training loss 0.027

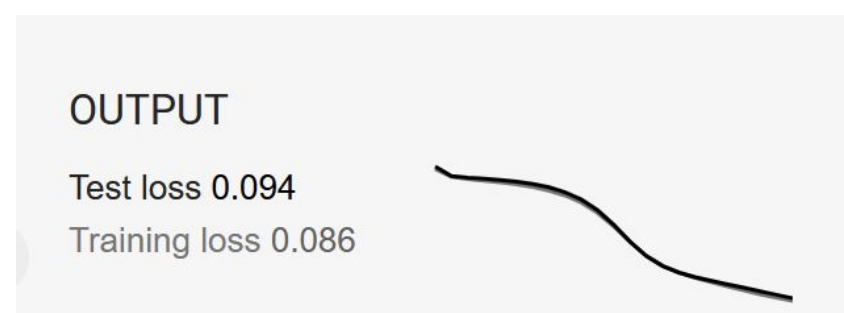
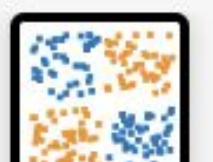


Colors shows data, neuron and weight values.



CHALLENGE 1

- **GOAL:**
 - Test Loss < 0.200
- **Requirements:**
 - Exclusive or dataset
 - Noise: 25



DATA

Which dataset do you want to use?



Ratio of training to test data: 50%



Noise: 50



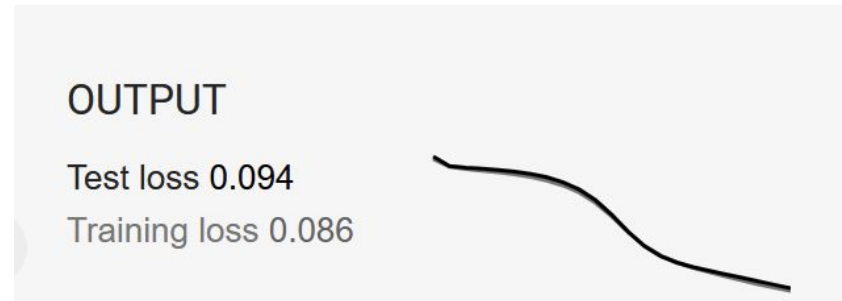
Batch size: 16



REGENERATE

CHALLENGE 2

- **GOAL:**
 - Test Loss < 0.250
- **Requirements:**
 - Spiral dataset
 - Noise: 50



DATA

Which dataset do you want to use?



Ratio of training to test data: 50%



Noise: 50



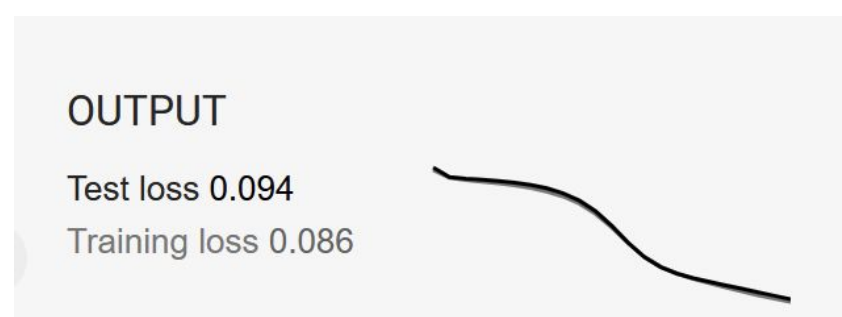
Batch size: 16



REGENERATE

CHALLENGE 3

- **GOAL:**
 - Test Loss < 0.150
- **Requirements:**
 - Circle dataset
 - Noise: 25
 - <5 neuron



DATA

Which dataset do you want to use?



Ratio of training to test data: 50%



Noise: 50



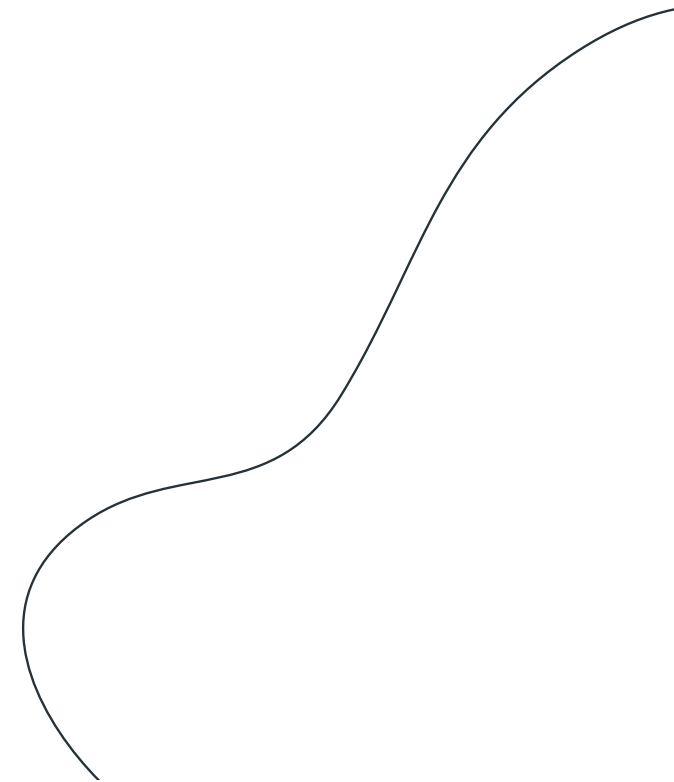
Batch size: 16



REGENERATE

Tying it back in

- Models are never 100% accurate
- Small errors in a model can mean major changes
- Nearly *impossible* to back-validate (understand)





**what about
Tesla?**

Self-driving cars



Journalistic media

Reuters

Tesla recalls 1.85 million US vehicles over unlatched hood issue



Jul 30, 2024 • By David Shepardson

NBC NEWS

Tesla recalls more than 375,000 vehicles for power steering issue



1 hour ago • By Matt Lavietes

MT MotorTrend

2023 Tesla Model Y Yearlong Review: How Does Full Self-Driving Work?



Jan 22 • By Alex Leasne

BUSINESS INSIDER

I drive a Cybertruck, and I'm sick of people flipping me off. I wish they understood how helpful this car is for me.



Jan 26 • By Angela Kenzslowe

yahoo/finance

Elon Musk insists Tesla isn't a car company as sales falter



Apr 24, 2024 • By Hamza Shaban

yahoo/finance

Tesla stock rises after company pledges return to growth after Q4 results disappoint



Jan 30 • By Pras Subramanian

AP

Tesla sales dropped 1.1% in 2024, its first annual decline in a dozen years



Jan 2 • By Tom Krisher & Bernard Condon

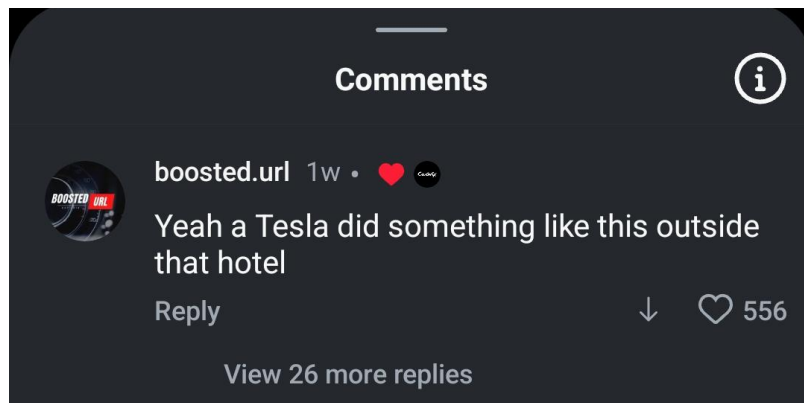
AP

Tesla sales fall for second straight quarter despite price cuts, but decline not as bad as expected



Jul 2, 2024 • By Tom Krisher

Social Media (Instagram)



Interactive Digital Media

r/RealTesla · 12d ago

Tesla is Collapsing.

24K votes · 2.3K comments

r/electricvehicles · 22d ago

Finally did it. Out with the Tesla.

3.7K votes · 818 comments

r/Wellthatsucks · 2y ago

Dude left his Tesla in a garage for a month...

57K votes · 4.2K comments

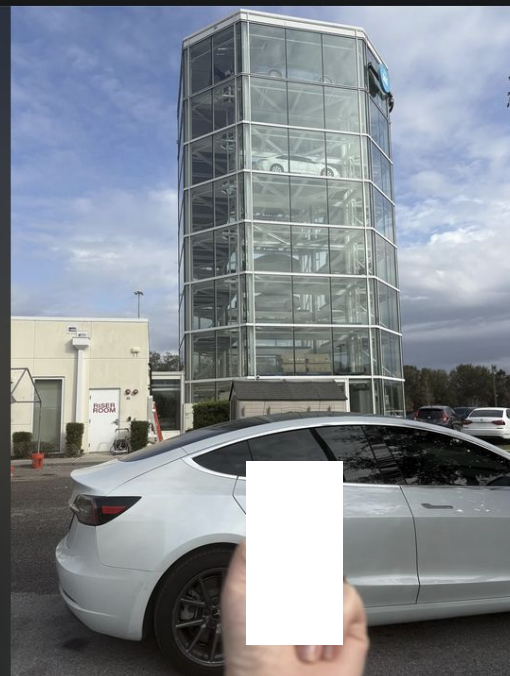
r/europe · 14d ago

Tesla Sales Plunge through Europe

126K votes · 4.8K comments

r/pics · 20 days ago
ThePetiteBaker

My bubbie would be proud that I stood for our values (sold Tesla)



66K

5.9K

12

Share

r/RealTesla · 12 days ago
Zestyclose-Habit-970

Tesla is Collapsing.

For the first time in over a decade, Tesla's sales declined year-over-year.

The company delivered 1.79 million vehicles in 2024, falling short of 2023's 1.81 million—a 1.1% drop. On the surface, this might seem small, but in an industry where growth is everything, this is a disaster. Legacy automakers like BYD, Hyundai, and others are beginning to eat Tesla's lunch.

Germany: Tesla sales crashed by a staggering 60% in January 2025, with just 1,277 registrations in the EU's largest auto market. This isn't a fluke—it's a market-wide rejection.

France: Another 63% sales collapse in the same period.

California: Tesla's home turf, where it once reigned supreme, saw a 11.6% drop in registrations while competitors gained market share.

The cracks in Tesla's foundation are no longer just visible—they're gaping holes. Tesla's brand value dropped by \$15 billion in 2024, a massive loss that signals a shift in public perception. The endless delays, price cuts, quality control issues, and Musk's erratic behavior have eroded consumer trust.

Let's not forget the PR nightmare of endless recalls, self-driving crashes, and Musk's alienation of core demographics. This isn't just a temporary dip—this is a full-blown identity crisis.

r/teslainvestorsclub · 1 mo. ago
hairy_quadruped

For the good of Tesla, the company, Musk the CEO has to go.

Musk is the CEO and public face of Tesla. Back in its early days (pre-2018) he was awkward but enthusiastic, progressive and apolitical. You would buy a Tesla-made car because it was different, fun, fast, smart and relatively green. The company as led by Musk kick-started the electric car as a viable option and revolutionised the car industry.

Now, Musk has gone down a very murky rabbit hole. His public face is less about his companies, and more about his politics. He has huge influence, and not in a way the most of the world wants.

A European study has shown that 30% of Tesla owners in the Netherlands are considering selling their car or have already done so. Tesla sales in Q4 2024 are down 40% compared to the previous year. Global sales are down 1.1%, the first ever drop in sales since 2011.

Anecdotally, in Australia, everyone I have talked to has said they would not consider buying a Tesla now. Tesla sales in Australia for 2024 are down 1.5% for the Model 3 and 26% for the Model Y.

There are many reasons why this decline could be occurring. Interest rates are still up. The Model Y refresh is pending. But I think a huge part is the disenchantment of buyers because of Musk's public face.

I think Musk should go. Musk is damaging Tesla. He should not be CEO. I think as shareholders we should protect our interests and vote for him to be removed as CEO.

1.7K 965 1 Share

Journalistic media – *self driving*

NBC NEWS

Tesla Autopilot linked to hundreds of collisions, has ‘critical safety gap,’ Federal regulator says

Apr 26, 2024 • By Lora Kolodny & Rob Wile



BUSINESS INSIDER

A safety group graded 14 driver-assistance systems. Tesla's self-driving option was the worst.

Mar 12, 2024 • By Camilo Fonseca



Forbes

Car Automation Programs—Including Tesla’s—Get Poor Ratings From Safety Group

Mar 12, 2024 • By James Padraig Farrell



AP

Questions about the safety of Tesla's ‘Full Self-Driving’ system are growing

Aug 28 • By Tom Krisher



CNN

Feds investigating safety of Tesla's ‘Full Self-Driving’ feature

Oct 18 • By Chris Isidore

Rolling Stone

I Took a Ride in a ‘Self-Driving’ Tesla and Never Once Felt Safe

Aug 19, 2024 • By Miles Klee

WIRED

Tesla Autopilot Was Uniquely Risky—and May Still Be

Apr 26, 2024 • By Aarian Marshall

San Antonio Express-News

Tesla is safest in world, says driver whose Cybertruck self-drove into pole

Yesterday • By Annasofia Scheve



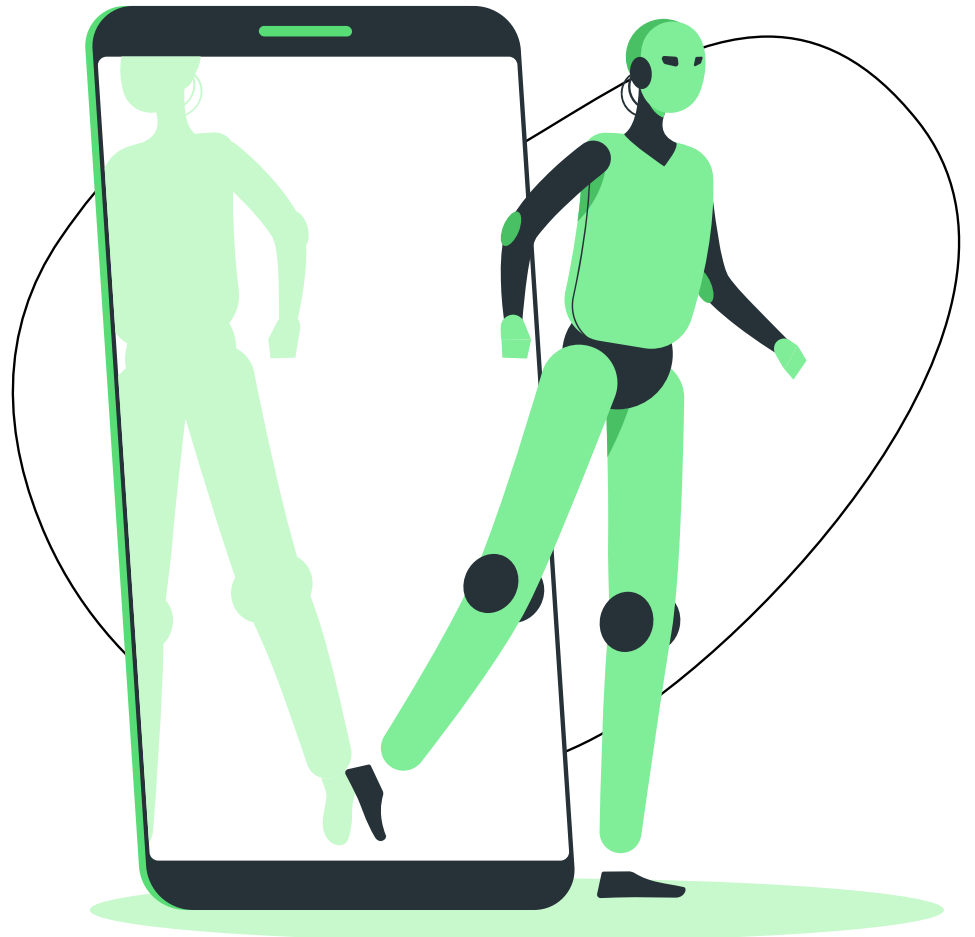
Stock price



A COMPUTER
CAN NEVER BE HELD ACCOUNTABLE

THEREFORE A COMPUTER MUST NEVER
MAKE A MANAGEMENT DECISION

Circa IBM, 1979



Thanks!

Additional Resources

- [StatQuest](#)
- [MIT OpenCourseware Intro to ML](#)
- Tensorflow (TF) python library



Questions

(talk to your neighbors!, individual submission)

Technical questions:

- 1) Will test loss ever equal 0? Why?
- 2) How does Deep Learning improve?
- 3) Can we *always* understand the models we create?

Journalism questions:

- 4) Before this presentation, do you think AI was accurately described in mass media?
- 5) How does the language used in headlines and news stories shape the public's expectations of Tesla's technology?
- 6) Would you ride in a self-driving car? Why or why not?

11. L'SPACE Mission Concept Academy



L'SPACE MCA

*Planetary Habitat Operations & ExploratioN
Investigation eXpedition*

MISSION CONCEPT REVIEW

TEAM 1 - P.H.O.E.N.I.X

Submission date - 6/15/2025



Table of Contents

Table of Contents	2
Table of Figures	3
Table of Acronyms	4
1.0 Mission Concept Review	5
1.1 Mission Statement	5
1.2 Science Traceability Matrix	6
1.3 Summary of Mission Location	10
1.4 Mission Requirements	12
1.5 Physical Environmental Hazards	15
1.6 System Evaluation Criteria	17
1.7 Concept of Operations	19
1.8 Alternative Mission Concepts	20
1.9 Programmatrics	23
1.9.1 Team Organization	23
1.9.2 Schedule Basis of Estimate	26
1.9.3 Budget Basis of Estimate	29
1.10 Conclusion	31
Bibliography or references	32
Declaration of Generative AI and AI-Assisted Technologies in the Writing Process	36
Appendix	37

Table of Figures and Tables

Figure 1.1: SWIM Map	11
Figure 1.2: TES Dust Cover Index + SWIM Map	11
Figure 1.3: Team 01 Organizational Chart	23
Figure 1.4: Team Leadership	24
Figure 1.5: Science Subteam	24
Figure 1.6: Engineering Subteam	25
Figure 1.7: Programmatic Subteam	25
Figure 1.8: Personnel Salary Cost Estimates	25
Table 1.1: Science Traceability Matrix	8
Table 1.2: Requirements Matrix	14
Table 1.3: Mission Role Descriptions	30

Table of Acronyms

Abbreviation	Definition
MCR	Mission Concept Review
SMD	Science Mission Directorate
STM	Science Traceability Matrix
ESDMD	Exploration Systems Development Mission Directorate
RTG	Radioisotope Thermoelectric Generator
ISRU	In-Situ Resource Utilization
MLI	Multi-Layered Insulation
GNC	Guidance, Navigation, and Control
IMU	Inertial Measurement Unit
GNSS	Global Navigation Satellite System
SWIM	Subsurface Water Ice Mapping
CRISM	Compact Reconnaissance Imaging Spectrometer for Mars
JMARS	Java Mission Planning and Analysis for Remote Sensing
JPL	Jet Propulsion Laboratory
ERE	Employee Related Expenses
LOX	Liquid Oxygen
CDH	Command and Data Handling
ConOps	Concept of Operations
PDR	Preliminary Design Review
CDR	Critical Design Review

SYS	System
-----	--------

1.0 Mission Concept Review

1.1 Mission Statement

P.H.O.E.N.I.X (Planetary Habitat Operations & Exploration Investigation eXpedition) is a low-cost, unmanned rover mission conceptualized to land in the northern mid-latitudes of Mars. The primary goal is to explore the area and analyze geological indicators of subsurface water and ice. The mission will pay particular attention to debris aprons, stratigraphy, and mineralogical composition to gather the most crucial data, which will be useful for future Mars expeditions. This mission aims to expand scientific knowledge of Mars' climate and determine information about the history of planetary water sources. Following in the footsteps of the 2008 Phoenix Mission, the team is emerging from the shadows of prior research and venturing into a new environment to support future human exploration by assessing dust risks and in-situ resource utilization (ISRU) potential.

Additionally, the mission aims to enhance scientific understanding of Mars' geological and climatic history and lay the groundwork for future human exploration of the Red Planet. This mission aligns with the goals of NASA's Science Mission Directorate (SMD) and Exploration Systems Development Mission Directorate (ESDMD) by providing a means of assessment for dust hazards and evaluating the feasibility of oxygen production. The collected data will support the development and adaptation of site locations and life-support systems for future landings by identifying subsurface water conditions and characterizing geological and atmospheric conditions.

1.2 Science Traceability Matrix

The P.H.O.E.N.I.X mission concept is intended to lay the groundwork for future human exploration efforts by investigating the environment through its conditions of dust, gases on the surface, temperatures, and ice that may be on the subsurface of Mars. Investigating atmospheric conditions will enable the understanding of water sources on the Martian planet by identifying glacier locations and analyzing them for safe and efficient use. P.H.O.E.N.I.X is derived from the objectives of interpreting how the environment on Mars can impact organisms, as well as how much it has changed over time, and its effect on the existence of water sources. This further study serves to better prepare for future human exploration by ensuring safe interactions with resources on Mars.

Testing the ratio of particular gases, such as Deuterium and Hydrogen, which are found in hydrated volcanic rocks on the surface of Mars, serves to track possible locations of water. Locations of a high D/H ratio will be beneficial to know of the potentiality of water, while other varying ratios can be compared to Earth's ratios to determine if that water can support life [13] [15]. This investigation will also lead to clarification of located water's history of where and how it was formed to trace past life and climate records.

Inspection of dust accumulation and characteristics of the Martian soil will give a perception of how accessible ice is to the surface for water extraction. Understanding the type of soil on Mars allows for efficient water extraction through the development and production of equipment that will accommodate easy access areas [1]. Comprehension of the behavior of dust storms on Mars will also aid in preventing hazards for the safety of astronauts and their equipment for long-term missions [2].

By examining the radiation effects on water samples taken with P.H.O.E.N.I.X on Mars, a rate of water conservation can be assured for astronauts through the use of a Radiation Assessment Detector [14]. With a variation of water samples, a deeper insight may be obtained into the best water system and water cycle for future Mars exploration and habitation efforts. Developing strategies and instrumentation for water recycling and preservation is critical to ensure astronauts' safety and ensure the crew is well-informed on how the effect of radiation on Mars will alter the chemical properties of water for precautionary use.

The impact between asteroids and subsurface ice on Mars can lead to the discovery of uniquely formed crystals that may contain water, which further motivates the goal of locating water. When an asteroid comes into strong contact with possible areas of ice, water may be heated or trapped within the crystal rocks formed from this

interaction [13]. This investigation explores the geological history of Mars and its evolution to the present state through the interaction between the dynamic internal and external forces on planet Mars that have formed and reshaped its surface through time. These interactions are evident to have changed the movement, stability, and distribution of water and can further give insight into how to locate preserved water life to select future landing sites for human missions.

Table 1.1

Science Goals	Science Objectives	Science Measurement Requirements		Instrument Performance Requirements		Predicted Instrument Performance	Instrument	Mission Requirements
		Physical Parameters	Observables					
“HBS-1LM: Understand the effects of short- and long-duration exposure to the environments of the Moon, Mars, and deep space on biological systems and health, using humans, model organisms, systems of human physiology, and plants” — Moon to Mars Objectives, NASA	Assess the Martian environmental impacts on varied enclosed and protected Earth water models for astronaut internal use, heat dissipation, LOX and methane rocket propellant, and agricultural recycling.	Receive and monitor water cycle data for potential radioactive isotope presence, chemical reactions, and environmental contamination that bypasses protected storage, generating new developments in material science to help ensure astronaut safety across the wide spectrum of water applications.	Use gamma spectrometry to monitor for alpha, beta, and gamma radiation at twelve intervals over a one-year period, logging data for transmission back to Earth.	TBD	TBD	TBD	TBD	TBD
				TBD	TBD	TBD		
				TBD	TBD	TBD		
				TBD	TBD	TBD		
	Investigate the effects of Martian dust accumulation and regolith characteristics on the accessibility and stability of near-surface water ice to	Measure regolith grain size, porosity, dust layer thickness, and thermal conductivity over target region.	Use GPR reflection delays, thermal probe data, and surface albedo variation to infer dust cover and subsurface ice location within a 10 km traverse.	TBD	TBD	TBD	TBD	TBD
				TBD	TBD	TBD		
				TBD	TBD	TBD		
				TBD	TBD	TBD		

	support in-situ resource utilization and reduce environmental health risks for future human missions.							
"Q10.3b: What are the long-term endogenic and exogenic controls on the presence of liquid water on terrestrial planets?"—Origins, Worlds, and Life: A Decadal Strategy for Planetary Science and Astrobiology 2023–2032	Determine the Deuterium to Hydrogen (D/H) ratio in hydrated volcanic rock on Mars' surface.	Define the relative abundance of protium and deuterium within samples of hydrogen from hydrated volcanic rock.	Collect absorbance spectra in the 2500–25,000 nm range of H in selected hydrated volcanic rock samples at multiple surface sites.	TBD	TBD	TBD	TBD	TBD
	Determine the crystal structure of minerals formed by asteroid impacts interacting with exposed subsurface ice.	Identify chemical structure, crystal structure, and bond structure of Olivine from asteroids.	Collect raman spectra in the 11,111–33,333 nm range of Olivine in selected asteroid rocks at multiple surface sites.	TBD	TBD	TBD	TBD	TBD

Table 1.1: Science Traceability Matrix

1.3 Summary of Mission Location

Mars is a terrestrial planet with a thin atmosphere composed mostly of carbon dioxide. Its surface, like other terrestrial planets, is covered with volcanoes, craters, and tectonic interactions. Mars has water in the form of ice at its poles and in glacial features. Dust storms and high radiation levels present challenges to future human expeditions. These features and challenges offer important data for missions such as P.H.O.E.N.I.X pertaining to human survival [17].

Erebus Montes, situated in Arcadia Planitia at approximately 39.0° N, 192.1° E, has been selected as the primary focus region for P.H.O.E.N.I.X. This selection for the mission location is determined by Erebus Montes' exceptional alignment with customer constraints, selected scientific objectives, and the need for terrain that offers a safe and feasible landing.

In alignment with customer location criteria, the mission location must be within a latitude of 60° North or South and may have any longitude, must be within a Potential High Priority Radar Targeting Zone, must be within 10 km of subsurface ice at a depth of 0-1m or within 5 km of an impact-exposed ice area. The data for this location shall be derived from SWIM maps, JMARS, and CRISM.

The Science Traceability Matrix (STM) focuses on several goals: investigating the stability and accessibility of near-surface water ice, characterizing Martian regolith and dust properties, determining the deuterium-to-hydrogen (D/H) ratio in hydrated volcanic rocks, and analyzing the mineralogy of asteroids that interacted with impact-exposed ice. Erebus Montes offers an excellent combination of features to address these goals [15].

Erebus Montes lies in the northern mid-latitudes, a zone repeatedly identified by NASA and the planetary science community as an attractive landing site to be further studied [24]. This region is shown to have abundant access to shallow, subsurface ice within the 0-1m depth and exposure of Hesperian-Noachian era terrain, an era marked by many asteroid impacts and volcanic activity [25] [26]. The exposure means Erebus Montes offers an abundance of impact craters that have exposed clean subsurface ice, with targets for mineralogical and crystal analysis and investigation into geological features such as lava tubes.

A few regions of interest in Erebus Montes align with the P.H.O.E.N.I.X. objectives include: 39.7° N, 190.6° E; 39.5° N, 194° E; 38.5° N, 192.8° E; 39.5° N, 191.5° E; and 37.9° N, 190.8° E. [25]. As a whole, these regions offer ice-rich lobate

debris aprons, Amazonian-aged subsurface ice, recent ice-exposing impact craters, buried craters, lava tube caves, contact with Amazonian volcanism, contact with Amazonian lava flows, and evidence for glacial and periglacial processes [25] [27].

Erebus Montes is a fairly dusty region, shown in *Figure 1.2*; however, due to the relatively flat grade in the area, there are suitable landing options to avoid the high dust regions when communication is most pertinent. [25] Therefore, Erebus Montes is the best option for P.H.O.E.N.I.X to reach a good balance between safety and the science objectives, while conforming to the customer requirements.

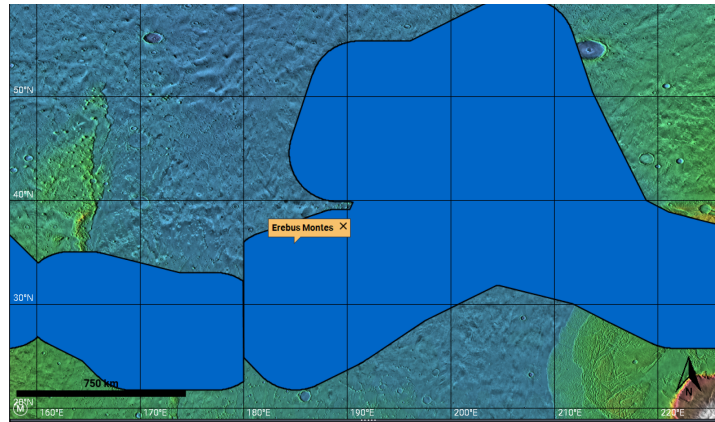


Figure 1.1: SWIM Map

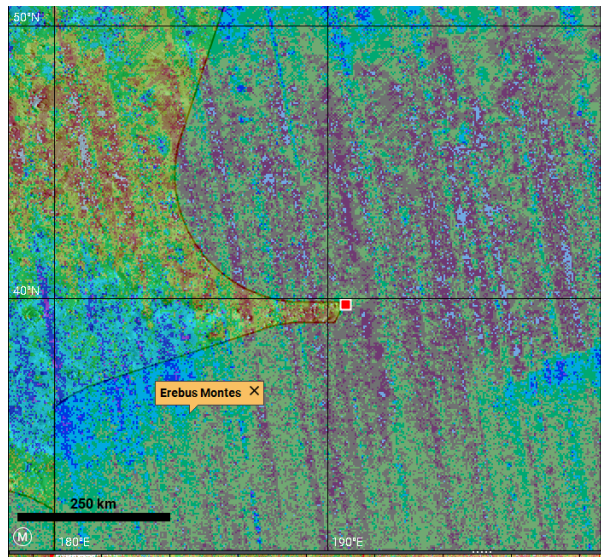


Figure 1.2: TES Dust Cover Index + SWIM Map

1.4 Mission Requirements

Customer constraints are a key driver of mission architecture, which determines the high-level requirements concerning mass, volume, and budget. Team P.H.O.E.N.I.X seeks to meet the system constraints presented by NASA, serving as the funding agency for the Mission Concept Academy's Discovery-class mission.

The spacecraft shall not exceed a mass of 200 kg. In a stored configuration, the spacecraft shall not exceed the dimensions of 2.5 m x 2.5 m x 2.5 m. This volume will house all the electronics, instruments, and payload suite. The spacecraft shall maintain the stored configuration for the entirety of the launch, transit, and entry into the Martian atmosphere. In an expanded form, there is no volume or mass constraint placed on the spacecraft. The spacecraft shall demonstrate resistance to temperatures consistent with atmospheric entry and descent. The spacecraft shall incorporate a landing attenuation system capable of withstanding surface impact.

After deployment on the landing site selected, the spacecraft shall traverse the terrain effectively to travel a minimum of 10 km. The spacecraft shall demonstrate an ability to traverse various Martian terrains, including sandy regions, icy regions, and small, medium, and large-sized rocks. The spacecraft shall demonstrate the ability to endure fluctuations in Martian atmospheric conditions, including dust storms, diurnal temperature variations, and reduced atmospheric pressure.

The spacecraft shall carry a scientific payload containing all instrumentation to complete science objectives. The volume of the scientific payload shall not exceed a cube of dimensions 0.5 m x 0.5 m x 0.5 m, nor a mass of 15 kg. This is to ensure the mission satisfies the human exploration goal and gets samples from the Martian surface that can be transmitted back to Earth for research. Furthermore, this research will contribute a great deal to the future of sustainability on Mars and future manned missions.

P.H.O.E.N.I.X is a discovery mission and not a flagship mission; hence, the budget allocated to this mission is 450 million USD and shall be used effectively for the manufacturing of the spacecraft, its components, employee-related expenses (ERE), and testing of the spacecraft. The Spacecraft system shall not have a Radioisotope Thermoelectric Generator (RTG) or any similar power generation system. Furthermore, any radioactive material is allowed for use on other spacecraft subsystems, but cannot exceed a cumulative mass of 5kg of radioactive material on all subsystems. The spacecraft must be ready for integration with the other systems by October 1st, 2029, and must be ready for launch on December 1st, 2029. The launch site shall be in Cape Canaveral in Florida.

Req #	Requirement	Rationale	Parent Req.	Child Req.	Verification Method
0.1	System shall survive the Martian environment for TBD years	The system must be able to survive the Martian environment to fulfill its purpose and send data back to earth ground station and potentially return Martian samples		SYS.02	Demonstration
0.2	Shall investigate the presence of ice glaciers on Mars for future missions and sustainability	Foundational science driver for the mission	Customer	SYS.01 SYS.03 SYS.05 SYS.06 SYS.07 SYS.08	Scientific Review
SYS.01	The system shall have sufficient power to carry out the objectives for the duration of its mission	System needs power to operate, communicate back to earth and carry out its objectives	0.1, 0.2		Test
SYS.02	System shall maintain operating temperatures and survive the harsh thermal environment on the Martian surface	The system and its scientific instrumentation must be kept in operating temperature ranges in order to function properly	0.1		Test
SYS.03	System shall traverse the Martian surface smoothly and reach the required science points of interest	Points of interests are marked across potential high priority Radar targeting zones on Mars that are defined by the thickness of the atmosphere to allow for easy landing and research point	0.2		Test
SYS.04	System shall not exceed a total mass of 200 kg	Constraints provided by NASA for the mission	Customer		Inspection
SYS.05	Critical systems including power shall have a backup capable of complete operation	In the case of failure, if a critical system fails, the backup can takeover and still carry out the mission	0.1		Analysis

SYS.06	System must withstand the solar winds for the duration of its mission	All components on the rover must be strong enough to withstand the strong solar winds on mars	0.1		Test
SYS.07	System shall send and receive data collected with the science instrumentation back to the earth ground station	Data sent back to the earth ground station about Mars will be essential to future scientific research for sustainability on mars	0.2		Analysis
SYS.08	System shall comply with all applicable planetary protocol regulations	NPR 8020.12D *Planetary Protection Provisions for Robotic Extraterrestrial Missions*	0.2		Analysis

Table 1.2: Requirements Matrix

1.5 Physical Environmental Hazards

Mars's harsh environment presents a myriad of challenges and potential setbacks for exploration. Using remotely operated spacecraft has its challenges, with a successful exploration mission being an undertaking that requires years of work and coordination. The challenges the red planet poses range from planet-wide dust storms at a magnitude unseen on Earth. Due to the thin atmosphere, temperatures are so variable that the surface temperature can be up to 24 degrees Celsius hotter than the atmospheric temperature, less than two meters from the surface [9].

One of the most notable hazards is dust storms and the damage inflicted by the dust. Mars is no stranger to planet-wide dust storms [1] [2], which ended Opportunity's mission [1]. While planet-wide dust storms are relatively rare, regional dust storms are a more regular occurrence [2]. These dust storms can prevent sunlight from reaching the rover, compromising solar power and potentially the mission itself. This also presents unknowns in the form of their impact on surface radiation and atmospheric circulation [3] and possibly affects the thermal systems via dust accumulation acting as insulation [1]. Dust accumulation could also potentially block or coat lenses on the science instruments and navigation cameras, presenting a risk to data collection and navigation.

The dust itself also poses a hazard as it is fine and abrasive, with an average radius of 1.5 μm [2]. The nature of the dust poses a wear and tear risk, especially around more delicate or exposed systems like joints [1]. These dust particles, which come in a wide range of sizes and shapes and can even get down to .1 μm in size [1], pose a threat to hardware if they were to penetrate the instruments.

Mars's temperature range also poses a hazard for a rover mission, with temperatures hitting as low as -153 degrees Celsius [4], and as such, this presents a challenge with keeping all electronic components within operational temperatures. At incredibly low temperatures, metals can become brittle [5], and any liquid components, such as lubricants, can freeze [1]. Moreover, the temperatures on Mars vary over a wide range, hitting highs of 21 degrees Celsius during the day in equatorial regions [6] and varying significantly a few feet off the surface from ground temperature [6]. Due to this, contraction and expansion due to temperature variation must be taken into account [1], and that could introduce stresses along the rover's body. This all speaks to how carefully a thermal system will have to be designed to keep all electronic parts within their operational temperature range.

Due to its almost nonexistent atmosphere, the Martian surface is also exposed to high amounts of radiation in the form of galactic cosmic rays and Solar energy particles

[1]. This radiation also poses a hazard for the electronics aboard and is known to cause circuitry issues [8]. The lack of an atmosphere also leaves the Martian surface vulnerable to radiation from solar flares, which can be more concentrated.

The terrain of Mars itself is a hazard, with the majority of the planet covered in rough terrain with prominent amounts of mountainous material and hilly and cratered material [10]. All these rough terrains would provide significant navigational hazards for surface exploration, with rugged terrain and large slopes creating the possibility of the rover flipping or being otherwise rendered incapable. The Martian surface also presents smaller-scale navigational risks, such as sharp jagged rock formations, such as the one Curiosity encountered in 2014 [9]. These small razor-like formations tore at Curiosity's wheels, and many more unexpected formations could await on the unexplored surface [16]. Especially since a formation like that one would not be visible from satellite imagery. The unknown minutia of the rocky terrain is in and of itself a hazard.

The impact of the spacecraft's trajectory on Mars must also be considered. Due to the different atmospheric conditions on Mars [12], which necessitate precision calculations for a successful entry and landing.

When it comes to planetary protection, it is also important to keep in mind appropriate standards of sterilization to prevent any microbes or bacteria from Earth from reaching Mars [11]. This is important to prevent contamination to the ecosystem of study on Mars, and prevent foreign life from interacting with any possible life on Mars. The potential life on Mars must be kept isolated lest terrestrial forms of microbial life overrun it. In order to accomplish this, multiple sterilization tests must be performed, which can last weeks to months to ensure the accuracy of data testing on Mars and the reduction of biological hazards on any potential Mars life systems [18].

Achieving a successful mission to Mars demands unwavering precision at every stage, as risks and challenges exist at every turn. Such challenges when it comes to Mars include weather patterns, radiation, and the terrain on which the spacecraft will land. It is crucial for the team members working on this mission to understand and mitigate the multiple physical environmental hazards present to ensure a successful mission for P.H.O.E.N.I.X.

1.6 System Evaluation Criteria

The primary criteria team P.H.O.E.N.I.X will use in the evaluation of different options for each spacecraft subsystem shall be cost efficiency to satisfactory design constraint completion. While P.H.O.E.N.I.X will develop a state-of-the-art system, evaluations of successful heritage systems from other missions will determine necessary subsystem redesign and what systems may be implemented similarly from previous missions. In these evaluations, the Technology Readiness Level (TRL) of the system at this phase would be a 6, despite previous performance due to intended readiness testing and system redesign. Though the system is intended for use in the same environment, system modifications in conjunction with distinct mission-necessary instrumentation and mass allocation

Previous success was found by the Sojourner Rover, which was manufactured by NASA's Jet Propulsion Laboratory (JPL), where the rover spent 83 days on Mars exploring the Martian terrain, taking chemical and atmospheric measurements. This rover was powered by Ga-As solar cells and a silver-zinc battery. The primary source of the rover's power was the solar array during daylight operation [6].

Considering the customer constraints given by L'SPACE, the team's rover may not utilize a Radioisotope Thermoelectric Generator (RTG), which leads to the most feasible option of using solar arrays to power the rover. Although the team's rover will utilize solar arrays, several factors will still influence its Technology Readiness Level (TRL). These include the various stresses the rover will encounter, differences in volume and mass constraints compared to the Sojourner rover due to the team's specific payload, the increased number of scientific instruments onboard, and the rover's capability to collect samples from the Martian surface, a task that Sojourner was not designed to perform.

Each terrain will present unique challenges to the rover to achieve the science goal of locating ice glaciers for deposits of ice below the surface of Mars, whereas Sojourner's goal was to demonstrate a low-cost method for delivering scientific instrumentation to the red planet. Additionally, the team must ensure that all of the systems, including the payload, maintain operating temperatures to survive the harsh thermal environment on the Martian surface with temperatures as low as -153 degrees Celsius and as high as 21 degrees Celsius at daylight time [6].

This will lead to making use of Multi Layered Insulation (MLI) as well as multiple heaters to balance the temperature fluctuations and ensure a high thermal inertia as the rover travels to various research points. The team would also want to ensure an accurate state estimate of the rover and pathfinding, for which there are various options

to be considered, such as an Inertial Measurement Unit (IMU) or Global Navigation Satellite System (GNSS) using the Mars Reconnaissance Orbiter, which is currently orbiting Mars. Many operating constraints affect how much power can be generated by the solar arrays and whether it can be enough to power the scientific instrumentation, rover propulsion, and the Command and Data Handling system (CDH).

1.7 Concept of Operations

P.H.O.E.N.I.X shall be a semi-autonomous exploration rover, designed to contribute to the goals of the NASA Science Mission Directorate (SMD) and Exploration Systems Development Mission Directorate (ESDMD). The Concept of Operations (ConOps) encompasses the operational steps across landing, all activities on the Martian surface, and decommission.

P.H.O.E.N.I.X shall begin surface deployment procedure upon T-1 sol, Martian day, of landing at the designated chosen landing site. The rover shall begin activation of the system operational instruments. The power systems shall first be stabilized. Upon power stabilization, the scientific instruments shall be deployed and brought online, and initial communication and telemetry tests shall be conducted. Thermal control systems shall be activated for the appropriate daylight temperature, which would include heaters, ensuring the electronics are within the operating temperature range. The rover shall then calibrate the scientific instruments and await initial command from ground operations located at Kennedy Space Center.

After verification of all systems, P.H.O.E.N.I.X shall begin autonomous travel to the designated science site at TBD rate of travel by the design of the rover and the environment, which shall occur at TBD sol after surface deployment procedure and instrumental calibration.

Traversing to the science site will take time; hence, P.H.O.E.N.I.X shall consist of a day mode and night mode to better allocate available power during the autonomous travel period. Night mode significantly reduces the travel rate and instrumental operation to aid with power conservation. In all modes, power will be focused on thermal control systems and maintaining appropriate temperatures throughout the system. The transition from day mode to night mode shall repeat throughout the Martian sol cycle during the autonomous travel period to the designated science site.

Upon arrival at the science site, P.H.O.E.N.I.X shall switch from either day or night mode to science mode. Once switched to science mode, P.H.O.E.N.I.X. will deploy its science instrumentation for use similarly to that of Mars 2020 Perseverance [28]. Once science instrumentation is deployed, P.H.O.E.N.I.X shall begin calibration of science instruments and ready systems for data collection.

Once science instruments have been successfully deployed and calibrated, P.H.O.E.N.I.X shall begin data and sample collection of ice on the Martian surface. P.H.O.E.N.I.X shall relay all collected data during its time in science mode to the Mars Reconnaissance Orbiter, which shall relay stored data to Earth for scientific research on the future of sustainability on Mars.

Upon completion of the data collection objectives at the designated travel site, P.H.O.E.N.I.X shall travel to the next site and repeat travel mode and science mode procedures until completion of the mission objective.

1.8 Alternative Mission Concepts

Before the finalization of the mission concept for PHOENIX, the team explored a range of alternative options. The team discussed various ideas for alternative mission designs. These alternatives addressed mission architecture, location, focusing on astronaut risk, and scientific objectives. The decisions were made collectively to ensure that the final mission met all assigned criteria, both scientific and practical. The proposed mission is aligned with NASA's strategic goals and reflects team consensus.

1.8.1 Objectives

The team evaluated several different possible science goals before selecting the final primary objective: Glacier depth tracking, seasonal glacial trends, geographic indicators of water artifacts, and geological water and ice indicators. Two that were ultimately not chosen due to mission constraints could be valuable on future missions.

Water chemicals: Will require detoxification technology or synthetic biological implementation, such as the use of a microbial bacterium called *Bacillus subtilis* strain 168, to remove the toxic perchlorate that is present within the Martian water. This will provide the increased logistical risk, plus the risk of the microbe not surviving deep space travel [20].

Ice depth: Human habitats will require large water supplies, and ice provides hope for water extraction for human consumption and potential propellant fuel via electrolysis to produce liquid oxygen (LOX) and methalox that can be utilized for interplanetary travel. By identifying the depth of ice and geographic features that indicate deeper ice formations, future habitation sites can be more effectively identified and selected. This is the objective that will be carried out for the mission.

1.8.2 Location

Two main geographical options were presented for landing and exploration: The mid-latitudes and the polar regions.

Mid-latitudes: The equatorial region of Mars provides more solar power, as well as more moderate temperatures than the polar regions, and it also offers fewer environmental risks for colonies. Another thing to consider when choosing the mid-latitude location is its geological value, as this specific zone contains many of the answers when it comes to investigating the Martian past.

Polar regions: Polar regions provide the highest chance of finding large volumes of ice. This ice will likely be very deep and difficult to analyze as a liquid, and melting

samples would require energy. The far polar regions also pose a risk of seasonal darkness as the poles point away from the sun. These annual dark periods also create seasonal water movements that can be only partially studied by satellite, requiring surface instrumentation.

1.8.3 Spacecraft Type

Telescope: The primary limitations of telescopes to observe terrestrial features are finite capabilities regarding chemical composition identification and observation during dust storms that are very frequent on Mars. There would be strong limitations by orbital paths creating short perception windows, and Martian weather formations, such as dust storms, limiting visibility. A telescope would drastically decrease mission costs, risks, and implementation timeline. Despite the decrease in costs and risks, telescoping technology wouldn't be ideal to study the Martian surface, as the orbital velocity of the telescope is extremely fast, up to thousands of meters a second, which is not ideal and leaves large gaps in transmission windows. Furthermore, it is not possible to identify ice using a telescope as it is buried beneath the Martian surface and would require further inspection using scientific instrumentation such as a spectrophotometer for accurate measurements and data.

Satellite: A satellite would provide a wide scanning area and long operational lifetime, but would have limited resolution, and would not be capable of collecting samples of physical quantities necessary to determine water depth or the chemical composition of a particular area. Measurements relating to water-created geographic formations would be entirely limited by the resolution on board; thus, a satellite is not ideal. Prior research done by the Mars Reconnaissance Orbiter is valuable. It brought back high-resolution imagery and subsurface data maps that could be studied on Earth. That information laid the groundwork for current missions being done by surface rovers and by rovers in the past decade. Currently, NASA's Perseverance [12] is collecting samples of Martian cores to return to Earth, which has never been done. Satellites and landers complement the science being done on Earth, while rovers bring new data and collect samples for study. These samples would provide invaluable new information and crucial analysis for further crewed missions.

Lander: A lander would allow for on-surface exploration and testing. A lander would introduce risks related to atmospheric entry, requiring additional subsystems, and therefore increase development and operational costs. A lander would not be able to travel from its initial landing location and would therefore be highly susceptible to any flight path deviations. A lander would also be limited to a single location for samples to

be collected, as it is a stationary vehicle and lacks the mobility instruments that a rover consists of.

1.8.4 Crewed Status

Manned: A manned mission would allow for practical experiments on human life on another planet, long-term effects of partial gravity; however would serve as a full system test for habitation modules, water sanitation systems, sustainable food sourcing, and air recycling systems. Many of these modules are not near enough to the application and would not be attainable with the mission budget. Furthermore, proposing a crewed mission would be unprecedented. The duration of a crewed mission poses imminent health risks for the crew. Current propulsion systems would be unable to land crews on Mars in fewer than nine months [19]. Long-term exposure to solar radiation both during the journey and during surface operations could be detrimental to the crewmembers. Producing a safe, long-term environment is an additional risk. Astronauts are unable to grow enough crops for sustenance while on the surface, and would face difficulties in producing the necessary amount of oxygen to sustain crop life.

Unmanned: An unmanned mission exploratory would be feasible within the allocated budget due to the lack of life support systems, and with reasonable hybrid remote control and autonomy, scientific experimentation is feasible for future habitation without uncertainty risk to human life. All of NASA's missions to Mars have been unmanned, which include the Phoenix lander [22], Curiosity rover [14], Sojourner rover [8], and Perseverance [16]. With temperatures going way below freezing point at night and much more than the boiling point at daytime [6]. Furthermore, the radiation levels are dramatically greater than what astronauts in the International Space Station (ISS) have experienced [12]. This makes a manned mission extremely dangerous and not cost-effective, as each seat on SpaceX's Dragon capsule or Starship will cost approximately 55 million USD [31]. As a discovery mission, a crew is not necessary to conduct the relevant science. It would also be very efficient to utilize hybrid autonomous mission control systems that have been the norm in most of NASA's missions.

1.9 Programmatics

1.9.1 Team Organization

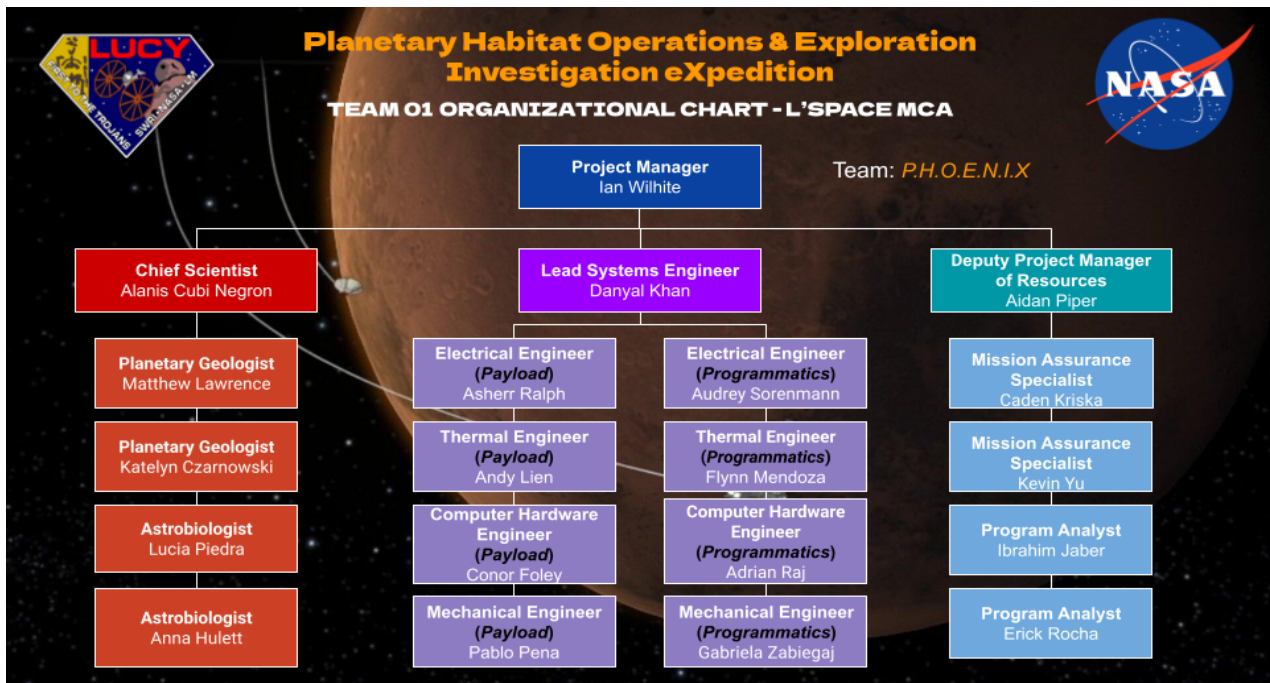


Figure 1.3: Team 01 Organizational Chart

Workloads for major deliverables will be analyzed by the team to determine relevant tasks to be assigned to each subteam as dictated by the project manager and/or team leads. To ensure consistent progress, team leads will further delegate tasks to specific individuals as it relates to their role within the sub-team (i.e., bases of estimate will be given to both a program analyst and a mission assurance specialist).

Team organization will follow the structure outlined by the organizational chart, shown in Figure 1.1. All subteam roles have two team members assigned to them, with engineering roles having the distinction of being either focused on payload integration or programmatic. Roles across the team were selected through a democratic voting process to select the best individuals for the role based on their prior roles and experience.

The decision-making process will consist of input from all team members regarding the particular problem, but will ultimately be up to the discretion of the project manager and team leads on a broader scale. In instances where a decision is time sensitive, relevant subteam members will be contacted for input if the team leads and project manager deem it necessary before making a final judgment. Additionally,

differences in team opinions will be handled through trade studies and analysis if time persists to fully comprehend the benefits and shortcomings of each approach. This approach allows for the input and analysis of all members to be considered, covering any potential biases that may be present. Considering this information, the team leads and the project manager will deliver a final decision regarding the issue. Should a scenario arise where there is not time for a fully-fledged trade study, the team will make a decision following the aforementioned protocol for time-sensitive decisions. Lastly, conflict resolution within the team will be addressed by the leadership team working with those involved to comprehend and resolve the scenario. LSPACE mentors and staff will be involved should the conflict either prove too challenging to de-escalate or the conflict involves the team leadership.

As a team, the members bring a range of prior skills and experience, ranging from aerospace industry internships, leadership, and hands-on experience in student organizations, to prior experience and completion of a LSPACE program, equipping the team with strong baseline capabilities, which will develop the mission concept. If there are any gaps in technical knowledge or confusion, the team will consult LSPACE resources such as skill modules or relevant role mentors. The following tables show a breakdown of the weekly time commitment of each team member as well as their role, with *Figure 1.1* being the team leads, *Figure 1.3* representing the science subteam, *Figure 1.4* for engineering, and *Figure 1.5* for programmatic:

TEAM LEADERSHIP		
Name	Role	Hrs/Week
Ian Wilhite	PM	10
Alanis Cubi Negron	CS	10
Danyal Khan	LSE	10
Aidan Piper	DPMR	10

Figure 1.4: Team Leadership

SCIENCE SUBTEAM		
Name	Role	Hrs/Week
Matthew Lawrence	Planetary Geologist	10-15
Katelyn Czarnowski	Planetary Geologist	8-10
Lucia Piedra	Astrobiologist	10
Anna Hulett	Astrobiologist	3-4

Figure 1.5: Science Subteam

ENGINEERING SUBTEAM		
Name	Role	Hrs/Week
Asherr Ralph	EE Payload	6-8
Audrey Sorenmann	EE Programmatic	8-15
Andy Lien	TE Payload	10
Flynn Mendoza	TE Programmatic	6-7
Conor Foley	CDH Payload	3-10
Adrian Raj	CDH Programmatic	10-15
Pablo Pena	ME Payload	3-4
Gabriela Zabiegaj	ME Programmatic	5

Figure 1.6: Engineering Subteam

PROGRAMMATIC SUBTEAM		
Name	Role	Hrs/Week
Caden Kriska	Mission Assurance Specialist	2-3
Kevin Yu	Mission Assurance Specialist	4
Ibrahim Jaber	Program Analyst	10
Erick Rocha	Program Analyst	4

Figure 1.7: Programmatic Subteam

1.9.2 Schedule Basis of Estimate

The Schedule Basis of Estimate spans phases C to F, beginning with the completion of the Mission Concept Academy (MCA) and ending with the completion of the mission lifecycle. Scheduling will be based on the assumption that all planning is centered around fiscal years instead of calendar years. This assumption allows for simplification as the integration date of October 1, 2029, aligns with the end of the federal fiscal year. P.H.O.E.N.I.X must be fully tested, integrated, and ready to launch to leverage the launch window to Mars on December 1st.

Ground Rules

The scope of analysis features phases C-F only, beginning at the submission of the Preliminary Design Review (August 18, 2025), and ending with the System Integration Date (October 1, 2029), followed by the Launch Readiness Date (December 1, 2029). These constraints reflect the narrow launch window to Mars and the necessary integration period before launch. A 15% time contingency is therefore imposed on the critical task path to mitigate risks from unexpected delays.

Assumptions

Fiscal Year (Oct 1–Sept 30) is used instead of calendar year to align with NASA and federal budget cycles. Phase C begins in FY26. Any acquisitions are slated to begin at the beginning of the next fiscal year after the completion of the CDR, projected to be Q3 of 2026. Personnel are expected to work at least the number of hours as stated in Tables 1-4 (Section 1.9.1) each week for approximately 44 to 48 weeks each fiscal year, considering federal holidays, vacations, and illness. The interest rate given by the financing agency is 2.6% APR. The launch, Entry Descent Landing system (EDL), and transit will be handled by contractors.

Drivers

Stakeholders for this mission shall determine its scope, and each stakeholder has mission expectations that must be accounted for in mission planning and execution.

The NASA Science Mission Directorate (SMD) serves as the mission sponsor and funding agency. The NASA Exploration Systems Development Mission Directorate (ESDMD) acts as a subsidiary of the NASA SMD, focusing on human exploration needs for interplanetary travel and habitation. The NASA SMD and ESDMD have interests relating to the feasibility of human habitation, and therefore, all scientific objectives must relate directly to the key directorates of the funding agencies, and propose feasible budgets and timelines to contribute meaningfully to their respective causes.

The MCA Team 01 serves to plan the P.H.O.E.N.I.X mission from Phases C–F. The team is interested in high-level system objectives and ensuring that all subsystems are designed, integrated, and tested to meet mission requirements for science return, reliability, and launch readiness.

The mission will outsource many subsystems to contractors. Contracted subsystems and processes include Entry Descent and Landing (EDL), Guidance, Navigation and Control (GNC), transit, and launch. These contractors will have an interest in clearly outlined documentation, timely expectations, open communication, budget allocations, and minimal redesign. **The contractors are interested in understanding the scope of work for the system and what can be done to accomplish the given scope as efficiently as possible.**

NASA Headquarters (HQ) will serve as a reviewing agency for all Key Decision Points (KDPs) before the beginning of each phase. HQ is interested in maintaining the established budget and timeline as initially proposed, and reviewing deliverable extensions and budget overages to determine continued mission feasibility. HQ is therefore interested in receiving comprehensive documentation for the entirety of the mission.

Kennedy Space Center (KSC) will serve as the largest contracting agency and will be ultimately responsible for launching the final design. The KSC is therefore interested in maintaining all timelines for integration tests and ensuring the on-site system integration date is upheld.

System Timeline

Phase C: Final Design (Q3 2025 – Q3 2026)

Phase C is primarily focused on finalizing the system design, followed by generating documentation as it pertains to the system, subsystem, and component, and the fabrication of the aforementioned elements. Additionally, all prior phase documentation is updated as trade studies are continued to provide a means of verification for later stages. Key requirements as set out in NPR(s) 7120.5 and 7123.1, where applicable. Phase C encompasses a CDR and PRR (project readiness review) before concluding with a SIR (system integration review) as major deliverables [29] [30].

Phase D: Assembly, Integration, & Test (Q4 2026 – Q3 2029)

Phase D consists of the full system integration and the development to attain a favorable assessment. Individual software and hardware components are evaluated and integrated before being assembled to validate and verify through testing conditions. Conditions are determined by previous trade studies and research meant to simulate

mission environments. Any issues that arise either during testing or in ensuring the system meets client expectations need to be addressed as well. All issues impeding system function must be resolved before the completion of the full system integration. Assuming a successful review at KDP 5, the system is then cleared to launch from the Kennedy Space Center in Cape Canaveral. Phase D closes out with a Post Launch Assessment Review (PLAR) as the vehicle is in transit to Mars [29] [30].

Phase E: Operations (Q4 2029 – TBD)

Phase E consists of early operations propelling towards Mars, cruise, Martian atmospheric Entry Descent and Landing (EDL), science conduction, and data return. This phase is where the main science needs that drive the mission are addressed through the onboard science payload. Engineering and science data obtained from the mission are transmitted back and analyzed, and final reports and post-flight evaluations are written. Plans regarding the decommissioning and deactivation of the system are finalized as the vehicle completes its flight. [29]

Phase F: Closeout (TBD)

After the functional life of the rover, mission staff will begin post-mission data analysis, then final reporting and decommissioning. The functional life of the rover is TBD, and dependent on system performance, environmental factors including dust storms, and instrumentation accuracy. Post-mission data analysis will include developing data-driven conclusions of science objectives as described in the Science Traceability Matrix (STM). Final reporting will include analysis of engineering system performance, failure analysis on any system degradation, and a consolidated evaluation of system operational performance.

1.9.3 Budget Basis of Estimate

The Budget Basis of Estimate for P.H.O.E.N.I.X is developed for phases C through F of the mission's life cycle. To determine a Budget Basis of Estimate, a few key rules, drivers, and assumptions will be made: Firstly, a \$450M cost cap is established specifically for the Rover System as given by the Mission Task Document. All other components of the mission will have independent budgets that are managed separately. Secondly, a fixed rate inflation of 2.6% annually will be assumed following the practice of NASA. Third, the team will use the following Salary Estimation Table (Table 1.4) for estimating the personnel budget, derived from the mission task document and adjusted for the 28% benefits rate. The table assumes a minimal team of all current members without any additional support staff to provide a cost floor and will be further refined. In addition, funding should be allocated for 30 additional support staff, assumed to be split $\frac{2}{3}$ technicians and the remainder engineers or scientists, depending on mission phase. A breakdown of the roles can be found in Table 1.3.

Role	Description
Scientists	Responsible for mission experiment design and data analysis.
Engineers	Responsible for engineering decision making for P.H.O.E.N.I.X assembly, design, and testing.
Technicians	Responsible for assisting and providing technical support to engineers and scientists with manufacturing, testing, and assembling P.H.O.E.N.I.X.
Administration	Responsible for handling human resources, scheduling, and mission cost tracking.
Managers	Responsible for organizing mission budgets, scheduling, personnel, and key teams for mission success

Table 1.3: Mission Role Descriptions

PERSONNEL SALARY COST ESTIMATIONS		
Role	Salary (\$/yr)	Count
Scientists	102,400	4
Engineers	102,400	8
Technicians	76,800	0
Administration	76,800	4
Management	153,600	4

Figure 1.8: Personnel Salary Cost Estimates

Personnel travel costs will be estimated through the City Pair Program for airfare in addition to lodging through Fedrooms and per diem reimbursement for meals and rentals. Tests are conducted at relevant NASA centers across the country, and launch takes place at Cape Canaveral, Florida. Key personnel will be flown in to oversee and conduct in-person testing of relevant components and subsystems with rental cars, lodging, and meals priced out using the aforementioned resources [19] [21].

Outreach costs are costs that relate to the team's effort in increasing public awareness of P.H.O.E.N.I.X and the impact that it will have on the scientific community and the end science goals.

A detailed budget for P.H.O.E.N.I.X will be developed as it advances towards the PDR (Preliminary Design Review). The budget will include breakdowns of costs for each Phase of the mission as well as a per-item cost breakdown. Following the totals of each component budget, a safety factor of 1.3 will be applied for any delays, hiccups, and potential issues that may arise during the mission's lifetime. Also referred to as the Total Cost Margin at the PDR stage.

1.10 Conclusion

The P.H.O.E.N.I.X mission concept successfully addresses key scientific objectives related to the assessment of Martian water accessibility, dust risks, regolith properties, and environmental hazards, with a clear focus on enabling safe and sustainable future human exploration. By targeting the northern polar region of Mars and building on prior missions such as the 2008 Phoenix lander [22], the team has established a coherent science traceability matrix that aligns with NASA's strategic goals for human spaceflight, ISRU development, and environmental safety [23]. This MCR demonstrates the mission's feasibility, with well-defined objectives, a compelling scientific rationale, and a forward-looking vision for data-driven site selection and astronaut health protection.

Looking ahead, the team will transition toward the System Requirements Review (SRR) by refining instrument specifications, defining mission requirements, and addressing current TBDs in performance metrics and hardware integration. Furthermore, the team would expand on its instrument calibration plans, simulate data return paths, and further evaluate terrain navigation strategies for enhanced landing and sampling precision. These developments will ensure the mission's continued maturity into the Preliminary Design Review (PDR) phase and position P.H.O.E.N.I.X as a foundational effort in supporting the long-term goal of Mars habitation.

Bibliography or references

1. Neukart, Florian. "Towards Sustainable Horizons: A Comprehensive Blueprint for Mars Colonization." *Heliyon*, February 15, 2024.
<https://pmc.ncbi.nlm.nih.gov/articles/PMC10884476/#se0160>.
2. He, Fei, Zhaojin Rong, Zhaopeng Wu, Jiawei Gao, Kai Fan, Xu Zhou, Limei Yan, Yuqi Wang, and Yong Wei. "Martian Dust Storms: Reviews and Perspective for the Tianwen-3 Mars Sample Return Mission." *MDPI*, July 17, 2024.
<https://www.mdpi.com/2072-4292/16/14/2613>.
3. Martinez, G. M., C. N. Newman, A. De Vicente-Retortillo, E. Fischer, N. O. Renno, M. I. Richardson, A. G. Fairén, et al. "The Modern Near-Surface Martian Climate: A Review of in-Situ Meteorological Data from Viking to Curiosity - Space Science Reviews." *SpringerLink*, April 25, 2017.
<https://link.springer.com/article/10.1007/s11214-017-0360-x>.
4. "It's Cold on Mars - NASA Science." *NASA*, October 18, 2024.
<https://science.nasa.gov/blog/its-cold-on-mars/>.
5. Chernov, V.M., B.K. Kardashev, and K.A. Moroz. "Low-Temperature Embrittlement and Fracture of Metals with Different Crystal Lattices – Dislocation Mechanisms." *Nuclear Materials and Energy*, April 8, 2016.
<https://www.sciencedirect.com/science/article/pii/S235217911530017X>.
6. "Mars Pathfinder - NASA Science." *NASA*, November 6, 2024.
<https://science.nasa.gov/mission/mars-pathfinder/>.
7. "Mars Reconnaissance Orbiter - NASA Science." *NASA*, March 25, 2025.
<https://science.nasa.gov/mission/mars-reconnaissance-orbiter/>.

8. Greicius, Tony, and Naomi Hartono, eds. "Mars Pathfinder - Mars Missions - NASA Jet Propulsion Laboratory." NASA. Accessed June 13, 2025.
<https://www.jpl.nasa.gov/missions/mars-pathfinder-sojourner-rover/>.
 9. "Mars: Facts - NASA Science." NASA, April 22, 2025.
<https://science.nasa.gov/mars/facts/>.
10. A review of thrust-vectoring schemes for fighter applications | Joint Propulsion Conferences. Accessed June 14, 2025.
<https://arc.aiaa.org/doi/abs/10.2514/6.1978-1023>.
11. The unseen impact of cosmic rays on electronics. Accessed June 11, 2025.
<https://www.electronicsspecifier.com/news/blog/the-unseen-impact-of-cosmic-rays-on-electronics>.
 12. Howell, Elizabeth. "Radiation Resistance Is Baked into the Perseverance Mars Rover. Here's Why That's Important." Space, May 6, 2021.
<https://www.space.com/mars-rovers-radiation-protection-xilinx>.
 13. "Curiosity Science Highlights - NASA Science." NASA, May 28, 2025.
<https://science.nasa.gov/mission/msl-curiosity/science-highlights/#Water>.
 14. "Curiosity Science Instruments - NASA Science." NASA, April 7, 2025.
<https://science.nasa.gov/mission/msl-curiosity/science-instruments/>.
 15. TM; Donahue. "Evolution of Water Reservoirs on Mars from D/H Ratios in the Atmosphere and Crust." Nature. Accessed June 14, 2025.
<https://pubmed.ncbi.nlm.nih.gov/7700352/>.

16. Hand, Eric. "Road Hazards Threaten Rover: To Limit Wheel Damage from Sharp Rocks, the Curiosity Mars Rover Detours into Sandy Valleys." *Science* 345, no. 6195 (2014): 365–66. <http://www.jstor.org/stable/24745098>.
17. "USGS I-1083 Geologic Map of Mars." Lunar and Planetary Institute (LPI). Accessed June 13, 2025. https://www.lpi.usra.edu/resources/mars_maps/1083/.
18. "Planetary Protection: How to Explore Mars and Other Worlds Responsibly." The Planetary Society. Accessed June 13, 2025. <https://www.planetary.org/articles/planetary-protection-explore-responsibly>.
19. "Mars - NASA Science." NASA, May 19, 2025. <https://science.nasa.gov/mars/>.
20. "Detoxifying Mars: The Biocatalytic Elimination of Omnipresent Perchlorates." NASA, January 4, 2024. <https://www.nasa.gov/general/detoxifying-mars/>.
21. https://www.gsa.gov/travel/plan-book/per-diem-rates/per-diem-rates-results?action=perdiems_report&fiscal_year=2025&state=FL
22. "Mars Phoenix - NASA Science." NASA, November 3, 2024. <https://science.nasa.gov/mission/mars-phoenix/>.
23. Keeter, Bill. 2024. "NASA Strategic Plan - NASA." Nasa.gov. February 13, 2024. <https://www.nasa.gov/ocfo/strategic-plan/>.
24. Lunar and Planetary Institute. 2015. First Landing Site/Exploration Zone Workshop for Human Mission to Mars. LPI Contribution No. 1879. Houston, TX: Lunar and Planetary Institute. https://www.lpi.usra.edu/lpi/contribution_docs/LPI-001879.pdf.

25. Viola, D. A., and R. E. Milliken. 2015. "Mid-Latitude Martian Ice as a Target for Human Exploration, Astrobiology, and In Situ Resource Utilization." Houston, TX, June 8–10. Houston: USRA-Houston.
<https://www.hou.usra.edu/meetings/explorationzone2015/pdf/1011.pdf>.
26. Warner, Nicholas H., Sukesh Gupta, Shih-Yuan Lin, Jung-Rack Kim, Jean-Pierre Müller, and Julie Morley. 2010. "Late Noachian to Hesperian Climate Change on Mars: Evidence of Episodic Warming from Transient Crater Lakes Near Ares Vallis." *Journal of Geophysical Research: Planets* 115 (E6).
<https://doi.org/10.1029/2009JE003522>.
27. Sinha, Rishitosh K., and Dwijesh Ray. 2021. "Extensive Glaciation in the Erebus Montes Region of Mars." *Icarus* 367: 114557.
<https://doi.org/10.1016/j.icarus.2021.114557>.
28. NASA. 2020. "Mars 2020/Perseverance National Aeronautics and Space Administration." https://mars.nasa.gov/files/mars2020/Mars2020_Fact_Sheet.pdf.
29. "3.0 NASA Program/Project Life Cycle." NASA, June 7, 2024.
<https://www.nasa.gov/reference/3-0-nasa-program-project-life-cycle/>.
30. NASA. *NASA Procedural Requirements 7120.5E: NASA Space Flight Program and Project Management Requirements*. Accessed June 15, 2025.
<https://nодis3.gsfc.nasa.gov/displayDir.cfm?t=NPR&c=7120&s=5E>.
31. NASA Office of Inspector General.
<https://oig.nasa.gov/>

Declaration of Generative AI and AI-Assisted Technologies in the Writing Process

During the preparation of this document, the team used OpenAI's ChatGPT to assist with re-phrasing and content refinement. The tool was used to rephrase content for conciseness and completeness. After using this tool, the team reviewed and edited all content to ensure accuracy, original contribution, and technical fidelity. Team 01 takes full responsibility for the content of this deliverable.

Appendix

TBD / TBR #	Plans and Timeline for Resolution
1	STM will be complete when instrumentation is selected
2	Requirements will be solidified after the instrumentation is selected.
3	Rover performance metrics will be decided after system integration
4	Rover landing time will be decided after testing and demonstration.
5	Rover travel rate will be decided after testing of the whole system
6	Scientific Instrumentation Calibration time after testing scientific instrumentation.

Table A.1

Discussion:

Currently in the STM, there are some TBD sections that will mainly be decided after the science team selects the instrumentation needed for the mission and together with the engineering team finalize on the number and type of scientific instruments to use. Requirements will be more specific after the rover has been designed and analyzed with different modeling simulations and tested in an artificial environment to give a rough idea of how long the systems will last on Martian soil. Rover landing time will be decided on the launch date, when the launch window is open and the scientific instrumentation calibration will also be decided after rigorous testing of each instrument before the rover is set to land on Mars.



L'SPACE MCA

*Planetary Habitat Operations & ExploratioN
Investigation eXpedition*

SYSTEM REQUIREMENTS REVIEW

TEAM 1 - P.H.O.E.N.I.X

Submission date - 7/7/2025



Table of Contents

Table of Contents	2
Table of Figures and Tables	5
Table of Acronyms	6
1.0 System Requirements Review	10
1.1 Mission Statement	10
1.2 Science Traceability Matrix	11
Figure 1.2.1: Science Traceability Matrix	14
1.3 Summary of Mission Location	15
1.4 Mission Requirements	17
Figure 1.4.1: Requirements Table	18
1.5 System Definition	19
1.5.1 Spacecraft Overview	19
Figure 1.5.1.2: System Requirements Table	23
1.5.2 Mechanical Subsystem	24
1.5.2.1 Mechanical Subsystem Requirements	24
1.5.2.2 Mechanical Subsystem Overview	24
Figure 1.5.2.2.1: High-Level Rover Concept	25
Figure 1.5.2.2.2: Mass, Volume, and Power Subassembly Estimates	26
Figure 1.5.2.2.3: Mechanical Subassembly Requirements Table	26
1.5.2.3 Mechanical Subsystem Trade Studies	26
Figure 1.5.2.2.1: Leg Material Trade Study	26
Figure 1.5.2.2.2: Chassis Material Trade Study	27
Figure 1.5.2.2.3: Wheel Material Trade Study	28
Figure 1.5.2.2.4: Wheel Tread Trade Study	29
1.5.3 Power Subsystem	30
1.5.3.1 Power Subsystem Requirements	30
1.5.3.2 Power Subsystem Overview	30
Figure 1.5.3.2.1 Power Subassembly TRL Table	33
Figure 1.5.3.2.2 Power Subassembly Mass, Volume, and Power Estimate	33
1.5.3.3 Power Subsystem Trade Studies	33
Figure 1.5.3.3.1 Dust Mitigation Technologies Trade Study	33
Figure 1.5.3.3.2 Solar Panel Deployment Trade Study	34
Figure 1.5.3.3.3 Photovoltaic Cell Type Trade Study	35
Figure 1.5.3.3.4 Power and Battery Trade Study	36
Figure 1.5.3.3.5 Isolated Power System Trade Study	37
1.5.4 Command and Data Handling (CDH) Subsystem	38

1.5.4.1 CDH Subsystem Requirements	38
Figure 1.5.4.2.1: Software Architecture Flowchart	40
1.5.4.3 CDH Subsystem Trade Studies	41
Figure 1.5.4.3.1: Onboard Computer Trade Study	41
Figure A.1: RAD5545 SpaceVPX single-board computer	42
Figure 1.5.4.3.4: Data Interfaces Trade Study	43
Figure A.3: RS-422 Pinout Table	44
Figure 1.5.4.3.6: Telecommunications Trade Study	44
1.5.5 Thermal Management Subsystem	46
1.5.5.1 Thermal Management Subsystem Requirements	46
Figure 1.5.5.2.1: Thermal Subassemblies	48
Figure 1.5.5.2.2: Heat Flow Maps	49
1.5.5.3 Thermal Management Subsystem Trade Studies	49
Figure 1.5.5.3.1: MLI (Outer Layer) Trade Study	49
Figure 1.5.5.3.3: Heat Pipes Trade Study	51
Figure 1.5.5.3.4: Electrical Heater Trade Study	52
Figure 1.5.5.3.5: Thermal Sensor Trade Study	53
1.5.6 Payload Subsystem	54
1.5.6.1 Payload Subsystem Requirements	55
1.5.6.2 Payload Subsystem Overview	56
Figure 1.5.6.2.1: Instrumentation Table	59
1.5.6.3 Payload Subsystem Trade Studies	59
Figure 1.5.6.3.1: Thermal Management Requirements Table	59
Figure 1.5.6.3.2: Ice Accessibility Instrumentation Trade Study	60
Figure 1.5.6.3.4: HDO and H ₂ O Transmittance Spectrum from Curiosity [54]	62
Figure 1.5.6.3.5: Crystal Structure Instrumentation Trade Study	63
1.5.7 Recovery and Redundancy	63
1.5.8 Interface Control	66
Figure 1.5.8.1: N ² System Interfaces Chart	66
Figure 1.5.8.2: System Block Diagram	70
1.6 Risk Analysis	72
Figure 1.6.1: Risk Matrix	73
Figure 1.6.2: Risk Analysis Matrix	76
1.7 Programmatic	77
1.7.1 Organizational Chart	77
Figure 1.7.1: Organizational Chart	77
1.7.2 Schedule Basis of Estimate	78
Ground Rules	78

Assumptions	78
Drivers	79
1.7.3 Schedule Estimate	79
1.7.4 Cost Basis of Estimate	81
1.7.5 Cost Estimate	82
Figure 1.7.5.1: P.H.O.E.N.I.X Preliminary Budget and Pie Chart	83
1.7.6 Change Control	83
Figure 1.7.6.1: Life Cycle Cost Model	84
1.8 Conclusion	84
References/Bibliography	85
Declaration of Generative AI	94
Appendix	95
Table A.1	96
Figure A.2(RAD5545 SpaceVPX single-board computer)	97

Table of Figures and Tables

Figure 1.2.1: Science Traceability Matrix	14
Figure 1.4.1: Requirements Table	18
Figure 1.5.1.2: System Requirements Table	23
Figure 1.5.2.2.1: High-Level Rover Concept	25
Figure 1.5.2.2.2: Mass, Volume, and Power Subassembly Estimates	26
Figure 1.5.2.2.3: Mechanical Subassembly Requirements Table	26
Figure 1.5.2.2.1: Leg Material Trade Study	26
Figure 1.5.2.2.2: Chassis Material Trade Study	27
Figure 1.5.2.2.3: Wheel Material Trade Study	28
Figure 1.5.2.2.4: Wheel Tread Trade Study	29
Figure 1.5.3.2.1 Power Subassembly TRL Table	33
Figure 1.5.3.2.2 Power Subassembly Mass, Volume, and Power Estimate	33
Figure 1.5.3.3.1 Dust Mitigation Technologies Trade Study	33
Figure 1.5.3.3.2 Solar Panel Deployment Trade Study	34
Figure 1.5.3.3.3 Photovoltaic Cell Type Trade Study	35
Figure 1.5.3.3.4 Power and Battery Trade Study	36
Figure 1.5.3.3.5 Isolated Power System Trade Study	37
Figure 1.5.4.2.1: Software Architecture Flowchart	40
Figure 1.5.4.3.1: Onboard Computer Trade Study	41
Figure A.1: RAD5545 SpaceVPX single-board computer	42
Figure 1.5.4.3.4: Data Interfaces Trade Study	43
Figure A.3: RS-422 Pinout Table	44
Figure 1.5.4.3.6: Telecommunications Trade Study	44
Figure 1.5.5.2.1: Thermal Subassemblies	48
Figure 1.5.5.2.2: Heat Flow Maps	49
Figure 1.5.5.3.1: MLI (Outer Layer) Trade Study	49
Figure 1.5.5.3.3: Heat Pipes Trade Study	51
Figure 1.5.5.3.4: Electrical Heater Trade Study	52
Figure 1.5.5.3.5: Thermal Sensor Trade Study	53
Figure 1.5.6.2.1: Instrumentation Table	59
Figure 1.5.6.3.1: Thermal Management Requirements Table	59
Figure 1.5.6.3.2: Ice Accessibility Instrumentation Trade Study	60
Figure 1.5.6.3.4: HDO and H2O Transmittance Spectrum from Curiosity [54]	62
Figure 1.5.6.3.5: Crystal Structure Instrumentation Trade Study	63
Figure 1.5.8.1: N^2 System Interfaces Chart	66
Figure 1.5.8.2: System Block Diagram	70

Figure 1.6.1: Risk Matrix	73
Figure 1.6.2: Risk Analysis Matrix	76
Figure 1.7.1: Organizational Chart	77
Figure 1.7.5.1: P.H.O.E.N.I.X Preliminary Budget and Pie Chart	83
Figure 1.7.6.1: Life Cycle Cost Model	84
Figure A.2(RAD5545 SpaceVPX single-board computer)	97

Table of Acronyms

Abbreviation	Definition
AC	Alternating Current
ADV	Action/Decision Vector
AI	Artificial Intelligence
APR	Annual Percentage Rate
AZUR	AZUR Space Solar Power GmbH
BOL	Beginning of Life
CAD	Computer-Aided Design
CCB	Change Control Board
CCHP	Constant Conductance Heat Pipe
CDH	Command and Data Handling
CDR	Critical Design Review
CF	Carbon Fiber
CM	Configuration Management
ConOps	Concept of Operations
COTS	Commercial Off-The-Shelf
CP-MU	Critical Protection - Monitoring Unit
CRISM	Compact Reconnaissance Imaging Spectrometer for Mars
DC	Direct Current

Abbreviation	Definition
DMU	Data Management Unit
DRE	Dust Removal Efficiency
DSN	Deep Space Network
DSON	Deep Space Optical Network
ECR	Engineering Change Request
ECC	Error-Correcting Code
EDS	Electrodynamic Dust Shield
EMI	Electromagnetic Interference
ERE	Employee Related Expenses
ESDMD	Exploration Systems Development Mission Directorate
FMEA	Failure Modes and Effects Analysis
FPS	Fluid Protection System
GNC	Guidance, Navigation, and Control
GNSS	Global Navigation Satellite System
GPR	Ground Penetrating Radar
HBS	Human Biology System
HDO	Semi-heavy Water (Hydrogen-Deuterium Oxide)
IMU	Inertial Measurement Unit
ISRU	In-Situ Resource Utilization

Abbreviation	Definition
JMARS	Java Mission Planning and Analysis for Remote Sensing
JPL	Jet Propulsion Laboratory
LOX	Liquid Oxygen
MCCET	Mission Concept Cost Estimate Tool
MCR	Mission Concept Review
MG	Mission Goal
Mini-TLS	Miniature Tunable Laser Spectrometer
MLI	Multi-Layered Insulation
MRO	Mars Reconnaissance Orbiter
MDR	Mission Definition Review
PCM	Phase Change Material
PDR	Preliminary Design Review
PLM	Product Lifecycle Management
PDS	Power Distribution System
PWR	Power
RAD	Radiation Assessment Detector
RFI	Radio Frequency Interference
RIMFAX	Radar Imager for Mars' Subsurface Experiment
RLS	Raman Laser Spectrometer

Abbreviation	Definition
ROI	Region of Interest
ROSE	Roll-Out Solar Array
RSR	Remote Sensing Reflectance
RTG	Radioisotope Thermoelectric Generator
SDR	Software Defined Radio
SMD	Science Mission Directorate
SRB	Systems Review Board
SRR	System Requirements Review
STM	Science Traceability Matrix
SYS	System
TCS	Thermal Control System
TBD	To Be Determined
TBR	To Be Resolved
TLS	Tunable Laser Spectrometer
TRL	Technology Readiness Level
UHF	Ultra High Frequency
VCHP	Variable Conductance Heat Pipe

1.0 System Requirements Review

1.1 Mission Statement

P.H.O.E.N.I.X (Planetary Habitat Operations & Exploration InvestigatioN eXpedition) is a low-cost, unmanned Mars rover mission designed to investigate subsurface ice reservoirs and characterize environmental hazards to support future human exploration. As part of NASA's Discovery-class architecture, the mission will land in the northern mid-latitudes of Mars, a region with high potential for shallow subsurface ice, favorable solar access, and traversable terrain. The mission aligns with the priorities of NASA's Science Mission Directorate (SMD) and Exploration Systems Development Mission Directorate (ESDMD) by targeting in-situ resource utilization (ISRU), hazard mitigation, and habitability research.

Science goals are derived from NASA's HBS-1LM Moon to Mars Objective and the Origins, Worlds, and Life Decadal Strategy goal Q10.3b. Four key objectives guide the mission: (1) assess the effects of radiation on a pressurized Earth-fluid sample using a submersible gamma neutron probe, informing ISRU and life support safety; (2) analyze subsurface stratigraphy and dielectric properties with RIMFAX radar to evaluate ice accessibility; (3) determine the Deuterium-to-Hydrogen (D/H) ratio in hydrated volcanic rock with a Miniature Tunable Laser Spectrometer to trace water source evolution; and (4) identify the crystal structure of asteroid-impact minerals using a Raman Laser Spectrometer to study endogenic and exogenic processes affecting water distribution.

To accomplish these objectives, P.H.O.E.N.I.X is engineered for long-duration autonomous operation in harsh Martian conditions. Its mechanical subsystem utilizes a heritage rocker-bogie suspension, titanium fittings, and an aluminum chassis for resilient mobility across 10+ km of variable terrain. The power subsystem includes ROSA-style solar panels, a 500 Wh lithium-ion battery, and a smart distribution unit for efficient, fault-tolerant energy management. The CDH system features radiation-hardened processing and redundant communication pathways. Thermal control maintains internal temperatures from -120°C to +30°C using multilayer insulation and resistive heating. All subsystems meet planetary protection guidelines and mission constraints on mass, volume, and cost.

By locating accessible water ice, monitoring radiation exposure, and expanding understanding of Martian water cycles, P.H.O.E.N.I.X delivers critical data to guide astronaut landing site selection and surface system design. The mission represents a significant step toward enabling a sustainable human presence on Mars.

1.2 Science Traceability Matrix

The STM focuses on two main goals for the mission. The first goal is the Human Exploration goal, HBS-1LM, which is addressed by two objectives. The first objective shown in the STM aims to investigate the long duration Martian environmental impacts on a protected and pressurized earth-fluid sample, documenting unknown hazards that may threaten the integrity of future mission-critical life support, rocket propellant, and agricultural fluids in transportation, long-duration storage, and recycling. The CP-MU DMU-100 Submersible Gamma Neutron Probe was chosen to complete the objective, using a passive ionization chamber to monitor gamma radiation levels in $\mu\text{Sv/h}$ and recording data at weekly intervals over a one-year period for transmission back to Earth. The second science objective shown in the STM, aims to investigate how subsurface stratigraphy, dielectric properties, and dust layer thickness influence the accessibility and long-term stability of near-surface ice. The Radar Imager for Mars' Subsurface Experiment (RIMFAX) is the selected instrument for this objective, using ground-penetrating radar to analyze radar signal delays and reflection strength, allowing to identify subsurface layer boundaries, material transitions, and dielectric properties indicative of dust and possible ice-rich zones [18]. From these observables, dielectric permittivity and radar wave velocity can be estimated to derive subsurface material properties such as layer thickness, composition variation, and porosity across a 10 km traverse [18]. There is direct alignment with NASA's HBS-1LM science goal of understanding the environmental effects, risks, and hazards faced when exposing mission-critical fluids and their protective storage systems to the harsh Martian surface during long-duration missions, as safeguarding life support systems, rocket propellant, and recycled fluids from radiation hazards is vital to mission success, astronaut health, and prevention of physical injury from depressurization and stable access to subsurface ice is essential for life support, fuel production, and long-term habitat sustainability. In addition, these objectives support mission constraints by operating within the instrument's 15kg allocated mass, volume constraint, and resolution requirements while providing essential periodic data that will advance material science and engineering innovation for fluid storage systems that will be utilized during long-duration missions on Mars and environmental data to inform ISRU planning and reduce operational risk in future human missions to Mars [23, 31].

The second goal is the Science Exploration goal, Q10.3b, which is also addressed by two objectives. In the first objective the deuterium-to-hydrogen ratio in hydrated volcanic rock serves as a geochemical tracer in understanding the history of water on Mars by providing insights into the sources, losses, and recycling of water. Using the Miniature Tunable Laser Spectrometer (TLS) the objective will collect absorbance spectra in the 2500–25,000 nm range of H in selected hydrated volcanic rock samples at multiple surface sites in order to define the relative abundance of

protium and deuterium within samples of hydrogen from hydrated volcanic rock. This will demonstrate an understanding of the long-term controls that have influenced the availability of liquid water on Mars through both endogenic, such as internal volcanic and geologic processes, and exogenic, such as surface-atmospheric interactions. The second objective aims to determine the crystal structure of minerals formed by asteroid impacts that interact with exposed subsurface ice within 0-1m depth as derived from the broader scientific goal of understanding the long-term endogenic and exogenic controls on the presence of liquid water on planet Mars. The selection of a Raman Laser Spectrometer with a predicted spectral resolution of 10 cm^{-1} and a peak separation capability of $6\text{--}8\text{ cm}^{-1}$ will allow for precise and accurate identification of hydroxyl groups and collect raman spectra in Olivine in selected asteroid rocks at multiple surface sites. This investigation explores the geological history of Mars and its evolution to the present state through the interaction between the dynamic forces on planet Mars that have formed and reshaped its surface through time as stated in the scientific goal. Furthermore, the goal is derived from multiple stakeholders and customer constraints. The stakeholder's experiment constraint reserves 185 kg total of mass for the system so perfectly falling within mass constraints, and an overall budget of \$450 million to ensure that only compact, cost-effective science instruments can be used. Under the prohibited materials constraint, the Radioisotope Thermoelectric Generator or RTG is prohibited, and radioactive materials are limited to under 5 grams, which are not used or exceeded, concluding that these experiments help create the opportunity to carry out these objectives to serve the mission's purpose.

Science Goals	Science Objectives	Science Measurement Requirements		Instrument Performance Requirements		Predicted Instrument Performance	Instrument	Mission Requirements
		Physical Parameters	Observables	Range	1 $\mu\text{Sv/h}$ to 10 Sv/h			
<p><i>"HBS-1LM: Understand the effects of short- and long-duration exposure to the environments of the Moon, Mars, and deep space on biological systems and health, using humans, model organisms, systems of human physiology, and plants."</i> — Moon to Mars Objectives, NASA</p>	<p>Investigate the long duration Martian environmental impacts on a protected and pressurized earth-fluid sample for unknown hazards that may threaten the integrity of future mission-critical life support, rocket propellant, and agricultural fluids.</p>	<p>Periodically monitor the Earth fluid sample for risks, hazards, and contamination that may bypass the custom-engineered Fluid Protection System's protective layers and document via data generation.</p>	<p>Use a passive ionization chamber to monitor gamma radiation levels in $\mu\text{Sv/h}$, recording data at weekly intervals over a one-year period for transmission back to Earth.</p>	<p>Range</p> <p>Operating Temperature</p> <p>Accuracy</p> <p>Time Constant</p>	<p>1 $\mu\text{Sv/h}$ to 10 Sv/h</p> <p>30°C to +57°C</p> <p>$\pm 5\%$</p> <p>12 seconds slow</p>	<p>1 $\mu\text{Sv/h}$ to 10 Sv/h</p> <p>30°C to +57°C</p> <p>$\pm 10\%$</p> <p>2 seconds fast, 12 seconds slow</p>	<p>CP-MU DMU-100 Submersible Gamma Neutron Probe</p>	<p>The instrument must survive fluid submersion for a minimum of one year while measuring for potential radiation contamination within the fluid protection system.</p>
	<p>Investigate how subsurface stratigraphy, dielectric properties, and dust layer thickness affect the accessibility and long-term stability of near-surface water ice, in support of in-situ resource utilization and environmental risk reduction for future human exploration.</p>	<p>Estimate dielectric permittivity and radar wave velocity to characterize subsurface material properties, including layer thickness, composition changes, and porosity variations across a 10 km traverse.</p>	<p>Analyze radar signal delay and reflection strength to determine layer boundaries, depth to subsurface features, and dielectric (ϵ) contrasts indicative of dust deposits and possible ice-rich zones.</p>	<p>Penetration Depth</p> <p>Frequency Range</p> <p>Permittivity Range</p> <p>Vertical Resolution</p>	<p>$\geq 10 \text{ km}$</p> <p>100-1200 MHz</p> <p>$\Delta\epsilon \leq 0.1$</p> <p>$\geq 15 \text{ cm}$</p>	<p>$\geq 10 \text{ m}$</p> <p>150-1200 MHz</p> <p>$\Delta\epsilon \leq 2$</p> <p>15 cm - 30 cm</p>		<p>The instrument must study the difference in permittivity to identify insulating dust layers and potential ice-rich zones</p>
								<p>The instrument must detect the subsurface layering to a depth of at least 10 m to assess ice stability underneath dust and regolith</p>

<p><i>"Q10.3b: What are the long-term endogenic and exogenic controls on the presence of liquid water on terrestrial planets?"— Origins, Worlds, and Life: A Decadal Strategy for Planetary Science and Astrobiology 2023–2032</i></p>	<p>Determine the Deuterium to Hydrogen (D/H) ratio in hydrated volcanic rock on Mars' surface.</p>	<p>Define the relative abundance of protium and deuterium within samples of hydrogen from hydrated volcanic rock.</p>	<p>Collect absorbance spectra in the 2500–25,000 nm range of H in selected hydrated volcanic rock samples at multiple surface sites.</p>	<table border="1"> <thead> <tr> <th>Wavenumber Range</th><th>3593.3-35 94.3 cm⁻¹</th><th>3593.3-3594.3 cm⁻¹</th></tr> </thead> <tbody> <tr> <td>Spectral Resolution</td><td>0.0001 cm⁻¹</td><td>0.0001 cm⁻¹</td></tr> <tr> <td>Sensitivity</td><td><80 ppb</td><td>10 ppb</td></tr> <tr> <td>Integration Time</td><td>1 s</td><td>2.4 s</td></tr> </tbody> </table>	Wavenumber Range	3593.3-35 94.3 cm ⁻¹	3593.3-3594.3 cm ⁻¹	Spectral Resolution	0.0001 cm ⁻¹	0.0001 cm ⁻¹	Sensitivity	<80 ppb	10 ppb	Integration Time	1 s	2.4 s	<p>Miniature Tunable Laser Spectrometer (Mini-TLS)</p>	<p>System must navigate to and collect samples of hydrated volcanic rock.</p>
Wavenumber Range	3593.3-35 94.3 cm ⁻¹	3593.3-3594.3 cm ⁻¹																
Spectral Resolution	0.0001 cm ⁻¹	0.0001 cm ⁻¹																
Sensitivity	<80 ppb	10 ppb																
Integration Time	1 s	2.4 s																
<p>Determine the crystal structure of minerals formed by asteroid impacts interacting with exposed subsurface ice.</p>	<p>Identify chemical structure, crystal structure, and bond structure of Olivine from asteroids.</p>	<p>Collect raman spectra in the 11,111–33,333 nm range of Olivine in selected asteroid rocks at multiple surface sites.</p>	<table border="1"> <thead> <tr> <th>Mineral Identification Accuracy</th><th>±10%</th><th>≥ 90%</th></tr> </thead> <tbody> <tr> <td>Detection Sensitivity</td><td>≤ ~100 ppm</td><td>6–8 cm⁻¹ peak separation</td></tr> <tr> <td>Power Consumption</td><td>20 - 30W</td><td>Between 20 - 30 watts</td></tr> <tr> <td>Spectral Resolution</td><td>10 cm⁻¹</td><td>10 cm⁻¹</td></tr> </tbody> </table>	Mineral Identification Accuracy	±10%	≥ 90%	Detection Sensitivity	≤ ~100 ppm	6–8 cm ⁻¹ peak separation	Power Consumption	20 - 30W	Between 20 - 30 watts	Spectral Resolution	10 cm ⁻¹	10 cm ⁻¹	<p>Raman Laser Spectrometer (RLS)</p>	<p>System must have the ability to heat volcanic rock to 935 K to study structural water released as gas.</p>	
Mineral Identification Accuracy	±10%	≥ 90%																
Detection Sensitivity	≤ ~100 ppm	6–8 cm ⁻¹ peak separation																
Power Consumption	20 - 30W	Between 20 - 30 watts																
Spectral Resolution	10 cm ⁻¹	10 cm ⁻¹																

Figure 1.2.1: Science Traceability Matrix

1.3 Summary of Mission Location

The location selected for the P.H.O.E.N.I.X mission is the Erebus Montes region of Arcadia Planitia. The two factors which play into selecting a mission location are: its adherence to the customer constraints and the location containing regions of interest for completion of the science objectives. Erebus Montes is located within 60° latitude North or South, the Potential High Priority Radar Targeting Zone (PHPRTZ), and a region containing excess subsurface ice within the upper meter of the regolith.

Erebus Montes has ample regions of scientific interest to complete the objectives located within the STM. The objectives necessitate the presence of hydrated volcanic rock and asteroid impacts which exposed subsurface ice. The region is situated between two Amazonian lava flows and contains exposed terrain from the older Noachian-Hesperian era [50]. This access to both new and old geological terrain with glacial processes offers the ability to categorize the way water ice has interacted with Martian geological and climate changes [51]. The TES dust index in **Figure 1.X** shows the region is moderately dusty, posing challenges to the systems operation and communication. However, this lends the advantage of the subsurface ice being more cold and therefore more stable [50]. There is a flat pocket of less dust in the Northwestern corner of the ROI where the rover will land to avoid communication issues during deployment.

The P.H.O.E.N.I.X ROI is a 60 km wide, 17 km long ellipse. The ROI sits on a region of Noachian-Hesperian transition terrain in the Northeastern region of Erebus Montes [50]. In the Northwest corner of the ROI there is a concentric crater fill (CCF). CCFs form through asteroids contacting ice-rich regions with subsequent glacial movement carving the crater walls [54]. This introduces the asteroid minerals to interactions with ice, interactions which are important to understand the way water can change crystal structures. Evidence points towards asteroids bringing life-sustaining elements (C, H, H, P) to Mars [68]; many studies hypothesize that organics may be preserved in ice-rich environments [66]. The possibility of organics within asteroid minerals is real and must be studied at the CCF of interest.

There are multiple ice rich lobate debris aprons (LDA) in the Southern region of the ROI [50]. LDAs are formed when rock debris piles up next to escarpments. The ROI LDAs consist of the Noachian-Hesperian crust, a period with mass volcanic activity [54] [65]. The Noachian-Hesperian terrains that feed into LDAs have been found to contain hydrated minerals suggesting the LDAs would make hydrated volcanic rock easily accessible [66]. This makes Erebus Montes' LDAs a compelling target for collecting preserved, hydrated volcanic material.

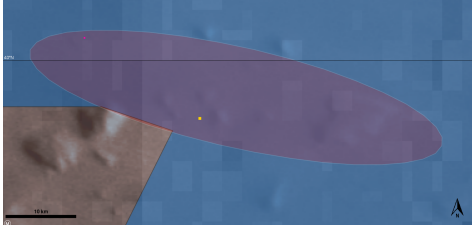
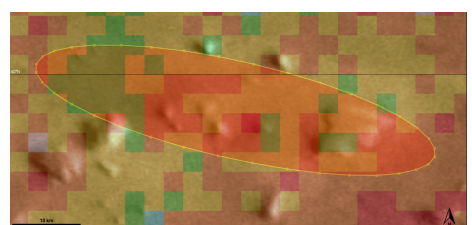
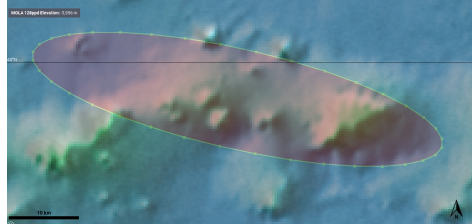
<p>ROI Overlaid with PHPRTZ This displays the region of interest within the contractors requirements. Additionally the small pink and yellow squares show the locations of CCFs and LDAs respectively.</p>	
<p>ROI TES Dust Index As stated Erebus Montes is dusty, but in the ROI there are regions where the rover can avoid dust.</p>	
<p>ROI Elevation Map The region has large cliffs where the LDAs are present. These cliffs will need to be navigated to study hydrated volcanic rock.</p>	

Figure 1.X: P.H.O.E.N.I.X ROI JMARS Maps

1.4 Mission Requirements

Customer constraints are a key driver of mission architecture, which determines the high-level requirements concerning mass, volume, and budget. Team P.H.O.E.N.I.X seeks to meet the system constraints presented by NASA, serving as the funding agency for the Mission Concept Academy's Discovery-class mission.

The spacecraft shall not exceed a mass of 200 kg. In a stored configuration, the spacecraft shall not exceed the dimensions of 2.5 m x 2.5 m x 2.5 m. This volume will house all the electronics, instruments, and payload suite. The spacecraft shall maintain the stored configuration for the entirety of the launch, transit, and entry into the Martian atmosphere. In an expanded form, there is no volume or mass constraint placed on the spacecraft. The spacecraft shall demonstrate resistance to temperatures consistent with atmospheric entry and descent. The spacecraft shall incorporate a landing attenuation system capable of withstanding surface impact.

After deployment on the landing site selected, the spacecraft shall traverse the terrain effectively to travel a minimum of 10 km. The spacecraft shall demonstrate an ability to traverse various Martian terrains, including sandy regions, icy regions, and small, medium, and large-sized rocks. The spacecraft shall demonstrate the ability to endure fluctuations in Martian atmospheric conditions, including dust storms, diurnal temperature variations, and reduced atmospheric pressure.

The spacecraft shall carry a scientific payload containing all instrumentation to complete science objectives. The volume of the scientific payload shall not exceed a cube of dimensions 0.5 m x 0.5 m x 0.5 m, nor a mass of 15 kg. This is to ensure the mission satisfies the human exploration goal and gets samples from the Martian surface that can be transmitted back to Earth for research. Furthermore, this research will contribute a great deal to the future of sustainability on Mars and future manned missions.

P.H.O.E.N.I.X is a discovery mission and not a flagship mission; hence, the budget allocated to this mission is 450 million USD and shall be used effectively for the manufacturing of the spacecraft, its components, employee-related expenses (ERE), and testing of the spacecraft. The Spacecraft system shall not have a Radioisotope Thermoelectric Generator (RTG) or any similar power generation system. Furthermore, any radioactive material is allowed for use on other spacecraft subsystems, but cannot exceed a cumulative mass of 5g of radioactive material on all subsystems. The spacecraft must be ready for integration with the other systems by October 1st, 2029, and must be ready for launch on December 1st, 2029. The launch site shall be in Cape Canaveral in Florida.

Req #	Requirement	Rationale	Parent Req.	Child Req.	Verification Method	Req Met
MG 0.1	System shall survive the martian environment for 1 year	The system must be able to survive the martian environment to fulfill its purpose and send data back to earth ground station and potentially return martian samples		SYS.02	Demonstration	Met
MG 0.2	Shall investigate the presence of ice glaciers on Mars for future missions and sustainability	Foundational science driver for the mission: Human habitation requires large volumes of drinkable water, water for propellant and agricultural use for long term sustainability missions on Mars	Customer	SYS.01 SYS.03 SYS.05 SYS.06 SYS.07 SYS.08 CDH.01 CDH.02	Demonstration	Met

Figure 1.4.1: Requirements Table

The system-level requirements for the P.H.O.E.N.I.X mission are derived directly from NASA's customer constraints and ESDSD objectives. These top-level requirements form the foundation upon which all subsystem requirements are built and are essential to ensure the spacecraft can successfully complete its science operations and contribute valuable data toward future human exploration of Mars.

The first MG states that the spacecraft must survive the Martian environment for the full duration of its science operations. This includes enduring extreme temperatures, dust storms, and radiation conditions typical of the Martian surface. Demonstrating environmental survivability is critical for collecting and transmitting meaningful data back to Earth.

The second MG states that the system shall investigate subsurface ice on Mars, aligning with both the scientific and human exploration goals. This foundational objective drives the selection of instrumentation, rover mobility capabilities, and site selection criteria. It supports key downstream system requirements such as power (SYS.01), thermal regulation (SYS.02), mobility (SYS.03), communications (SYS.07), and planetary protection (SYS.08).

Each mission goal has been decomposed into a series of child system requirements (SYS), with clearly defined verification methods such as demonstration,

test, analysis, and inspection. For instance, mobility requirements ensure the system can traverse at least 10 km over varied Martian terrain, while power and thermal systems must maintain subsystem functionality during solar cycles and cold nights.

1.5 System Definition

1.5.1 Spacecraft Overview

The P.H.O.E.N.I.X spacecraft is a low-cost Mars rover designed to investigate near-surface water ice and assess environmental risks to support future human exploration. The system architecture integrates six core subsystems: Mechanical, Power, Command & Data Handling (CDH), Thermal, Payload and Comms.

The Mechanical Subsystem comprises the chassis, rocker-bogie suspension, and wheels, this subsystem provides structural integrity and terrain adaptability. It must withstand static loads up to 1500 N, vibrational frequencies up to 2000 Hz, shock loads up to 6000 N, and maintain $\geq 95\%$ actuation performance throughout the mission (MECH.01–MECH.05). The Power Subsystem comprises ROSA-based solar panels, a 500 Wh lithium-ion battery, and a redundant power distribution unit. The subsystem must generate at least 200 Wh per sol, handle 120 W peak loads, and maintain safe operation from -30°C to $+50^{\circ}\text{C}$ (PWR.01–PWR.05). The Command and Data Handling Subsystem comprises onboard processing and communication between systems and Earth. Requirements include a 1 GHz processor, 1 Mbps uplink, and 16 Kbps downlink, with sufficient bandwidth to handle telemetry and science data (CDH.01–CDH.02). The Thermal Subsystem regulates temperature-sensitive components using passive insulation and active heating. It maintains the system within 303–313 K and instrument-specific thermal ranges (TCS.01). The Payload Subsystem contains all instruments include RIMFAX (subsurface radar), a Gamma Neutron Probe (radiation monitoring), a Miniature Tunable Laser Spectrometer (D/H ratio), and a Raman Laser Spectrometer (mineralogy). Each must meet strict mass/volume limits and operate under mission-specific scientific thresholds.

All subsystems are designed within a maximum stored configuration of 2.5 m x 2.5 m x 2.5 m, a mass cap of 200 kg, and a cost ceiling of \$450M, with readiness milestones targeted for integration by October 2029 and launch by December 2029.

Req #	Requirement	Rationale	Parent Req.	Child Req.	Verification Method	Req. met?
MG 0.1	System shall survive the martian environment for a minimum of one year.	The system must be able to survive the martian environment to fulfill its purpose and send data back to earth ground station and potentially return martian samples		SYS.02 CDH.04	Demonstration	Met
MG 0.2	Shall investigate the presence of ice glaciers on Mars for future missions and sustainability	Foundational science driver for the mission: Human habitation requires large volumes of drinkable water, water for propellant and agricultural use for long term sustainability missions on Mars	Customer	SYS.01 SYS.03 SYS.05 SYS.06 SYS.07 SYS.08 CDH.01 CDH.02	Demonstration	Met
SYS.01	The system shall have sufficient power to carry out the objectives for the duration of its mission	System needs power to operate, communicate back to earth and carry out its objectives	MG 0.1 MG 0.2	PWR.01 PWR.02	Test	Met
SYS.02	System shall maintain operating temperatures and survive the harsh thermal environment ranging from on the martian surface	The system and its scientific instrumentation must be kept in operating temperature ranges in order to function properly	MG 0.1	TCS.01	Test	Met
SYS.03	System shall traverse the martian surface smoothly and reach the required science points of interest	Points of interest are marked across potential high priority Radar targeting zones on Mars that are defined by the thickness of the atmosphere to allow for easy landing and research point.	MG 0.2	CDH.01 CDH.02 CDH.03 CDH.04 MECH.01 MECH.02 MECH.03 MECH.04	Test	Met
SYS.04	System shall not exceed a total mass of 200kg	Constraints provided by NASA for the mission	Customer		Inspection	Met
SYS.05	System shall have a backup that is always ready to take over	In the case of failure, if the main system fails, the backup can takeover and still carry out the	MG 0.1		Analysis	Met

		mission				
SYS.06	System must withstand the solar winds for the duration of its mission	All components on the rover must be strong enough to withstand the strong solar winds on mars	MG 0.1		Test	Met
SYS.07	System shall send and receive data collected with the science instrumentation back to the earth ground station	Data sent back to the earth ground station about Mars will be essential to future scientific research for sustainability on mars	MG 0.2	CDH.01 CDH.02 CDH.03 CDH.04	Analysis	Met
SYS.08	System shall comply with all applicable planetary protocol regulations	NPR 8020.12D *Planetary Protection Provisions for Robotic Extraterrestrial Missions*	MG 0.2		Analysis	Met
SYS.09	Radioactive material used for any subsystem excluding the power subsystem shall not exceed a total mass of 5g	Constraints provided by NASA for the mission	Customer		Inspection	Met
SYS.10	System shall not make use of a Radioisotope Thermoelectric Generator (RTG) or any derivative thereof for power generation	Constraints provided by NASA for the mission	Customer		Inspection	Met
SYS.11	System shall not exceed the dimensions of 2.5 m x 2.5 m x 2.5 m while in its stored configuration	Constraints provided by NASA for the mission	Customer		Inspection	Met
SYS.12	System shall not exceed a cost of \$450M	Constraints provided by NASA for the mission	Customer		Inspection	Met
CDH.01	The Command and Data Handling (CDH) system shall have a minimum uplink rate of 1 Mbps and a minimum downlink rate of 16 Kbps.	The system must be able to send scientific and telemetric data to and from Earth.	SYS.03 SYS.07	CDH.02	Analysis	Met
CDH.02	The CDH system shall have a minimum processing rate of 1 GHz.	The system must be able to process the scientific and telemetric data it receives from both Earth and instrumentation/sensors.	SYS.03 SYS.07 CDH.01	CDH.03 CDH.04	Test	Met

CDH.03	The CDH system shall have a minimum memory of 8 GB of RAM.	Provides working memory for executing flight software, processing sensor data, running algorithms, and sending commands.	SYS.03 SYS.07 CDH.02		Inspection	Met
CDH.04	The CDH system shall have a minimum storage of 10 TB.	Due to incoming datastreams and intermittent opportunities for uplink, large onboard data storage helps limit data loss and data can be stored for the duration of the mission.	MG.0.1 SYS.03 SYS.07 CDH.02		Inspection	Met
MECH.0 1	The chassis shall tolerate a static load up to 1500 N.	The system must not risk fracture or fatigue that would result in complete structural failure and inability to carry out the mission.	MG.01		Analysis	Met
MECH.0 2	Mechanical subsystems shall tolerate vibrations up to 2000 Hz.	The system must be able to tolerate vibrations from travel.	SYS.03		Analysis	Met
MECH.0 3	Suspension sub assembly shall tolerate shock loads up to 6000 N.	The system must be able to tolerate shock loads from travel.	SYS.03		Analysis	Met
MECH.0 4	Suspension sub assembly shall withstand a 45 degree tilt in any direction.	The system must be able to tolerate tilts from travel.	SYS.03		Demonstration	Met
PWR.01	The system shall generate at least 200 Wh per sol under average Martian insolation and withstand peak power draws of 120 W for a minimum of 30 minutes up to 3 times per Sol.	Supports nominal rover operation, mobility, communication and science payloads	SYS.01		Analysis	Met
PWR.02	Solar panels shall deploy autonomously and tolerate up to 20 m/s wind.	Ensures survivability under common Martian conditions	SYS.06		Test	Met
PWR.03	The system shall maintain operation of critical components between -30°C to +50°C.	Ensures battery and electronics functionality	SYS.06		Test	Met

PWR.04	The system shall minimize integration risk using EMI shielding to absorb shockwaves and modular connectors to divert signals from critical components.	Reduces failure during integration and operations	SYS.05		Test	Met
PWR.05	Provide redundant power paths for critical systems via RCE's and power and analogue modules	Enhances fault tolerance by dividing power distribution and handling between two computers, helping to reduce uptime	SYS.01 SYS.05		Test	Met
TCS.01	The Thermal Control System (TCS) shall help maintain the system at the allowable temperature range of 303 K to 313 K.	This ensures the TCS keeps components within safe temperature limits to prevent failure from Mars' extreme thermal conditions.	SYS.02		Test	Met
PAYL.01	RIMFAX shall detect radar signal changes in subsurface layers down to 10 meters depth.	Fulfills Human Exploration science objective #2 by identifying ice-rich zones defined by a permittivity difference of less than or equal to 0.1.	MG.02		Test	Met
PAYL.02	CP-MU Submersible Gamma Neutron Probe shall measure and record radiation dosage measurements ranging from 1 μ Sv/h to 10 Sv/h.	Fulfills Human Exploration science objective #1 by recording Martian environmental radiation impact data in the transported Fluid Protection System over a minimum one year duration period.	MG 0.1		Test	Met
PAYL.03	Miniature Tunable Laser Spectrometer shall collect and receive data from hydrated volcanic rock within a 1-second integration time.	Fulfills Science Exploration science objective #2 by determining the Deuterium to Hydrogen (D/H) ratio.	SYS 0.7		Test	Met
PAYL.04	Raman Laser Spectrometer shall collect Olivine Raman spectra in the 11,111–33,333 nm range.	Fulfills Science Exploration science objective #2 by identifying the chemical structure, crystal structure, and bond structure of Olivine from asteroids.	TCS.05		Test	Met

Figure 1.5.1.2: System Requirements Table

1.5.2 Mechanical Subsystem

1.5.2.1 Mechanical Subsystem Requirements

The mechanical subsystem contains the chassis, suspension, and wheels, and must ensure structural integrity, terrain adaptability, and environmental resilience throughout the mission.

The chassis must withstand static loads up to 1500 N, shock loads up to 6000 N, and vibrational frequencies up to 2000 Hz, as verified by finite element analysis (FEA). The system shall withstand 45° tilts and maintain functionality across rugged terrain, minimizing risk of tip-over or mechanical failure. All moving components shall preserve at least 95% of range of motion over the mission duration, with dust-tolerant designs verified in CAD. Components must resist performance degradation from dust, radiation, and thermal cycling typical of the Martian environment. Verification methods include FEA simulations and CAD-based tolerance analysis for thermal, mechanical, and particulate stress cases.

These requirements are derived from system requirements and are designed to minimize mechanical risks over the intended mission lifetime.

1.5.2.2 Mechanical Subsystem Overview

Each subassembly within the mechanical subsystem has been designed with emphasis on safe traveling ability, reliable performance in Martian conditions, and integration of subassemblies. The challenges that influenced such decisions include traversing rugged terrain, exposure to extreme temperatures, and strict mass criterion [26]. The rover will encounter rocky obstacles, thermal cycling, and various loads, and the mechanical subsystem was designed with these challenges in mind.

The chassis is the structural backbone of the rover, holding all subsystems together. For a durable and lightweight frame, the chassis will be made of aluminum 6061. The chassis will offer protection to scientific instruments and other subassemblies from dust and radiation exposure. The chassis will feature thicker aluminum walls with a tantalum coating, which is proven to significantly reduce radiation [21]. The chassis will connect to the suspension system with a differential through titanium fittings, which will allow the chassis and its inner components to remain at the average position of the suspension system for increased stability.

The rover will implement a rocker-bogie suspension system. Featured on all NASA Martian rover missions, this suspension system has demonstrated its ability to consistently and safely traverse the ragged Martian surface and was therefore chosen for this mission [39]. This suspension system consists of six wheels connected through a pivoting linkage system that allows each wheel to move independently and climb over obstacles twice the diameter of the wheels.

The rocker refers to the longer pivoting arms, which connect to the front wheels and the bogies. The bogie refers to the ‘responding’ arms attached to the rockers that connect to the middle and rear wheels. As the rover encounters obstacles, the rockers and bogies pivot independently at the joints to maintain constant contact with the ground. The chassis remains at the average pitch angle of the two rockers, which are connected to each other and the chassis through a differential. The differential tilts as obstacles are encountered to maintain at least one rocker wheel on the ground at all times for stability.

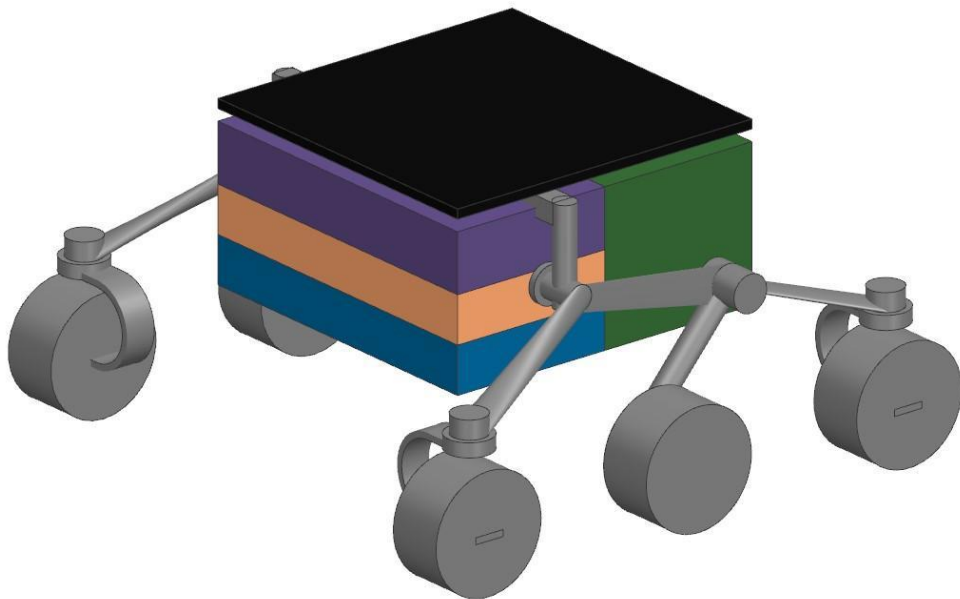


Figure 1.5.2.2.1: High-Level Rover Concept

The rocker and bogie bars will be made of titanium tubing, like past rovers. The rocker is L-shaped, with one end attached to a drive wheel and the other attached to the bogie through a pivot point. The bogie is similarly L-shaped, with one end attached to a drive wheel and the other attached to an idle wheel used for balance. The bars will connect to the wheel mounts through titanium fittings, allowing for each wheel to have independent motion. The rockers connect to the bogies through a pivot joint, and the rockers connect to each other and the chassis through a differential. The differential connects the rockers to the chassis through similar titanium fittings as those used on the wheel mounts, which allows for the rockers to pivot independently and the chassis to remain at its average position. This system distributes the rover’s weight equally among the six wheels, allowing for balanced loads. Furthermore, this will avoid one wheel or leg joint wearing faster than another, which is an added benefit of the rocker-bogie system along with excellent obstacle handling.

Subassembly	Mass (kg)	Dimensions (m^3)	Max Power Draw (W)
Chassis	65	3	0
Suspension	20	8.75	0
Wheels	3	0.02	200

Figure 1.5.2.2.2: Mass, Volume, and Power Subassembly Estimates

Similar aluminum chassis have been flown on past NASA Martian rovers, but not in the intended environment. Similarly, the rocker-bogie system has been implemented on every NASA Martian rover. The fundamental concept is flight proven, but hardware for PHOENIX will not be exactly similar to those flown on previous missions. Since geometries and specific component designs will be modified to fit PHOENIX's design, the chassis and suspension systems will have a TRL of 7.

Subassembly	TRL	Justification
Chassis	7	Similar chassis are flown on every rover mission, but the particular version designed for PHOENIX will be different from past rovers. At the highest, PHOENIX's chassis will demonstrate operation in a similar, but not actual, environment.
Suspension	7	Concept is flight proven, but the particular version designed for PHOENIX will be different from past rovers. At the highest, PHOENIX's suspension system will demonstrate operation in a similar, but not actual, environment.
Wheels	7	Aluminum wheels with symmetrical treads have substantial flight heritage (e.g., Sojourner, Spirit, Opportunity), and the performance characteristics are well-understood in Martian environments.

Figure 1.5.2.2.3: Mechanical Subassembly Requirements Table

1.5.2.3 Mechanical Subsystem Trade Studies

Mechanical Subsystem Trade Study on Leg Material

Figure 1.5.2.2.1: Leg Material Trade Study

The legs of the suspension system must support the weight of the rover during travel, handle shock loads experienced throughout travel, and avoid performance degradation throughout constant loads and thermal cycling. Four aspects were weighed equally to determine the optimal material for the legs: density, load-bearing ability, shock absorption, and thermal performance. Three materials were considered for the legs - aluminum 6061, titanium, and a carbon fiber composite - based on common aerospace materials and previously used rover leg materials.

The legs' material is favored to have a high density unlike other components of the mechanical subsystem. Having a center of mass closer to the ground is beneficial for stability, so the three materials were ranked by their densities. Titanium had the highest of 4.51 g/cm³. Aluminum 6061 had the second highest of 2.7 g/cm³, and CF composite had the lowest of 1.5-2 g/cm³.

High shear strength is an important criterion to ensure the legs could reliably tolerate all encountered loads, particularly static and shock loads. Having a high shear strength avoids risk of material fatigue and ensures the legs can comfortably tolerate all loads. Titanium had the highest shear strength of approximately 500+ MPa. Aluminum 6061 had the second highest of around 200 MPa, and CF composite ranged from 50-150 MPa.

High fracture toughness is another important characteristic for the leg material due to the suspension system requiring shock absorption ability. High fracture toughness reduces the risk of cracks propagating in the material, which is a significant risk due to frequent shock loads encountered during travel by the suspension system. Titanium had the highest fracture toughness of 100 MPa·m^{1/2}. Aluminum 6061 had the second highest of 29 MPa·m^{1/2}, and CF composite had the lowest possible fracture toughness, ranging from 5 to 50 MPa·m^{1/2}.

Adequate thermal performance is another important factor as the rover must withstand extreme thermal cycling in the Martian environment. A material with a low coefficient of thermal expansion was favored since thermal cycling would have less of an impact. CF composite had the lowest thermal expansion coefficient of 1-5 $\mu\text{m}/\text{m}\cdot^\circ\text{C}$. Titanium had the second lowest of 8.6 $\mu\text{m}/\text{m}\cdot^\circ\text{C}$, and aluminum 6061 had the highest of 23.5 $\mu\text{m}/\text{m}\cdot^\circ\text{C}$.

Based on the scoring, titanium ranked as the highest overall leg material choice. This aligns with previous rover leg materials, and Perseverance implemented titanium tubing as its leg material [32].

[Mechanical Subsystem Trade Study for Chassis Material](#)

Figure 1.5.2.2.2: Chassis Material Trade Study

The chassis has similar expectations as the legs of the rover, and it must support the weight of the rover during travel and handle shock loads experienced throughout travel. Four aspects were considered to determine the optimal material for the chassis: density, load-bearing ability, shock absorption, and thermal performance. Four materials were considered for the legs - aluminum 6061, carbon fiber composite, and stainless steel - based on common aerospace materials and previously used rover chassis materials.

The chassis' material is favored to have a low density, and the density criterion was weighed the heaviest in order to adhere to mass requirements as the chassis is the largest component of the mechanical subsystem. The four materials were ranked by their densities, with the lowest densities ranked the highest. Aluminum 6061 and CF composite had satisfactorily low densities of 2.7 g/cm^3 and $1.5\text{-}2 \text{ g/cm}^3$ respectively, both ranking as a 1. Stainless steel's density of $7.5\text{-}8 \text{ g/cm}^3$ was far too high considering the mass budget and ranked a 5.

High shear strength is an important criterion to ensure the chassis could reliably tolerate all encountered loads, particularly static and shock loads. Having a high shear strength avoids risk of material fatigue throughout the mission lifetime and ensures the chassis can comfortably tolerate all loads. Stainless steel had the highest shear strength of $500+ \text{ MPa}$, and aluminum 6061 had the second highest of approximately 200 MPa . CF composite ranges due to its anisotropic properties, and its shear strength can be anywhere from $50\text{-}150 \text{ MPa}$, putting it in last place.

High fracture toughness is another important characteristic for the leg material due to the suspension system requiring shock absorption ability. High fracture toughness lessens the risk of cracks propagating in the material, which is a significant risk for the chassis as it experiences shock loads and is under constant static loading. Stainless steel and aluminum 6061 each had a fracture toughness above $25 \text{ MPa}\cdot\text{m}^{1/2}$ which ranked them both a 1. CF composite ranked a 4 with a fracture toughness ranging from 5 to $50 \text{ MPa}\cdot\text{m}^{1/2}$

Adequate thermal performance is another important factor as the rover must withstand extreme thermal cycling in the Martian environment. A material with a low coefficient of thermal expansion was favored since thermal cycling would have less of an impact. CF composite had the lowest thermal expansion coefficient of $1\text{-}5 \mu\text{m/m}\cdot^\circ\text{C}$. Aluminum 6061 and stainless steel had the highest of $23.5 \mu\text{m/m}\cdot^\circ\text{C}$ and 17.3 respectively, putting them at a 5 and 4. Based on the scoring, aluminum 6061 was ranked as the highest overall chassis material choice.

Mechanical Subsystem Trade Study for Wheel Material

Figure 1.5.2.2.3: Wheel Material Trade Study

The wheel subsystem design emphasizes the need for a lightweight and durable material that ensures mobility and reliability throughout its function. To determine the most suitable material, 3 candidate materials were selected: aluminum, titanium, and fiberglass. The selection of these materials was based on 4 criteria for critical performance: density, load-bearing, shock absorption, and thermal performance. Each criterion was weighted equally at 25% each, reflecting the team's equal prioritization of mass, strength, durability, and performance.

Density is the criterion that impacts the overall system mass, affecting the maneuverability and energy efficiency of the rover. Load-bearing indicates the maximum pressure (MPa) that the wheels can withstand in varied terrain stresses before becoming permanently deformed and non-functional. Shock absorption measures the rover's ability to endure impacts from terrain obstacles. Finally, thermal performance measures the integrity of the wheels based on their material in varying temperatures.

For the criterion of density, Aluminum and fiberglass scored a 1, given that their densities are 2.7 g/cm^3 and $2.4\text{--}2.76 \text{ g/cm}^3$, respectively. Titanium scored a 4 due to its high density of 4.51 g/cm^3 . In the load-bearing category, aluminum and titanium received the highest scores with shear strengths of 207 and 550, respectively. Fiberglass received the lowest score with a shear strength of roughly 30 MPa. When measuring the shock absorption of the materials, titanium came in first with a fracture toughness of $100 \text{ MPa}\cdot\text{m}^{1/2}$. This was followed by aluminum with a fracture toughness of $29 \text{ MPa}\cdot\text{m}^{1/2}$ and fiberglass ($0.6\text{--}2 \text{ MPa}\cdot\text{m}^{1/2}$). Finally, in the thermal performance category, fiberglass and titanium received the highest scores with coefficients of thermal expansion of $5\text{--}10 \mu\text{m/m}\cdot^\circ\text{C}$ and $8.6 \mu\text{m/m}\cdot^\circ\text{C}$, respectively. Aluminum slightly fell behind with a higher coefficient of thermal expansion of $23.5 \mu\text{m/m}\cdot^\circ\text{C}$.

Aluminum consistently received top scores in most categories, scoring a 1 in the density and load-bearing criteria. The material had a slightly weaker performance in shock absorption and thermal performance, scoring a 2. Overall, aluminum demonstrated structural resilience and a low density (therefore a lower mass under constant volume), making it the highest-ranked option with a total score of 87.5%. Titanium offered strong load-bearing, shock absorption, and thermal performance, receiving top scores in all of the criteria. However, the high density of titanium resulted in a criteria score of 4. This averaged to a final composite score of 81.25%, making it the second-best candidate. Although fiberglass is a very light material with a low coefficient of thermal expansion, it severely underperformed in both load-bearing and shock absorption, with a score of 5 and 4, respectively. These structural characteristics resulted in the lowest composite score of 56.25%.

Mechanical Subsystem Trade Study for Wheel Tread

Figure 1.5.2.2.4: Wheel Tread Trade Study

The wheel tread design affects the rover's ability to handle varying terrain conditions, resist wear over time, and remain operationally reliable through repeated usage. The criteria selected for the wheel tread were wear resistance, grip, and reliability, weighted at 30%, 30%, and 40% respectively. Wear represents how well the tread is able to resist abrasion over time. Grip measures how effectively the tread is

able to maintain traction on different surfaces. Finally, reliability will measure the fatigue life of the tread pattern.

Because quantitative data (coefficient of kinetic friction or specific fatigue cycles) was not consistently available across all tread types, this trade study utilized a relative performance scoring system based on industry-standard design knowledge. Symmetrical treads are uniquely beneficial in that their symmetric patterns allow for even wear throughout the wheel, improving tread life. Directional treads typically wear faster, making it fall behind symmetrical and asymmetrical treads in wear performance [22]. Asymmetrical treads take advantage of engraving patterns that allow for stronger cornering grips [22]. Similarly, directional treads take advantage of lateral grooves that allow for the wheel to maintain contact with wet surfaces and resist hydroplaning at high speeds. After applying the weighted scores, symmetrical treads emerged as the optimal choice with a final cumulative score of 77.5%, followed by asymmetrical treads (60%) and directional treads (30%).

1.5.3 Power Subsystem

1.5.3.1 Power Subsystem Requirements

The following requirements were created to ensure that the rover's power subsystem shall operate in its full capacity for the entire duration of the mission. These requirements are grounded in the rover and its external experiment's energy needs while traversing Martian terrain, operating science equipment, and communicating to and from Earth. Each requirement aligns with expected environmental extremes, mobility objectives, and mission safety margins.

The generation of 200 Wh per sol (PWR.01) ensures the rover can maintain baseline functionality and guarantees survivability during periods of low insolation or dust storms. Deployment and survivability constraints (PWR.02, PWR.04) were instituted to ensure the safety of the rover during landing procedures and regular operation. The operating temperature range (PWR.03) supports electrical and thermal compatibility across systems. Risk mitigation systems (PWR.05) safeguard against failure and simplify system-level design.

1.5.3.2 Power Subsystem Overview

The power subsystem was designed with a strong emphasis on power efficiency, system reliability, and modular integration. Each subassembly has been engineered to address Mars-related challenges such as extreme temperatures, accumulation of dust due to weather activity, and a restricted mass budget.

The Power Generation for the Mission is achieved by utilizing two high-efficiency 4G32C solar panels manufactured by AZUR Space. Together, the panels have a

surface area of 1.2 square meters, and are equipped with a Maximum Power Point Tracking controller (MMPT). To mitigate risks from partial shading and potential hot spot formation, the system will integrate external bypass diode protection. Bypass diodes will be placed across solar cell strings (every 5–8 cells) to maintain power output integrity and protect against failure propagation in case of local damage or dust accumulation. This controller allows the panels to adjust dynamically in order to optimize electrical system output during weather events and varying solar conditions. The deployment mechanism of the panels is designed for self-deployment upon Martian touchdown. The mechanism is built to withstand wind gusts up to 20m/s. This subassembly, and Roll-Out Solar Array (ROSA) received a TRL of 5 for this application.

To address dust accumulation on the equipment, which can lead to reduced power output over time, evaluation of three dust mitigation strategies occurred via a trade study: Electrodynamic Dust Shield (EDS), vibration-based cleaning, and passive anti-reflective coatings. The EDS method scored the highest in overall effectiveness and integration potential. It achieved high marks in dust removal efficiency, (Grade 1), low power consumption (Grade 1), high reliability due to lack of moving parts (Grade 1), and low integration mass and complexity (Grade 1), for a total weighted score of 100%. In contrast, passive coatings and vibration methods scored significantly lower, with final weighted scores of 50% and 82.5% respectively. Based on these results, EDS will be integrated into the solar panel design in order to preserve the functionality and lifespan of the solar arrays.

Power storage is provided by an EaglePicher SAR-10211-based lithium ion battery pack that is rated at 500Wh and a lifetime of 2000 cycles. The batteries will be configured in a 4S6P arrangement that delivers high efficiency. Each cell will be individually monitored by a Battery Monitoring System with overcharge, over-discharge, and thermal runaway protections in place. This battery pack supports a wide range of power delivery, with peak outputs of up to 120 W for 30-minute bursts, and continuous draw of up to 20 W [1]. To withstand the extreme temperature swings on Mars (-80°C to $+20^{\circ}\text{C}$), the battery is enclosed within a thermally insulated sleeve incorporating Phase Change Material (PCM) that passively regulates temperature around 0°C – 30°C [1]. Active resistive heaters embedded within the enclosure provide supplemental heating when PCM capacity is exceeded. Thermal vacuum chamber tests with EaglePicher SAR-10211 cells have demonstrated effective temperature stability from -40°C to $+60^{\circ}\text{C}$, but with the PCM-integrated housing still under environmental validation, this subassembly is currently assigned TRL 5, while the bare cell chemistry stands at TRL 7 due to extensive flight heritage under NASA's Orion Multi-Purpose Crew Vehicle.

In determining the most effective thermal regulation method for battery and subsystem protection, a thermal trade study was conducted. Three methods were

evaluated: resistive heaters with MLI insulation, PCM thermal storage compartments, and a pipe grid with PCM thermal buffering. Each was graded across performance, mass, energy efficiency, and reliability. The pipe grid + PCM system scored highest (86.25%), with optimal energy efficiency and reliability. It offered passive thermal buffering and minimal risk from moving parts. PCM compartmental systems followed closely at 77.5%, while simple resistive heaters and MLI lagged (76.25%) due to higher energy usage and less precise thermal control. Based on this study, the hybrid PCM + heater configuration remains the baseline with future integration of pipe-grid enhancement under evaluation.

Power Distribution is implemented through a hybrid redundant bus architecture, which combines central routing with distributed load switching. The system incorporates current-limiting smart FETs, microcontroller-based load prioritization logic, and real-time health telemetry. Each power rail includes EMI filtering, overcurrent protection, and modular plug-in interfaces for subsystem compatibility. The distribution unit is based on a modified commercial-off-the-shelf (COTS) avionics design and has reached TRL 6.

The power subsystem incorporates space-qualified DC-DC converters with galvanic isolation to supply regulated, stable power to the externally mounted scientific experiment. These converters are critical for providing the required 28 V DC output at up to 45 W peak load, ensuring power quality and electrical isolation for sensitive payload electronics. DC-DC converters operate by receiving unregulated or semi-regulated DC voltage from the rover's main power bus and converting it to a precisely regulated output voltage. Internally, these converters use high-frequency switching and transformer isolation to achieve both voltage transformation and galvanic isolation, which prevents ground loops and protects sensitive payloads from electrical noise, surges, and transients originating elsewhere in the system. The selected converters feature output voltage ripple below 2%, isolation withstand voltages greater than 1 kV, and efficiency typically above 90% [64]. Their compact form factor and robust EMI filtering make them ideal for integration in the rover's constrained external payload bay, where space, mass, and environmental shielding are at a premium.

Integration-wise, the DC-DC converters are mounted within the payload's thermally regulated housing, minimizing exposure to temperature extremes and mechanical vibration. The converter is a space-qualified, commercially available unit with extensive use in planetary and orbital missions. However, as it has not been flown in this exact configuration or integrated with this specific payload, it is assessed at TRL 7 (system prototype demonstrated in a space environment). This TRL reflects both the maturity of the underlying technology and the integration status within our subsystem.

As the battery thermal enclosure remains the least mature component, the entire power subsystem is currently assessed at TRL 5. Additional environmental testing is required to advance the system to full flight readiness.

Subassembly	TRL	Justification
Solar Panel + MPPT	6	ROSA-derived design validated in terrestrial analog and orbital environments
LiFePO ₄ Battery with PCM	5	COTS cells qualified; integrated PCM in development
Power Distribution Unit	6	Based on COTS hardware with flight heritage
Overall Power Subsystem	5	Limited by battery thermal integration

Figure 1.5.3.2.1 Power Subassembly TRL Table

Subassembly	Mass (kg)	Volume (cm ³)	Max Power Draw (W)
Solar Array	3.5	11,000	N/A (Power generation only)
Battery Pack	4	9,000	120
Power Distribution	1.5	4,000	5
Cabling & Interfaces	1	3,000	<1
Total	10	27,000	~120 W (peak)

Figure 1.5.3.2.2 Power Subassembly Mass, Volume, and Power Estimate

1.5.3.3 Power Subsystem Trade Studies

Power Subsystem Trade Study for Dust Mitigation Technologies

Figure 1.5.3.3.1 Dust Mitigation Technologies Trade Study

Dust accumulation on solar panels is one of the most significant challenges to sustained power generation for Mars surface missions. Since the Pathfinder landing in 1997, Mars rovers such as Spirit and Curiosity have experienced a consistent daily average power loss of approximately 0.2% due to dust settling on their solar panels in the absence of active cleaning measures. This gradual decline, observed across multiple missions, highlights the need for effective dust mitigation strategies to maintain energy availability and extend rover operational lifetimes [20].

To address this, a trade study has been created to compare three leading dust mitigation technologies: Electrodynamic Dust Shield (EDS), Vibration-Based Cleaning (Chladni Patterns), and Passive Coatings (Hydrophobic/Anti-Static). The evaluation focused on four criteria: effectiveness, reliability/robustness, power consumption, and mass & integration. These criteria were weighted at 35%, 25%, 20%, and 20% respectively, reflecting the mission-critical importance of maintaining high solar array output and system reliability, while also considering the constraints of limited power and mass on the rover.

The Electrodynamic Dust Shield (EDS) technology, which uses transparent electrodes to generate electric fields that actively repel and remove dust, emerged as the top performer. EDS has demonstrated over 90% Dust Removal Efficiency (DRE) in both laboratory and Mars-analog field tests, with minimal power consumption (less than 1% of array output) and no moving parts, making it highly reliable and straightforward to integrate [7].

In contrast, Vibration-Based Cleaning employs actuators to create resonance patterns that dislodge dust from the panel surface. While this method can achieve moderate dust removal (typically 50–90%), it introduces additional moving parts, increasing the risk of mechanical failure and requiring more power for operation [7].

Passive Coatings, such as hydrophobic or anti-static layers, provide a lightweight and power-free solution by reducing dust adhesion, but they do not actively remove settled dust and their long-term durability under Martian conditions is still under study [75].

Scoring was assigned based on published performance data and the technology readiness of each option. EDS received the highest marks across all criteria, due to its proven effectiveness, robust design, and ease of integration. Vibration cleaning was penalized for its complexity and reliability concerns, while passive coatings, though excellent in reliability and integration, scored lower for effectiveness. As a result, EDS is recommended as the primary dust mitigation approach for the rover's solar arrays, with passive coatings considered as a potential supplementary measure. This recommendation is strongly supported by current research and NASA technology demonstrations, ensuring the greatest likelihood of sustained power generation throughout the mission.

Power Subsystem Trade Study for Solar Panel Deployment

Figure 1.5.3.3.2 Solar Panel Deployment Trade Study

The criteria taken into account was mass, stowed volume, reliability, and complexity with weights of 25%, 30%, 30%, and 15% respectively, reflecting the critical importance of minimizing launch mass and stowed volume, while ensuring reliable deployment and manageable integration risk.

Quantitatively, ROSA demonstrated the lowest mass and stowed volume among the options, scoring a 1 (optimal) in both categories. For example, ROSA's mass per unit area is typically less than 20 kg for a 10 kW array [51], compared to 30–35 kg for equivalent mechanical hinge systems, as demonstrated in recent NASA ISS deployments. Ultraflex arrays, as used on the InSight lander, offer a moderate

compromise, with a typical mass of 6–10 kg per wing and a stowed volume of approximately 0.05-0.1 m³ per array for Mars-class missions [35].

Reliability was assessed based on flight heritage and deployment success rates. Mechanical hinges, with extensive use on Spirit, Opportunity, and Curiosity, scored a 1 for reliability due to their proven track record in Martian conditions. ROSA, while newer, has demonstrated successful deployment on the International Space Station and is being adopted for upcoming planetary missions, earning a reliability score of 2. Ultraflex, with successful deployments on Mars Phoenix and InSight, scored a 3, reflecting some flight heritage but also highlighting increased complexity and moderate risk [36].

Complexity was evaluated by the number of moving parts and deployment steps. ROSA and Mechanical Hinge mechanisms both scored a 2, while Ultraflex scored a 3 due to its tensioned structure and additional deployment steps.

When total weighted scores were calculated, ROSA achieved the highest overall score (88.75%), followed by Ultraflex (63.75%) and Mechanical Hinge (47.5%). These results indicate that ROSA offers the best balance of mass, volume, reliability, and manageable complexity for Mars surface operations.

Power Subsystem Trade Study for V Cell Type

Figure 1.5.3.3.3 Photovoltaic Cell Type Trade Study

Selecting the optimal photovoltaic (PV) cell type is a critical aspect of the Mars rover power subsystem, as it directly influences power generation efficiency, mass, and long-term reliability under harsh planetary conditions. For this trade study, three leading space-qualified PV technologies were compared: Spectrolab XTE-SF (triple-junction), AZUR SPACE 3G30C (triple-junction), and AZUR SPACE 4G32C (quad-junction). The criteria and their weights were chosen to reflect the most significant factors affecting Mars surface missions: Beginning-of-Life (BOL) efficiency (15%), End-of-Life (EOL) efficiency (35%), radiation resistance (20%), and specific power (30%). EOL efficiency was given the highest weight because the ability of the solar array to maintain performance over the mission's duration is crucial for sustained science operations, especially given the harsh Martian environment and exposure to radiation and dust. Specific power was also heavily weighted, as minimizing array mass is essential for rover mobility and payload accommodation. Radiation resistance is vital due to the thin Martian atmosphere, which provides limited shielding from cosmic rays and solar energetic particles, while BOL efficiency remains important for maximizing initial energy conversion.

Scoring was based on manufacturer datasheets, published test results, and recent reviews of PV performance in space environments. The AZUR SPACE 4G32C quad-junction cell outperformed the other options, achieving a BOL efficiency of 32.5%, EOL efficiency above 28%, radiation-induced power loss below 5%, and a specific power exceeding 370 W/kg [9]. In comparison, both the Spectrolab XTE-SF and AZUR SPACE 3G30C triple-junction cells demonstrated lower EOL efficiencies (26–27%), higher radiation degradation (5–10% power loss), and specific powers in the 300–350 W/kg range [10][11].

Based on the weighted scoring, the AZUR SPACE 4G32C quad-junction cell has been chosen as the rover's solar array. Its combination of high efficiency, excellent radiation resistance, and superior specific power offers the best balance of performance and risk mitigation for Mars surface operations, supporting sustained science activities throughout the mission.

[Power Subsystem Trade Study for Storage and Battery System](#)

Figure 1.5.3.3.4 Power and Battery Trade Study

Lithium-ion batteries are a common energy storage solution in spacecraft and rovers due to their high energy density and above-average cycle life. Not all lithium ion batteries are equally suited for operation on the Martian surface or extended mission duration. Possible battery configurations were examined: commercial Li-ion packs, custom LiFePO₄ assemblies, and aerospace-certified lithium-ion battery systems.

The evaluation criteria included thermal stability (25%), cycle life (25%), flight heritage (30%), and integration complexity (20%). These weights reflect the critical need for reliability under Martian extremes, the need for long-term functionality over several hundred Martian sols, and the reduction of integration risk for flight-ready systems.

The EaglePicher SAR-10211 aerospace-certified lithium-ion battery was ultimately selected. This battery has strong heritage in space applications, including NASA's Orion MPCV and the Dream Chaser spacecraft. Its performance in high-reliability, high-radiation environments makes it particularly well-suited to a Mars surface mission. It scored highest in flight heritage (Grade 1) and thermal performance (Grade 1), while offering acceptable integration complexity and volume. While slightly heavier than commercial options, its safety profile and robust telemetry support provided a compelling margin of confidence for mission longevity. The final configuration includes PCM-based thermal housing, which further enhances survivability during cold Martian nights. This subassembly, although composed of TRL 7 components, is rated at TRL 5 overall due to ongoing validation of the integrated thermal housing.

[Power System Trade Study for Isolated Power System](#)

Figure 1.5.3.3.5 Isolated Power System Trade Study

The integration of an externally mounted scientific payload on the Mars rover requires an isolated power system to ensure reliable operation of sensitive instruments under strict environmental and operational constraints. The payload, with a mass of 15 kg and dimensions of 0.5 m x 0.5 m x 0.5 m, demands a stable, regulated 28 V DC supply capable of delivering 45 W peak during sampling and 5 W in standby mode. Due to its sensitivity to voltage fluctuations, electromagnetic interference (EMI), and thermal gradients, the power architecture must provide galvanic isolation, superior voltage regulation, and minimal EMI susceptibility, while integrating efficiently with the rover's limited mass and volume budgets.

Three technical options were evaluated: an isolated DC-DC converter, transformer-based AC-DC isolation, and a dedicated battery pack with isolated charger [12]. The trade study was evaluated using six criteria: voltage regulation, isolation quality, EMI susceptibility, integration complexity, reliability, and power efficiency. They were weighted to reflect mission-critical priorities: ensuring stable power for sensitive electronics, minimizing integration risk, and supporting long-duration operation in the harsh Martian environment. Voltage regulation and isolation quality were given the highest weights (25% each), recognizing the payload's susceptibility to noise and the need to prevent ground loops or leakage currents that could compromise scientific data integrity. EMI susceptibility (20%) was prioritized due to the proximity of high-power actuators and antennas, while integration complexity (15%), reliability (10%), and power efficiency (5%) rounded out the assessment, consistent with best practices in planetary payload design.

The isolated DC-DC converter emerged as the top choice, offering excellent voltage regulation (less than 2% ripple), full galvanic isolation (>1 kV withstand), and proven EMI filtering in a compact, space-qualified package [12]. This approach is widely adopted in NASA and ESA science payloads, providing high reliability and efficiency (>90%) with minimal added mass or integration burden. Best practice is to contact VPT or a similar supplier for a space-qualified, isolated DC-DC converter with a 28 V output [8]. Vendors such as VPT and Vicor routinely provide custom output voltages for space missions, ensuring optimal integration and performance for the payload. If a custom 28 V output module is not available, the next best approach is to use a standard model such as the SVRFL2815S (15 V, 100 W) in combination with a space-qualified, isolated boost converter to step up to 28 V, or to use two compatible modules in series if approved by the manufacturer [8]. While this introduces additional complexity and some efficiency loss, it remains a feasible backup if procurement or schedule constraints preclude a custom module.

Transformer-based AC-DC isolation, while capable of delivering high isolation quality, scored lower due to increased mass, volume, and integration complexity, as well as moderate efficiency and heritage for low/medium power applications. The dedicated battery pack option, though providing full isolation and ride-through capability, was penalized for added mass, thermal management complexity, and the need for periodic recharging and monitoring.

Given the external mounting requirement, the selected power system must also withstand temperature swings from -20°C to +40°C in operation (and -40°C to +60°C survival), with rapid changes mitigated by suitable thermal shielding or active heating [27]. The DC-DC converter solution is compatible with these needs, as it can be housed within the payload's thermally regulated enclosure and placed at a safe distance from vibration and EMI sources, as required by the integration constraints [7]. This ensures the integrity of precision atmospheric sensors and the mass spectrometer, both of which are highly sensitive to electrical and mechanical disturbances.

The trade study supports the implementation of a space-qualified isolated DC-DC converter as the optimal solution for powering the external experiment payload. This architecture delivers the required voltage stability, isolation, and EMI protection, while minimizing integration complexity and supporting the constraints of mass, volume, and environmental requirements of Mars surface operations.

1.5.4 Command and Data Handling (CDH) Subsystem

1.5.4.1 CDH Subsystem Requirements

The CDH (Command & Data Handling) Subsystem consists of the Onboard Computer (OBC) subassembly, Data Storage subassembly, Data Interfaces subassembly, and Telecommunications subassembly. In order to meet all of the mission requirements, the subsystem must be able to navigate and analyze its surroundings and goals for mission success.

The Command and Data Handling (CDH) Subsystem enables spacecraft coordination, autonomy, and communication. It integrates four key subassemblies Onboard Computer (OBC), Data Storage, Data Interfaces, and Telecommunications each of which supports critical mission functions. The OBC executes flight software and manages autonomy routines. Its performance, memory, and radiation tolerance are vital for maintaining control and system integrity in the harsh Martian environment. Data Storage ensures scientific and telemetry data are logged reliably and accessibly, necessitating sufficient capacity, fast write speeds, and resilience to environmental degradation. Data Interfaces serve as the internal communication backbone, linking the OBC to instruments, actuators, and sensors with reliable timing and low signal noise key for coordinated subsystem execution and fault response [5, 6]. Telecommunications

handles the uplink and downlink of mission data between the rover and Earth via orbital relays. Efficient encoding, low power draw, and fault-tolerant transmission are essential to maintaining operational awareness and ensuring scientific return. Each subassembly is interdependent, and failure in any one of them risks total mission loss.

In order for the CDH Subsystem to meet all of its requirements, constant verification and testing of subcomponents is needed for maximum performance. Methods would include demonstrations of the technological capabilities in the CDH Subsystem in a safe space, using effective programming for debugging and early software testing.

1.5.4.2 CDH Subsystem Overview

The Command and Data Handling (CDH) Subsystem serves as the brains of the rover, managing data processing, storage, communication, and coordination across all subsystems. It includes four key subassemblies: the Onboard Computer (OBC), Data Storage, Data Interfaces, and Telecommunications.

The selected Onboard Computer is the RAD5545, a flight-proven, radiation-hardened processor with a Technology Readiness Level (TRL) of 9 [2, 4]. Its multi-core 1 GHz-class architecture and >2 GB of memory provide ample computing power for autonomy routines, sensor fusion, and real-time control tasks. The processor's radiation tolerance and heritage from previous missions ensure reliability in the harsh Martian environment.

For data logging and instrument outputs, the rover employs a Non-Volatile Memory Express (NVMe) Solid State Drive. This device offers >512 GB of storage and high-speed data transfer rates exceeding 2000 MB/s [6]. Its high TRL, coupled with efficient power consumption and tolerance to environmental stress.

Subsystem-level communication is handled through RS-422, a space-proven serial interface with strong noise immunity, deterministic timing, and low integration complexity [5]. It connects all subsystems to the OBC, enabling command routing and telemetry gathering in real time.

For external communications, an Ultra High Frequency (UHF) radio was selected. This device operates at TRL 9 and offers low power consumption, omnidirectional coverage, and a long flight heritage on missions such as Curiosity and Perseverance [14]. It provides a communication relay between the rover and the Mars Reconnaissance Orbiter (MRO), which then transmits data to Earth via the Deep Space Network (DSN). The UHF system is particularly well-suited for the limited bandwidth and latency-tolerant nature of planetary missions.

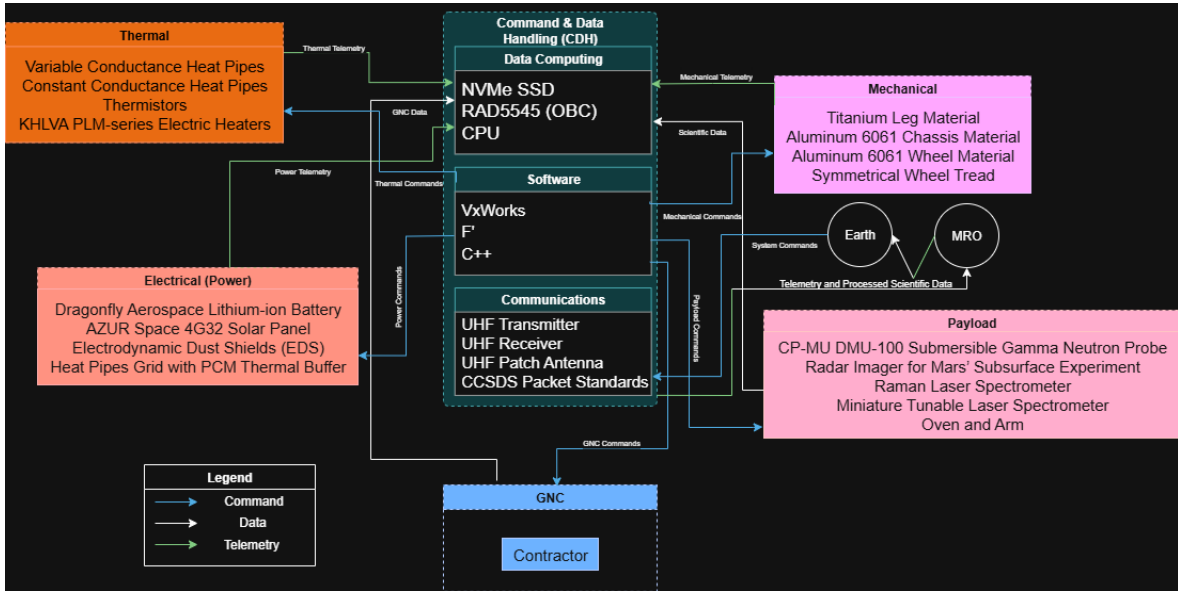


Figure 1.5.4.2.1: Software Architecture Flowchart

The CDH subsystem is structured around three functional blocks: Data Computing, Software Execution, and Communications. These blocks together manage the collection, processing, prioritization, and transmission of data. A software architecture diagram illustrates how the CDH interfaces with other rover systems, using RS-422 for physical connections and standardized software protocols for message handling and execution. The Electrical Power System (EPS), which includes lithium-ion batteries and deployable solar panels with electrodynamic dust shields, is tightly integrated with the CDH system. The CDH receives real-time telemetry from the EPS battery voltage, current draw, charge status, solar panel efficiency, and internal temperature and compares this data against expected operating profiles. When deviations are detected, CDH commands can modify EPS behavior: enabling/disabling charging, deploying solar arrays, or redistributing power across subsystems. Power modes such as science mode, sleep mode, and emergency mode are also managed via CDH logic based on power and mission conditions.

Thermal regulation is another key interface. The thermal control system includes passive elements such as multi-layer insulation (MLI) and active elements like electric heaters and variable conductance heat pipes [2, 27]. Thermistors throughout the rover provide temperature data to the CDH, which responds by activating or deactivating heaters or adjusting heat pipe flow [27]. For colder Martian nights, the CDH can initiate power-conserving overnight heating cycles and shut down non-essential systems to preserve critical functionality. All thermal telemetry is logged and used to refine thermal response strategies and plan future power availability.

Although the GNC subsystem is provided by an external contractor, the CDH subsystem is responsible for processing the GNC data onboard. The OBC receives measurements from the IMU, including accelerometer and gyroscope data, and fuses them with wheel odometry and actuator feedback through an Extended Kalman Filter [16]. This provides an accurate real-time state estimate of the rover's position, velocity, and orientation, which is essential for localization and path planning. CDH software then uses this information to calculate error between the current and target state, sending corrective commands to the mobility subsystem to close the loop [16].

The CDH software is written in C++ due to its performance efficiency and suitability for real-time embedded systems. Code development shall be done through Visual Studio Code inside Docker containers for embedded portability, and managed using Git version control [17]. The modular software architecture separates drivers, control routines, and communication layers to reduce risk and enhance reliability. Safety-critical logic is incorporated to maintain spacecraft operability even under adverse conditions.

Commands from Earth are prepared by mission control and sent during scheduled DSN communication windows. These messages are relayed via the MRO to the rover's UHF radio. Following CCSDS standards, these commands include instructions to activate instruments, update configurations, modify science plans, or adjust mobility parameters [15]. The CDH system checks message integrity and routes commands to the appropriate subsystems. Priority execution ensures that time-sensitive commands (e.g., fault recovery or power reallocation) are handled immediately, while others are queued and executed as bandwidth and system state allow [15].

All data generated on the rover telemetry, health logs, science measurements is collected and processed by the CDH subsystem before transmission. The data is compressed, timestamped, compressed into packets, and assigned priority. Critical telemetry such as power levels, internal faults, and system temperatures are prioritized over less urgent science data. These packets are transmitted via UHF to MRO during scheduled overpass windows and subsequently sent to Earth. The CDH system ensures redundant transmission of urgent data and manages lower-priority data buffering for delayed downlink opportunities.

1.5.4.3 CDH Subsystem Trade Studies

[CDH Subsystem Trade Study for Onboard Computer](#)

Figure 1.5.4.3.1: Onboard Computer Trade Study

The OBC serves as the core of the CDH subsystem, managing software execution, inter-subsystem coordination, sensor fusion, and autonomous tasking. It

must reliably support navigation, data management, and communication protocols in a high-radiation, energy-limited environment. This trade study evaluates the RAD750, RAD5545, Cobham GR712RC, and Pumpkin OBC (CubeSat Kit) across five weighted criteria: Processing Performance (30%), Radiation Tolerance (20%), Memory Capacity (15%), Mass & Power Efficiency (25%), and Flight Heritage/Technology Readiness Level (10%).

Processing Performance (30%) received the highest weight due to the computational demands of autonomy, real-time sensor fusion, and data handling for science payloads. The OBC must handle task parallelism efficiently to avoid command delays or data loss. Radiation Tolerance (20%) is an essential safeguard against single-event effects (SEEs) and total ionizing dose (TID) risks are significant over long mission durations. Memory Capacity (15%) supports instrument buffering, log storage, and data pre-processing. Mass & Power Efficiency (25%) is a combined factor representing the importance of every watt and gram within the strict system constraints. Flight Heritage/TRL (10%) offers assurance that the system has performed reliably in similar missions, reducing integration risk and shortening testing timelines.

Figure A.1: RAD5545 SpaceVPX single-board computer

RAD5545 features a multi-core 1GHz-class processor, over 2GB of memory, and is radiation-hardened beyond 100 krad, making it ideal for executing autonomous algorithms, instrument control, and onboard data management [4]. Its moderately high TRL (8–9) reflects successful use in a variety of missions. RAD750 remains widely used and well-proven with high radiation tolerance and strong flight heritage, but its lower processing performance (200–500 MHz) and less memory make it less favorable for autonomous operations. Cobham GR712RC is based on a dual-core LEON3 processor and performs adequately in power and radiation terms, but its limited memory and weaker processing speed place it behind for high-autonomy scenarios [18]. Pumpkin OBC, while lightweight and efficient, lacks radiation protection and processing capability. It is more suited to CubeSat-class missions in low Earth orbit rather than long-term missions [19].

The RAD5545 was selected as the OBC. Its computational power, memory capacity, and robust radiation protection support high-throughput science, autonomy, and real-time system management [4]. The system's growing flight record further supports its viability for deep space missions making it a great fit for the rover.

CDH Subsystem Trade Study for Data Storage

Figure 1.5.4.3.3: Data Storage Trade Study

The mission is expected to gather and transmit data at different times, and is

therefore required to store the collected data efficiently to support scientific operations involving high-resolution imaging and complex sensor data. Selection of proper data storage is therefore significantly relevant to the performance of the CDH subsystem as a means to log and transmit data for analysis. The trade study evaluates Micro Secure Digital (SD) cards, Embedded MultiMediaCards (eMMCs), and Non-Volatile Memory Express Solid State Drives (NVMe SSDs) as potential storage solutions using four weighted criteria: Data Storage Capacity (35%), Data Transfer Speed (25%), Radiation Tolerance (20%), and Power Consumption (20%).

Storage Capacity (35%) was given the highest weight due to the intent to collect and store large volumes of multispectral and subsurface data from the instruments. Transfer Speed (25%) was prioritized next as several instruments will produce large datasets that must be quickly written to prevent scientific data loss. Radiation Tolerance (20%) is essential for safeguarding mission-critical data against noise and stray interference, primarily utilizing error-correcting codes (ECCs). Power Consumption (20%) directly affects system longevity and thermal load; however, since storage systems are not always in use and thermal load can be accounted for by the TCS subsystem, this criterion can be allocated less weight.

Micro SD cards score the lowest on capacity and radiation tolerance, which are mission-critical for long-term reliability and scientific throughput. Their largest strength is extremely low power consumption. eMMC offers a better balance with moderate capacity, acceptable speeds for sensor data capture, and manageable power usage. Though not radiation-hardened, its industrial design gives it an edge over consumer SD cards. NVMe SSDs provide excellent capacity and speed, which is vital for fast camera data dumps and buffering. However, they consume significantly more power and are heavier and bulkier, which is not ideal under mission constraints.

The NVMe SSD was selected as the primary data storage option for its performance in capacity and speed, which outweighs the tradeoff in power draw and moderate radiation robustness. The Phison 8TB M.2 PCIe Gen4 NVMe SSD passed NASA TRL 6 certification in December of 2022, and would be ideal for data storage.

[CDH Subsystem Trade Study for Data Interfaces](#)

Figure 1.5.4.3.4: Data Interfaces Trade Study

The CDH subsystem must support robust data communication between onboard sensors, actuators, and the Onboard Computer (OBC). The selected data interface must facilitate consistent throughput, low error rates, and compatibility with spaceflight hardware. This trade study evaluates RS-422, MIL-STD-1553, I2C, and Ethernet as candidate data interface protocols for P.H.O.E.N.I.X, using five weighted criteria: Data Rate (30%), Noise Tolerance (25%), Physical Complexity (20%), Time Accuracy

Preservation (15%), and Technology Readiness Level (10%).

Data Rate (30%) received the highest weight due to the need to stream continuous sensor data—including camera feeds and GPR logs—into the CDH system with minimal delay or buffering. Noise Tolerance (25%) is especially critical in the harsh Martian environment, where electromagnetic interference and radiation events may corrupt signals unless handled by fault-tolerant protocols. Physical Complexity (20%) was included to account for ease of integration and the routing burden on the spacecraft harness. Lower wire count and compact topology reduce mass and integration risk. Time Accuracy Preservation (15%) is needed to synchronize timestamps and ensure determinism in time-sensitive science sequences and actuator commands. Technology Readiness Level (10%) provides assurance of reliability based on mission heritage and space qualification.

Figure A.3: RS-422 Pinout Table

RS-422 offers modest data rates (10–50 Mbps), but provides incredible noise tolerance (rad-hard, fault-tolerant implementations exist), low physical complexity , and strong time determinism. Its spaceflight heritage gives it the highest TRL score. MIL-STD-1553 is the most robust and fault-tolerant protocol considered, with strong shielding and redundant architecture. However, it suffers from very low data rates (<1 Mbps) and high physical complexity, making it less favorable for large data real-time science streaming or camera feeds. I2C is extremely lightweight, modular, and simple to implement, making it ideal for short-range internal board-level communication. However, it is poorly suited for spacecraft-scale interfaces due to limited data rate, very poor noise tolerance, and lack of time determinism. Ethernet provides very high data rates (>100 Mbps) and is widely adopted in terrestrial systems. However, its minimal noise tolerance and bulkier shielded cable assemblies present integration and timing challenges, especially in spaceflight environments without specialized protocol layers.

RS-422 was selected as the optimal data interface. Its strengths in noise tolerance, time determinism, and space-proven reliability make it ideally suited for the Martian environment, where command accuracy and telemetry integrity are mission-critical.

CDH Subsystem Trade Study for Telecommunications

Figure 1.5.4.3.6: Telecommunications Trade Study

The telecommunications subsystem is responsible for sending scientific data and health telemetry from the Martian surface to Earth. For P.H.O.E.N.I.X, this requires a communications system that is low in power consumption, robust to environmental constraints, and capable of transmitting significant volumes of data while mitigating risk

to transmission interference. This trade study evaluates Software Defined Radios (SDRs), Deep Space Networks (DSNs), Deep Space Optical Networks (DSONs), and Ultra High Frequency (UHF) Radios as candidate telecommunications architectures using the four weighted criteria: Power Consumption (35%), Data Rate (25%), Technology Readiness Level (25%), and Directionality (15%).

Power Consumption (35%) received the highest weight due to the scale of power cost in poorer telecommunications candidates, and the net cost that would have on mission lifespan. Data Rate (25%) was emphasized to ensure timely offloading of science data and prevent onboard data storage bottlenecks. Technology Readiness Level (25%) was prioritized to reduce implementation risk, as there are many heritage systems and newer developments. Directionality (15%) was included to assess risks related to poor alignment and aiming. Lower directionality systems simplify antenna design and improve robustness.

Ultra High Frequency (UHF) Radio offers extremely low power consumption (<5W), omnibearing directionality, and high technology readiness with consistent performance in NASA missions including Phoenix, Curiosity, and Perseverance [32]. While its data rate is relatively limited (1–10 Mbps), the benefits in power and technological reliability indicate favorable implementation. Software Defined Radio (SDR) performed moderately well across all categories. While consuming slightly more power (5–10W), SDRs allow flexible reconfiguration in software and can support a wide range of frequencies and protocols. This adaptability is valuable for redundancy, though it lacks the ultra-low power edge of UHF. Deep Space Networks (DSNs) are well-established and used for Earth return, but its integration onboard involves relay communications rather than direct-to-Earth links from a low-cost rover. Its moderate power draw and data rate (10–50 Mbps) make it viable, but its directional requirements and complexity limit onboard implementation. Deep Space Optical Network (DSON) scored lowest due to extreme power consumption (>40W), low TRL, and high directionality sensitivity.

Ultra High Frequency (UHF) Radio was selected as the optimal telecommunications method due to its superior balance of low power draw, high reliability, and simple, robust integration. Its low directional sensitivity and TRL 9 flight heritage on previous Mars missions make it ideal for surface operations with relay to orbiting assets. The data rate, while lower than other options, is generally sufficient and can be mitigated through integration and relay support from orbiting assets like the MRO.

1.5.5 Thermal Management Subsystem

1.5.5.1 Thermal Management Subsystem Requirements

The thermal subsystem includes MLI coatings, heat pipes, radiators, and optional radioisotope heater units. It must protect critical hardware from Martian hazards such as dust storms and radiation, while maintaining thermal stability throughout the mission.

The thermal components of the subsystem must protect the designated instrumentation and powering system to ensure no failure that will result in the mission being compromised. Such components include MLI coatings, which shall aid in thermally isolating the system to maintain its operational temperature range. The MLI design includes an outer cover layer, which is key to protecting the under layers and rover hardware from the outer environment, radiation, and micrometeoroids. It also consists of levels of reflective layers underneath the outer cover, as well as minimizing thermal conduction from the exterior to the interior. The MLI shall also have an innermost layer called the inner cover, which faces the interior hardware. This layer must generate a minimal amount of particulate contaminants, aid in reducing stress for the interior reflective layers, and not be aluminized to reduce the risk of an electrical short, which is a fire hazard. These layers shall be separated by a form of netting in the design to minimize thermal conductivity within the layers. For the separation of the inner cover and the reflective layers, the design must utilize adhesives, adhesive transfer tapes, and/or metalized tape to aid in the thermal conductivity properties. Emissivity and absorptivity values must be taken into consideration to thermally isolate the system. The design shall also implement a form of ventilation within the MLI with the inclusion of perforations in areas of the MLI to aid in outgassing to minimize pressurization within the MLI.

To ensure the rover system is able to function properly without freezing in the Martian environment in adherence to the system's requirements, an active TCS is necessary to tackle this challenge. One such active TCS is an RHU, the RHU will provide passive heating to the system using an isotopic radioactive material via radioactive decay. To control the heating, heat pipe designs shall be implemented and integrated into the system to equally distribute heat around the system. Radiators shall be used for excessive heat dissipation. These design measures shall help in meeting the system requirements.

In order for the TCS to meet the system requirements, methods of verification and validation must be conducted to ensure each component meets the requirements. These methods include CAD thermal modeling of the subassemblies. After acquiring results, the components shall be tested in a thermal vacuum chamber at one of NASA's research facilities to validate the thermal modeling analysis on CAD. The components

shall then be tested with other subsystems in a mission simulation testing area to ensure all thermal subsystems comply with the mission system requirements.

1.5.5.2 Thermal Management Subsystem Overview

The thermal subsystem comprises of MLI (multilayer insulation) coatings, heat pipes, thermal sensors, and electric heaters. With no thermal controls, the system was expelling abundant amounts of heat, losing 4000W of heat. In order to insulate the rover, double-sided mylar was decided to be the best option, as it is one of the most effective at preventing heat from radiating out, with an exceptionally low emissivity value. The entire rover will be coated with double-sided mylar MLI. The TRL of this MLI is 5 as it has heritage. For the inner layer of the MLI blanket, goldized Kapton has been selected for its high absorptivity and low emissivity. Since the system is so cold, it was decided that those were the traits to prioritize, taking in more warmth from the sun and preventing heat from leaving. The TRL of goldized kapton is 5 for the same reason as the double mylar MLI.

The majority of instrumentation on the rover can operate within the same temperature range of 303 K to 313 K, however the mini-TLS requires a lower temperature for operation. To solve this, the mini-TLS will be placed further from overly hot components such as the oven, and will have heat pipes removing excess heat. This is doubly necessary since the mini-TLS itself is prone to overheating. These heat pipes will remove a controlled amount of heat from the area dedicated to the Mini-TLS to the outside environment. Since the Mini-TLS has a more delicate operational temperature these heat pipes will be separate from the ones around the other instruments. The heat pipes here will be variable conductance heat pipes, so that the amount of heat expelled can be controlled as the outside temperature or heat sink temperature drops. The TRL of variable conductance heat pipes is 5, because it has successfully operated in space environments, but is not legacy technology nor has been on similar missions [2, 3].

The other system of heat pipes will move heat from the oven to the RLS, RIMFAX, gamma neutron probe, and OBC which need to be kept at higher temperatures. The oven itself will produce notably high temperatures while in use and the heat pipes will allow that heat to be dissipated to the rest of the system. The heat pipes used will be constant conductance heat pipes, so that this system is passive. These are easier to integrate and have a higher TRL than variable conductance heat pipes. The TRL of constant conductance heat pipes is 7, because very similar units have successfully operated in space before but not on identical missions.

For the hot end of expected daytime temperatures, ~100W of heating is still needed. In order to solve this, a selection of electric heaters was made to be connected to the computer system along with thermal sensors. A thermal sensor will be dedicated

to each instrument, to monitor each instrument is within the operational temperature and to alert the system if they start to fall out of that range. Connected to the thermal sensors, there will be electric heaters to provide the necessary heat to maintain the operational temperatures. The thermal sensors will be a thermistor, and the electric heaters will be KHLVA, PLM-series. With these heaters Q_{net} would equal zero.

	Mass	Dimensions	Max power
VCHP	1.6kg	0.5 m long, 2 cm radius	70W
CCHP	3.2kg	1 m long, 2 cm radius	0W
Electric Heater	0.4kg	6 in ²	40W

Figure 1.5.5.2.1: Thermal Subassemblies

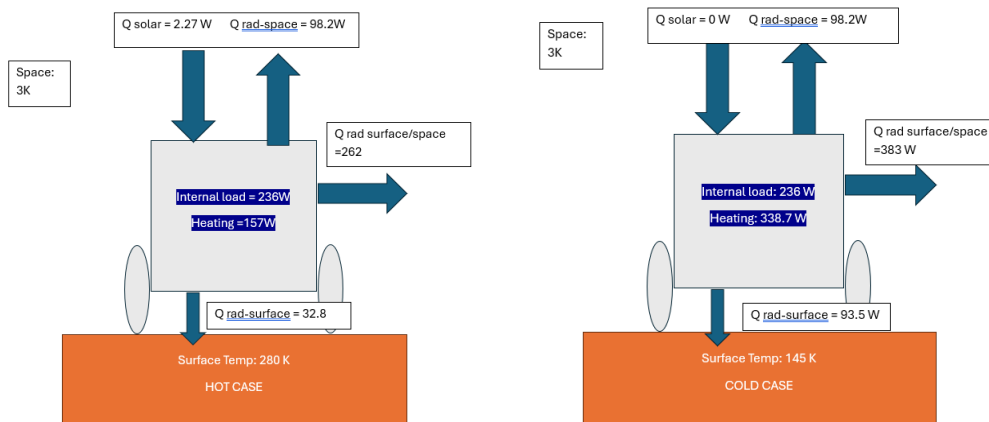


Figure 1.5.5.2.2: Heat Flow Maps

1.5.5.3 Thermal Management Subsystem Trade Studies

Thermal Management Subsystem Trade Study for MLI(Outer Layer)

Figure 1.5.5.3.1: MLI (Outer Layer) Trade Study

To find the ideal outer cover of the multilayer insulation (MLI) system that can help tackle the environmental, cosmic, and solar challenges P.H.O.E.N.I.X. will face on the mission, a trade study was conducted on 4 potential candidates of the system; beta cloth, beta cloth aluminized, double sided mylar, and kapton coated and backed.

These outer cover materials are evaluated on criteria set in stone based on mission requirements. One of the criteria set for the outer cover is the operational temperature range, weighted at 25%, as the material chosen for the outer cover must

be able to withstand extreme day/night seasonal temperature swings in the Martian region of Erebus Montes. Another is the evaluation of tensile strength, which is weighted at 15%, as the outermost layer of the MLI it is crucial that the structural integrity of the outer cover must be able to withstand extreme weathering throughout the mission duration. Finally, two extremely vital criteria when it comes to the selection of material are the emissivity and absorptivity values of the chosen material, each weighing 30%. It is vital to keep the system thermally isolated from the environment around it; therefore, when choosing the outer cover, low absorptivity and low emissivity are favored.

The Beta cloth offers the capability of withstanding extreme temperatures ranging from 122.15K to 533.15K [13], which is more than enough to cover the Martian temperature swings. The material's tensile strength increased with the addition of PTFE Teflon coating to combat MMODs(micrometeoroids) and UV radiation. The Beta cloth however, has a high absorptivity, which is not ideal when it comes to an environment like Mars, where daytime temperatures can skyrocket. It also offers high emissivity values, which is not favorable when it comes to making sure the hardware doesn't overheat. Its application in past spacecraft, capsules, and rovers makes it an exemplary candidate. The Aluminized version of the Beta cloth, although having similar properties to its parent the Beta cloth, shares similar emissivity and absorptivity values which are not favored. The Kapton Coated and Backed offers a great temperature range in par with its Beta cloth variants but lacks the tensile strength when it comes to withstanding the weathering from MMODs. It also falters when it comes to ensuring low absorptivity with its relatively moderate range. In an environment where low emissivity is favored, the Kapton only provides a moderate level of emissivity, which will affect the thermal balancing of the entire system. The Double Sided Mylar offers an excellent temperature range of 22K to 394K [14] which is enough to cover the temperature swings of the Martian atmosphere. The material also offers a decent tensile strength which is important when it comes to the selection of the outer layer and withstanding the weathering of MMODs and dust storms. The Double Sided Mylar, unlike its other counterparts being compared in the trade study, has a low absorptivity value and low emissivity value. Meaning that in our calculations it conserved the most heat. Aluminized Beta Cloth for comparison was losing 2290W of heat compared to 154W lost with double sided mylar. Making it the best choice for, being the closest to reach a Qnet of zero.

The Double Sided Mylar was ultimately selected for the outer cover material due to not only its ability to withstand extreme temperature swings on the Martian surface but also its exceptionally low absorptivity value and low emissivity tops off the other candidates when it comes to the deployment in the Martian environment and ensuring the system doesn't freeze or overheat.

Thermal Management Subsystem Trade Study for MLI(Interior Layer)

Figure 1.5.5.3.2: MLI (Interior Layer) Trade Study

Throughout the mission duration, the interior layer will be required when it comes to aiding in minimizing conductance from the outside to the inside and vice versa. A trade study was conducted on 3 potential candidates when it comes to combating this challenge. These include: Aluminized Kapton, Aluminized Mylar, and Goldized Kapton. These requirements are evaluated per the mission systems requirements.

These materials are evaluated on criteria set for them: OTR (Operational Temperature Range), TRL, absorptivity, and emissivity. OTR is set to 25% to ensure that it meets on par with the operational temperature range of the outer cover, inner cover, and materials used to bind them together. TRL is set to 15% as these proposed materials are heritage and have been flown in past missions, but are included to reduce any lingering risk. Absorptivity is at one of the highest levels at 30%, due to ensuring that there is a minimal amount of conductivity throughout the layers when heat passes through. Emissivity value was also valued at 30% and was added to ensure emissivity values are in the low-mid ranges, which aid in minimizing conductivity as well.

Aluminized Kapton offers an excellent temperature range at 23.15K to 563.15K [15], which aids in not only working in the extreme Martian environment but also when the rover enters a hot case or a cold case scenario. The TRL was assessed as this type of interior layer was proven in both Mars missions and deep space missions as well making it TRL 5-6, which helps assess the technological risks. However, it has high values of absorptivity, thus when it comes to ensuring that the inner layers minimize conductance as much as possible to ensure thermal isolation of the system. Emissivity values were at the low-mid range when it comes to minimizing conductance, as well as for the Aluminized Kapton. The Aluminized Mylar, although having similar absorptivity and emissivity values as the Aluminized Kapton, does not meet temperature requirements, with it being 213.15K to 423.15K [51], and will at times shrink when the rover approaches its hot case, which will affect the structural integrity of the MLI system especially for the long-term duration. The Goldized Kapton possessed a greater temperature range and better absorptivity when compared to its two other components. Thus, it is favorable when it comes to wanting to achieve as minimal conductance as possible.

Goldized Kapton was ultimately chosen as the ideal interior layer when it comes to attempting to minimize as much thermal conductance as possible in order to aid in thermal balancing. Such perks include its exceptional temperature range, heritage levels of TRL proven in past space missions, as well as high absorptivity and low-mid

emissivity values. These perks aid in solidifying its choice in being an ideal interior layer for the MLI when it comes to meeting systems requirements.

Thermal Management Trade Study for Heat Pipes

Figure 1.5.5.3.3: Heat Pipes Trade Study

Heat Pipes are necessary when it comes to distributing heat evenly throughout the rover system and maintaining thermal balance. This trade study evaluates the 3 heat pipe candidates, which include: Variable Conductance Heat Pipe(VCHP), Constant Conductance Heat Pipe(CCHP), and Thermosyphon. This is to ensure that these selections meet the mission system requirements.

These pipes are evaluated based on criteria set for them, such as operational temperature range(OTR), TRL, reliability, and complexity. The OTR is set at 30% because it is crucial that these heat pipes work under a desirable temperature to reduce the risk of cascading failures, which jeopardize the mission. The TRL is set at 15% to evaluate whether the technology is mature enough for this mission. The reliability is set to the highest at 35%, to ensure that the heat pipe can operate in extreme conditions, along with long durations which is crucial when it comes to thermal control. Complexity is set at 20% to ensure whether the heat pipe design can be integrated into the system without having to alter other subsystems.

The VCHP is a passive heater that contains a reservoir containing a non-condensable gas(NCG). The gas acts as a thermal spring, expanding and contracting as the pressure inside the heat pipe changes with varying temperatures [2]. The temperature range of the VCHP ranges from around 120K to 374K [2] , which makes it a great choice for a heat pipe. The TRL of the proposed heat pipe is space proven and has been flown before in space, thus making it a TRL-5. The VCHP is reliable as well and it can accommodate passive heating for long-duration missions. However, for the VCHP to work in the Martian environment, it must be designed with wicks for it to work properly in any orientation, mainly affected by gravity [3]. The CCHP works similarly to a VCHP, transferring heat from one location of the pipe to another via evaporation and condensation. It has a decent temperature range of 200K to 423K [4], which makes it work as well as its VCHP counterpart. The TRL for the CCHP is set at a TRL-5 as it has been used on past Mars rover TCS before. Like its VCHP counterpart, it has proven to be reliable when it is deployed for long-duration missions. The CCHP can work properly without any concern for the effects of the Martian gravity being applied to it. The Thermosyphon has a lower heat transfer capacity, which is a negative factor when it comes to being applied in the Martian environment. The TRL levels for the Thermosyphon are as low as there are no records that indicate it can withstand the Martian gravity, which is significantly less than that of Earth which it has relied for its

Earth-based applications. It has proven to be reliable when it comes to other heat pipe alternatives, but very complex when transitioning to a different gravitational orientation of Mars, which can hinder its efficiency.

Both the VCHP and CCHP were chosen following the rover design. This system shall work in unison to provide thermal stability of the system as a whole. It shall have two loops to control the heat sink which is the outer environment. This selection will aid in meeting the system requirements for P.H.O.E.N.I.X.

Thermal Subsystem Trade Study for Electrical Heaters

Figure 1.5.5.3.4: Electrical Heater Trade Study

An active heating subsystem must be implemented into the system itself as a whole to meet the mission system requirements. A trade study was conducted on 3 electrical heater candidates to fulfill the requirements; the KHLVA, PLM-Series Electrical Heater, SHK series Electrical Heater, and the Polyimide Thermofoil HK Series Electrical Heater.

Power is set to the highest at 30% since it is more favorable to be as power efficient as to thermal efficiency, due to the limited power supply. Mass is set at 25% as the compactness and its weight are important factors when it comes to meeting (SYS.04). TRL is set at 20% to ensure that the proposed electrical heater is mature for Martian applications. The temperature Range is at 25% to evaluate whether the proposed electrical heater has an acceptable temperature range that allows the system to operate properly.

The KHLVA, PLM-Series Electrical Heater offers a low power draw at 0.775W/cm^2 , which is favored when power is limited [17]. This heater is also very compact being 2x1 inch and 0.01 in thick, making it small and easy to integrate. The heater was deployed through launches of NASA CubeSat satellites, marking it at a high level of TRL. This series offers an exceptional temperature limit of 216K to 505K, which is sufficient to keep the rover system operational. The SHK Series has a similar power draw as its KHLVA, PLM-series counterpart, also numbering at 0.775W/cm^2 . The heater also offers compactness when it comes to dimensional constraint considerations. The SHK was used in CubeSats as well, demonstrating a higher degree of TRL. However, the SHK temperature ranging window is not up to par with its KHLVA counterpart, it still offers a great range at 238K to 423K [47] with the inclusion of Aluminum foil. The Polyimide Thermofoil HK Series electrical heater draws a higher power per cm^2 at 3W/cm^2 , which is significantly higher than the two other electrical heaters [34]. This specific heater, like its other counterpart, is extremely lightweight and easy to integrate into any component of the spacecraft/rover. The TRL of this specific electrical heater is also high as well as it was also used in CubeSats. The Polyimide

also offers an impressive range of 73K to 473K [47], which, like the KHLVA series and SHK series, will be able to keep the rover at operating temperatures.

The KHLVA, PLM Series Electrical heater was chosen as it meets the power draw efficiency, along with an exceptional temperature range. The KHLVA also demonstrated that it was flight-proven via CubeSats along with its compactness, making it an ideal candidate. This selection aids in meeting the system requirements for P.H.O.E.N.I.X.

[Thermal Subsystem Trade Study for Thermal Sensors](#)

Figure 1.5.5.3.5: Thermal Sensor Trade Study

Thermal sensors are an absolute component when it comes to designing of the TCS subsystem. A trade study was conducted on 3 thermal sensors: the Thermocouple, Thermistor, and RTD sensors, to ensure these work per the system requirements.

Sensitivity is set at 25% to ensure that the sensors can read any small temperature changes; high sensitivity is preferred. Accuracy is set at 20% for the measurement of how accurate the reading is to the actual temperature. Reliability is set at 25% which is to ensure that the sensor can withstand long-term missions. Response time is also set at 30% is crucial to detect a temperature change as fast as possible without any delay.

The Thermocouple has a low and small sensitivity, which is not ideal when trying to obtain a change in temperature data. The accuracy of the thermocouple is in the medium range, hence the grading. This particular is durable and resistant to corrosion due to a protective metal sheath, hence why it has an excellent reliability value. However, a sensor encased in a protective metal sheath is more resistant to wear and corrosion over time, but it costs more and offers less sensitivity. Its response time, like its sensitivity, lacks overall, making it not that great and not that bad in general. The Thermistor, unlike the thermocouple, has a high sensitivity making it ideal when measuring any minor flux in temperature. The accuracy of this sensor is also in the medium range when it comes to measuring results. It lacks durability when it comes to being deployed for long-duration missions, thus a redundant system needs to be implemented. Its response time is also similar to the thermocouple when it comes to detecting change. The RTD has a moderate level of sensitivity, which is not as impressive as a thermistor. However, the accuracy levels of the RTD are not that good and thus not recommended when it comes to implementing it into the system. The RTD also has good durability, but not as impressive as the thermocouple when it comes to long-duration missions. The RTD has a better response time overall than the thermocouple and the thermistor, but it will not help when it comes to this trade study. The grading for three of these instruments is based on National Instrument data [25].

Ultimately, the thermistor was chosen as the heat sensor for the system as a whole, as its grading is better off from the other candidates. Its sensitivity and reliability make it an ideal candidate when it comes to being utilized on P.H.O.E.N.I.X.

1.5.6 Payload Subsystem

To meet the Human Exploration Goal, *HBS-1LM*, the mission will conduct scientific experiments to achieve the 2 objectives on this focus. The detailed breakdown for the following payload selected is provided in the sections 1.5.6.2, 1.5.6.3. The selected instrumentation to achieve the objective of investigating the long duration Martian environmental impacts on a protected and pressurized earth-fluid sample for unknown hazards that may threaten the integrity of future mission-critical life support, rocket propellant, and agricultural fluids, is the CP-MU DMU-100 Submersible Gamma Neutron Probe [28]. This instrumentation is the best selection to conduct the experiment, and meet the selected scientific measurement requirements to periodically monitor the Earth fluid sample for risks, hazards, and contamination that may bypass the custom-engineered Fluid Protection System's protective layers and document via data generation. To further meet the Human Exploration Goal, the second objective sets to investigate how subsurface stratigraphy, dielectric properties, and dust layer thickness affect the accessibility and long-term stability of near-surface water ice, in support of in-situ resource utilization and environmental risk reduction for future human exploration, with the Radar Imager for Mars' Subsurface Experiment (RIMFAX) to be the ground penetrating radar instrumentation in use [18]. This instrument met the highest criteria to conduct the experiment and use GPR reflection delays, estimating dielectric permittivity and radar wave velocity to characterize subsurface material properties, including layer thickness, composition changes, and porosity variations across a 10 m traverse. The mission will also meet a Science Exploration Goal, Q10.3b, by conducting scientific experiments to achieve the 2 objectives on this focus. The selected instrumentation to achieve the objective of determining the Deuterium to Hydrogen (D/H) ratio in hydrated volcanic rock on Mars' surface, is the Miniature Tunable Laser Spectrometer (Mini-TLS) as it met the best criteria to be used to define the relative abundance of protium and deuterium within samples of hydrogen from hydrated volcanic rock. Concluding with the last objective, which is to determine the crystal structure of minerals formed by asteroid impacts interacting with exposed subsurface ice, the instrumentation meeting the highest criteria was the Raman Laser Spectrometer (RLS). This instrument will identify chemical structure, crystal structure, and bond structure of Olivine from asteroids.

1.5.6.1 Payload Subsystem Requirements

The payload subsystem consists of four science instruments selected to achieve the mission's primary objectives as defined in the Science Traceability Matrix (STM).

Each instrument requirement is derived from its scientific function, expected performance under Martian conditions, and its interface with other subsystems such as thermal control, command and data handling, and mechanical mounting.

The Radar Imager for Mars' Subsurface Experiment (RIMFAX) supports the goal of identifying accessible water ice deposits. It must detect dielectric differences down to a depth of 10 meters with a permittivity sensitivity ≤ 0.1 . To meet this requirement, the instrument must be mounted on a stable platform with minimal electromagnetic interference and sufficient power and data bandwidth [18]. It must also interface with the mobility subsystem to maintain ground coupling while traversing varied terrain.

The Submersible Gamma Neutron Probe (SGNP) addresses the objective of monitoring radiation hazards to mission-critical fluids. It shall operate continuously for at least one Martian year, detecting gamma and neutron radiation levels between $1 \mu\text{Sv/h}$ and 10 Sv/h . To support long-duration performance, the instrument requires thermal stability within operational bounds and mechanical integration within a sealed fluid testbed. The probe must be electrically and thermally isolated while still interfacing with CDH for periodic data collection and transmission.

The Miniature Tunable Laser Spectrometer (Mini-TLS) enables analysis of the Deuterium-to-Hydrogen (D/H) ratio in hydrated volcanic rock. It must collect absorbance spectra with a sensitivity better than 80 ppb and an integration time of ≤ 1 second. The spectrometer must be mounted on a mobility-accessible arm or stable surface to acquire accurate samples, with localized thermal control and vibration damping to maintain optical calibration. Integration with CDH is required for both real-time command and high-resolution data logging.

The Raman Laser Spectrometer (RLS) is used to analyze the crystal structure of Olivine and other minerals formed via ice-impact interactions. It must collect spectra in the 11,111–33,333 nm range and resolve features with at least 10 cm^{-1} spectral resolution. This instrument operates effectively only within a thermal envelope of 228 K to 313 K, requiring close coordination with the thermal control system (TCS). In addition, the RLS must be positioned to access mineral targets and avoid shadowing or dust contamination.

Each instrument's performance is subject to verification through functional testing under simulated Martian conditions (temperature, radiation, and mechanical stresses). Requirements also include placement, power draw, signal conditioning, and structural mounting interfaces, which will be fully specified in the Interface Control Document (ICD). Together, these instruments ensure the P.H.O.E.N.I.X payload can deliver high-resolution, high-value science within the constraints of volume, mass ($\leq 15 \text{ kg}$), and energy budget allocated to the payload subsystem.

1.5.6.2 Payload Subsystem Overview

The chosen instrument to achieve the first objective is the CP-MU DMU-100 Submersible Gamma Neutron Probe. Waterproof and made to withstand high heat applications, it is durable, and built to last as a tried-and-true TRL level-6 scientific safety instrumentation actively utilized by first responders, nuclear facilities, and hazmat teams in extreme environments, proving its worth through a history of reading Gamma radiation dosage in multiple sources such as water, nuclear reactor cores, and fuels. It will now extend its earth legacy to a multi-planetary one, operating inside of the team's custom-engineered and rover-attached Fluid Protection System (FPS) for monitoring a protected earth fluid sample for Martian environmental impacts and contamination in weekly intervals over a one year duration. This recorded data will provide a strong contribution to materials science and engineering breakthroughs, uncover unknown threats to mission-critical fluids, and aid in the engineering of the next generation fluid storage systems that are necessary for astronaut safety and sustaining of long-duration missions on Mars. With a dosage recording range of $1 \mu\text{Sv/h}$ to 10 Sv/h and 12 seconds slow time constant (response time), the neutron probe is capable of precise, accurate, and stable contamination detection across subtle to extreme Gamma radiation level increases. The instrument was originally designed by the manufacturer for mobile operation using batteries, but the team has implemented a hardwire power method via rover where it will use an estimated maximum power of 270 mW. The instrument is designed to be compact, maintaining a lightweight mass of 1.3 kg and a total volume of 3362 cm^3 , fitting well within the 15kg total mass and $0.5 \text{ m} \times 0.5\text{m} \times 0.5\text{m}$ total volume constraints for the human exploration mission goal.

The main instrument selected to support the second objective is the Radar Imager for Mars' Subsurface Experiment (RIMFAX). This ground-penetrating radar system is designed to characterize subsurface stratigraphy and identify dielectric contrasts that can indicate dust layers, material transitions, and potential ice-rich zones. RIMFAX operates between 150 and 1200 MHz, allowing it to achieve vertical resolutions down to 15 cm in the shallow subsurface and detect features as deep as 10 meters under ideal conditions [18]. It works by transmitting radar pulses into the ground and measuring the delay and strength of reflected signals, which can then be used to estimate dielectric permittivity and radar wave velocity [18]. From these values, the instrument enables indirect assessments of porosity, composition changes, and regolith layering, all critical to evaluating the accessibility and stability of near-surface ice. The instrument includes a folded dipole antenna mounted on the rear of the rover chassis, oriented downward to allow continuous ground-facing data collection during the traverse. This antenna transmits and receives radar signals across a wide bandwidth, helping to resolve both shallow and deeper subsurface structures with high fidelity. It collects data continuously along the rover's traverse, generating radargrams that

provide a 2D view of subsurface structure. The system is compact around 3 kg, requires relatively low power (~5–10 W), and involves no moving parts, reducing the risk of mechanical failure. It also fits within the mission's experiment mass and volume constraints. With a Technology Readiness Level (TRL) of 9, it is flight-proven, having successfully operated on NASA's Perseverance rover. Its performance, reliability, and data return make it the most effective and mission-aligned instrument for achieving the subsurface science objectives.

The instrument chosen to fulfill the mission's third objective (Determine the Deuterium to Hydrogen (D/H) ratio in hydrated volcanic rock on Mars' surface) was the Miniature Tunable Laser Spectrometer. Specifically, the Mini-TLS is included in the mission to perform the task of defining the relative abundance of protium and deuterium within samples of hydrogen from hydrated volcanic rock. To carry out its task, the instrument needed to collect absorbance spectra in the 3593.3-3594.3 cm⁻¹ range of H in selected hydrated volcanic rock samples at multiple surface sites. It collects its data through a process very similar to its predecessor, the Tunable Laser Spectrometer (TLS). This process begins with sample collection. Once a sample has been acquired, it is put into an oven where it is then heated up. During this process, the water molecules inside of the rock are released as water vapor (both the HDO and H₂O), and this evolved gas is redirected to a different chamber with a tunable infrared laser. For this mission, the laser will be tuned to detect the absorption of HDO and H₂O. Since deuterium absorbs a different wavelength of light than protium, the Mini-TLS is able to distinguish between the two and perform the D/H ratio calculation (D/H Ratio = [HDO]/[H₂O]). At only 1 kg and 23.5 × 16.3 × 15.5 cm, the instrument is low power taking less than 8 watts [17]. The instrument has an approximate technology readiness level of 6, as it has been tested in analog Mars conditions but has not been utilized in a mission.

The selected instrumentation to achieve the science exploration goal and its last objective includes the Raman Laser Spectrometer (RLS) which is designed to analyze and detect what materials from Mars are made of based on its reactive reflection to laser light. It is designed to function by analyzing the crystal, chemical, and bond structure on a sample of Martian rock fragments and asteroid olivine that has been altered by geophysical and environmental forces to determine what elements may be within those samples. The scientific goal of investigating how the dynamic forces on planet Mars have altered the existence of water in its liquid form is pursued through the direct analysis of the surface and subsurface chemical composition. The instrument conforms to the mission's rover with a mass of 2.4 kg and a volume of approximately 81 × 98 × 125 mm³ [24]. It has a power consumption of 20 to 30 watts that varies with the temperature and operation mode along with performance metrics that ensure evident mineral detection as well as detection of trace components. This instrument will

collect Raman spectra with a range between 11,111 to 33,333 nanometers of olivine within the selected location of Erebus Montes. The TRL of the RLS instrument is at a 9 based on environmental testing and system level integration [24]. It begins to function when a laser beam is directed into a held sample in its analysis chamber. As the laser interacts with the molecules in the sample, it provokes the Raman effect which is where a small portion of the light is inelastically scattered. This scattering results from changes in the vibrational energy levels of the molecules, producing unique shifts in light energy. These shifts correspond to specific vibrational modes, which it detects and converts into spectral peaks. This collection of data creates a Raman spectrum that reveals the sample's molecular and mineral composition to better understand Martian geology [14].

Overall Payload Subsystem TRL is a 6, determined by our lowest TRL payload.

Instrument	Mass	Dimensions/Volume	Max Power
CP-MU DMU-100 Submersible Gamma Neutron Probe (Probe) + External Box	1.3kg	3362 cm ³	0.25 Watts
Radar Imager for Mars' Subsurface Experiment (RIMFAX)	3 kg	1552.32 cm ³	10 Watts
Miniature Tunable Laser Spectrometer (Mini-TLS)	1 kg	5937.28 cm ³	8 Watts
Raman Laser Spectrometer (RLS)	2.4 kg	992.25 cm ³	30 Watts
Totals	7.7 kg	11843.85 cm ³	48.25 Watts

Figure 1.5.6.2.1: Instrumentation Table

1.5.6.3 Payload Subsystem Trade Studies

Payload Subsystem Trade Study for Fluid Protection & Testing System

Figure 1.5.6.3.1: Thermal Management Requirements Table

Selecting the optimal instrument for monitoring gamma radiation in the Earth sample proposed three options for comparison within the trade study: *CP-MU DMU-100 Submersible Gamma Neutron Probe*, *Mirion TN-15*, and *CT007-T Thermal Neutron Detector*. Instrument evaluation was initiated based upon the following criteria and associated weight (in order of priority that is most critical for science objective success): Size(40%), Submersed Durability(25%), Data Transmission Method(25%), Mass(10%).

The first and most important criteria to consider is the scientific instrument's size as it must internally reside within the custom Fluid Protection System(FPS), requiring a

length of no more than 25cm x 25cm. Excessive instrument size would result in requiring a larger scale system, potentially increasing overall mass, fluid capacity, material requirements, costs, and involving additional hazards with internal pressurization, rover balance and terrain-induced physical damage. All three instruments (among others found outside of the trade study) easily met this requirement as most compact Neutron Detectors fall within the measurements.

The second criteria Submersed Durability is critical to the life expectancy of the instrument and fulfilling the scientific goal by its ability to generate periodic data of gamma radiation dosage for more than one year while submerged in multiple variations of fluid for data transmission back to earth. Neither the CT007-T Thermal Neutron Detector nor the Mirion TN-15 are able to withstand being submerged in fluid without the requirement of a custom housing, which could induce additional risks of instrument failure as it would be submerged for at least one year. The CP-MU DMU-100 Submersible Gamma Neutron Probe is a perfect fit to not only meet, but exceed expectations in this criteria as it is not only intended to be submerged in water, but can also be used in fuels as it was designed for use in reactor cores, components, and spent fuel rods to generate dose rate measurements of gamma radiation. The durability, versatility of fluids, and tried and true usage in the nuclear industry sparks confidence of reliable data retrieval over a fully submerged one year period, if not longer.

The third criteria Data Transmission Method is critical to allow radiation dose data generated by the instrument to be transmitted directly to the rover's command processing unit. Many compact scientific instruments use wireless transmission for ease of use, but would not be feasible due to potential signal interference, the FPS's protective housing preventing outgoing signal transmission, or a sub-optimal transfer speed rate of data. To mitigate as many risks as possible a wired ethernet connection is required for reliable, interference-free, and timely transfer speeds without the risk of signal loss when handling data vital to the objective. Out of all three instruments, the CP-MU DMU-100 Submersible Gamma Neutron Probe wins first place due to a unique feature not commonly seen in compact instrumentation, allowing ethernet connection.

The fourth criteria, Mass, plays an important role in instrument selection as the FPS encompasses the scientific instrument, protective housing, internal fluids, wiring, and mount that all must total under 15 kg mass to fit within the HBS-1LM Human Exploration Goal constraint. To allocate enough mass for the heaviest parts of the system without risking exceeding constraint, the instrument is required to be compact with mass not exceeding 2kg. Due to being compact instrumentation, all three instruments evaluated met this requirement, with most averaging 60-70% of the maximum kg.

Based upon the conducted trade study results, requirements, logic, and quality of

data, the scientific instrument chosen to fully achieve the Human Exploration Goal is the CP-MU DMU-100 Submersible Gamma Neutron Probe. Scoring in at 3362 cm³, under 1.3 kg in total mass (for both the external detector box and probe combined), engineered for long-duration submersal, a wide range fluid type versatility, proven track record in the nuclear industry, and an efficient Ethernet-based data transmission.

[Payload Subsystem Trade Study for Ice Accessibility Instrumentation](#)

Figure 1.5.6.3.2: Ice Accessibility Instrumentation Trade Study

To determine the best instrument for measuring near-surface ice accessibility and understanding regolith effects, the following three options were compared: RIMFAX, HP³, and a combined RIMFAX + HP³ system. A weighted scoring system was used, where a score of 1 is the best and 5 is the worst, and the highest percentile total score wins.

The highest weight of 22% was given to depth and quality factors as subsurface layers and possible areas of ice will need to be detected. RIMFAX got the best score here because it is able to reach ~10 meters with high resolution [18], while HP³ was more limited and had issues deploying on the InSight Mars station in 2018 [76], so received the higher (worse) score. Mass and volume were weighted highest at 25% because of the customer's constraints where the total system must stay within 15 kg for mass and 0.5 m³ for volume. The combined system (RIMFAX + HP³) scored worse here since it would likely break both limits.[18, 76] Instruments that are already flight-proven were prioritized hence why the TRL was weighted at 18%. RIMFAX and HP³ both flew on Mars, but RIMFAX got a slightly better score due to smoother integration on the Perseverance rover. Thermal Stability criteria is about how well the instrument can contribute to measuring temperature weighted at a 10% for data purposes. HP³ scored better here since it was designed to measure heat flow. RIMFAX doesn't directly do that but still contributes through context. Data Volume was weighted at an (15%) as this about how much data is produced and whether it can be handled easily. RIMFAX scored better since its radargrams are compact. The combined system would create too much data for the current bandwidth.

The end results showed RIMFAX to come out on top. It gave the best performance for depth and resolution, stayed within mission limits, and carried less risk. The hybrid system was too heavy and complex, and HP³ on its own didn't give enough subsurface clarity. Based on this trade study, RIMFAX is the most balanced and reliable option for the science mission goals.

[Payload Subsystem Trade Study for Deuterium:Hydrogen Ratio Trade Study](#)

Figure 1.5.6.3.3: Deuterium:Hydrogen Ratio Trade Study

In order to select the best instrument to measure the deuterium to hydrogen (D/H) ratio in hydrated volcanic rock on Mars' surface, a trade study was conducted to analyze the scientific potential of 3 instruments (and/or instrument combinations): The Mini Tunable Laser Spectrometer (Mini-TLS), Orbitrap, and the Tunable Laser Spectrometer (TLS). These instruments were evaluated based on the following: mass, measurement precision, volume, power consumption, support system, and reliability. Each criteria was given a certain weight in alignment with the mission, with the lowest being weighted at 10% and the highest 3 criterias weighted at 20%.

Beginning with one of the highest rated criterias, measurement precision is weighted at 20%. Measurement precision is extremely important to the mission because correct data is imperative to good science. To fulfill this objective in particular, a very high resolution is required. An instrument must be able to fully distinguish between Hydrogen and Deuterium to minimize spectral overlap and measurement uncertainty.

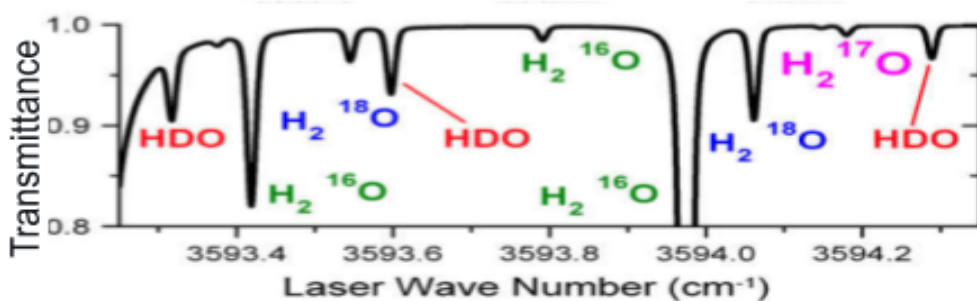


Figure 1.5.6.3.4: HDO and H_2O Transmittance Spectrum from Curiosity [54]

The second criteria that is weighted at 20% is reliability. This is a less quantifiable, but just as important metric. The system that is chosen will go through tough conditions including dust, radiation, and frequent temperature changes. Additionally, the system must last long enough to deliver important scientific data back to Earth. This criteria is judged based on how exposed the instrument is to failure under Martian conditions as well as past successes under similar conditions.

The third with a 20% weight is the support system. Due to the requirements of the scientific objective to measure D/H ratio in volcanic rocks, many spectrometers need a system to obtain the evolved gas from these samples. This could include pyrolysis, laser ionization, chemical extraction, vacuum sublimation, etc. To account for the power draw, mass, volume, and overall needs of this support system, this criteria is given a heavy weight to ensure the system is relatively free standing.

The next criteria, power draw, is weighted at 15%. Power, especially when RTGs

are forbidden by the customer, is a huge consideration for a rover. Since power is limited, instruments that have low power requirements help to reduce risk of overloading the system and increase the amount of science which can be achieved.

Mass and volume are weighted at 10% and 15% respectively. The rover must fit within strict mass and size constraints imposed by the customer. Either of these criteria in excess reduces the allocation of mass and volume to the rest of the rover. This places critical systems to operate the rover at risk of failure if they are forced into trade-offs. Volume is weighed slightly more due to the abundance of lightweight spectrometers that were possible instruments, but volume often being too large to justify for the rover.

The conclusion of this trade study was that the Mini-TLS was the best fit for this mission with the highest score of 80.63%. Its lightweight and compact volume make it the ideal choice to optimize the mass and volume constraints. Its development from the TLS led to its very high level of precision, 10 times more sensitive than the TLS is. Additionally it does require an oven like the TLS, but a smaller one because it requires 1/100th of the gas. However, it is given a lower score in reliability because the TLS has proved itself on Mars in similar conditions to where P.H.O.E.N.I.X will be deployed.

Orbitrap represents the very best in terms of precision, but this comes at a cost. Its mass and volume both exceed that of Mini-TLS and partially of TLS. It also faces the need for a large support system including a vacuum and laser ionization system to obtain gas. This is scored roughly the same as TLS because at max temperature the oven on TLS maxes out its power connection power and requires a lot of thermal insulation [38]. As a whole the vacuum and laser would require a similar power level, and although the thermal insulation would be less, a vacuum requires reinforced materials.

[Payload Subsystem Trade Study for Crystal Structure Instrumentation](#)

Figure 1.5.6.3.5: Crystal Structure Instrumentation Trade Study

To evaluate the best instrument for determining crystal structure on Mars, a trade study was conducted to compare these three candidates: the Raman Laser Spectrometer (RLS), SuperCam, and CheMin (XRD/XRF). The goal for the trade study was to assess which system best aligns with the science objective to determine the crystal structure of minerals formed by asteroid impacts interacting with exposed subsurface ice.

The criteria chosen for this trade study were based on their relevance to mission success and the constraints mentioned by the stakeholders. Power consumption was weighted at 15% because limited power availability due to the system's mass and

reliance on solar energy makes low power instruments more favorable for prolonged operations. Durability against solar winds was assigned a 10% weight, as instruments must withstand the charged particle exposure to ensure the data is protected and not lost in the harsh Martian environment. Heat required carried a 30% weight, recognizing that instruments reduce the risk of mission complications due to Mars' extreme temperature range. Finally, operational lifetime was given the highest weight at 45%, since instrument success would fulfill the mission's objectives across its planned duration. Each instrument was graded on a 1 to 5 scale, where 1 indicates the best performance and 5 indicates the worst. These scores were then multiplied by the assigned weight percentage and then all the scores across all criteria were summed to generate a total weighted score for each instrument. Raman Laser Spectrometer (RLS) scored 100%, SuperCam scored 71.25%, and CheMin (XRD/XRF) scored 85.00%

The Raman Laser Spectrometer had the winning total score with 100% which shows its best performance across all critical mission constraints. It demonstrated to meet every weighted criteria. While SuperCam and CheMin have strengths in specific areas, their higher heat requirements, shorter lifespans, and increased power draw made them less suitable under the mission requirements. In conclusion, the Raman Laser Spectrometer was selected as the optimal instrument for determining the crystal structure of minerals formed by asteroid impacts interacting with exposed subsurface ice.

1.5.7 Recovery and Redundancy

Recovery and redundancy are key risk mitigation tools for preventing system loss of various kinds. Each subsystem is responsible for identifying possible risks and various recoveries and redundancies that can be implemented to prevent catastrophic mission failure.

Mechanical Subsystem

The rover chassis is too large to feasibly implement redundancies. Individual attachment points shall incorporate redundancies through a FOS in attachments, however, these methods allow for cascading failure under large loads and alone are not satisfactory. Recoveries are possible for wheel assembly failure in isolation through robust autonomous locomotion controllers utilizing partial functioning systems.

Power Subsystem

The rover contains multiple redundant electrical systems that shall work alongside the primary power systems in the event that an issue renders the primary systems unusable or inactive. The rover's design includes primary and secondary power sources. In the event of solar panel degradation, the power subsystem will revert

to Lithium ion batteries in order to continue operating instead of carrying a backup set of panels in the payload, as they would be too massive. There is a second, redundant battery included in the mission payload in the event that the primary backup battery does not operate as expected. If the power system goes offline, the included power buffer shall prevent power loss or surges that could harm the mission operation.

Command & Data Handling (CDH)

The rover will store its own local world map, and is capable of using its elevation relative to its surroundings as a heuristic for signal propagation effectiveness, and therefore if the rover loses contact with the MRO, or earth ground station it will be able to autonomously search for acceptable command signals. Due to the lightweight nature and incredible importance of the OBC and data storage devices, failure mitigation can be implemented through duplicate OBCs and data storage such that [there will be two of each]. Larger subassemblies including the antenna, however, do not justify complete redundancy due to their large mass and volumetric constraints. Antenna failure follows graceful degradation and therefore is unlikely to become completely inoperative, but rather to

Thermal Control System

The Thermal Control System subassembly's redundancy shall focus on the heat pipes, thermal sensors, and electrical heaters. There will be two systems of heat pipes, so that every instrument does not rely on the same system. A failure in one should not affect the other instruments. There shall also be multiple thermal sensors per instrument to ensure cross-verification of the measuring of the instrumentation temperature. This also ensures that in the event of failure, the other will be able to monitor the instrumentation and keep the TCS intact. Redundant heaters will be implemented. For the Thermal Recovery, there shall be a recovery software implementation where if the TCS fails, a fail-switch sensor sends the signal to command the TCS, primarily the electrical heater to commence a re-startup sequence.

Payload Subsystem

The payload subsystem will address recovery and redundancy for each instrumentation in the event of issues arising with their function or performance. CP-MU DMU-100 has a freeze risk that will be addressed by running testing during the night to heat up the internal housing fluid environment as the instrument operates at a minimum of 30°C which is warm. On Mars, clays and ice-dust layers can tamper RIMFAX's radar pulses and disrupt its depth, to confront this, the instrument will stick to the low end of its 150–1200 MHz band, limit the soundings to 2–4 m, and stack multiple passes for a clear return. For the Raman spectrometer, a quick calibration check will be made before

and after every run and only trust fully quantitative data when the sample sits at the controlled 935 K, outside those windows spectra is treated as qualitative data. With the Mini-TLS, rather than investing in extra cooling gear, measurements will be conducted at night, when Martian temperatures reliably stay between –10 °C and 20 °C, keeping the laser and optics within requirements.

1.5.8 Interface Control

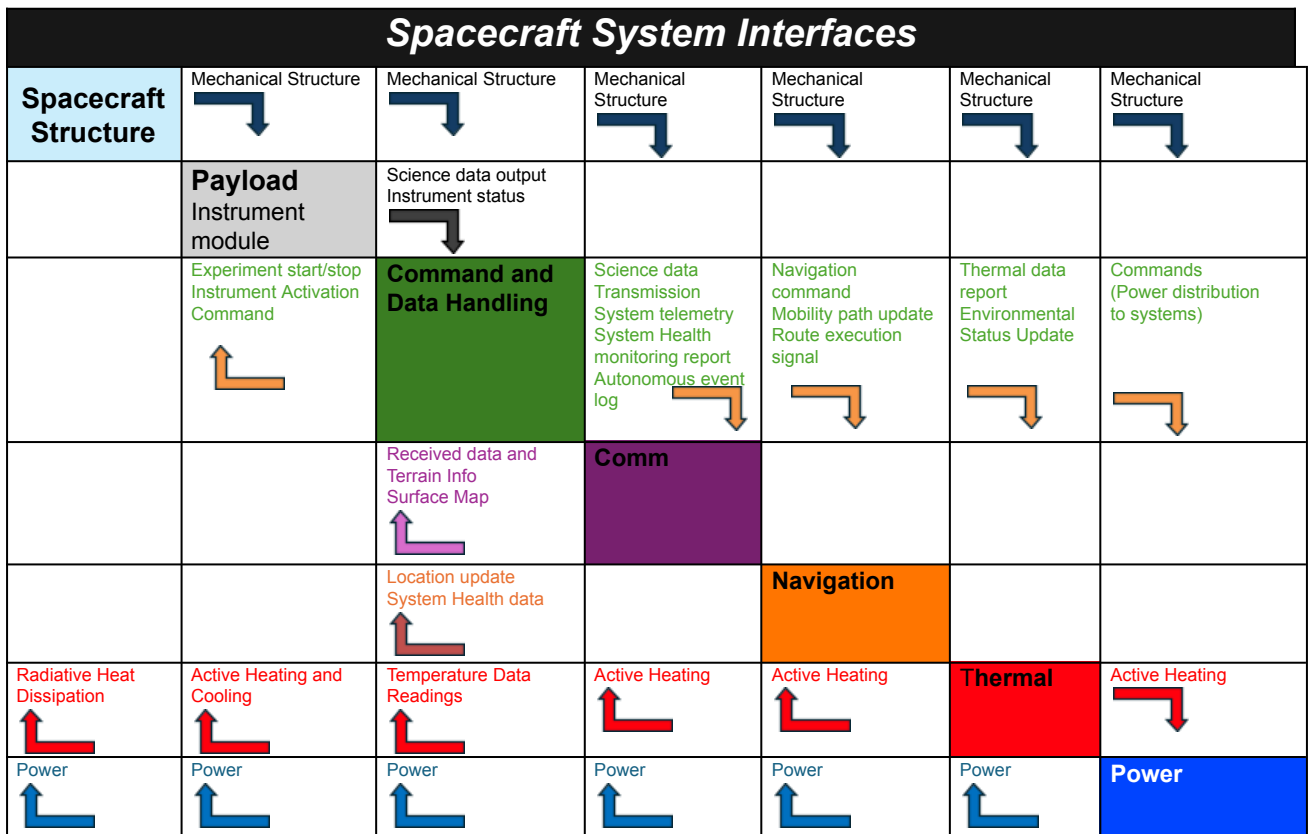


Figure 1.5.8.1: N² System Interfaces Chart

The system interface diagram shows the relationship between each subsystem and how each subsystem interfaces with the other. These subsystems include the following: structures, payload, data handling, comms, navigation, thermal and power. Each of the subsystems play a distinct role and are crucial to the success of this mission. By mapping out the interfaces, failure modes can be identified and mitigated early on in the design process of the rover.

Each subsystem is configured to have its own specific function but it all comes down to system integration, hence the N² chart is a visual representation of how all subsystems will have to work together in sync, ultimately supporting the spacecraft's goals and ensuring operational integrity.

The spacecraft structure is the foundational subsystem, it consists of the chassis, wheels, motors, actuators and all mechanical components that are physically present on the rover. This subsystem is positioned at the highest level on the interface chart because it serves as the primary housing and structural support for all the other subsystems. The key functions of this subsystem include providing support and physical protection to all internal and external subsystems ensuring structural solidity of the spacecraft.

The main system interfaces the structure subsystem receives outputs from the power and thermal control subsystem. The structure is reliant on the power subsystem to supply electrical energy to the mechanical components, such as the motors on the wheels or any actuators the rover will have. This reinforces the rover's mobility and the operation of any deployable or moving parts, such as a deployable radiator used by the thermal control subsystem or deployable solar cells used for generating electrical power. Adequate power supply is essential for maintaining the rover's navigation, scientific experimentation and data collection capabilities.

Furthermore, the chart also illustrates the most vital output to the spacecraft structure which is heat dissipation through the structure from the TCS subsystem. TCS is a critical system that keeps the spacecraft structure, any components and electronics within nominal temperature ranges considering the harsh thermal environment on Mars with temperatures that go as low as XX degree celsius and as high as XX degrees celsius. Despite these extreme temperature fluctuations, it is important to keep the structural elements of the spacecraft and any mounted subsystems operational.

The spacecraft structure is essential to the integration of all subsystems which highlight the unidirectional flow of power and thermal management into the spacecraft structure, emphasizing its dependence on these subsystems for flight readiness.

The payload subsystem, which is the instrument module, houses all of the scientific instrumentation that is designed to achieve both the scientific and human

exploration goals provided by NASA that is the customer. This suite of instrumentation is an integral part of the mission, as it enables collection and transmission of valuable scientific data that pertains to future sustainability and manned missions on Mars.

The instrument module consists of distinct and unique instruments, each having its own functionality but working towards achieving the desired science objectives.

This subsystem solely sends inputs to the CDH subsystem but receives outputs from CDH, TCS and the power subsystem. The payload sends an instrument status signal to the CDH subsystem which includes an onboard computer that processes that signal and decides if the instrumentation is currently offline, if that is true, the CDH subsystem outputs an experiment activation command signal to the payload subsystem, where the instrumentation begins data collection. Once the data has been collected and the instruments have performed their operation at the research point, the scientific data is then inputted into the CDH subsystem which then sends an experiment stop signal to the payload subsystems turning all of the instruments offline to conserve power. This closed loop interaction ensures that scientific experiments are conducted efficiently and that payload operates only when required, saving power and conserving the instrument's operational lifetime.

The outputs that the payload subsystems receive from TCS is in the form of active heating and cooling. Each instrument in the payload has its own nominal operating temperature range and going above or below it would compromise on the effectiveness of data collection and instrument redundancy. To counteract this, the TCS provides heating through the means of a heat pipe or cooling through cryogenic cooling systems, depending on the time of the day and solar loads the structure receives.

Furthermore, it also receives an output in the form of electrical power from the power subsystem as all of the instrumentation will require power to function and start experimenting.

The Command and Data Handling (CDH) subsystem serves as the central data repository for all of the scientific data that is transmitted to and from the instrumentation to the onboard computer. This subsystem is responsible for smooth data flow throughout the duration of the mission. The CDH subsystem interacts with each of the subsystems in a certain order, first interacting with the payload subsystem where it interacts in a closed loop, with inputs from the payload and output from the CDH subsystem back into the payload.

This subsystem also inputs an autonomous event log and an overall system health report to the communications subsystem which then relays this information to the MRO that relays that same scientific data back to the earth ground station.

The CDH subsystem also inputs different signals and commands into the navigation, TCS and power subsystem. The inputs into the navigation include path and mobility data based on the surface terrain data that it receives from the communications subsystem as well as the navigation command to direct the rover on where to find the next science research point of interest. It also transmits a thermal data report to the TCS subsystem that includes the temperature at the surface of the mars so that the TCS can heat or cool all of the subsystems accordingly. Finally, it inputs commands and signal feeds into the power subsystem for how much power is required for the system at the moment.

This is all done simultaneously as the CDH subsystem receives outputs from the communications, TCS and power subsystems. The outputs it receives from communications include terrain mapping data information. TCS sends a thermal status update to the CDH subsystem to ensure it is operating as required and is allocating the heat based on the thermal data report of the environment and lastly, it receives electrical power from the power subsystem as the onboard computer does need power to function.

The comm subsystem is a very important interface as it is responsible for sending and receiving important data from and to the MRO. This subsystem outputs data and commands received from MRO back to the onboard computer that is part of the CDH subsystem and also sends terrain and surface mapping data back into CDH so the onboard computer can come up with various efficient pathfinding routes and nearest research points for the rover to reach.

It also receives outputs from the TCS as it includes electronics that must be kept under operating temperatures as well as electrical power to operate.

The TCS subsystem is a critical subsystem that will guarantee success of the mission given the extreme thermal environment on Mars. Every subsystem requires either active heating or cooling. For instance, the payload would need both active heating and cooling, this is because the instruments operate nominally under specific operating temperature ranges and hence the instrument would either need cooling or heating.

This subsystem gets inputs from the CDH subsystem and outputs from the power as the TCS does require electrical power to operate.

Finally, the power subsystem lays all the groundwork to ensure all of the other subsystems and components operate and have the required voltage to function. Considering the fact that the rover will be semi-autonomous, everything will be connected to the onboard computer through spacewire that will then be connected to the power distribution unit which will be connected throughout the rover's main chassis

to transfer power to each component.

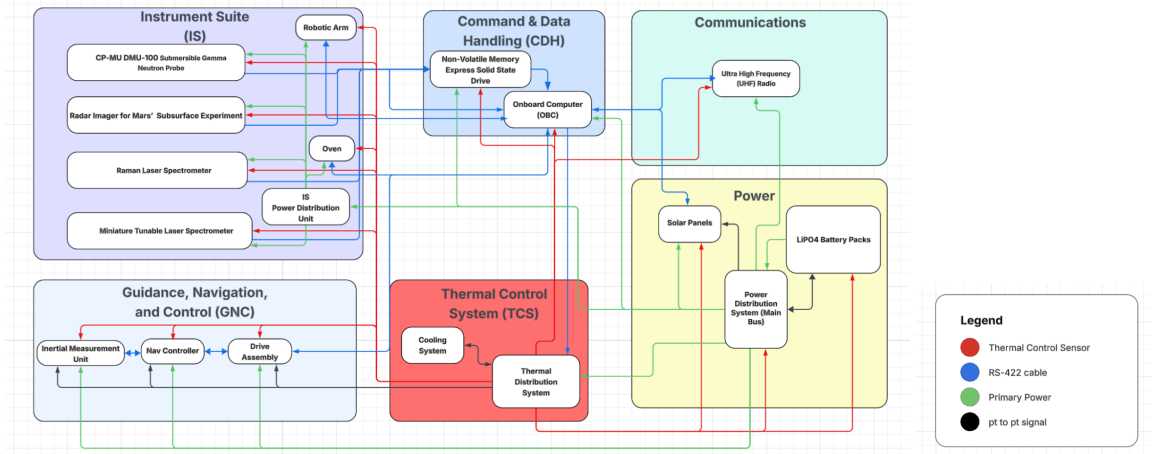


Figure 1.5.8.2: System Block Diagram

The block diagram is a more detailed version of the N² chart as it gives a better understanding of how each subsystem is interfacing with each other and what sort of connections they have with each other. At the top left, the instrument suite (IS) is located which contains all of the scientific instruments such as a spectrometer, a neutron probe, a robotic arm, an oven and a power distribution unit. The function of the robotic arm is to collect rock samples from the martian surface which will then be heated up in the oven to collect gas that will then be measured by the spectrophotometer to gather valuable scientific information. These instruments, however, receive primary power from the power distribution unit that is located in the instrument suite. The IS power distribution unit receives primary power from the main power distribution System that receives electrical power from the LiPO4 battery packs which it then sends to the solar panels and every single subsystem component in the system. The power distribution system is also connected to both the solar panels and the LiPO4 battery packs through a pt to pt signal connection, this connection is bi-directional to the battery packs as the signals ensure the PDS knows the status of the battery pack and it then feeds the amount of power available to the solar panels. The TCS subsystem includes a cooling system and a TDS, the TDS is connected to every single subsystem component through thermal sensors that ensure all of the components in the spacecraft are operating nominally. The cooling system is responsible for decreasing the temperature of the spacecraft components, in the case that it gets extremely hot, especially during the daylight hours and that's where the radiators dissipate the heat and cool the systems down. The Cooling system interfaces with the TDS through a pt to pt signal which sends each other the status of both systems ensuring they are maintaining their operational integrity and so that in the case of a failure, one of the systems could be shut down or backup heaters/coolers can take over.

The GNC subsystem houses all of the mechanical subsystems and these consist of the inertial measurement unit, a navigation controller and a drive assembly. All of these subsystems receive their primary power from the PDS and have thermal control sensors on them to ensure they are under nominal temperature and do not excessively heat up to a point where they lose their navigation capability. They are also connected to the TCS through pt to pt signals, sending status and health reports to ensure each of the subsystems are operating properly. They are also connected with each other through RS-422 cables to ensure streamlined data and command execution with each other.

The navigation controller determines and executes the rover's pathfinding capability. It processes navigation commands, plans routes between waypoints, and calculates the necessary steering and speed adjustments to follow the calculated path. The controller uses algorithms to ensure the rover avoids any obstacles, follows smooth paths and maintains stability; it does that by generating target velocities and steering angles that are then sent to the drive system. In autonomous mode, it can also adapt to changing terrain to update the route in real time.

The drive assembly is the mechanical and electrical subsystem that physically moves the rover. It includes motors, wheels, gearboxes and any associated control components. The way this subsystem works is it receives commands from the navigation controller through the RS-422 cable connection on how fast the rover should move and in what direction and then translates these into actual movements the rover performs on the surface. It allows the rover to perform complex maneuvers on challenging terrain for which the boogie rover system was integrated.

The IMU is a sensor package that measures the rover's orientation, acceleration and orientation. This system contains a gyroscope, an accelerometer and a magnetometer. The IMU consists of an accelerometer and gyroscope, which provide real time data on the rover's lateral accelerations and angular velocities. This data is essential for navigation and stability, This allows the rover to utilize dead reckoning techniques and localization algorithms to track its position and orientation even when GNSS systems are unavailable.

1.6 Risk Analysis

Every space mission carries unique risks due to the complexity of spacecraft design and operations. The team is committed to identifying and mitigating these risks wherever possible.

By consensus, the team determined that the most effective methods for identifying risks include thorough failure modes and effect analysis (FMEA), in-depth fault tree analysis (FTA), and expert reviews. These approaches ensure that potential issues are uncovered early and addressed proactively.

To evaluate each risk, a matrix was created that carefully considers both the likelihood of occurrence and the potential consequences. This structured process allows efficient prioritization of risks to allocate resources for the areas of greatest concern.

As the spacecraft advances through the early stages of development and conceptual design, the team has established a robust plan to mitigate risks. This plan is centered around three strategies which include contingency planning, redundancy and weekly risk tracking.

Contingency planning is key to ensuring mission success and dealing with unexpected failures. Each subsystem will be equipped with backup protocols to address both major and minor failures. These protocols will define immediate actions, escalation procedures and recovery steps to minimize the impact of each failure.

Redundancy is embedded throughout the spacecraft's design to enhance reliability and protect critical functions. This involves incorporating backup components, parallel systems and alternative algorithms for continuous operation of the system. Should a component fail, redundant systems are ready to take over instantly maintaining the component and system's operational integrity. This approach not only mitigates the risk of the mission due to single failure modes but also provides flexibility for the spacecraft to adapt to any unforeseen challenges it might encounter.

Each subsystem comes with its own risks and they need to be assessed and mitigated early on in the development phase of the spacecraft.

Due to the presence of sharp, embedded rocks on Mars, there is a risk of wheel skin puncture or grouser breakage, resulting in compromised wheel integrity. This could reduce rover mobility or cause immobilization. The mitigation strategy the team will use for this risk is to use thicker wheel treads, adaptive driving algorithms, and regular wheel imaging to monitor and avoid high-risk terrain.

Furthermore, the rover is also at a risk of suspension fatigue due to its large mass and frequent traverses across the Martian surface leading to loss of shock

absorption thus increasing risk of mechanical failure during rough terrain navigation. To mitigate this risk, robust materials will be used for suspension components, do periodic load analysis on the OBC, and design redundancy in suspension components.

The thermal control subsystem is also at a risk of failure and as this is a critical subsystem, there are certain risks associated with it. Bearing in mind the extreme temperature swings on Mars, the TCS may fail to maintain optimal temperature exposing electronics to extreme temperature conditions which could cause permanent damage to the electronics and compromise the mission. The way this risk is to be mitigated is to make use of MLI, redundant heaters, and real-time thermal monitoring. To mitigate this risk, backup heaters need to be included in the rover in case one of the heaters malfunction, the other can take over.

The instrumentation subsystem also comes with its risks and as a result of the abundance of the Martian dust, it may infiltrate the instruments and hinder their ability to function and record accurate data. The method to mitigating this risk is to make use of dust seals, protective covers, and periodic instrument cleaning routines.

The other issue is the fact that the instrumentation is at risk of getting misaligned or damaged due to mechanical shock during landing which will lead to inaccurate scientific data or instrument failure. The method to mitigate this risk is to employ shock absorbing mounts and post-landing calibration of the instrumentation to ensure accurate data readings.

L L I K E	5		8 →	7 → , 11 →		
L I H O O	4			10 → , 16 →		
L I H O O	3		9 → , 19 →	15 →	13 →	
L I H O O	2		15 →	1 → , 2 → , 4 →	14 → , 18 → , 20 → , 3 →	17 → , 6 →
L I H O O	1				5 →	
		1	2	3	4	5
		CONSEQUENCES				

Figure 1.6.1: Risk Matrix

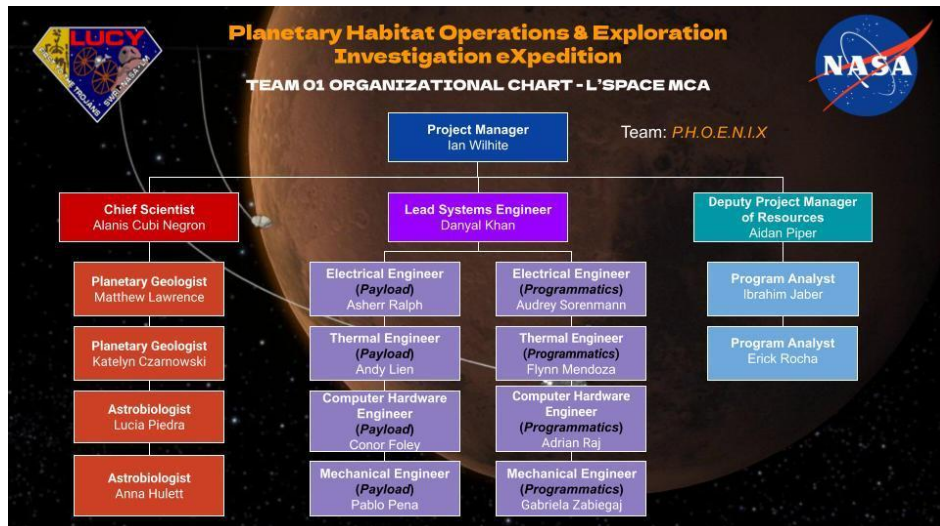
ID	Function	Failure Mode	Effects	Sev	Cause	Occ	Prevention	Det	RPN	Actions	Approach
1	Mechanical Subsystem	Wheel skin puncture or grouser breakage	Reduced mobility or immobilization	3	Sharp, embedded rocks on Mars	2	Thicker wheel treads, adaptive driving algorithms, regular wheel imaging	6	36	The main action is to monitor the damage and adjust operations to avoid hazardous terrain.	Mitigate
2		Suspension fatigue	Loss of shock absorption, increased risk of mechanical failure	3	High mass and frequent traverses	2	Robust suspension materials, periodic load analysis, redundancy	7	42	Reducing speed and avoiding rough terrain can help slow further fatigue.	Research
3		Loss of drive or steering calculator	Reduced mobility, inability to steer or drive one or more wheels	7	Hardware or cable failure, wear over time.	0	Redundant actuators, regular actuator health checks.	4	0	Switching to backup or manual control is the most logical step.	Mitigate
4		Loss of shock absorption capability	Increased transmission of shocks to chassis and instruments	3	Material fatigue, extreme temperature cycling.	0	Use of advanced materials (e.g., shape memory alloys), regular health monitoring.	5	0	Rough terrain should be avoided if this failure persists	Mitigate
5	Thermal Subsystem	Heat Pipe failure	Loss of thermal regulation, risk of overheating or freezing	3	Faulty manufacturing, extreme pressure changes	1	Redundant heat pipes, redundant thermal control systems in the form of heaters	3	9	Rely on electric heaters, plan for alternate cooling systems	Mitigate
6		Multi-layer insulation (MLI) degrades over time.	Increased heat loss, reduced thermal protection.	7	Micrometeoroid impacts, material aging, radiation	3	Use of high-durability MLI, periodic thermal performance checks.	3	63	Operate rover primarily during warm periods away from areas of high radiation	Research
7		Electric Heater Failure	Loss of active thermal regulation, risk of overheating or freezing	8	Material aging, overheating, electric failure	1	Redundant heaters, separate circuitry	1	8	Rely on redundant heaters and heat pipes	Research
8		Thermal sensor Failure	Loss of thermal monitoring, risk a system failure is not reported	7	Material aging, overheating, electric failure	1	Redundant sensors, separate circuitry	7	49	Rely on redundant sensors, develop a software recovery plan	Mitigate

9	RIMFAX signal attenuation	reduce the depth it penetrates and degrade the signal-to-noise ratio	2	Materials like clays or ice-dust mixture which absorb and scatter radar energy	0	Running at its low end frequency of 150-1200 MHz band as low frequencies penetrate better	0	0	Reduce depth objective to 2 m - 4m for clear data and schedule multiple low frequency soundings	Research
10	Payload Subsystem	RLS calibration drift	calibration change throughout image collection	3	temperature swings disrupt calibration due to temperature sensitivity	0	calibration verification before and after each science run	0	heating samples to 935 K and cooling them down to 120 K to reserve fully calibrated quantitative measurements for high temperature, and qualitative data for lower temperature	Mitigate
11		Mini TLS overheating risk	overheating, wavelength drift, or shutdown	0	Running over max operating temperature of 20 C	0	only run at temperature between -10 C up to 20 C	0	scheduling measurements strictly during nighttime	Mitigate
12		CP-MU DMU-100 freeze risk	instrument shutdown ending data transmission before meeting the one year minimum planned operation	6	Temperature below 0°C	3	Thermal material layer(s) built into instrument housing	3	Running testing during the night to heat up internal housing fluid environment as the instrument operates at a minimum of 30°C which is warm	Mitigate
13		Loss of battery capacity or failure to recharge	Reduced operational time, possible mission loss.	9	Repeated charge/discharge cycles, extreme temperatures.	5	Battery health monitoring, thermal management, redundant batteries.	5	225	Utilize a second battery. If second battery is also inoperable, begin powering down noncritical systems to reduce power load
14	Power Subsystem	Electrical short in power distribution	Loss of power to subsystems, reduced redundancy.	8	Dust, material degradation, component failure.	4	Robust insulation, regular voltage monitoring.	6	192	Shut down the system and reboot, if the issue persists then continue to monitor. Perform analysis on systems to ensure they remain within operational capacity.

15		Reduced power generation from solar panels	Insufficient power for operations	7	Dust accumulation, mechanical damage.	7	Dust removal systems.	3	147	Reduce subsystem power usage to redirect remaining power to critical systems. If transmission is impossible, store data for potential future collection	Mitigate
16		Drift in transistors not allowing them to turn on/off	Loss of signals for power distribution	5	Radiation ionizing deposits within technological components	7	Shielding systems, radiation-hardened materials in manufacturing	3	105	Perform maneuvers to shield components from further damage, reduce operation of damaged systems, continue to monitor	Mitigate
17		Processor failure	Loss of command/control, mission halt	10	Hardware defect, radiation, overheating	4	Use radiation-hardened processors, implement thermal control, redundant processors	8	320	Physical Redundancy by having two OBCs	Mitigate
18	CDH Subsystem	Memory corruption	Loss of stored data, erratic behavior	2	Radiation, aging	8	Use ECC memory, regular memory scrubbing, software validation	3	48	Offboard system cleansing processes, rad-hard memory units	Research
19		Data uplink/downlink loss	Loss of communication with ground, inability to send/receive commands	2	Antenna failure, RF interference, ground station issue	8	Antenna redundancy, RF shielding, multiple ground stations	4	64	Autonomous source finding recovery behavior	Research
20		Command errors	Incorrect commands executed, potential for unsafe actions	8	Software bug, memory corruption	4	Command validation, memory error detection, queue integrity checks	2	64	Increase detection using verification codes	Research

Figure 1.6.2: Risk Analysis Matrix

1.7 Programmatics



1.7.1 Organizational Chart

Figure 1.7.1: Organizational Chart

Current workload distribution follows a similar structure to past deliverables where the deliverable is split into broad sections which are then assigned to subteams by the project manager. Subteam leads then assign individual tasks and sections to individuals or small groups on their subteam. By tracking progress with a shared spreadsheet, the team reinforces mutual accountability while setting a clear pace for the completion of the deliverable. An updated organizational chart, seen in Figure 1.7.1, reflects the departure of dedicated mission assurance specialists. In response to changes in personnel, all team members are now expected to document and mitigate risks as they perform their expressly assigned tasks while the DPMR coordinates high-level tracking and communication regarding risks.

The decision-making methodology of the team remains largely unchanged from its original iteration, focusing on input from the entire team before the leadership makes a decision. This process proved effective following the addition of a separate science experiment payload and the subsequently associated descope. As the decision was not time-sensitive, the team was able to discuss the options regarding how to incorporate the addon and the benefits and drawbacks of each approach. By taking in feedback from all members, this approach led to success in a real-world environment. After

considering the feedback, team leads and the project manager selected an external mounting option.

Moving forward, there are a few areas where the team can improve. Firstly, by implementing a lightweight system of informal progress check-ins, whether it be at the beginning of each subteam's weekly meeting or through some asynchronous upload of a research summary, trade study, or section drafts, the team reduces procrastination without overburdening members. Secondly, reinforcing active usage of the task tracker will ensure everyone can get a status update on the team's progress at just a glance.

In recent weeks, the team has faced some challenges ranging from personnel turnover to the sudden announcement of a third-party spacecraft being integrated into the mission. The team distributed the responsibility of mission assurance across the entire team. Key impacts were identified across all three subteams and a cohesive plan to move forward within the new design constraints and considerations was devised.

1.7.2 Schedule Basis of Estimate

The Schedule Basis of Estimate centers around the non-negotiable ground rules, crucial assumptions, and primary drivers regarding the overall scheduling of the mission. Spanning project phases C to F, beginning with the submission of the PDR and subsequent KDP C and ending with the completion of the mission lifecycle, this basis aims to convey the surrounding context and scope for the following estimation, highlighting potential risks and justifying crucial assumptions in regards to each phase of the mission in regards to the schedule [29]. The team is interested in high-level system objectives and ensuring that all subsystems are designed, integrated, and tested to meet mission requirements for science return, reliability, and launch readiness.

Ground Rules

The scope of this estimation begins with PDR submission (August 18, 2025) before continuing along the standard NASA mission life cycle sectioned by a few notable hard dates. In order to leverage the 2029 Mars launch window, full system integration, corresponding to Phase D just prior to launch, must be completed by the System Integration Date of October 1, 2029 to be closely followed by the successful completion of KDP E prior to the Launch Readiness Date of December 1, 2029 [10]. These constraints reflect the narrow launch window to Mars and the necessary integration period before launch.

Assumptions

Fiscal Year (Oct 1–Sept 30) is used instead of calendar year to align with NASA and federal budget cycles. Phase C is projected to begin alongside FY 2026.

Fabrication begins following the completion of the CDR Schedule margin to address any unknown issues that may arise, particularly with phases C and D prior to launch, is going to vary based on each of the specific tasks slated for completion during the phase. With the addition of a science experiment designed by a third party, additional time is likely to be needed for testing and successful full-scale integration via external mounting to the PHOENIX platform. Entry Descent Landing system, and transit will be handled by external contractors. Operating time on the Martian surface is a baseline floor and not accounting for any mission extensions dependent on system integrity [10].

Drivers

Major drivers for this mission will be the time allotment for phases C and D due to the scope and intensity of the work undertaken in those phases [10]. Phase C encompasses the maturation of preliminary designs in regards to both hardware and software, flushing out strategies for implementation, integration, verification, and validation, and fabrication or acquisition of hardware. Identification and assessment of mission risks continues to check any unplanned increases in cost, scope creep, etc in the leadup to launch [29]. Due to the complexity of the tasks and major deliverables such as the CDR and SIR coupled with the planned onboarding of new technicians at the initialization of the phase, the phase is projected to span all of FY 2026 and 2027 and part of FY 2028 [10]. Phase D, accounting for full system integration, must now consider additional challenges brought about by the third-party science payload attached to PHOENIX while ensuring the mission remains on task to meet key deadlines as defined above.

1.7.3 Schedule Estimate

This schedule estimation is derived from previous NASA endeavors to the Martian surface. Pathfinder and its Sojourner rover, despite being a microrover with a budget around 330-340 million dollars adjusted for inflation, show an example of a discovery-class mission with a similarly aggressive timeline as PHOENIX [17, 47]. Twin rovers Spirit and Opportunity represent individual payloads more akin to the scale of this mission's rover with masses of 185 kilograms and smaller in volume 1.5x2.3x1.6m [47, 32]. InSight serves as the most recent example of a Martian mission that best aligns with the budget of this mission and a good basis for determining the longevity of more modern flight-proven hardware—heritage sourced from the 2008 Phoenix Lander [33]. Each phase, delineated by the KDP at its closure, will further be broken down based deliverables requiring a presentation to the SRB, launch, and arrival.

Phase C will consist of a period of 28 months dedicated to finalizing system documentation and begin fabrication of hardware and coding any necessary software [33]. Technicians, overseen on-site and on board by the LSE, will assist the team in

fabricating engineering and flight units. Phase C starts with the completion of KDP C tentatively set for the beginning of FY 2026 on October 1st, 2025 and lasting for the next 30 months, terminating with the end of the first quarter of FY 2028. Key tasks are expected to last 27 months with a 3 month margin of roughly 11 percent when rounded to the nearest day. Successful completion of the CDR, projected to be 14 months into the phase, based around a margin of one month to address any issues with finalization of documentation alongside personnel onboarding challenges that may arise, will allow the team to start fabrication. Similarly, InSight passed its CDR in mid-May 2014 before entering integration and testing at the end of May 2015 [35, 36]. Occurring in March of 2028, the System Integration Review (SIR) serves as the culmination of Phase C overseen by the SRB just prior to the start of Phase D [33].

Phase D consists of full system-level integration and testing to be successfully completed by the system integration date (SID) of October 1, 2029 alongside the start of FY 2029 [10]. Lasting from April 1, 2028 to the SID, Phase D starts with clearing KDP D before transitioning into full system-wide testing and integration [33]. Compared to the typical timeline for Phase D, this mission has additional months allotted to crucial testing. InSight serves as a prime example of a risk that this mission has to address. InSight missed its 2016 launch window due to a French-made seismometer being delayed due to a technical failure, leading to an additional 150 million dollars being spent on the mission [37]. Due to the third-party science experiment, PHOENIX faces similar risk to InSight but without the flexibility of delay, requiring more conservative testing and integration margins. The mission-critical risk necessitates a more cautious approach to testing and integration with a higher margin than likely needed out of an abundance of caution. A period of 18 months is planned for Phase D's integration and testing, with realistic expectations of completion in 15 months but a reserve of three months, which would align it closer to the testing timeline for Spirit and Opportunity alongside Pathfinder [17, 39]. Following the FRR on October 1, 2029, the mission will be cleared for the December 1 launch assuming approval and satisfaction of KDP E.

Phase E consists of the mission cruise, entry, descent, and landing (EDL), and surface operations [33]. Assuming a Homann transfer is used, an average travel time is around 9 months [78]. The science instrumentation used on the rover is slated to at a minimum deliver trustworthy data from the surface of Mars for at least a year based on preliminary analysis from the team's scientists. During this time, the rover would complete the driving scientific procedures and acquire data to further the construction of an answer regarding its driving questions regarding the potential groundwork for human habitation with subsurface ice. At this stage, mission personnel are reduced to a bare minimum to monitor the rover's progress and address any issues that may jeopardize the completion of the mission. Mission extensions may be granted based on the overall integrity of the system as a whole to maximize the extracted information. A plan for

decommissioning through the decommissioning review would be formulated to be implemented in closeout regardless of any extensions.

Phase F consists of the decommissioning of the system alongside the analysis and storage of data returned from the mission for future usage [33]. As with other rover missions, the exact timeline for this phase is unknown and can develop rapidly if critical mission systems fail. Lastly, the final report is drafted as crucial lessons learned are documented for future reference [33].

1.7.4 Cost Basis of Estimate

The Budget Basis of Estimate (BoE) for P.H.O.E.N.I.X defines the ground rules, assumptions, and cost drivers used to develop the preliminary cost estimate for phases C through F of the mission's life cycle. The purpose of the BoE is to clearly define how cost estimates were developed from the rules, assumptions, and drivers.

Ground Rules

A \$450M cost limit is established specifically for the Rover System, encompassing all expected mission costs including personnel, travel, outreach, hardware, testing, direct costs, as well as cost margins of safety [10]. The BoE only targets Phase C through F. Costs will be estimated primarily using parametric models. It is assumed that these tools provide an accurate reflection of the anticipated cost. These estimates are then aggregated into a budget template that is derived from the Lucy Mission Budget.

Assumptions

A constant 2.6% yearly compounding inflation rate is assumed to estimate the budget across the entire mission's lifecycle [61]. It is assumed that personnel turnover will be minimal. In cases where turnover does occur, replacement costs are expected to be negligible and are covered by the total cost margin. Outreach costs relate to the team's effort in increasing public awareness of P.H.O.E.N.I.X and the impact that it will have on the scientific community and the end science goals. A graphic designer and a social media specialist will be hired full time for the duration of the mission to develop, publish, and distribute outreach content. Personnel travel costs will be estimated through the City Pair Program for airfare, FedRoom for lodging, and per diem reimbursement for meals and rentals. Tests are conducted at relevant NASA centers across the country, and launch takes place at Cape Canaveral, Florida. Key personnel will be flown in to oversee and conduct in-person testing of relevant components and subsystems with rental cars, lodging, and meals priced out using the aforementioned resources [61] [62].

Drivers

The primary cost drivers for P.H.O.E.N.I.X include items such as scope changes or descopes, which can shift the required designs and greatly impact system costs. External government policies such as changes in import tariffs may introduce some budget uncertainty, especially for foreign-sourced hardware. Lastly, any unforeseen engineering testing failures may lead to cost inflation due to vendor lead times and/or potential redesigns. A comprehensive budget for P.H.O.E.N.I.X will be developed as it advances towards the PDR. The full budget will include breakdowns of costs for each phase of the mission as well as a per-item cost breakdown. To account for any delays, uncertainties, and unexpected problems, a 30% total cost margin will be applied to the budget totals. This margin aligns with the standard 70% confidence level in lifecycle cost estimates at the PDR stage [29].

1.7.5 Cost Estimate

The total estimated cost for P.H.O.E.N.I.X is approximately 405 million dollars, as detailed in the Figure 1.7.5.1. This cost encompasses the full scope of the mission and includes personnel, travel, outreach, facilities, and other direct costs. The budget is organized into four primary categories: Personnel, Travel, Outreach, and Direct Costs. Personnel is broken down further into six roles: science, engineering, technical, administrative, management, and outreach. Staffing allocations were planned per mission phase and are summarized in the top portion of Figure 1.7.5.1 in blue. The baseline team assumes a minimal configuration with additional support staff only during peak build and integration periods. 30 additional support staff were added during early phases, split $\frac{2}{3}$ technicians and $\frac{1}{3}$ engineers or scientists. Salaries are assumed fixed except for inflation rates with a 28% benefits rate applied [10].

Costs for travel were estimated using federal resources including the City Pair Program for airfare, FedRooms for lodging, and standard GSA per diem rates for meals and rentals. Outreach costs include the full-time employment of a graphic designer and a social media specialist, whose salaries were derived using U.S. Bureau of Labor Statistics data [61]. The dominant costs for P.H.O.E.N.I.X are the direct mission costs. These direct costs include items such as the Mechanical Subsystem and Science Instrumentation, calculated using Cost Estimating Relationships (CERs) from the MCCET. These CERs are from the NCIM Version 9c. Inputs to the calculations are mass, power, and design life where applicable [29].

The final budget incorporates a 30% Total Cost Margin to accommodate unexpected costs, ensuring a 70% confidence level in budget sufficiency at the Preliminary Design Review stage. An estimated budget can be seen in Figure 1.7.5.1, covering personnel, outreach, travel, and spacecraft related expenses.

Active Microwave Instruments RIMFAX <ul style="list-style-type: none"> - Mass: 3kg - Power: 5 to 10 watts 	$1,244 * TotalMass^{0.36} * TotalMaxPwr^{0.50}$ $1,244 * 3^{0.36} * 10^{0.50} = 5842.302394$ Using this CER value, plugged into MCCET to calculate cost breakdown per phase.
---	--

Personnel Phase Allotment Table						
# People on Team	Phase C	Phase C	Phase C-D	Phase D	Phase E	Phase F
Year	FY 1	FY 2	FY 3	FY 4	FY 5	FY 6
Science Personnel:	10	10	5	5	15	15
Engineering Personnel:	15	15	15	15	10	10
Technicians:	30	30	30	30	0	0
Administration Personnel:	5	5	5	5	5	5
Management Personnel:	4	4	4	4	4	4
Total Personnel	64	64	59	59	34	34

P.H.O.E.N.I.X Preliminary Budget						
Mission Phase	Phase C	Phase C	Phase C-D	Phase D	Phase E	Phase F
Year	Year 1	Year 2	Year 3	Year 4	Year 5	Cumulative Total
PERSONNEL						
Science Personnel	\$ 800,000	\$ 820,800	\$ 420,800	\$ 431,200	\$ 1,324,800	\$ 1,356,000
Engineering Personnel	\$ 1,200,000	\$ 1,231,200	\$ 1,262,400	\$ 1,293,600	\$ 883,200	\$ 904,000
Technicians	\$ 1,800,000	\$ 1,846,800	\$ 1,893,600	\$ 1,940,400	\$ -	\$ 7,480,800
Administration Personnel	\$ 300,000	\$ 307,800	\$ 315,600	\$ 323,400	\$ 331,200	\$ 339,000
Project Management	\$ 480,000	\$ 492,480	\$ 504,960	\$ 517,440	\$ 529,920	\$ 542,400
Total Salaries	\$ 4,580,000	\$ 4,699,080	\$ 4,397,360	\$ 4,506,040	\$ 3,069,120	\$ 3,141,400
Total ERE	\$ 1,278,278	\$ 1,311,513	\$ 1,227,303	\$ 1,257,636	\$ 856,591	\$ 876,765
Personnel Margin	\$ 1,464,570	\$ 1,502,648	\$ 1,406,166	\$ 1,440,919	\$ 981,428	\$ 1,004,541
TOTAL PERSONNEL	\$ 7,322,848	\$ 7,708,586	\$ 7,396,432	\$ 7,766,553	\$ 5,417,482	\$ 5,675,658
TRAVEL						
Total Flights Cost	\$ 4,000	\$ 3,000	\$ 5,500	\$ 6,000	\$ 5,000	\$ 17,000
Total Hotel Cost	\$ 4,960	\$ 3,720	\$ 6,820	\$ 7,440	\$ 6,200	\$ 21,080
Total Transportation Cost	\$ 667	\$ 500	\$ 917	\$ 1,000	\$ 833	\$ 3,000
Total Per Diem Cost	\$ 2,196	\$ 1,647	\$ 3,020	\$ 3,294	\$ 2,745	\$ 9,333
Travel Margin	\$ 5,000	\$ 5,000	\$ 5,000	\$ 5,000	\$ 5,000	\$ 30,000
Total Travel Costs	\$ 16,823	\$ 14,228	\$ 22,362	\$ 24,507	\$ 21,835	\$ 62,617
OUTREACH						
Total Outreach Materials	\$ 10,000	\$ 12,000	\$ 15,000	\$ 18,000	\$ 20,000	\$ 25,000
Total Outreach Venue Costs	\$ 5,000	\$ 6,000	\$ 8,000	\$ 10,000	\$ 12,000	\$ 15,000
Total Outreach Travel Costs	\$ 7,000	\$ 8,000	\$ 10,000	\$ 12,000	\$ 15,000	\$ 18,000
Total Outreach Services Costs	\$ 10,000	\$ 12,000	\$ 15,000	\$ 20,000	\$ 25,000	\$ 30,000
Total Outreach Personnel Costs	\$ 143,000	\$ 143,000	\$ 143,000	\$ 143,000	\$ 143,000	\$ 143,000
Outreach Margin	\$ 17,500	\$ 18,100	\$ 19,100	\$ 20,300	\$ 21,500	\$ 23,100
Total Outreach Costs	\$ 192,500	\$ 204,277	\$ 221,025	\$ 240,717	\$ 261,096	\$ 287,133
DIRECT COSTS						
Mechanical Subsystem	\$ 19,106,400	\$ 19,106,400	\$ 30,000,400	\$ 21,788,000	\$ 2,180,000	\$ 2,180,000
Power Subsystem	\$ 12,403,200	\$ 12,403,200	\$ 10,399,200	\$ 10,868,000	\$ 1,088,000	\$ 1,088,000
Thermal Control Subsystem	\$ 1,003,200	\$ 1,003,200	\$ 6,226,933	\$ 1,144,000	\$ 228,000	\$ 228,000
Comms & Data Handling Subsystem	\$ 5,449,200	\$ 5,449,200	\$ 5,831,600	\$ 6,406,000	\$ 622,000	\$ 622,000
Guidance, Nav., & Control Subsystem	\$ 5,449,200	\$ 5,449,200	\$ 5,831,600	\$ 6,406,000	\$ 622,000	\$ 622,000
Science Instrumentation	\$ 5,586,000	\$ 5,586,000	\$ 5,978,000	\$ 6,370,000	\$ 490,000	\$ 24,500,000
Spacecraft Cost Margin	\$ 9,799,440	\$ 9,799,440	\$ 12,813,547	\$ 10,596,400	\$ 1,046,000	\$ 45,100,827
Total Spacecraft Direct Costs	\$ 58,796,640	\$ 60,325,353	\$ 80,879,107	\$ 68,537,515	\$ 6,928,704	\$ 7,091,880
Manufacturing Facility Cost	\$ 500,000	\$ 500,000	\$ 1,000,000	\$ 1,500,000	\$ 500,000	\$ 250,000
Test Facility Cost	\$ 7,250,400	\$ 7,250,400	\$ 12,954,000	\$ 11,544,000	\$ 296,000	\$ 39,590,800
Facility Cost Margin	\$ 1,550,080	\$ 1,550,080	\$ 2,790,800	\$ 2,608,800	\$ 159,200	\$ 109,200
Total Facilities Costs	\$ 9,300,480	\$ 9,542,292	\$ 17,615,330	\$ 16,673,718	\$ 1,054,541	\$ 740,376
Total Direct Costs	\$ 68,097,120	\$ 69,867,645	\$ 84,994,636	\$ 85,411,234	\$ 7,983,245	\$ 7,832,256
Total MTDC	\$ 58,796,640	\$ 60,325,353	\$ 80,879,107	\$ 68,537,515	\$ 6,928,704	\$ 282,559,198
Total Project Cost	\$ 80,529,011	\$ 82,847,326	\$ 112,941,012	\$ 99,237,123	\$ 14,271,928	\$ 14,462,251
F&A %						
ERE - Staff	10%	10%	10%	10%	10%	10%
Inflation Rate	28%	28%	28%	28%	28%	28%
Science Personnel Salary	5	80,000				
Engineering Personnel Salary	5	80,000				
Technician Salary	5	60,000				
Administration Personnel Salary	5	60,000				
Project Management Salary	5	120,000				
Outreach Personnel Combined Salary	5	143,000				
F&A %						
Personnel	\$ 41,287,558					
Travel	\$ 162,372					
Outreach	\$ 1,406,748					
Spacecraft Direct	\$ 282,559,198					
Total Facilities Co	\$ 55,126,937					
F&A %						
Graphic Designer	65000					
Social Media Specialist	78000					
P.H.O.E.N.I.X Budget Breakdown						
Total Facilities Costs	12.5%					
Spacecraft Direct Costs	74.3%					
Personnel	10%					
Outreach	0.6%					
Travel	1.3%					
Graphic Designer	0.1%					
Social Media Specialist	0.1%					

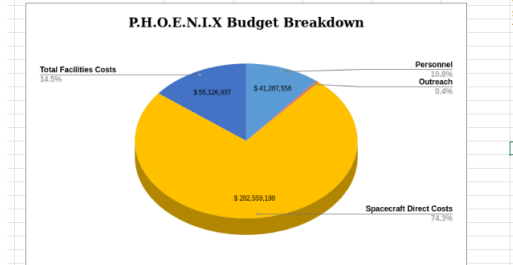


Figure 1.7.5.1: P.H.O.E.N.I.X Preliminary Budget and Pie Chart

1.7.6 Change Control

Once the mission has reached production, any engineering changes made will need to be formulated into an ECR (Engineering Change Request) and reviewed by a CCB (Change Control Board) [30]. The CCB will be comprised of leaders from the engineering team, science team, and programmatic team to ensure that all mission aspects of the change are considered. The team will be using a PLM package such as Siemens Teamcenter or PTC Windchill to retain version control for any CAD changes. Any engineering CAD changes will be drafted in the PLM, and attached to the ECR for review.

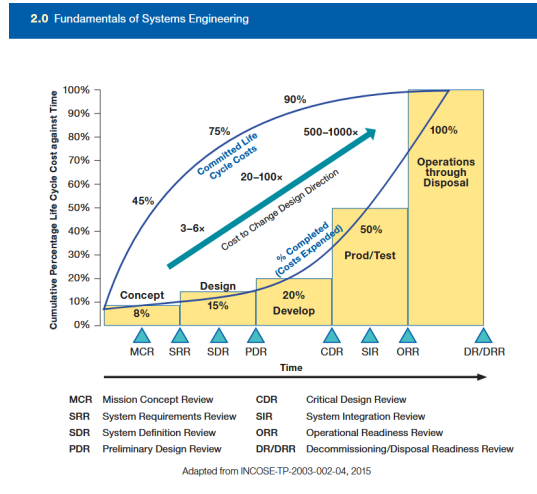


Figure 1.7.6.1: Life Cycle Cost Model

Note that as the mission reaches production, the cost to change the design direction is increased massively [29]. Hence avoiding engineering design changes at production is essential. Any design scope changes will need to go through a CCB as well as a cost estimate of the design change will need to be provided. Major changes suggested by SRBs will be tracked and their implementation progress documented on a team-wide tracker with each one being given its own specific reference number, allowing for feedback to be directly incorporated into further mission deliverables.

1.8 Conclusion

Through the SRR, P.H.O.E.N.I.X has matured the mission concept by updating all science objectives, finalizing scientific instrumentation, baselining all engineering components through trade studies, identifying potential risks to the mission at a

subsystem level, providing an updated basis for schedule and overall mission budget based on NASA best practices. As the team transitions toward the Mission Definition Review (MDR) and the closeout of Phase A, the focus will shift to completing remaining tasks including resolving outstanding TBD/TBR items, expanding risk mitigation strategies, and improving the fidelity of the cost model and integrated schedule. This upcoming phase will solidify system definitions, interfaces, and integration strategies, laying the groundwork for a robust Preliminary Design Review.

References/Bibliography

1. AMS Energy. "Frequently Asked Questions." AMS Energy. Accessed July 6, 2025. <https://www.amsenergy.com/frequently-asked-questions/>
2. Advanced Cooling Technologies, Inc. "Non-Integrated Warm-Reservoir Variable Conductance Heat Pipes (VCHPs) with Hybrid Wicks for Lunar Landers and Rovers." Advanced Cooling Technologies, Inc. Accessed July 6, 2025. <https://www.1-act.com/resources/learning-center/case-studies/non-integrated-war-m-reservoir-variable-conductance-heat-pipes-vchps-with-hybrid-wicks-for-lunar-la-nders-and-rovers/>
3. Advanced Cooling Technologies, Inc. "Variable Conductance Heat Pipes (VCHP): When, How, and Why to Use Them in Space Systems." Advanced Cooling Technologies, Inc. Accessed July 6, 2025. <https://www.1-act.com/thermal-solutions/space/variable-conductance-heat-pipes/>
4. BAE Systems. RAD5545 Space VPX Single Board Computer. Accessed July 6, 2025. <https://satsearch.co/products/bae-systems-rad5545-space-vpx-single-board-computer>.
5. Brainboxes. "What Are the Pin-Outs of the 9-Pin D Connector for My RS232 or RS422?" Accessed July 6, 2025. <https://www.brainboxes.com/faq/what-are-the-pin-outs-of-the-9-pin-d-connector-for-my-rs232-or-r>.
6. Chernov, V. M., B. K. Kardashev, and K. A. Moroz. "Low-Temperature Embrittlement and Fracture of Metals with Different Crystal Lattices – Dislocation Mechanisms." Nuclear Materials and Energy 7 (2016): 72–79. <https://www.sciencedirect.com/science/article/pii/S235217911530017X>.
7. Cho, H., J. Woo, J. Park, J. Lee, and S. Cho. "Dust Removal on Solar Panels of Exploration Rovers Using Chladni Patterns." Scientific Reports 15, no. 1 (2025): 1814. <https://doi.org/10.1038/s41598-025-86363-7>.

8. Donahue, T. M. "Evolution of Water Reservoirs on Mars from D/H Ratios in the Atmosphere and Crust." *Nature*. Accessed June 14, 2025.
<https://pubmed.ncbi.nlm.nih.gov/7700352/>.
9. Dragonfly Aerospace. "28-300 Battery Module Lithium-Ion Battery." Dragonfly Aerospace, June 19, 2024.
<https://dragonflyaerospace.com/components/battery-module/>.
10. Dunmore Aerospace. "Aluminized Polyimide Film." Dunmore Aerospace. Accessed July 6, 2025.
<https://www.dunmore.com/products/aluminized-polyimide-film.html>
11. Dunmore Aerospace. "Beta Cloth & Beta Fabric." Dunmore Aerospace. Accessed July 6, 2025.
<https://www.dunmore.com/products/beta%E2%80%91cloth.html>
12. Dunmore Aerospace. "Double Aluminized Polyester Film." Dunmore Aerospace. Accessed July 6, 2025.
<https://www.dunmore.com/products/double-aluminized-pet-film.html>
13. Dwyer Instruments, LLC. "Self-Adhesive Polyimide Flexible Heaters 302 °F Max (KHRA-KHLVA-KHA Series)." Dwyer Omega. Accessed July 6, 2025.
<https://www.dwyeromega.com/en-us/self-adhesive-polyimide-flexible-heaters-302-f-max/p/KHRA-KHLVA-KHA-SERIES/>
14. European Space Agency. "The Raman Laser Spectrometer for the ExoMars Rover Mission." Accessed July 6, 2025.
https://exploration.esa.int/web/mars/-/59423-rull-et-al-2017?utm_
15. GammaGuard. T007-T Thermal Neutron Detector. Accessed July 6, 2025.
<https://gammawatch.com/ct007-t-thermal-neutron-detector/>
16. Gitzendanner, Rob. "Batteries Enabling Planetary and Deep Space Exploration." EaglePicher Provides Essential Battery Technology for NASA's Artemis I Launch. Accessed July 6, 2025. <https://www.eaglepicher.com/sites/default/files/Batteries%20Enabling%20Planetary%200721.pdf>.
17. Greicius, Tony, and Naomi Hartono, eds. "Mars Pathfinder - Mars Missions." NASA Jet Propulsion Laboratory. Accessed June 13, 2025.
<https://www.jpl.nasa.gov/missions/mars-pathfinder-sojourner-rover/>.
18. Hamran, S.E., Paige, D.A., Amundsen, H.E.F. et al. Radar Imager for Mars' Subsurface Experiment—RIMFAX. *Space Sci Rev* 216, 128 (2020).
<https://doi.org/10.1007/s11214-020-00740-4>

19. Hand, Eric. "Road Hazards Threaten Rover: To Limit Wheel Damage from Sharp Rocks, the Curiosity Mars Rover Detours into Sandy Valleys." *Science* 345, no. 6195 (2014): 365–66. <http://www.jstor.org/stable/24745098>.
20. He, Fei, Zhaojin Rong, Zhaopeng Wu, Jiawei Gao, Kai Fan, Xu Zhou, Limei Yan, Yuqi Wang, and Yong Wei. "Martian Dust Storms: Reviews and Perspective for the Tianwen-3 Mars Sample Return Mission." *Remote Sensing* 16, no. 14 (2024): 2613. <https://www.mdpi.com/2072-4292/16/14/2613>.
21. Howell, Elizabeth. "Radiation Resistance Is Baked into the Perseverance Mars Rover. Here's Why That's Important." *Space.com*, May 6, 2021. <https://www.space.com/mars-rovers-radiation-protection-xilinx>.
22. Kal Tire. "Directional, Asymmetrical & Symmetrical Tread Patterns." Accessed July 6, 2025. [https://www.kaltire.com/en/directional-asymmetrical-symmetrical-tread-patterns.html#:~:text=side%20or%20diagonal\)-,Benefits,Summer%20to%20summer%20performance](https://www.kaltire.com/en/directional-asymmetrical-symmetrical-tread-patterns.html#:~:text=side%20or%20diagonal)-,Benefits,Summer%20to%20summer%20performance).
23. Kee Plan." NASA, February 13, 2024. <https://www.nasa.gov/ocfo/strategic-plan/>.
24. Lunar and Planetary Institute. "LPSC 2022 Abstract #1915." Accessed July 6, 2025. <https://www.hou.usra.edu/meetings/lpsc2022/pdf/1915.pdf>.
25. Lunar and Planetary Institute. First Landing Site/Exploration Zone Workshop for Human Mission to Mars. LPI Contribution No. 1879. Houston, TX: Lunar and Planetary Institute, 2015. https://www.lpi.usra.edu/lpi/contribution_docs/LPI-001879.pdf.
26. Martinez, G. M., C. N. Newman, A. De Vicente-Retortillo, E. Fischer, N. O. Renno, M. I. Richardson, A. G. Fairén, et al. "The Modern Near-Surface Martian Climate: A Review of In-Situ Meteorological Data from Viking to Curiosity." *Space Science Reviews* 212 (2017): 295–338. <https://link.springer.com/article/10.1007/s11214-017-0360-x>.
27. Minco. "HK6900 – Polyimide Thermofoil™ Heaters." Minco. Accessed July 6, 2025. https://www.minco.com/catalog/?catalogpage=product&cid=3_1-polyimide-thermofoil-heaters&id=HK6900
28. Mirion Technologies. TN-15™ High Sensitivity Ultra-compact Thermal Neutron. Accesssd July 6th, 2025. <https://www.mirion.com/products/technologies/spectroscopy-scientific-analysis/ga>

mma-spectroscopy/detectors/scintillation-czt-detectors-accessories/tn-15-high-sensitivity-ultra-compact-thermal-neutron

29. NASA Cost Estimating Handbook, Appendix J – Joint Cost and Schedule Confidence Levels, 2020.
https://www.nasa.gov/wp-content/uploads/2020/11/ceh_appj.pdf
30. NASA Office of Inspector General, NASA's Management of the Space Launch System Stages Contract, IG-17-017, June 2017.
<https://oig.nasa.gov/docs/IG-17-017.pdf>
31. NASA Office of Inspector General. NASA's Plans for Human Exploration Beyond Low Earth Orbit. IG-17-017, 2017. <https://oig.nasa.gov/docs/IG-17-017.pdf>.
32. NASA. Mars 2020/Perseverance Fact Sheet. 2020.
https://mars.nasa.gov/files/mars2020/Mars2020_Fact_Sheet.pdf.
33. NASA. NASA Procedural Requirements 7120.5E: NASA Space Flight Program and Project Management Requirements. Accessed June 15, 2025.
<https://nодis3.gsfc.nasa.gov/displayDir.cfm?t=NPR&c=7120&s=5E>.
34. NASA. “7.0 Thermal Control,” in Small Spacecraft Technology State of the Art (SST-SoA). Accessed July 6, 2025.
<https://www.nasa.gov/smallsat-institute/sst-soa/thermal-control/#7.2>
35. NASA. “Construction to Begin on 2016 NASA Mars Lander.” NASA Jet Propulsion Laboratory. Accessed July 6, 2025.
<https://www.jpl.nasa.gov/news/construction-to-begin-on-2016-nasa-mars-lander/>.
36. NASA. “InSight Mission - NASA Science.” Last modified 2025.
<https://science.nasa.gov/mission/insight/>.
37. NASA. “JPL Mission Details (Archived).” Archived version from January 28, 2018.
<https://web.archive.org/web/20180128115920/https://www.jpl.nasa.gov/missions/details.php?id=5917>.
38. NASA. “LAR-TOPS-250 Patent.” Accessed July 6, 2025.
<https://technology.nasa.gov/patent/LAR-TOPS-250>.
39. NASA. “Mars Exploration Rovers: Spirit and Opportunity.” Accessed July 6, 2025.
<https://science.nasa.gov/mission/mars-exploration-rovers-spirit-and-opportunity/>.
40. NASA. “NASA Begins Testing Mars Lander for Next Mission to Red Planet.” NASA Jet Propulsion Laboratory. Accessed July 6, 2025.

- <https://www.jpl.nasa.gov/news/nasa-begins-testing-mars-lander-for-next-mission-to-red-planet/>.
41. NASA. "Opportunity Rover Mission Comes to End." NASA Jet Propulsion Laboratory. Accessed July 6, 2025.
<https://www.jpl.nasa.gov/news/nasas-opportunity-rover-mission-on-mars-comes-to-end/>.
42. NASA. "Perseverance Science Instruments". Accessed July 6, 2025
<https://science.nasa.gov/mission/mars-2020-perseverance/science-instruments/>
43. NASA. "Spaceflight Lifecycle Diagram." Accessed July 6, 2025.
https://www.nasa.gov/wp-content/uploads/2019/02/seh_figure_3-0_1_spaceflight_lifecycle.jpg.
44. National Instruments. "Measuring Temperature with Thermocouples, RTDs, and Thermistors: Sensitivity." National Instruments. Accessed July 6, 2025.
<https://www.ni.com/en/shop/data-acquisition/sensor-fundamentals/measuring-temperature-with-thermocouples-rtds-and-thermistors.html#Sensitivity>
45. National Instruments. "Measuring Temperature with Thermocouples, RTDs, and Thermistors: Sensitivity." National Instruments. Accessed July 6, 2025.
<https://www.ni.com/en/shop/data-acquisition/sensor-fundamentals/measuring-temperature-with-thermocouples-rtds-and-thermistors.html#Sensitivity>
46. Neukart, Florian. "Towards Sustainable Horizons: A Comprehensive Blueprint for Mars Colonization." *Heliyon*, February 15, 2024.
<https://pmc.ncbi.nlm.nih.gov/articles/PMC10884476/#se0160>.
47. PMI. "Mars Pathfinder Case Study." Project Management Institute. Accessed July 6, 2025. <https://www.pmi.org/learning/library/mars-pathfinder-case-study-13318>.
48. Phison. "SSD Solutions." Accessed July 6, 2025.
<https://www.phison.com/en/solutions/ssd>.
49. Planetary Society. "Curiosity Wheel Damage." Accessed July 6, 2025.
<https://www.planetary.org/articles/08190630-curiosity-wheel-damage>.
50. Planetary Society. "Planetary Protection: How to Explore Mars and Other Worlds Responsibly." Accessed June 13, 2025.
<https://www.planetary.org/articles/planetary-protection-explore-responsibly>.
51. Redwire. "Roll-Out Solar Array Flysheet." June 2023.
<https://redwirespace.com/wp-content/uploads/2023/06/redwire-roll-out-solar-array-flysheet.pdf>.

52. Satsearch. "SQUID3 Space Aluminized Mylar Film." Satsearch. Accessed July 6, 2025. <https://satsearch.co/products/squid3-space-aluminized-mylar-film>
53. ScienceDirect. "Artificial Intelligence in Planetary Missions." Accessed July 6, 2025. <https://www.sciencedirect.com/science/article/pii/S0032063316300058>.
54. Sinha, Rishitosh K., and Dwijesh Ray. "Extensive Glaciation in the Erebus Montes Region of Mars." *Icarus* 367 (2021): 114557. <https://doi.org/10.1016/j.icarus.2021.114557>.
55. Smart Modular. "T6CN M.2 2280 PCIe NVMe SSD." Accessed July 6, 2025. <https://www.smartm.com/product/t6cn-m2-2280-pcie-nvme-ssd>.
56. Spirit. "Spirit Rover." Marspedia. Accessed July 6, 2025. <https://marspedia.org/Spirit>.
57. Technical Associates. CP-MU Submersible Gamma Neutron Probe. Accessed July 6, 2025. <https://tech-associates.com/cp-mu-gn-submersible-gamma-neutron-probe/>
58. Tires Easy. "Directional Tire Tread Patterns." Accessed July 6, 2025. <https://www.tires-easy.com/knowledge-center/tire-basics/directional-tire-tread-patterns>.
59. Trail Tire. "Asymmetrical, Symmetrical or Directional Tread?" Accessed July 6, 2025. <https://trailtire.com/blog/asymmetrical-symmetrical-or-directional-tread/>.
60. Trail Tire. "Asymmetrical, Symmetrical or Directional Tread?" Accessed July 6, 2025. <https://trailtire.com/blog/asymmetrical-symmetrical-or-directional-tread/>.
61. U.S. Bureau of Labor Statistics. "CPI Inflation Calculator." Accessed July 6, 2025. https://www.bls.gov/data/inflation_calculator.htm.
62. U.S. General Services Administration. "Per Diem Rates Results, FY2025, Florida." Accessed July 6, 2025. https://www.gsa.gov/travel/plan-book/per-diem-rates/per-diem-rates-results?action=perdiems_report&fiscal_year=2025&state=FL.
63. USGS. "I-1083 Geologic Map of Mars." Lunar and Planetary Institute. Accessed June 13, 2025. https://www.lpi.usra.edu/resources/mars_maps/1083/.
64. VPT, Inc. "SVRFL2800S Series DC-DC Converter Datasheet." Accessed July 6, 2025. <https://www.vptpower.com/products/datasheet/svrfl2800s-series-pdf>.

65. Viola, Donna A. Expanded Craters on Mars: Implications for Shallow, Mid-Latitude Excess Ice. PhD diss., University of Arizona, 2017. <https://repository.arizona.edu/handle/10150/625594>.
66. Viola, Donna A., and R. E. Milliken. "Mid-Latitude Martian Ice as a Target for Human Exploration, Astrobiology, and In Situ Resource Utilization." Paper presented at the 1st EZ Workshop for Human Missions to Mars, Houston, TX, June 8–10, 2015. <https://www.hou.usra.edu/meetings/explorationzone2015/pdf/1011.pdf>.
67. Viola, Donna. Arcadia Planitia: Acheron Fossae and Erebus Montes – Workshop Abstract #1011. Presented at the 1st EZ Workshop for Human Missions to Mars, Houston, TX, June 8–10, 2015.
68. Warner, Nicholas H., Sukesh Gupta, Shih-Yuan Lin, Jung-Rack Kim, Jean-Pierre Müller, and Julie Morley. "Late Noachian to Hesperian Climate Change on Mars: Evidence of Episodic Warming from Transient Crater Lakes Near Ares Vallis." *Journal of Geophysical Research: Planets* 115, no. E6 (2010). <https://doi.org/10.1029/2009JE003522>.
69. Webster, C. R., et al. "Tunable Laser Spectrometers for Space Science." Presented at the GSFC Instruments for Space Science Workshop, Greenbelt, MD, 2014.
70. Wilson, J, B Anderson, F Cucinotta, J Ware, and C Zeitlin. n.d. "Spacesuit Radiation Shield Design Methods." <https://ntrs.nasa.gov/api/citations/20060046504/downloads/20060046504.pdf>.
71. "A Review of Thrust-Vectoring Schemes for Fighter Applications." Accessed June 14, 2025. <https://arc.aiaa.org/doi/abs/10.2514/6.1978-1023>.
72. "Curiosity Science Highlights - NASA Science." NASA. Last modified May 28, 2025. <https://science.nasa.gov/mission/msl-curiosity/science-highlights/#Water>.
73. "Curiosity Science Instruments - NASA Science." NASA. Last modified April 7, 2025. <https://science.nasa.gov/mission/msl-curiosity/science-instruments/>.
74. "Detoxifying Mars: The Biocatalytic Elimination of Omnipresent Perchlorates." NASA. Last modified January 4, 2024. <https://www.nasa.gov/general/detoxifying-mars/>.
75. "Electrodynamic Shield to Remove Dust from Solar Panels on Mars." ERAU Space Congress Proceedings. Accessed July 6, 2025.

- <https://commons.erau.edu/cgi/viewcontent.cgi?article=3360&context=space-congress-proceedings>.
76. "Fate of NASA's InSight Mission." Archived version from November 16, 2018.
<https://web.archive.org/web/20181116012749/https://spaceflightnow.com/2016/03/05/fate-of-nasas-insight-mars-mission-to-be-decided-soon/>.
77. "It's Cold on Mars - NASA Science." NASA. Last modified October 18, 2024.
<https://science.nasa.gov/blog/its-cold-on-mars/>.
78. "Mars - NASA Science." NASA. Last modified May 19, 2025.
<https://science.nasa.gov/mars/>.
79. "Mars Pathfinder - NASA Science." NASA. Last modified November 6, 2024.
<https://science.nasa.gov/mission/mars-pathfinder/>.
80. "Mars Phoenix - NASA Science." NASA. Last modified November 3, 2024.
<https://science.nasa.gov/mission/mars-phoenix/>.
81. "Mars Reconnaissance Orbiter - NASA Science." NASA. Last modified March 25, 2025. <https://science.nasa.gov/mission/mars-reconnaissance-orbiter/>.
82. "Mars: Facts - NASA Science." NASA. Last modified April 22, 2025.
<https://science.nasa.gov/mars/facts/>.

Declaration of Generative AI and AI-Assisted Technologies in the Writing Process

During the preparation of this document, the team used OpenAI's ChatGPT to assist with re-phrasing and content refinement. The tool was used to rephrase content for conciseness and completeness.

During literature reviews, the team utilized Google's AI in Search to identify cited resources. The team thoroughly [read all sources]

During the preparation of this document, the team utilized online translation tools including Google Translate to aid in writing and editing.

After using various tools, the team reviewed and edited all content to ensure accuracy, original contribution, and technical fidelity. Team 01 takes full responsibility for the content of this deliverable.

Appendix

Changes	Description
MCR-RFA-1, Section 1.2	The measurement observables must directly relate to the physical parameters with which the STM was addressed and a CRF was filled due to changes in both our human exploration goal objectives to meet this RFA.
MCR-RFA-2, Section 1.3	A thorough description of each region of interest and how they fulfill the team's science objectives must be provided, and was also addressed by defining the region of interest.
CRF - Science objective 1# of HBS-1LM (waiting on approval)	Science objective 1# of HBS-1LM: The team is requesting a minor alteration to the science objective and add clarification within the STM from "various samples" (exact quantity was originally unspecified) to one single sample. Science objective 1# of HBS-1LM - STM observable: Change data transmission interval from "monthly" to "weekly".
CRF - Science objective 2# of HBS-1LM (waiting on approval)	The second objective of HBS-1LM's main purpose still remains the same, but the measurement approach to provide quantitative data had to change.

Table A.1 (Mission Change Log)

Leg Material						
Criteria	Explanation	Grade	Weight	Aluminu m 6061	Titaniu m	Carbon Fiber (CF) Compos ite
Density	Density (g/cm ³ or kg/m ³)	1 = > 4.5 g/cm ³ 3 = < 3.5 g/cm ³ 5 = < 1.5 g/cm ³	25%	3	1	4
Load-Bearing	Shear Strength (MPa) – Point at which permanent deformation begins	1 = > 300 MPa 3 = > 200 MPa 5 = < 100 MPa	25%	3	1	4
Shock Absorption	Fracture Toughness (MPa/m ^{1/2}) – Total energy absorbed before failure	1 = > 50 MPa/m ^{1/2} 3 = > 20 MPa/m ^{1/2} 5 = < 10 MPa/m ^{1/2}	25%	2	1	3
Thermal Performance	Coefficient of Thermal Expansion (μm/m·K)	1 = < 5 μm/m·°C 3 = < 10 μm/m·°C 5 = > 20 μm/m·°C	25%	5	3	1
		TOTALS:	100%	43.75%	87.50%	50.00%

Table A.2 (Leg Material Trade Study)

Chassis Material						
Criteria	Explanation	Grade	Weight	Aluminu m 6061	CF Compos ite	Stainles s Steel
Density	Density (g/cm³ or kg/m³)	1 = < 3 g/cm³ 3 = < 4.5 g/cm³ 5 = > 6 g/cm³	30%	1	1	5
Load-Bearing	Shear Strength (MPa) – Point at which permanent deformation begins	1 = > 300 MPa 3 = > 200 MPa 5 = < 100 MPa	20%	3	4	1
Shock Absorption	Fracture Toughness (MPa/m¹/₂) – Total energy absorbed before failure	1 = > 25 MPa/m¹/₂ 3 = > 15 MPa/m¹/₂ 5 = < 10 MPa/m¹/₂	30%	1	4	1
Thermal Performance	Coefficient of Thermal Expansion (µm/m·K)	1 = < 5 µm/m·°C 3 = < 10 µm/m·°C 5 = > 20 µm/m·°C	20%	5	1	4
		TOTALS:	100%	70.00%	62.50%	55.00%

Table A.3 (Chassis Material Trade Study)

Wheel Material						
Criteria	Explanation	Grade	Weight	Alumi num	Titani um	Fiber glass
Density	Density (g/cm³ or kg/m³)	1 = < 3 g/cm³ 3 = < 4.5 g/cm³ 5 = > 6 g/cm³	25%	1	4	1
Load-Bearing	Shear Strength (MPa) – Point at which permanent deformation begins	1 = > 150 MPa 3 = > 100 MPa 5 = < 50 MPa	25%	1	1	5
Shock Absorption	Fracture Toughness (MPa/m½) – Total energy absorbed before failure	1 = > 220 MPa 3 = > 120 5 = < 20 MPa	25%	2	1	4
Thermal Performance	Coefficient of Thermal Expansion (µm/m·K)	1 = < 10 µm/m·°C 3 = > 30 µm/m·°C 5 = > 50 µm/m·°C	25%	2	1	1
		TOTALS:	100%	87.50%	81.25%	56.25%

Table A.4 (Wheel Material Trade Study)

Wheel Tread						
Criteria	Explanation	Grade	Weight	Symmetrical	Asymmetrical	Directional
Wear	Abrasions resistance of the tread	1 = high, 3 = medium 5 = Fail	30%	2	3	5
Grip	Shows efficiency of wheel-ground interaction	1 = high, 3 = medium 5 = Fail	30%	3	1	1
Reliability	Fatigue Life (Cycles to crack initiation or tread breakoff)	1 = high, 3 = medium 5 = Fail	40%	1	3	5
		TOTALS:	100%	77.50%	65.00%	30.00%

Table A.5 (Wheel Tread Trade Study)

Dust Mitigation Methods						
Criteria	Explanation	Grade	Weight	Electrodynamic Dust Shield (EDS)	Vibration-Based Cleaning (Chladni Patterns)	Passive Coatings (Hydrophobic/Anti-Static)
Effectiveness	Ability to remove or prevent dust, maintain panel output over time	1 = high percentage dust removal; minimal power loss 3 = medium percentage dust removal; moderate power loss 5 = low percentage dust removal; significant power loss	35%	1	3	3
Power Consumption	Additional power required for operation (if any)	1 = low percentage of array output 3 = moderate percentage of array output 5 = high percentage of array output	20%	1	3	1
Reliability/R robustness	Performance over mission duration, resistance to failure or degradation	1 = proven in Mars-like conditions; no moving parts 3 = some moving parts or limited Mars testing 5 = high failure risk; unproven or complex	25%	1	3	1
Mass & Integration	Added mass and complexity to the rover system	1 = minimal integration impact 3 = moderate integration effort 5 = major integration or design changes	20%	1	3	1
		TOTALS:	100%	100.00%	50.00%	82.50%

Table A.6 (Dust Mitigation Methods Trade Study)

Solar Panel Deployment						
Criteria	Explanation	Grade	Weight	Mechanic al Hinge	Ultraflex	ROSA (Roll-O ut Solar Array)
Mass	Minimize launch mass (kg)	1 = optimal for launch constraints 3 = acceptable for mission parameters 5 = significantly impacts payload margin	25%	4	2	1
Stowed Volume	Minimize stowed volume (m³)	1 = minimal impact on rover design 3 = moderate accommodation required 5 = substantial accommodation required	30%	5	2	1
Reliability	Must deploy successfully on Mars	1 = extensive flight heritage 3 = some flight heritage 5 = limited testing or heritage	30%	1	3	2
Complexity	Lower complexity = less risk, easier integration	1 = simple mechanism; few moving parts; minimal deployment steps 3 = moderate complexity; manageable number of failure points 5 = high complexity; numerous moving parts; multiple failure points	15%	2	3	2
		TOTALS:	100%	47.50%	63.75%	88.75%

Table A.7 (Solar Panel Deployment Trade Study)

PV Cell Type						
Criteria	Explanation	Grade	Weight	Spectrolab XTE-SF	AZUR SPACE 3G30C	AZUR SPACE 4G32C (Quad-Junction)
BOL Efficiency	Measures the initial energy conversion efficiency of the PV cell	1 = ≥32% 3 = 29%-31.9% 5 = <29%	15%	1	3	1
EOL Efficiency	Efficiency after expected mission degradation	1 = ≥28% 3 = 26-27.9% 5 = <26%	35%	3	3	1
Radiation Resistance	Ability to withstand Mars radiation with minimal performance loss	1 = <5% power loss 3 = 5-10% power loss 5 = >10% power loss	20%	3	3	1
Specific Power	Power output per unit mass (W/g)	1 = >370 W/g 3 = 300-369 W/g 5 = <300 W/g	30%	3	3	1
		TOTALS:	100%	57.50%	50.00%	100.00%

Table A.8 (PV Cell Type Trade Study)

Power Storage and Battery System						
Criteria	Explanation	Grade	Weight	Li-ion NMC 18650 (COTS)	LiFePO4	LTO (Low Temp)
Energy Density	Energy produced per kg	1= >200 Wh/kg 3= 200-100 Wh/kg 5= <100 Wh/kg	30%	1	2	4
Temperature Tolerance	Function capacity during Martian weather events and Sol cycles	1= -30°C to +60°C 3= -10°C to +60 5= >0°C only	30%	4	2	1
Cycle Life	Number of charges available before battery capacity depletes	1= >2000 cycles 3= >1000 cycles 5= >500 cycles	25%	3	1	1
Mass	Amount of mass utilized by the individual battery	1= compact 3 = less compact 5= bulky	15%	1	2	3
		TOTALS:	100%	65.00%	81.25%	70.00%

Table A.9 (Power Storage and Battery System Trade Study)

Isolated Power System						
Criteria	Explanation	Grade	Weight	DC-DC Converter with Galvanic Isolation	Transformer-Based AC-DC Isolation	Battery Pack with Isolated Charger
Voltage Regulation	Ability to keep output voltage stable under all operating conditions	1 = <2% ripple, fast response, high stability 3 = 2–5% ripple, some fluctuation 5 = >5% ripple, unstable under load changes	25%	1	2	1
Isolation Quality	Degree of electrical separation from the main rover power bus	1 = full isolation, >1 kV withstand, minimal leakage 3 = partial isolation, moderate leakage 5 = no isolation, high leakage	25%	1	1	1
EMI Risk	Resistance to interference from other rover systems	1 = excellent filtering, minimal EMI/EMC risk 3 = moderate filtering 5 = poor filtering, high risk	20%	1	3	2
Integration Complexity	Effort and resources needed to install and connect the power system	1 = minimal added mass & volume, easy to integrate 3 = moderate mass/volume, some integration effort 5 = high mass/volume, complex integration	15%	1	3	2
Reliability	Likelihood of consistent, failure-free operation over the mission	1 = proven in spaceflight, minimal failure modes 3 = some heritage, moderate risk 5 = low heritage	10%	1	3	2
Power Efficiency	Power percentage delivered to the instrument	1 = >90% 3 = 80–90% 5 = <80%	5%	1	3	2
		TOTALS:	100%	100.00%	79.17%	91.67%

Table A.10 (Isolated Power System Trade Study)

Onboard Computer (OBC)							
Criteria	Explanation	Grade	Weight	RAD7 50	RAD5 545	Cobham GR71 2RC	Pumpkin OBC (Cube Sat Kit)
Processing Performance	Determines capacity to run flight software, autonomy, and instrument control.	1 = >1GHz, multi-core 2 = 500–1000MHz 3 = 200–500MHz 4 = 100–200MHz 5 = <100MHz	30%	3	1	4	5
Radiation Tolerance	Critical for deep space and Mars missions to avoid data corruption or total system failure.	1 = >100krad, SEE hardened 2 = 50–100krad 3 = 20–50krad 4 = 5–20krad 5 = <5krad	25%	1	1	2	5
Memory Capacity	Larger memory supports buffering of science data and autonomous ops.	1 = >2GB 2 = 1–2GB 3 = 512MB–1GB 4 = 128–512MB 5 = <128MB	20%	2	1	4	5
Mass & Power Efficiency	Important for small spacecraft; lower weight and power use extends mission life.	1 = <2W and <200g 2 = 2–5W and <500g 3 = 5–10W or ~1kg 4 = 10–20W or 1–2kg 5 = >20W or >2kg	15%	4	3	3	1
Flight Heritage / TRL	Indicates reliability and ease of integration; flight-proven systems reduce risk.	1 = TRL 9, >10 missions 2 = TRL 8–9, 3–10 missions 3 = TRL 7–8, 1–2 missions 4 = TRL 5–6, tested 5 = TRL <5, lab only	10%	1	2	3	3
		TOTALS:	100%	68.75%	90.00%	43.75%	20.00%

Table A.11 (Onboard Computer Trade Study)

Data Storage						
Criteria	Explanation	Grade	Weight	Micro Secure Digital (SD) Cards	Embedded MultiMediaCard (eMMC)	Non-Volatile Memory Express Solid State Drive (NVMe SSD)
Data Storage Capacity	Higher capacity allows storing more science data, and system logs. 1 = >512GB 2 = 256–512GB 3 = 128–256GB 4 = 64–128GB 5 = <64GB		35%	3	2	1
Data Transfer Speed	Faster read/write speeds allow faster instrument data dumps and reduce lag during operation. 1 = >2000MB/s 2 = 1000–2000MB/s 3 = 500–1000MB/s 4 = 100–500MB/s 5 = <100MB/s		25%	4	3	1
Radiation Tolerance	Radiation-hardened systems are necessary to prevent data corruption or permanent damage from cosmic rays. 1 = Radiation-hardened 2 = Industrial with ECC 3 = Industrial without ECC 4 = Consumer ECC 5 = Consumer, no protection		20%	5	3	2
Power Consumption	Low power consumption reduces heat production and power consumption, important for energy rationing on spacecraft. 1 = <0.5W 2 = 0.5–1W 3 = 1–1.5W 4 = 1.5–2.5W 5 = >2.5W		20%	2	1	4
		TOTALS:	100%	38.75%	68.75%	80.00%

Table A.12 (Data Storage Trade Study)

Data Interfaces							
Criteria	Explanation	Grade	Weight	RS-422	MIL-STD-1553	Intergrated Circuit (I2C)	Ethernet
Data Rate	Higher throughput supports high-bandwidth sensors, cameras, and data logs.	1 = >100 Mbps 2 = 50–100 Mbps 3 = 10–50 Mbps 4 = 1–10 Mbps 5 = <1 Mbps	35%	4	5	5	1
Noise Tolerance	Throughput robustness to noise and packet loss to mitigate data loss.	1 = Rad-hard & fault tolerant 2 = Rad-hard 3 = Some fault tolerance 4 = minimal 5 = none	25%	2	1	4	5
Physical Complexity	Connection simplicity for ease of assembly and system integration.	1 = 1–2 wires 2 = 3–5 wires 3 = 6–10 wires 4 = Ribbon/bulk 5 = Shielded bundle	20%	2	4	1	5
Time Accuracy Preservation	Necessary for priority management and time-sensitive processes.	1 = Fully deterministic 2 = Hard real-time 3 = Prioritized messages 4 = Best-effort 5 = Non-deterministic	10%	1	4	5	5
Technology Readiness	Space-qualified systems with successful mission histories.	1 = Flown >5x 2 = Flown 2–5x 3 = CubeSat/LEO only 4 = Tested only 5 = Never flown	10%	1	1	2	3
		TOTALS:	100%	62.50%	42.50%	33.75%	40.00%

Table A.13 (Data Interfaces Trade Study)

Telecommunications							
Criteria	Explanation	Grade	Weight	Software Defined Radio (SDR)	Deep Space Network (DSN)	Deep Space Optical Network (DSON)	Ultra High Frequency (UHF) Radio
Power Consumption	Low power systems are essential for energy-constrained environments like Mars.	1 = <5W 2 = 5–10W 3 = 10–20W 4 = 20–40W 5 = >40W	35%	2	4	5	1
Data Rate	High data rate enables faster transmission of science data, reducing risk of memory overflow.	1 = >100 Mbps 2 = 50–100 Mbps 3 = 10–50 Mbps 4 = 1–10 Mbps 5 = <1 Mbps	25%	3	3	1	4
Technology Readiness	Systems with high TRL have been flight-proven and carry lower implementation risk.	1 = TRL 9 2 = TRL 8 3 = TRL 6–7 4 = TRL 4–5 5 = TRL <4	25%	2	1	4	1
Directionality	Systems with low pointing or alignment needs are easier to implement and more fault-tolerant.	1 = Omnidirectional 2 = Wide-angle 3 = Narrow-angle 4 = Requires fine tracking 5 = Requires nanoradian precision	15%	2	3	5	1
		TOTALS:	100%	68.75%	53.75%	31.25%	81.25%

Table A.14 (Wheel Tread Trade Study)

MLI (Outer Cover)							
Criteria	Explanation	Grade	Weight	Beta Cloth	Beta Cloth Aluminized	Kapton Coated and Backed	Double Sided Mylar
Operational Temperature Range	Kelvin(K) (SYS.02)	1= exceptional temperature range 3 = moderate temperature range 5= does not meet the temperature range	25%	1	1	1	1
Tensile Strength	Evaluation of the tensile strength of the Beta cloth(kg/cm)	1= Good tensile strength value 3= Moderate tensile strength value 5= Low tensile strength value/no value	15%	1	1	4	2
Absorptivity	Evaluation of how much solar radiation is absorbed compared to how much it reflects. (α)	1= favorably low absorptivity 3= moderate absorptivity 5= high absorptivity	30%	5	5	3	1
Emissivity	Evaluation of the rate at which heat is radiated. Lower is favored for outer covers. (ϵ)	1= low emissivity 3=moderative emissivity 5=high emissivity	30%	4	3	2	1
		TOTALS:	100%	22.50%	30.00%	41.25%	71.25%

Table A.15 (MLI Outer Cover Trade Study)

MLI (Interior Layer)						
Criteria	Explanation	Grade	Weight	Aluminized Kapton	Aluminized Mylar	Goldized Kapton
Operational Temperature Range	Kelvin(K) (SYS.02)	1= exceptional temperature range 3 = moderate temperature range 5 = does not meet the temperature range	25%	1	2	1
TRL	Evaluation of the maturity of the proposed MLI material.	1 = Satisfactory TRL (TRL 5-6>>) 3 = Moderate TRL (TRL 3-4) 5 = Novice TRL (TRL 1-2)	15%	1	1	1
Absorptivity	Evaluation of how much solar radiation is absorbed compared to how much it reflects. (α)	1= high absorptivity 3= moderate absorptivity 5= low absorptivity	30%	5	5	2
Emissivity	The rate at which heat is radiated. Mid-low is favored for interior layers. (ϵ)	1= exceptionally low-mid emissivity 3= high-mid emissivity 5= high emissivity	30%	2	2	1
		TOTALS:	100%	62.50%	56.25%	92.50%

Table A.16 (MLI Inner Cover Trade Study)

Heat Pipes						
Criteria	Explanation	Grade	Weight	Variable Conductance Heat Pipe (Ammonia-Cold)	Constant Conductance Heat Pipe	Thermosyphon
Operational Temperature Range	Kelvin(K) (SYS.02)	1= can operate at low temperatures with an exceptional temperature range. 3= can operate at low temperatures within an acceptable temperature range. 5= small and limited temperature range.	30%	2	2	4
TRL	Evaluation of the maturity of the proposed heat pipe design.	1 = Satisfactory TRL (TRL 5-6>>) 3 = Moderate TRL (TRL 3-4) 5 = Low TRL (TRL 1-2)	15%	1	1	2
Reliability	Evaluation of whether the heat pipe design can perform in any condition.	1=Can operate in extremely harsh conditions 3= Can operate in relatively harsh conditions 5= cannot operate in harsh condition/can operate in normal conditions	35%	1	2	2
Complexity	Evaluation of whether the heat pipe design can be integrated into the system.	1=Integration is not complex 3= Requires effort to integrate. 5=Very hard to put into the system	20%	3	2	4
		TOTALS:	100%	82.50%	78.75%	50.00%

Table A.17 (Heat Pipes Trade Study)

Electrical Heaters						
Criteria	Explanation	Grade	Weight	KHLVA, PLM-Ser ies	SHK Series	Polyimi de Thermof oil HK Series
Power	PWR.01(W/cm^2)	1= low power consumption 3= moderate power consumption 5= high power consumption	30%	1	1	3
Mass	SYS.04(kg) Must be lightweight and easy to integrate.	1= lightweight and easy to integrate 3= moderate weight and requires some effort for integration 5= heavy and requires changing the system for integration.	25%	1	1	1
TRL	Evaluation of the technology-readiness level of the proposed electrical heater.	1 = Satisfactory TRL (TRL 5-6>>) 3 = Moderate TRL (TRL 3-4) 5 = Low TRL (TRL 1-2)	20%	1	1	1
Temperature Range	(SYS.02).	1= satisfactory temperature limit 3= smaller margin of the temperature limit 5= not a great temperature limit/does not fit the operating temperature range.	25%	1	2	1
		TOTALS:	100%	75.00%	68.75%	60.00%

Table A.18 (Electrical Heaters Trade Study)

Thermal Sensors						
Criteria	Explanation	Grade	Weight	Thermocouple	Thermistor	RTD sensors
Sensitivity	A measure of how sensitive the sensor is to small temperature changes	1: Exceptionally sensitive 3: Moderately sensitive 5. Low sensitivity	25%	5	1	3
Accuracy	The expected error range for the product	1: Exceptionally accurate to decimal places 3: Acceptably accurate with a margin of error of 1 or 2 degrees 5. The margin of error is exceptionally high	20%	3	3	5
Reliability	Evaluation of its ability to withstand long term missions	1: Very reliable 5: Minimally reliable	25%	1	4	3
Response Time	Measure of how fast the sensor can detect a temperature change	1: High 3: Medium 5: Low	30%	4	4	3
		TOTALS:	100%	34.00%	39.00%	32.00%

Table A.19 (Thermal Sensors Trade Study)

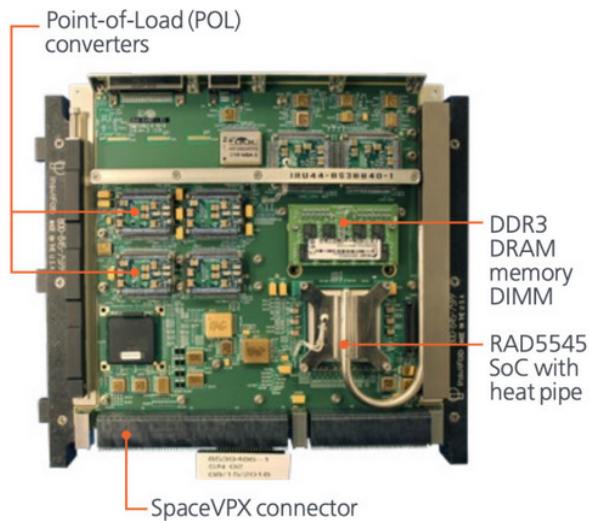


Figure A.20 (RAD5545 SpaceVPX single-board computer)

Pin 1	TXD-
Pin 2	TXD+
Pin 3	RTS-
Pin 4	RTS+
Pin 5	GND
Pin 6	RXD-
Pin 7	RXD+
Pin 8	CTS
Pin 9	CTS+

RS422/485 Pinout (9 Pin)

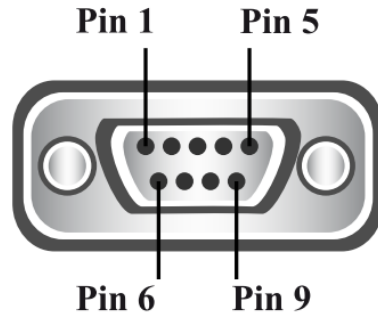


Figure A.21 (RS-422 Pinout Table)